

# **RICHARDS BAY ZIRCON**

by

Kevin John Pietersen

Submitted in fulfilment of the  
requirements for the degree of  
Masters of Science,  
in the  
Department of Geology and Applied Geology,  
University of Natal  
1992

Durban  
1992

## RICHARDS BAY ZIRCON

### ABSTRACT

Zircon from the zircon concentrate of Richards Bay Minerals was investigated with a view to understanding the morphology and provenance. The observations were applied to the reduction of uranium, thorium and other trace elements in the heavy mineral placer deposits. It is evident from differences in morphology, optical characteristics, cathodoluminescence, inclusion types and trace element analyses that the zircon is derived from numerous parent rocks. Rare earth element modelling reveals several possible parent rocks including rhyolites, granites, syenites, pegmatites and carbonatites.

Fission track U mapping of individual zircons indicated an enrichment of U in the rims and grain terminations. The U maps were used to devise and test several methods, including abrasion and partial dissolution, to reduce the combined U and Th concentration from 450-563ppm to below 400ppm. The effect of magnetic cleaning, density separation and size classification of the zircon concentrate on the U+Th concentration was found to be negligible. Air abrasion and HF acid dissolution successfully reduced the U+Th concentrations to between 332 and 383ppm.

The contribution of trace elements from inclusions, surface pit fillings and coatings, and foreign minerals within the zircon concentrate were evaluated by scanning electron microscope identification.

## PREFACE

The research described in this thesis was carried out in the Department of Geology and Applied Geology, University of Natal, Durban, from February 1991 to December 1992, under the supervision of Professor D.H. Cornell.

These studies represent original work by the author and have not been submitted in any form to another University. Where use was made of the work of others it has been duly acknowledged in the text.

## ACKNOWLEDGEMENTS

My sincere thanks to Richards Bay Minerals who sponsored this study. With special thanks to Mr J. Selby of RBM who initiated the project in 1990. I express my sincere gratitude to Prof. D.H. Cornell for his supervision, his time, and for his assistance in editing the drafts for this manuscript.

I would also like to thank:

Mr V. Hugo and all the technical staff at RBM for the questions and discussions every three months, and for being a polite and patient audience.

Ms L. Turner for her assistance and making abrasion equipment available for my use.

Prof. I. Rust and Mr J. Hattingh for their introduction to the superpanner.

Dr R. Hart at the Schonland Centre for the irradiation of the samples for fission track mapping.

Dr A. Maslenikov for the hydrothermal treatment.

Mr G. Chetty and Mr V."Moodley" Pakkiri for technical advice.

My father R. Pietersen and my brother A. Pietersen for their assistance in repairing the tumbler, the superpanner and the construction of the electromagnet density measurer.

Mr P. Evers and Ms F. Graham for their help with the SEM.

and finally, but not least, Ms A. Turner without who's help this manuscript would never have been completed on time. Thank you for your support.

## UNITS, SYMBOLS & ABBREVIATIONS

A	.....	Ampere
Å	.....	Ångström (1Å = 10 <sup>-4</sup> µm)
µA	.....	Micro-ampere
AB	.....	Abrasion
BSE	.....	Backscattered electrons
CL	.....	Cathodoluminescence
CS	.....	COMPLEX S-type zircon morphology
Ce/Ce*	.....	Cerium anomaly
D	.....	D-type zircon morphology
Eu/Eu*	.....	Europium anomaly
G1	.....	G1-type zircon morphology
HF	.....	Hydrofluoric acid
HF-AR	.....	Hydrofluoric aqua-regia acid mix
ICP-MS	.....	Inductively coupled plasma-mass spectrometer
kbar	.....	Kilobars
LP	.....	LOWER P-type zircon morphology
LREE	.....	Light rare earth element (La,Ce,Pr,Nd,Sm)
HREE	.....	Heavy rare earth element (Gd,Tb,Dy,Ho,Er,Tm,Yb,Lu)
NM	.....	Non-magnetic
PPM	.....	Parts per million
RBM	.....	Richards Bay Minerals
REE	.....	Rare earth element (La-Lu)
rpm	.....	Revolutions per minute
SEM	.....	Scanning electron microscope
SD	.....	Standard Deviation
SG	.....	Specific gravity
SS	.....	SIMPLE S-type zircon morphology
UP	.....	UPPER P-type zircon morphology
ZC	.....	Zircon Concentrate
ZCP	.....	Zircon Concentrate Product

## LIST OF FIGURES

- FIGURE 1.01:** Locality of the Richards Bay Minerals lease area.
- FIGURE 1.02:** Zircon separation flow-diagram after Hugo (1988).
- FIGURE 1.03:** Resources and annual production of the zircon producing countries. Data from Towner (1992).
- FIGURE 1.04:** Destinations of zircon produced in South Africa. Data from Towner (1992).
- FIGURE 2.01:** Zircon morphology classification of Pupin and Turco (1972) after Pupin (1980).
- FIGURE 2.02:** Faces and traces, Miller indices.
- FIGURE 2.03:** Modified and simplified version of Pupin's (1980) zircon morphology classification scheme.
- FIGURE 2.04:** Chondrite normalised REE profiles of the average, minimum and maximum from the literature.
- FIGURE 2.05:** Partition coefficients for zircon/magma from the literature, see the text for details.
- FIGURE 2.06:** Chondrite normalised REE profiles for several zircons from the literature.
- FIGURE 2.07:** Chondrite normalised REE profiles for lunar and meteorite zircons. Data from Ireland and Wlotzka (1992).
- FIGURE 2.08:** The chondrite normalised REE profile of monazite. Data from Rapp and Watson (1986).
- FIGURE 2.09:** The chondrite normalised REE profile of xenotime. Data from Åmli (1975)
- FIGURE 3.01:** Chondrite normalised REE of the source zircon and monazite from RBM.
- FIGURE 3.02:** Chondrite normalised REE profile of ZC-B91 NM compared to minimum, maximum and average values from the literature mentioned in Chapter 2.
- FIGURE 3.03:** Chondrite normalised REE profile of MP-891 compared to the minimum and maximum values of Rapp and Watson (1986).
- FIGURE 3.04:** Chondrite normalised REE profiles demonstrating precision of bulk samples: (A) BULLSRUN, (B) 125-250; and 100-grain sample (C) BULBOUS.
- FIGURE 3.05:** Chondrite normalised REE profiles of standards demonstrating accuracy, ICP-MS values and standard values from Govindaraju (1989): A) JB-1; B) W-1.
- FIGURE 3.06:** Calibration curves for three isotopes analysed on the ICP-MS, (A)  $^{238}\text{U}$ , (B)  $^{172}\text{Yt}$ , (C)  $^{151}\text{Eu}$ .
- FIGURE 4.01:** Distribution of crystal type with size.
- FIGURE 4.02:** Comparison of crystal type to colour, each zircon type calculated to 100%.
- FIGURE 4.03:** Distribution of the number of inclusions with size.
- FIGURE 4.04:** Comparison of crystal type with the number of inclusions in each type (each type calculated to 100%).
- FIGURE 4.05:** X-ray EDS spectrums for 6 types of inclusion in zircon: A) Ilmenite; B) Mn-Ilmenite; C) Apatite; D) Pyrite; E) Biotite; F) Alumina-silicate (Clay).
- FIGURE 4.06:** A) Sector zoning; B) Oscillatory zoning superimposed on sector zoning.
- FIGURE 4.07:** Calibration curve for the magnetic fluid micro-particle density measuring apparatus.
- FIGURE 5.01:** Chondrite normalised REE profile for D-type zircon, tabular P4-type and coloured D- and P-types.
- FIGURE 5.02:** Comparison of chondrite normalised REE profiles of large D-type zircon containing ilmenite (DINCL-1) and miscellaneous inclusions (DINCL-2).
- FIGURE 5.03:** Chondrite normalised REE profiles of the bulbous frosted zircon with high U and Th concentrations.

**FIGURE 5.04:** Chondrite normalised REE profiles of the metamict zircon.

**FIGURE 5.05:** Chondrite normalised REE profiles of the metamict zircon from Bull's Run.

**FIGURE 5.06:** Chondrite normalised REE profiles of the average values for the clear zircon, metamict zircon, bulbous zircon and Bull's Run zircon.

**FIGURE 5.07:** Chondrite normalised REE profiles of: A) Lebombo Rhyolite (Erlank, 1984 and Harris and Erlank, 1992); B) Wangu gneisses and biotite dykes and Ngoye gneiss (Scoggings, 1989); C) Bull's Run Carbonatites (Scoggings and Forster, 1989).

**FIGURE 5.08:** Chondrite normalised REE profiles of: A) Average granulite and amphibole gneiss (Weaver and Tarney, 1981); B) Granite fractionation series, pyroxene granite to leucogranite (Petersen, 1980); C) Granite fractionation series (Ward *et al.* 1992).

**FIGURE 5.09:** The partitioning of REE between major and accessory minerals in the coarse grained megacrystic biotite Dartmoor granite (From Ward *et al.*, 1992).

**FIGURE 5.10:** The chondrite normalised calculated REE profiles of source rocks for the D, P4 and COLOURED zircon with partition coefficients from: A) Dacites (Nagasawa, 1970); B) Granites (Nagasawa, 1970); C) Charnockite (Murali *et al.*, 1983); D) Felsic melt (Watson, 1980); E) Andesites and Diorites (Fujimaki, 1986); F) Average of the literature (Hinton & Upton, 1991); Calculated theoretical values (Hinton & Upton, 1991).

**FIGURE 6.01:** Comparison of U and Th concentrations in the starting material and the three acid dissolution experiments.

**FIGURE 6.02:** Chondrite normalised REE profiles of the starting material and the three acid dissolution products.

**FIGURE 6.03:** Chondrite normalised REE profiles of the starting material ZCP and the abraded product.

**FIGURE 6.04:** Comparison of U and Th concentrations in the starting material, HF acid treated material and the abraded and HF acid treated material.

**FIGURE 6.05:** Comparison of U and Th concentrations in the starting material, HF-AR acid treated material and the abraded and HF-AR acid treated material.

**FIGURE 6.06:** Element loss profile corrected for mass loss of the HF acid treated and air abraded products.

**FIGURE 6.07:** Element loss profile corrected for mass loss of the HF-AR acid treated and air abraded products.

**FIGURE 6.08:** Element loss profile corrected for mass loss of the air abraded product.

**FIGURE 6.09:** Comparison of U and Th concentrations in the starting material, the high density and low density separates.

**FIGURE 6.10:** Chondrite normalised REE profiles of the starting material and the high and low density separates.

**FIGURE 6.11:** Chondrite normalised REE profiles of ZC-B91 NM, the <90 $\mu\text{m}$  and >125 $\mu\text{m}$  size fractions.

**FIGURE 6.12:** Distribution of by mass of the 1.7A magnetic fraction of ZC-B91.

**FIGURE 6.13:** Distribution of by mass of the 1.6A Eriez magnetic fraction into 0.3A fractions on the Frantz.

**FIGURE 6.14:** Chondrite normalised profiles of 0.7A magnetic fraction and the non-magnetic ZC-B91.

**FIGURE 6.15:** Chondrite normalised profiles of ZCP-892, the magnetic fraction of ZCP-892 and the RBM monazite MP-691.

**FIGURE 6.16:** Comparison of U + Th concentrations of starting material and the treated products: (1) ZCP-892, (2) ZCP ABRADED, (3) ZC-B91 NM, (4) ZC HF DISSOLUTION, (5) ZC HF DISSOLUTION & ABRASION, (6) ZC HF-AQUA REGIA DISSOLUTION, (7) ZC HF-AQUA

*REGLA* DISSOLUTION & ABRASION, (8) LOWEST (100% D-TYPE).



## LIST OF PLATES

- PLATE 1.01:** Transmission light photomicrograph of the zircon concentrate (Bar is 200 $\mu$ m long).
- PLATE 4.01:** SEM BSE image of a zircon containing three unidentified inclusions (SEM 120813). The scale is shown at the bottom of the photograph.
- PLATE 4.02:** A 150 $\mu$ m long zircon containing multiple inclusions.
- PLATE 4.03:** SEM BSE image of a metamict zircon polished thin section containing numerous inclusions.
- PLATE 4.04:** SEM BSE image of a zircon containing a unidentified inclusion.
- PLATE 4.05:** SEM photomicrograph of a clay-filled open-mouthed pit in a zircon. Note the cracks in the surface coating over the clay-filling (SEM 120828).
- PLATE 4.06:** SEM photomicrograph of a D-type zircon with a large open pit filled with clay and covered by a coating which contains numerous pits (SEM 120849).
- PLATE 4.07:** SEM photomicrograph of a elongate S24-type zircon with a clay-filled pit with a constricted mouth (SEM 150517).
- PLATE 4.08:** SEM BSE image showing a section through an inclusion that intersects the surface of the zircon grain (SEM 120805).
- PLATE 4.09:** SEM photomicrograph close-up of a pit filled with clay platelets (SEM 150518 close-up of Plate 4.07).
- PLATE 4.10:** SEM photomicrograph of a cross-section of a clay-filled pit (SEM 120809).
- PLATE 4.11:** The iron-coated clay filling in a pit in a 100 $\mu$ m zircon grain before washing (A); and after washing in acid in a ultrasonic bath (B).
- PLATE 4.12:** Cathodoluminescence emission of a 110 $\mu$ m zircon with crystal growth zones (100), (101) and (211) identified, a zircon grain with a complex history.
- PLATE 4.13:** Cathodoluminescence emissions of a 120 $\mu$ m zircon showing a complex growth history.
- PLATE 4.14:** Two zircons with different origins: A) a fragment of an oscillatory growth zoned zircon; B) A fragment of a narrowly oscillatory zoned zircon.
- PLATE 4.15:** An oscillatory zoned zircon.
- PLATE 4.16:** Fission track distribution of U in a zircon, with enrichment of U in the pyramids (A) and rims (B) relative to the core (C).
- PLATE 4.17:** Fission track distribution of U in a grain with 4 (A-B) different growth zones, each with different uranium concentrations.
- PLATE 4.18:** Fission track distribution of U in a zircon with a U-poor overgrowth (A) compared to the U-rich core (B).
- PLATE 4.19:** Fission track distribution of U in a zircon with U-rich pyramids.
- PLATE 4.20:** Fission track distribution of U in a zircon with U-rich pyramids.
- PLATE 4.21:** Fission track distribution of U in a zircon with a U-rich inclusion within a U-poor core with a U-rich overgrowth.
- PLATE 4.22:** Transmitted light photomicrograph of the zircon in Plate 4.21 before it was polished.
- PLATE 6.01:** A SEM photomicrograph close-up of HF-pitted zircon, with a resistant rim.(SEM 220925).
- PLATE 6.02:** A SEM photomicrograph showing the preferential loss of alternating zones in the interior of a zircon from HF dissolution (SEM 220914).
- PLATE 6.03:** A SEM close-up of PLATE 6.02 clearly showing the dissolution of alternating grains (SEM 220909).
- PLATE 6.04:** A SEM photomicrograph of the interior of a zircon showing the preferential dissolution of alternating zones (SEM 220926).
- PLATE 6.05:** A SEM photomicrograph of the pitted surface of a zircon after HF dissolution (SEM 220911).
- PLATE 6.06:** A SEM photomicrograph of a S18-S19 zircon which shows increased dissolution along the traces where abrasion has occurred in the past (SEM 220912).
- PLATE 6.07:** A SEM photomicrograph showing the smooth-empty pit the was most likely filled with clay before HF partial dissolution (SEM 220910).
- PLATE 6.08:** A SEM photomicrograph of a naturally leached zircon. The darker zones show preferential leaching compared to the light zones (SEM 120803).
- PLATE 6.09:** A SEM photomicrograph of naturally leaching in metamict zircon (SEM 120806).

**PLATE 6.10:** A SEM photomicrograph of the naturally pitted surface of the grain in Plate 6.07 and 6.08 (SEM 120854).

**PLATE 6.11:** A SEM photomicrograph of pitting in alternating zones superimposed on the sector growth zones of a metamict zircon (SEM 120822).

**PLATE 6.12:** The slow-speed tumbler used in the wet abrasion experiments.

**PLATE 6.13:** The high-speed attrition-cell used in the wet abrasion experiments.

**PLATE 6.14:** The air-abrasion mill used in the air abrasion experiments. Designed after Krogh (1982).

**PLATE 6.15:** The components of the air abrasion mill, made to the same parameters as the mill used by Krogh (1982) for decreasing the discordance of dated zircons.

**PLATE 6.16:** A SEM photomicrograph of an experimental air abraded pyramid of a zircon (SEM 220917).

**PLATE 6.17:** A SEM photomicrograph of an experimentally air abraded zircon showing the lozenge shape, indicative of air abraded elongate zircons (SEM 220923).

**PLATE 6.18:** A SEM photomicrograph of an experimentally air abraded zircon showing the spherical shape, indicative of air abraded grains with low L/B values (SEM 220916).

**PLATE 6.19:** A close-up SEM photomicrograph of the surface of an experimentally air abraded zircon. Note the percussion marks. (SEM 220918).

**PLATE 6.20:** A close-up SEM photomicrograph of the surface of a naturally abraded metamict zircon (SEM 280818). Note the parallel ridges of percussion marks.

**PLATE 6.21:** The superpanner used for separation of high and low density separates.

## LIST OF TABLES

- TABLE 1.01:** World resources of economically mineable zircon (1000 metric tonnes) (Calculated and compiled from Towner, 1992).
- TABLE 1.02:** South African heavy mineral placer deposits that include zircon (Compiled and calculated from Towner (1992))
- TABLE 2.01:** Minimum, maximum and average values of zircon compiled from the literature.
- TABLE 2.02:** Partition coefficients for zircon from andesites and diorites (Fujimaki, 1986).
- TABLE 2.03:** Zircon/matrix partition coefficients for rare earth elements for dacites and rhyolites from Nagasawa (1970); and the calculated and average literature values from Hinton and Upton (1991).
- TABLE 2.04:** Experimentally derived partition coefficients from a peralkaline felsic melt (Watson, 1980).
- TABLE 2.05:** Monazite composition. Data from Rapp and Watson (1986).
- TABLE 2.06:** Xenotime analyses from Åmli (1975).
- TABLE 3.01:** Summary of rock standards used to calibrate the ICP-MS zircon and monazite analyses.
- TABLE 3.02:** ICP-MS element results for the zircon source material ZC-B91 NM and ZCP-892, and the monazite bulk sample MP-891.
- TABLE 3.03:** Summary of REE Calculations.
- TABLE 3.04:** ICP-MS element results for duplicate samples.
- TABLE 3.05:** ICP-MS element results for rock standards compared to the standard values of Govindaraju (1989).
- TABLE 4.01:** Distribution of state: metamict, coloured and clear.
- TABLE 4.02:** Distribution of crystal types in the bulk and size fractions.
- TABLE 4.03:** The distribution of crystal state in each crystal type group.
- TABLE 4.04:** Length/Breadth ratios distributions in the bulk and size fractions.
- TABLE 4.05:** Distribution of the number of inclusions within the bulk sample and sieve fractions (Excluding grains where inclusions could not be counted either from a frosted surface or opaqueness).
- TABLE 4.06:** Distribution of the number of inclusions compared to crystal type.
- TABLE 4.07:** Minerals identified as inclusions in zircon in the literature.
- TABLE 4.08:** List of minerals identified as inclusions in zircon.
- TABLE 4.09:** Analyses of zoned and unzoned portions of single zircons (Pidgeon, 1992).
- TABLE 5.01:** Y, REE, U and Th concentrations in clear zircon.
- TABLE 5.02:** Y, REE, U and Th concentrations in bulbous frosted zircon.
- TABLE 5.03:** Y, REE, U and Th concentrations in metamict zircon.
- TABLE 5.04:** Y, REE, U and Th concentrations in the metamict zircon from Bull's Run.
- TABLE 5.05:** Cerium, Europium anomalies and HREE concentrations in zircon and their related source rocks.
- TABLE 5.06:** Summary of the average Y, REE, U and Th concentrations in clear, frosted bulbous, metamict and Bull's Run zircon.
- TABLE 6.01:** Y, REE, Th and U results for the acid dissolution and air abrasion experiments.
- TABLE 6.02:** Parameters of abrasion methods described in the literature.
- TABLE 6.03:** Air abrasion experiment parameters and mass losses.
- TABLE 6.04:** Air abrasion results for the acid leached zircon.
- TABLE 6.05:** Y, REE, Th and U results for the starting, high density and low density material separated on the superpanner.
- TABLE 6.06:** The U, Th and Pb results of two size fractions of zircon classified by the mineral from which they were extracted (Aleinikoff, 1983).
- TABLE 6.07:** Y, REE, Th and U results for the size fractions.
- TABLE 6.08:** Point counting of the 0.7A and 1.0A magnetic fractions.
- TABLE 6.09:** Point counting results for the magnetic fractions of ZC (Percent).
- TABLE 6.10:** Y, REE, Th and U results for the source material and the magnetic fractions.
- TABLE 6.11:** Non-zircon SEM identified minerals in the 1.4A magnetic fraction and their approximate proportions (Cornell and Pietersen, 1992).

## LIST OF CONTENTS

ABSTRACT	...	i
PREFACE	...	ii
ACKNOWLEDGEMENTS	...	iii
UNITS, SYMBOLS AND ABBREVIATIONS	...	iv
LIST OF FIGURES	...	v
LIST OF PLATES	...	viii
LIST OF TABLES	...	x
<b>CHAPTER 1 - INTRODUCTION</b>		
1.1 INTRODUCTION	...	1
1.2 MINING AND CONCENTRATION OF ZIRCON	...	3
1.3 PRODUCTION AND MARKETS	...	3
1.4 AIM OF STUDY	...	7
<b>CHAPTER 2 - ZIRCON LITERATURE REVIEW</b>		
2.1 MORPHOLOGY AND CLASSIFICATION SCHEMES	...	9
2.1.1 LENGTH/BREADTH AND SIZE CLASSIFICATION SCHEMES	...	9
2.1.2 FOURIER SHAPE ANALYSIS	...	10
2.1.3 PUPIN'S TYPOLOGY CLASSIFICATION OF ZIRCON	...	10
2.1.4 CLASSIFICATION SCHEME USED IN THIS STUDY	...	13
2.2 ZIRCON CHEMISTRY	...	15
2.2.1 YTTRIUM AND RARE EARTH ELEMENTS	...	16
Chondrite Normalised Profiles	...	20
Cerium Anomalies (Ce/Ce')	...	23
Eu Anomalies (Eu/Eu')	...	23
2.2.2 URANIUM AND THORIUM	...	23
2.2.3 U, Th AND THE REE IN MONAZITE	...	24
2.2.4 Y AND REE IN XENOTIME	...	26
<b>CHAPTER 3 - METHODS OF ANALYSIS</b>		
3.1 INDUCTIVELY COUPLED PLASMA - MASS SPECTROMETER	...	28
3.2 SAMPLE PREPARATION	...	28
3.2.1 LARGE BULK SAMPLES	...	29
3.1.2.1 DIFFICULTIES WITH BULK SAMPLE PREPARATIONS	...	29
3.2.2 100-GRAIN SAMPLES	...	29
3.2.2.1 DIFFICULTIES AND SOLUTIONS WITH 100-GRAIN PREPARATION	...	30
3.3 ROCK STANDARDS	...	31
3.4 SOURCE OF ZIRCON SAMPLES	...	31
3.5 DESCRIPTION OF ANALYSES OF THE STARTING MATERIAL	...	32
3.6 A COMMENT ON DISCONTINUED ISOTOPES	...	35
3.7 A NOTE ON THE REE, U AND Th ICP-MS RESULTS	...	36
<b>CHAPTER 4 - GENERAL ATTRIBUTES OF THE ZIRCON CONCENTRATE</b>		
4.1 POINT COUNTING	...	43

4.1.1	COLOUR DISTRIBUTION OF ZIRCON	... 44
4.1.2	DISTRIBUTION OF CRYSTAL TYPES	... 44
4.1.3	COMPARISON OF CRYSTAL TYPE TO COLOUR OF THE CRYSTAL	... 46
4.1.4	ELONGATION COMPARED TO SIEVE FRACTION AND CRYSTAL STATE	... 47
4.1.5	DISTRIBUTION PATTERNS OF INCLUSIONS IN ZIRCON	... 48
4.1.6	DISCUSSION OF POINT COUNTING	... 50
4.2	BACKSCATTERED ELECTRON IMAGERY	... 50
4.2.1	BSE METHOD AND RESULTS	... 51
4.3	INCLUSIONS IN ZIRCON	... 52
4.3.1	LITERATURE ON INCLUSIONS IN ZIRCON	... 52
4.3.2	METHOD AND RESULTS	... 53
4.4	FILLINGS	... 54
4.4.1	LITERATURE ON GRAIN COATINGS	... 59
4.4.2	METHOD AND RESULTS	... 59
4.5	ZONING	... 62
4.5.1	LITERATURE ON ZONING IN ZIRCON	... 62
	Sector zoning in zircon	... 62
	Oscillatory growth zoning in zircon	... 63
4.5.2	CATHODOLUMINESCENCE	... 66
4.5.2.1	LITERATURE ON CATHODOLUMINESCENCE IN ZIRCON	... 66
4.5.2.2	METHOD AND RESULTS	... 66
4.6	COLOUR	... 70
4.7	FISSION TRACKS	... 70
4.7.1	LITERATURE ON NEUTRON-INDUCED FISSON TRACK ANALYSIS	... 70
4.7.2	METHOD OF FISSON TRACK ANALYSIS	... 71
4.7.3	RESULTS	... 72
4.8	DENSITY MEASUREMENT	... 77
4.8.1	PROBLEMS	... 78
 <b>CHAPTER 5 - ANALYSIS OF INDIVIDUAL ZIRCON GROUPS</b>		
5.1	CLEAR AND COLOURED ZIRCON	... 80
5.1.1	D-TYPE ZIRCON	... 80
5.1.2	P4-TYPE ZIRCON	... 80
5.1.3	COLOURED D- & P-TYPE ZIRCON	... 82
5.1.4	INCLUSIONS IN MEDIUM L/B D-TYPE ZIRCON	... 82
5.2	BULBOUS FROSTED ZIRCON	... 83
5.3	METAMICT ZIRCON	... 85
5.4	SUMMARY OF THE ANALYSES OF INDIVIDUAL ZIRCONS	... 90
5.5	PRELIMINARY PROVENANCE STUDY	... 91
 <b>CHAPTER 6 - EXPERIMENTAL REDUCTION OF U &amp; Th</b>		
6.1	PARTIAL DISSOLUTION	... 101
6.1.1	ALKALINE LEACHING LITERATURE	... 101
6.1.2	ACID AND PRESSURE LEACHING LITERATURE	... 102
6.1.3	EXPERIMENTAL LEACHING METHOD	... 103
6.1.4	LEACHING RESULTS	... 105
6.1.5	SEM PHOTOGRAPHS OF EXPERIMENTALLY LEACHED ZIRCON	... 106
6.1.6	SEM EVIDENCE FOR NATURAL LEACHING OF ZIRCON	... 113

6.2	ABRASION EXPERIMENTS	... 114
6.2.1	ABRASION EXPERIMENTS IN THE LITERATURE	... 114
6.2.2	NATURAL ABRASION IN THE LITERATURE	... 115
6.2.3	ABRASION METHODS	... 115
6.2.3.1	SLOW TUMBLER (LIQUID)	... 117
6.2.3.2	FAST ATTRITION CELL (LIQUID)	... 117
6.2.3.3	AIR ABRASION	... 118
6.2.4	AIR ABRASION RESULTS	... 119
6.2.5	SEM INVESTIGATION OF ABRASION	... 125
6.2.6	DISCUSSION OF AIR ABRASION RESULTS	... 128
6.3	SEPARATION BASED ON DENSITY AND SHAPE	... 128
6.3.1	DENSITY SEPARATION METHOD	... 129
6.3.2	SUPERPANNER RESULTS	... 130
6.4	SIZE CLASSIFICATION AND SIEVING	... 133
6.4.1	ZIRCON GRAIN SIZE LITERATURE	... 133
6.4.2	SIEVING METHOD	... 135
6.4.3	SIEVING RESULTS	... 135
6.5	MAGNETIC SEPARATION	... 137
6.5.1	MAGNETIC ZIRCON LITERATURE	... 137
6.5.2	METHOD OF THE FIRST MAGNETIC SEPARATION	... 138
6.5.3	RESULTS OF THE FIRST MAGNETIC EXPERIMENT	... 141
6.5.4	METHOD OF THE SECOND MAGNETIC EXPERIMENT	... 142
6.5.5	RESULTS OF THE SECOND MAGNETIC EXPERIMENT	... 143
6.6	EFFECT OF PROVENANCE ON U AND Th	... 144
6.7	CONCLUSION ON U AND Th REDUCTION REDUCTION METHODS	... 145

## **CHAPTER 7 - CONCLUSIONS AND FUTURE SUGGESTIONS**

## **CHAPTER 8 - REFERENCES**

## CHAPTER 1

### INTRODUCTION

#### 1.1 INTRODUCTION

Unconsolidated Holocene dunes and Pleistocene beach deposits north of Richards Bay in Natal contain heavy mineral placer deposits. These deposits contain five economic heavy minerals: ilmenite, leucoxene, rutile, zircon and monazite. The object of this study was, in brief, to gain a general understanding of the morphological and chemical attributes of the zircon concentrate (Plate 1.01) from the Richards Bay Mineral's lease area (Figure 1.01), with an emphasis on the U and Th concentrations of the zircon products. Possible methods for the reduction of U and Th were also investigated.

Zircon commonly originates in igneous rocks as an accessory mineral. Because of its high resistance to chemical and physical attack, zircon is also a common trace mineral in sedimentary and metamorphic rocks. Zircon is rarely found in economic concentrations in hard rock deposits and all present mining of zircon is in unconsolidated sediments. Economic deposits are commonly found in Quaternary alluvial, beach and dune sediments with heavy mineral concentrates between 10 and 20%. The heavy minerals usually include ilmenite, rutile, leucoxene, monazite, zircon and magnetite. No deposit in the world is mined solely for zircon. Zircon is usually a co- or by-product of ilmenite or rutile mining.

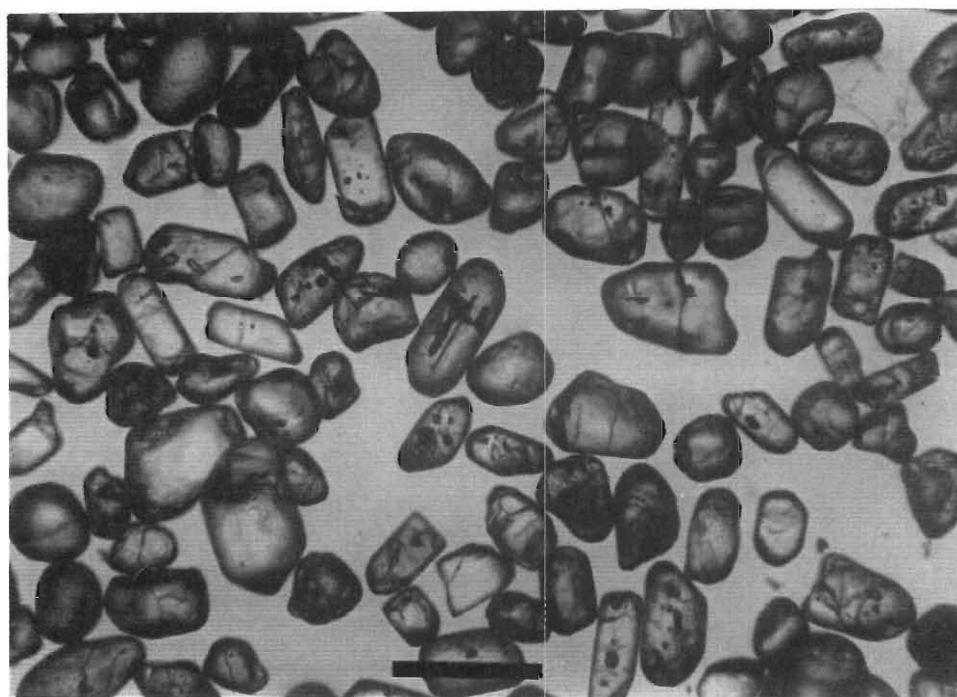


PLATE 1.01: Transmission light photomicrograph of the zircon concentrate (Scale bar: 200 $\mu$ m).

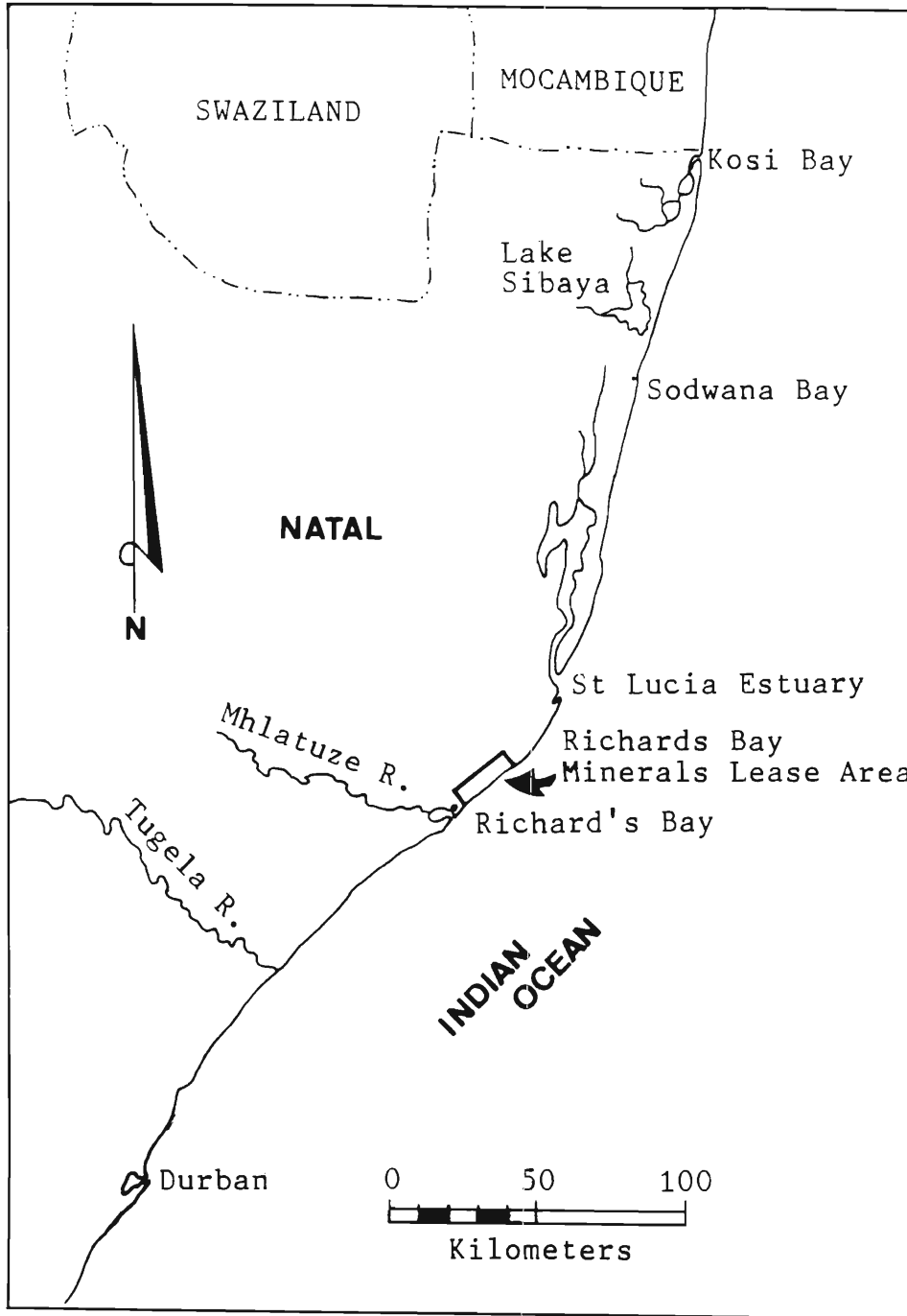


FIGURE 1.01: Locality of the Richards Bay Minerals lease area.



## 1.2 MINING AND CONCENTRATION OF ZIRCON

The suction-cutting method of mining using barges on man-made ponds is utilised in deposits with a low porosity substrate. This includes the deposits within the RBM lease area. Figure 1.02 is the flow diagram of the zircon concentration procedure. An initial heavy mineral concentrate is produced by gravimetric separation, the gangue minerals such as quartz and feldspar being pumped back to the dune reconstruction area. Further concentration and separation of the economic heavy minerals occurs in the Feed Preparation Circuit. Oversize gangue minerals are removed by screening and the magnetite is removed in a low intensity magnetic wet circuit. Following this the less magnetically susceptible ilmenite is separated by a high intensity magnetic wet circuit. The remaining heavy minerals undergo gravimetric separation and finally high intensity magnetic separation to separate monazite from the non-magnetics. The non-magnetics including rutile, zircon and leucoxene, are termed Rutile Head Feed. A high tension electrostatic separation technique is used to remove the rutile and leucoxene from the zircon.

The zircon concentrate is passed through wet gravimetric separators to remove the remaining low density gangue minerals. The zircon concentrate is then dried and passed through a smoker followed by a high tension electrostatic circuit to remove the remaining rutile. The zircon is then passed through screen-plate electrostatic separators followed by high intensity magnetic separators, the material removed by the magnetic separators being returned to the rutile circuit. The zircon concentrate (ZC) is then cleaned using sulphuric acid and passed through a final high intensity magnetic separator to produce the zircon concentrate product (ZCP). The ZC and the ZCP were sampled for this study.

## 1.3 PRODUCTION AND MARKETS

Reviews of production and the export and import trade of zircon are given by Towner (1992), Garnar (1989), and for the comparison of the change in markets since 1972/3 see Klemic *et al.* (1973).

Zircon ( $ZrSiO_4$ ) is a zirconium silicate which is the prime commercial zirconium bearing mineral. The principal uses of zircon sand or flour are in the production of ceramics, as refractories, abrasives, welding fluxes and high temperature mold linings. Garnar (1989) divided the uses of zircon for 1977 as follows:

Foundry sands	35%
Refractories	28%
Flour	20%
Abrasives	5%
Other	12%

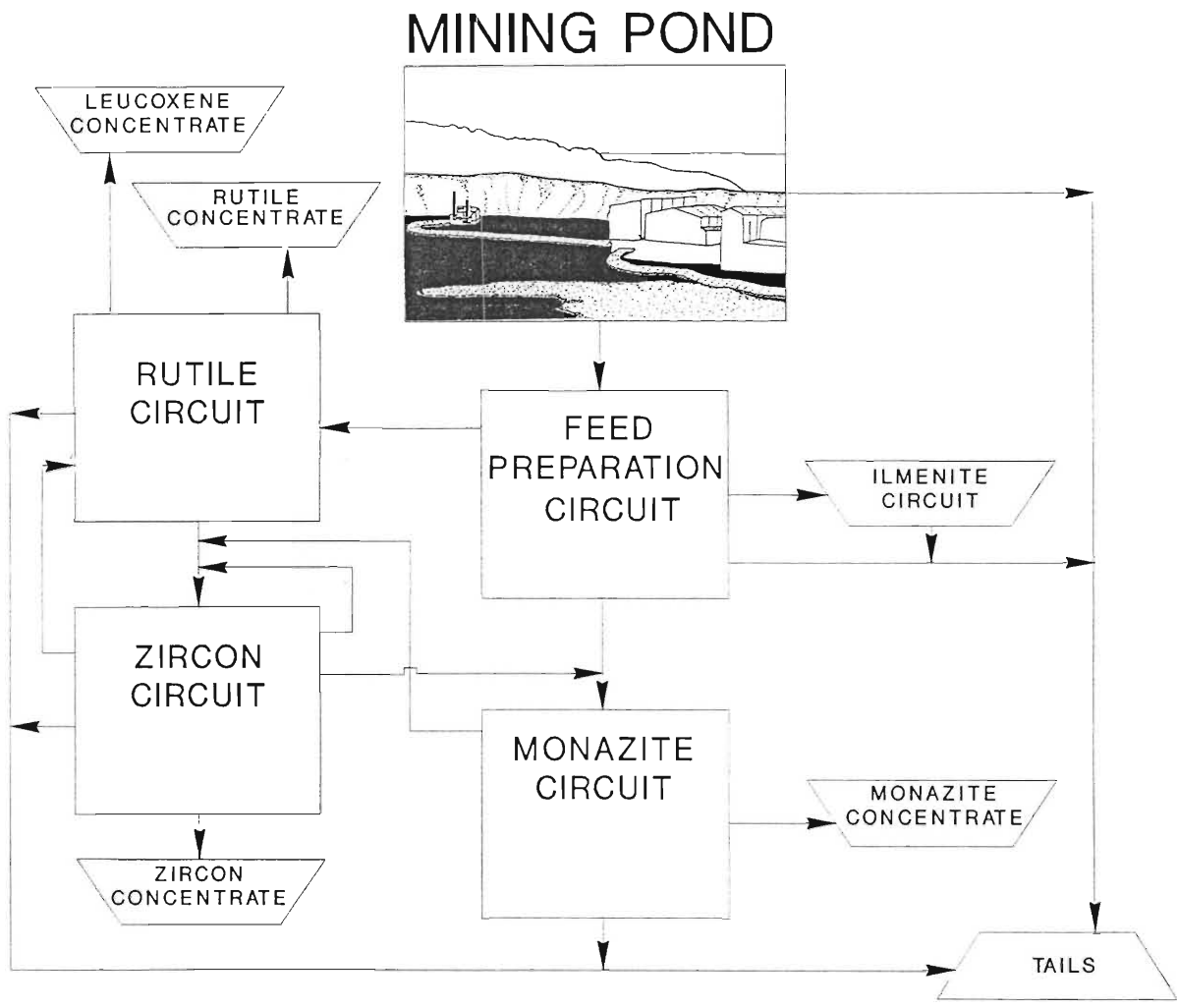


FIGURE 1.02: Zircon separation flow-diagram after Hugo (1988).

Zirconia ( $ZrO_2$ ), made by decomposing zircon, is used in nuclear shielding, corrosion resistant surfaces, photo-flashes, tanning, textile waterproofing, paint driers, medicinals, ceramics and in refractories. The market for micronized zircon or zircon flour is growing. The micronized zircon gives a satin finish to tiles and ceramics.

The approximate price of zircon dropped in 1992 to A\$150 (1992) per metric ton from the mid-1988 high of A\$600 (exchange rate, December, 1992: R1=A\$2.08). The price is presently back to the 1983 price of A\$420 per ton.

Australia and South Africa are the two largest producers and exporters of zircon, with a combined output of 70% of the world production, with the USA and CIS (former Soviet Union) producing a combined 20%. The world reserves of zircon are estimated to be 51 million tonnes (US Bureau of Mines, 1988). The economically exploitable resources of zircon of countries with heavy mineral placer deposits total 39 112 000 metric tonnes (see Table 1.01 and Figure 1.03) (Towner, 1992).

**TABLE 1.01:** World resources of economically mineable zircon (1000 metric tonnes) (Calculated and compiled from Towner, 1992).

Country	Resource(kt)	Annual (1987) Production(kt)	Cumulative (1925-1987) Production(kt)
South Africa	11 443	150	1 332 <sup>1</sup>
Australia	10 233	457	10 493
United States	5 900	86	2 321
India	3 560	16	234
Madagascar	3 000	0	3
Brazil	2 831*	15	213 <sup>1</sup>
China	1 428	15	111
Sri Lanka	400	1	34
Mozambique	316	0	0
Other	-- ---	19	178
CIS	-- ---	69	852 <sup>1</sup>
<b>Total:</b>	<b>39 112</b>	<b>835</b>	<b>15 770</b>

\*: Includes Baddeleyite and Caldasite.

<sup>1</sup>: Includes Baddeleyite

Towner (1992) names seven zircon deposits in South Africa (see Table 1.02) however only the northern Natal Coast is currently producing zircon. The mining of zircon on the West Coast is in the preliminary stages of development. Mining of zircon on the West Coast commenced at the beginning of November 1992.

**TABLE 1.02:** South African heavy mineral placer deposits that include zircon (Compiled and calculated from Towner (1992))

Locality	Ore (1000t)	Zircon (1000t)	Zircon Grade(%)
Bothaville	34000	884	2.6
Cape Morgan	64000	160	0.25
Ciskei Coast	64000	160	0.5
North Natal Coast	1 694000	10 164	0.6
Transkei Coast	249000	1 494	0.6
Umgababa	44000	572	1.3
West Cape Coast	100000	1 500	1.5

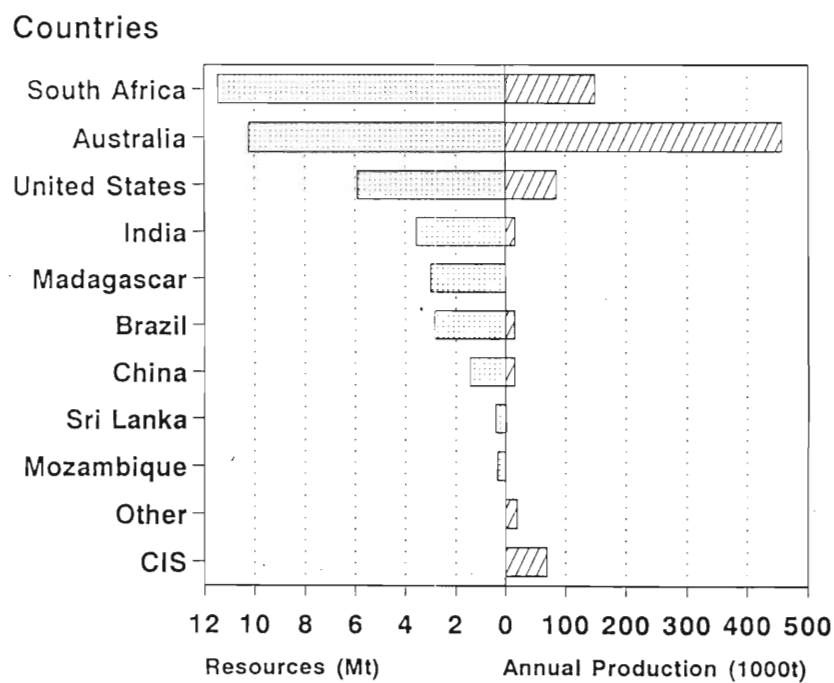


FIGURE 1.03: Resources and annual production of the zircon producing countries. Data from Towner (1992).

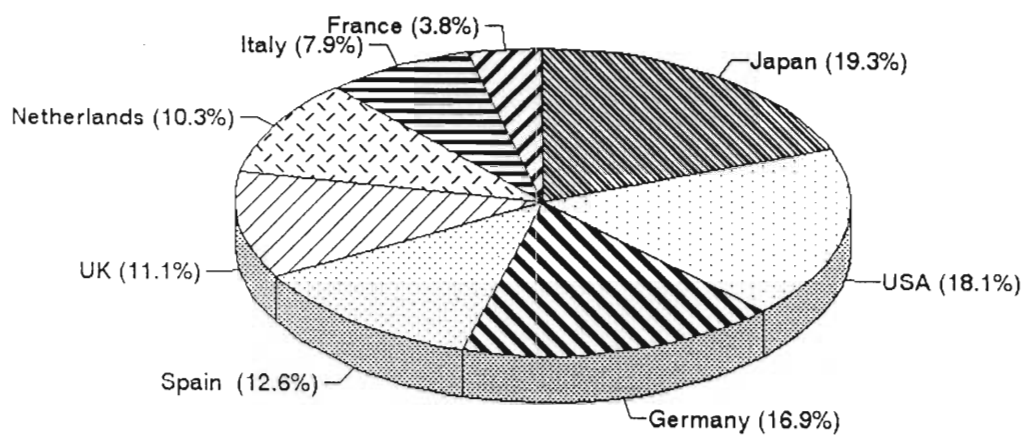


FIGURE 1.04: Destinations of zircon produced in South Africa. Data from Towner (1992).

All the South African deposits are Holocene or Pleistocene except for the Bothaville deposit which is a hardrock Permo-Carboniferous deposit in the Ecca formation. To date only three of the deposits have produced zircon concentrate, 126 000 tons from Cape Morgan, 1 300 000 tons from Natal North Coast, 47 000 tons from Umgababa, Natal South Coast and minor production of the West Cape Coast deposits.

In 1988 according to the British Geological Survey (1989) Japan was the largest importer of zircon with 197 592 metric tons (1989: 172 848t), with Italy being second with an annual import of 82 863 metric tons (1989: 84 814t).

In 1987 or 1988 South Africa (1987 value given if 1988 value was unavailable) exported the following tonnages according to Towner (1992) (Figure 1.04):

24 800 tons to Japan  
 23 300 tons to the USA  
 21 800 tons to Federal Republic of Germany (1987)  
 16 200 tons to Spain (1987)  
 14 300 tons to United Kingdom  
 13 300 tons to Netherlands  
 10 200 tons to Italy (1987)  
 4 880 tons to France

The oversupply of zircon concentrate on the world markets has resulted in competition between zircon producers. A zircon concentrate with the lowest impurities such as U and Th will sell best on the world market.

#### 1.4 AIM OF STUDY

The aim of the study was to obtain a general understanding of the morphological and chemical properties of zircon from Richards Bay Minerals with emphasis on the nature and the source of the impurities within the bulk zircon products. This information was to be used to plan and evaluate several experiments aimed at reducing the combined uranium (U) and thorium (Th) levels in the zircon concentrate and the zircon concentrate product from 550ppm to below 400ppm.

The project involved the regular analysis of U and Th in the zircon concentrate with detailed examination of the yttrium and the rare earth elements (REE), and a cursory examination of the elements such as Mg, Ti, Rb, Sr, Nb, Ta, Zr and Hf.

An initial study of the physical and chemical attributes of zircon was necessary to enable a meaningful interpretation of the results. A classification scheme for the detrital zircons had to be devised and implemented. Several systems of categorizing zircons were tested and finally a simplified version of Pupin's (1980) classification proved suitable and was applied to the detrital zircons.

The next step the identification and assessment of the abundance of inclusions, fillings and other heavy minerals and gangue minerals still present within the zircon concentrate.

An understanding of the distribution and quantity of U and Th within the zircon grains and the zircon concentrate was essential before the reduction of U and Th was attempted. Fission track mapping was considered the best method for establishing the U distribution in individual grains. Analyses of U, Th and REE by ICP-MS was used on individual zircon populations and bulk samples to evaluate starting materials and the results of experiments. Experiments with the aim of reducing the U and Th levels of zircon were planned and undertaken using the results of the aforementioned studies. The experiments included acid treatment, abrasion, acid treatment combined with abrasion, density separation, magnetic separation and size separation and a cursory look at provenance. The contribution to the total levels of U, Th, Y and the REE by several individual zircon types was also evaluated.

## CHAPTER 2

### ZIRCON LITERATURE REVIEW

#### 2.1 MORPHOLOGY AND CLASSIFICATION SCHEMES

Zircon is one of the few minerals on which morphology studies are commonly performed. Several methods of quantifying morphology, and using the results as petrographic indicators, are reported in the literature.

##### 2.1.1 LENGTH/BREADTH AND SIZE CLASSIFICATION SCHEMES

Length (L), breadth (B) and elongation (L/B) plots were used to differentiate zircon populations within individual or between separate rock units. Larsen and Poldervaart (1957) refined this technique by using the reduced major axis (RMA) method first described by Kermack and Haldane (1950). The RMA is an elementary statistic and graphic method of comparing bivariate populations. The RMA line plot of zircons was believed by Larsen and Poldervaart (1957) to approach the growth trend of zircon crystals, and it was therefore possible to genetically correlate zircons to specific rock units. Other authors tend to use the RMA to identify and measure sample populations instead of using the plot as an indicator of growth trends. The RMA is not the only method of comparing size and shape parameters. Hoffmann (1981) used the Chi-square test to evaluate and compare L, B and L/B-ratio data of different zircon populations.

To successfully apply the RMA or other size parameter techniques, large quantities (>200 grains) of unrounded and/or unbroken zircons are needed. The RMA method was considered an unsatisfactory method for classifying the northern Natal detrital zircons for two major reasons. Firstly the deposit contained over 50% rounded grains and a far higher percentage of broken grains. The application of the RMA method was therefore regarded to be a biased classification, with a leaning towards grains that were preferentially not rounded or broken. Inclusions, size and elongation making certain grains more susceptible to breaking. Secondly the information acquired from L, B, L/B and RMA measurements was considered to have little or no application to the major aims of the study. A cursory application of RMA to two samples (300 points each) indicated a overlapping and superimposing of several morphological types of zircon. A method of classification was required that would enable point counting and analyses of individual populations.

### 2.1.2 FOURIER SHAPE ANALYSIS

Byerly *et al.* (1975) used the harmonics obtained by Fourier analysis of 2-dimensional grain shapes to compare different zircon populations. Techniques of obtaining grain shape statistics (eg. image analysis, digitizing shape from 2-D photomicrographs) was experimented with, but were found too time consuming in relation to the usefulness of the data obtained. Such data is not genetically applicable to multi-grain analysis and does not assist in picking individual grain types for analyses. Therefore shape analysis was considered an unsatisfactory method for classifying the zircon populations in the zircon concentrate. The method may still be useful in provenance studies when comparing detrital zircons in the Natal interior or along the Natal coast.

### 2.1.3 PUPIN'S TYPOLOGY CLASSIFICATION OF ZIRCON

Pupin and Turco (1975) and Pupin (1980) used the relative dominance of principal prism and pyramid forms on zircon grains as a system of classification (Figure 2.01). The progressive steps of crystal morphology were alphanumerically named, from A to S with subtypes named from 1 to 25. Pupin's alphanumeric scheme will be used throughout this thesis to denote the different types of zircon crystals.

According to Pupin and Turco (1975) and Pupin (1980) this "typology" classification has a genetic foundation. They stated that the temperature of formation is the dominant control on the relative proportions of the {100} and {110} prisms, while the aluminosity (ie.  $(\text{Na}_2\text{O} + \text{K}_2\text{O})/\text{Al}_2\text{O}_3$ ) of the magma controls the proportions of {101} and {211} pyramids of the zircon crystals (Figure 2.01). On Pupin's classification diagram (Figure 2.01) the temperature of formation increases down the vertical axis and the aluminosity increases from left to right. The main implication of Pupin and Turco's (1975) classification scheme is that the relative proportions of pyramid and prism are controlled separately and independently by external magmatic controls. For example zircons crystallizing from hyperalkaline rock (ie. high aluminosity) such as rhyolite which is rapidly chilled from high temperature are found in the bottom right hand corner of the diagram; while zircons from slow cooling hyperaluminous rocks such as leucogranites are found in the top left-hand portion of the diagram. Pupin and Turco (1975) derived and tested their classification scheme in granitic rocks and is therefore limited in its application.

Vavra (1990) stated that Pupin and Turco's (1975) interpretation is inherently incorrect because it contradicts the kinematic considerations (ie. rate of growth and surface effects) of crystal growth. The growth rate of a single prism form not only affects the proportion of other prism forms, but also the proportion of the pyramidal forms. A valid model of zircon morphology must therefore



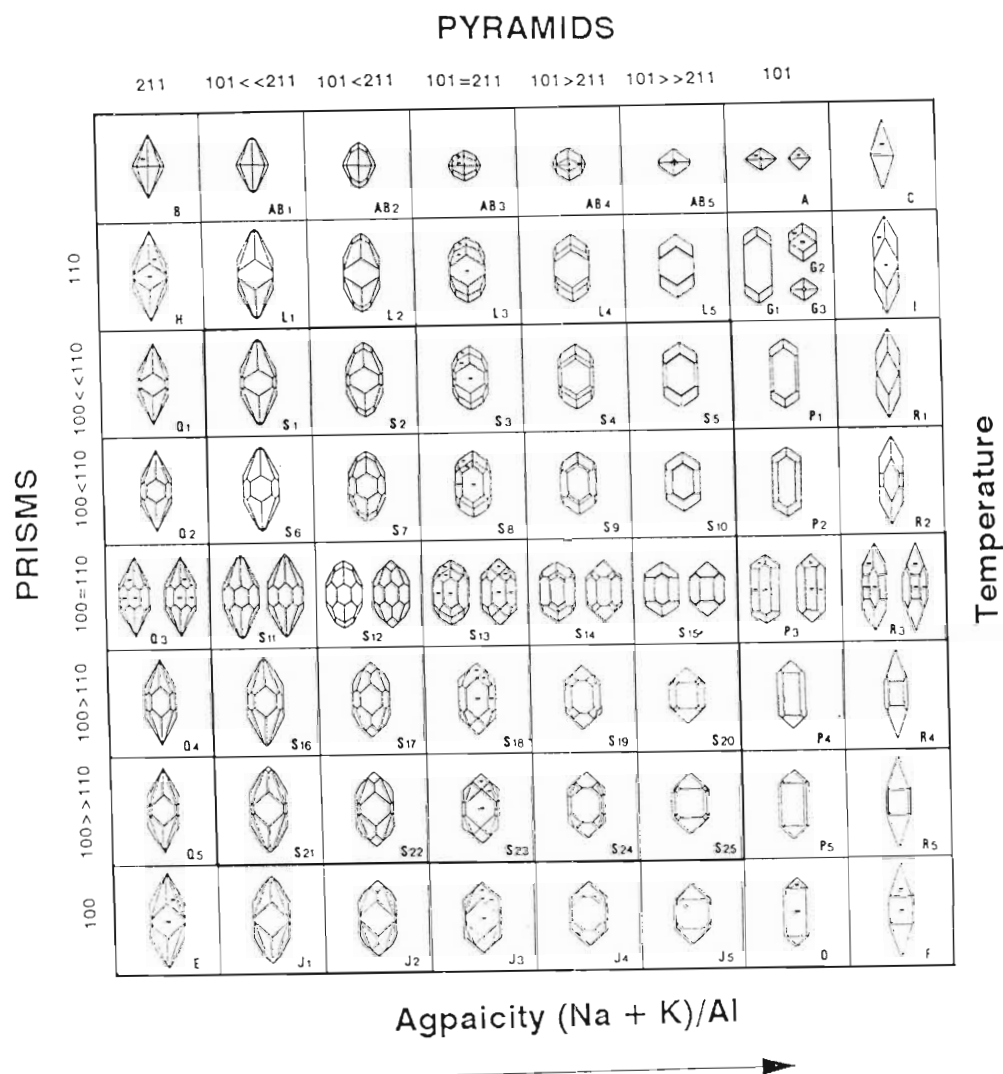
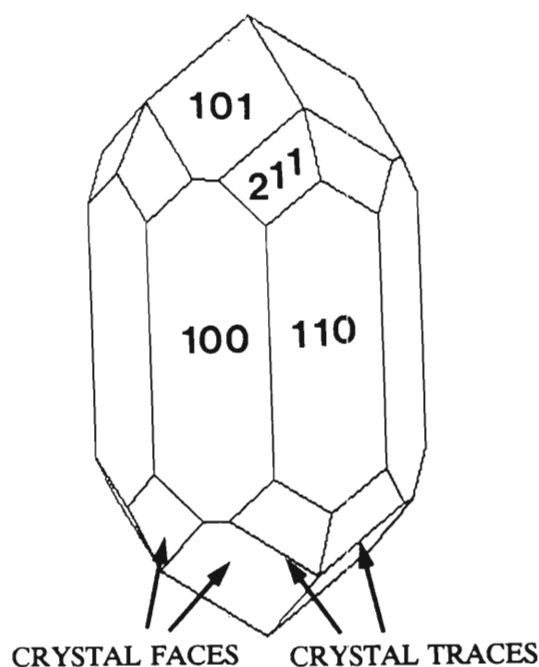


FIGURE 2.01: Zircon morphology classification of Pupin and Turco (1972) after Pupin (1980).

also consider the kinetic control on individual crystal faces.

Caruba and Turco (1971) classified the  $\{100\}$ ,  $\{110\}$  and  $\{101\}$  forms as F-faces (see Figure 2.02 for the crystallographic Miller indices). According to Dowty (1976) these F-faces (or Flat-faces) grow layer by layer. The nucleation of new layers in zircon is promoted by zircon-supersaturation. The  $\{211\}$  faces are classed as S-faces. S-faces or Stepped/Rough-faces do not grow layer by layer and do not require nucleation of new layers to grow and are thus able to grow faster than the F-faces in low zircon-saturated conditions. The growth of S-faces is not significantly affected by zircon-supersaturation (Chernov, 1984). Following this the  $\{211\}$  form will grow faster than the  $\{100\}$ ,  $\{110\}$  and  $\{101\}$  forms in low zircon-saturated environments. If the rate of growth of the  $\{211\}$  face does not slow down at low zircon-saturation, and because the diffusion of  $Zr^{4+}$  in magma is slow, the  $\{211\}$  face will grow out of existence. S-faces are also more likely to incorporate foreign elements and the rate of growth of  $\{211\}$  faces is therefore also dependent on the rate of absorption of foreign elements



**FIGURE 2.02:** Faces and traces, Miller indices.

(ie. the higher the level of impurities the slower the growth). The  $\{110\}$  form consistently absorbs less foreign elements (Carpena *et al.*, 1987 referred to in Vavra (1990); Hoffman and Long, 1984). According to Vavra (1990) the  $\{100\}$  form will grow more rapidly at low zircon supersaturation than the  $\{110\}$  form. Vavra (1990) concluded that the relative growth rates of the prism forms  $\{100\}$  and  $\{110\}$  are mainly controlled by zircon-supersaturation of the melt and the growth rate of  $\{211\}$  forms depend on the absorption rate of impurities onto this faces. Watson and Harrison (1983) stated that zircon saturation depends on the algaicity (ie.  $(\text{Na}_2\text{O} + \text{K}_2\text{O})/\text{Al}_2\text{O}_3$ ) and Zr concentration of a melt and depends little on the temperature,  $\text{SiO}_2$  or CaO concentrations of the melt. The growth rate of  $\{100\}$ ,  $\{110\}$  and  $\{101\}$  forms therefore increases with the algaicity of the melt. Pupin (1980) on the other hand considered the dominance of the  $\{101\}$  pyramid over the  $\{211\}$  pyramid to increase with algaicity; and the dominance of the  $\{100\}$  prism over the  $\{110\}$  prism to increase with temperature. The growth rate of the  $\{211\}$  form is not dependent on zircon-supersaturation but at low zircon saturation the growth rate does not slow down relative to the other faces. In most melts zircon-supersaturation increases as the magma crystallises. According to Vavra (1990) this results in an initial growth of  $\{211\}$  dominated zircon followed by  $\{100\}$ ,  $\{110\}$  and  $\{101\}$  dominated growth. The final zircon will not contain the  $\{211\}$  face on the surface. To apply a classification scheme such as Pupin's (1980), it requires a detailed study of the internal morphology of the zircon grains. Cathodoluminescence is the simplest and most effective method of studying the internal changes in morphologies.

In rhyolites, where rapid cooling occurs, the growth of the  $\{110\}$  form relative to  $\{100\}$  form is accelerated, prohibiting  $\{110\}$  from forming. The  $\{211\}$  growth is delayed by absorption of specific

foreign elements, and is not primarily related to zircon supersaturation. In anatectic melts where there is a high zircon supersaturation the effects of absorption are supported. In greatly undercooling rhyolites absorption is not supported and the {211} form do not occur. In conclusion zircons from rhyolites have the forms {100} and {110}.

Pupin's (1980) system is commonly applied in the literature, especially in Precambrian zircon studies. The main problem with Pupin's classification is that the database which is mainly for granitic type rocks is rarely added to, but is widely used in metamorphic rocks as a indicator of rock paragenesis.

#### 2.1.4 CLASSIFICATION SCHEME USED IN THIS STUDY

A simplified version shown in Figure 2.03 of Pupin's morphology scheme was used to classify zircon grains in the zircon concentrate. Even though this classification scheme may have some problems, it was considered a practical scheme for point-counting and analysing grains, with a potential genetic basis. The justification for the simplification is that the grains from the dunes are abraded and small abraded faces could not be satisfactorily differentiated from abraded traces (the line demarking the contact between two faces) under the binocular microscope that was used to point count the grains. The existence or identity of small {211} or {110} forms were impossible to ascertain.

Pupin's (1980) J5, S25, P5 and D zircons are combined into a single group labelled **D**. Point counting performed on the zircon concentrate showed that at least 17% of the zircon fell in the D-group.

D-type zircons are found in a variety of rock types, but are usually associated with high temperature (900°C), subalkaline rocks with dry melt conditions. D-type zircons have been found in trondhjemitic dykes (Pupin, 1980), albitites (Ohnenstetter *et al.* 1981), ophiolites, high temperature subalkaline anorogenic granites (Pupin *et al.* 1978), granodiorites (Corfu and Ayres, 1984) and trachytes and rhyolites (Pupin, 1980; Vavra 1990). Bossart *et al.* (1986) found quartz, clinozoisite-epidote and plagioclase inclusions within D-type zircon and conclude that physicochemical conditions may cause deviations from the normal typological temperature trend. Caruba *et al.* (1985) synthesised D-type zircon under hydrothermal conditions in temperatures ranging from 400 to 800°C.

The G1, P1, L5 and the S5 types were grouped together and labelled **G1**. These could be from calc-alkaline granodiorites, monzogranites and subsolvus granites according to Pupin (1980), hornblendites and felsic dykes (Corfu and Ayres, 1984), biotite-muscovite-alkaline-feldspar gneiss (Bossart *et al.*, 1986), granodiorites (Henjes-Kunst *et al.*, 1988), tonalites (Barth *et al.* 1989) and was confirmed to occur in granodiorites by Hannsman and Oberli (1991).

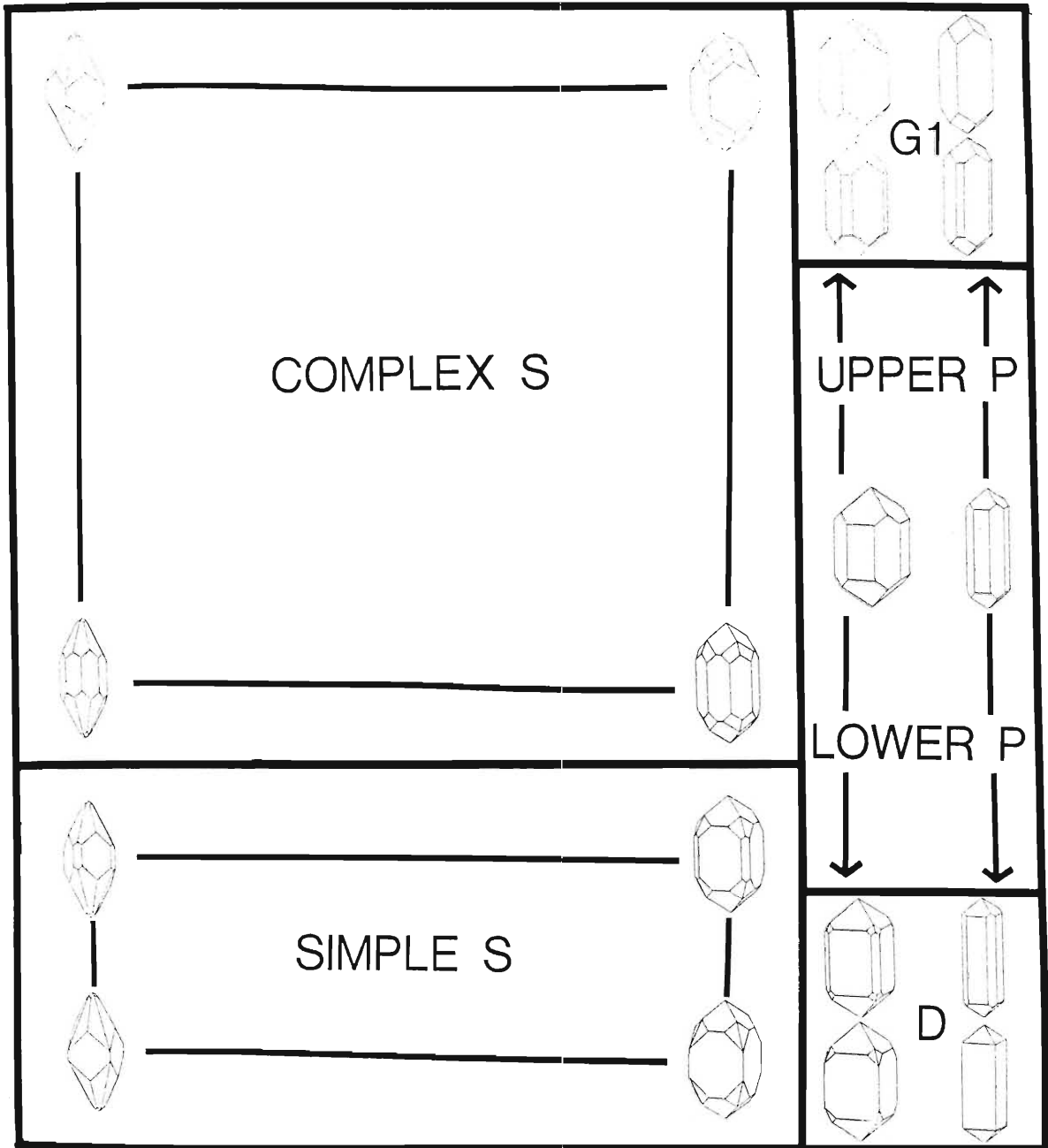


**FIGURE 2.03:** Modified and simplified version of Pupin's (1980) zircon morphology classification scheme.

The L1-4 type and all the S-type zircon morphology including and above S11-S14 were labelled **COMPLEX S**. These could be from migmatites, aluminous leucogranites, monzogranites according to Pupin (1980), hornblendite and calc-alkaline granitoids (Corfu and Ayres, 1984); biotite-muscovite-alkaline-feldspar gneisses (Bossart *et al.*, 1986); and from granodiorites, tonalites,

leucotonalites, trondhjemites and quartz diorites (Hannsmann and Oberli, 1991).

All S16-S19 zircons and the lower S and J zircons were grouped together and labelled **SIMPLE S**. These zircons may be from high temperature igneous rocks such as calc-alkaline rhyolites, tonalites, calc-alkaline granodiorites and sub-alkaline monzogranites according to Pupin (1980), granodiorites (Corfu and Ayres, 1984), calc-alkaline granitoids (Henjes-Kunst *et al.*, 1988), fayalite monzonite (Frost *et al.*, 1990) and monzogranites (Cocherie *et al.*, 1992).

Two transition groups were also chosen, the **UPPER P**-type which includes P3, S15, S10, P2 grains that tended towards P1 and G1 type; and a **LOWER P**-type which included P3, S15, S20 and P4 but tended towards P5 and D type zircon morphologies.

For point counting purposes three other groups were added to the basic 6 groups. These three groups incorporate unidentifiable rounded and broken grains. The three groups are **ROUNDED** which has no faces, **SINGLE** which has 1 unidentified face on the upper half of the grain and **MULTIPLE** which has more than 1 unidentified face.

## 2.2 ZIRCON CHEMISTRY

For general reviews on zircon and zircon chemistry see Speer (1980) and Deer *et al.* (1980). The chemical formula for zircon is  $ZrSiO_4$ . The "ideal" zircon, with no impurities, has 67.1%  $ZrO_2$  and 32.9%  $SiO_2$ . Ring *et al.* (1981) analysed zircon concentrate from Richards Bay Minerals, they obtained values for  $ZrO_2$  of 64.01% and  $SiO_2$  of 32.43%. Impurities constitute the remaining 3.56% of the zircon. According to Speer (1980) 57 elements have been identified as impurities in zircon. Zircon has two common types of solid solution series. The first is the  $HfSiO_4$  (*hafnon*)- $ZrSiO_4$  solid solution. The second is the  $(Y,HREE)PO_4$  (*xenotime*)- $ZrSiO_4$  solid solution series.

Zircon with 10 mol% or less  $HfSiO_4$  is called zircon, with 10-50 mol%  $HfSiO_4$  it is classified as hafnian zircon. Hafnon is the end-member mineral with 90-100 mol%  $HfSiO_4$ . Ahrens and Erlank (1969) compiled 463 zircon Hf analyses with a Hf range of 0.6 to 7.0 wt%. Ring *et al.* (1981) reported  $HfO_2$  analyses from the Richards Bay Minerals zircon concentrate of 0.88 to 1.40% (7460 to 11870ppm with an average of 10430ppm). The distribution of Hf in zircon is a subject of contention. Ayuso *et al.* (1984) reported zircon with Hf enrichment patterns from rim to core, and zircon with a large variability of Hf within and between grains. Hoffman and Long (1984) reported Hf enrichments in the {110} growth sectors compared to the {100} growth sector. Fujimaki (1986) reported a 30% Hf enrichment in the rims of a zircon. Clark *et al.* (1979) analysed zircon with Hf concentrations between 2.0% and 2.7% with homogenous concentrations of Hf within grains. Sinha *et al.* (1992) reported

HfO<sub>2</sub> concentrations from alternating zones in an oscillatory zoned zircon with the Hf enriched by 40% in the one set of the alternating zones.

From the aforementioned literature review the work of Owen (1987) who stated that Hf is not zoned in zircon and is therefore a good provenance indicator, must be treated with caution. Due to the zoning of Hf and Zr in zircon, Zr/Hf was not used as a provenance indicator and the analyses of RBM zircon for Zr and Hf was discontinued.

## 2.2.1 YTTRIUM AND RARE EARTH ELEMENTS

Dennen and Shields (1956), Hess (1962), Romans *et al.* (1975) and Hoffman and Long (1984) have reported Yttrium analyses. The substitution of Yttrium-rich xenotime, (Y,REE)PO<sub>4</sub>, which is isostructural with zircon is considered to be common in zircon. Zircon-xenotime intergrowths occur as a result of the ZrSiO<sub>4</sub>-YPO<sub>4</sub>-REEPO<sub>4</sub> solid solution series.

Medenbach (1976) quoted by Speer (1980) reported Y<sub>2</sub>O<sub>3</sub> and REE<sub>2</sub>O<sub>3</sub> concentrations in zircon of up to 25 wt%. Zircon with high Y and REE concentrations with values up to 15.89 wt% have been proven to be zircon-xenotime intergrowths by microprobe analysis (Robinson, 1978). Y in zircon analysed by Exley (1980) ranged between 5100 and 32300ppm. Robinson (1978) referred to in Speer (1980) surveyed 128 REE analyses of zircon and found that the REE abundances in decreasing order of magnitude are Yb > Y = Dy > Tm > Lu = Er = Gd > Tb = Eu = Ho = Ce > La > Sm > Nd = Pr. From Chapter 3 the zircon concentrate NM has the following order of REE abundances Y > Yb > Er > Dy > Lu > Ce = Ho > Tm = Gd > Nd > Sm = Tb > Pr > Eu. Zircon crystals preferentially incorporate the HREE<sup>3+</sup> ions because their ionic radii (0.98-1.05Å) are closer to that of the Zr<sup>4+</sup> ion (0.84Å) than the LREE<sup>3+</sup> (1.07-1.16Å). Ce<sup>4+</sup> and Eu<sup>2+</sup> are exceptions to the rule, with ionic radii of 0.97Å and 1.25Å respectively. The tetragonal structure of zircon and xenotime will preferentially incorporate smaller ions, such as the HREE<sup>3+</sup> and Ce<sup>4+</sup>. Monazite on the other hand is monoclinic and prefers the incorporation of large ions over small ions, i.e. monazite is LREE-rich (Mariano, 1989).

Romans *et al.* (1975) analysed zircons for xenotime related elements (Y, P, Dy) by mapping the distribution of these elements within zircons from Australian heavy mineral deposits by electron microprobe. Yttrium and phosphorus are either uniformly distributed, concentrated in zones, in xenotime-zircon solid solution substitution or as xenotime inclusions within zircon. Romans *et al.* (1975) reported that magnetic fractions of the Australian samples contain xenotime, monazite and tourmaline grains. Zircon and xenotime are considered to be isomorphous. Both minerals conform to the general formula ABO<sub>4</sub>, with A denoting Zr (0.84Å) or Y (1.02Å) and B denoting Si (0.26Å) or P (0.17Å). Traversing from pure zircon zones to xenotime-rich zones, Y and P values increased with

an accompanied increase in Ca, Al, Sc, Fe, U and S, and a decrease in Th, Zr, Hf and Si. Zircons in the 1.7A magnetic portion separated on a Frantz Isodynamic Separator were commonly found to have high proportions of substituted xenotime. Xenotime is highly magnetic predominately falling in the 0.45 to 0.50 magnetic portion (settings: 15° forward slope and 25° side slope). In the Australian heavy mineral deposits the removal of the most magnetic five percent of the product would reduced the Y from 0.35 to 0.23 wt%, a decrease of 34%.

The literature contains many analyses of REE in zircon, for example, Nagasawa (1970), Exley (1980), Törnroos (1982), Murali *et al.* (1983), Gromet and Silver (1983), Fujimaki (1986), Kapustin (1985), Sawka and Chappell (1988), Heaman *et al.* (1990), Hinton and Upton (1991), Ireland and Wlotzka (1992) for REE analyses and Lyakhovich and Lyakhovich (1983) reported Y analyses for metamict, cyrtolite and normal zircon. The minimum, maximum and average REE values from the aforementioned literature, excluding metamict and opaque zircon, are tabulated in Table 2.01 and plotted as chondrite normalised values in Figure 2.04.

The incorporation of different elements into a mineral from the magma or fluid in which it is growing depends on a variety of factors. Ionic radius and ionic charge of the particular ions, and temperature, pressure and composition of the magma are the main controlling factors.

The concept of *partition coefficients* is used to express the extent to which any particular element will be incorporated into a growing crystal. The partition coefficient of any element *M* being incorporated into zircon can be quantified by the equation:

$$k_M = [M]_{\text{ZIRCON}}/[M]_{\text{MAGMA}}$$

The value of the partition coefficient  $k_M$  is dependent on the variation in temperature, pressure and composition of the zircon and magma. A useful application of partition coefficients especially for REE, is to obtain a crude calculated REE chondrite normalised profile of the magma from which the zircon grew. Several sets of partition coefficients are plotted in Figure 2.05.

REE partition coefficients for minerals in andesites and diorites were calculated by Fujimaki (1986) (Table 2.02), for dacites and granites by Nagasawa (1970) in Table 2.03. Hinton and Upton (1991) compiled an average partition coefficient (Table 2.03) from the literature and calculated a minimum partition coefficient.

TABLE 2.01: Minimum, maximum and average values of zircon compiled from the literature.

Description:	AVERAGE	MINIMUM	MAXIMUM	ZC-B91 NM
La	20.68	0.00	148.00	10.22
Ce	69.44	2.29	300.00	36.02
Pr	1.92	0.01	16.00	4.13
Nd	37.00	0.07	229.00	14.58
Sm	9.92	0.15	44.00	9.69
Eu	2.86	0.12	15.00	2.19
Gd	90.88	0.75	800.00	24.2
Tb	8.86	0.36	60.00	8.99
Dy	183.82	5.30	800.00	89.8
Ho	50.12	2.20	142.00	35.2
Er	374.39	13.40	1400.00	142.69
Tm	64.94	3.78	186.00	27.59
Yb	446.48	6.40	1800.00	244.75
Lu	78.34	1.50	314.00	50.28
La/Lu	0.0274			0.0211
La/Sm	1.3132			0.6640
Yb/Gd	6.0791			12.5149
Ce/((La+Pr)/2)	2.0843			1.3343
Eu/((Sm+Gd)/	0.1936			0.4162

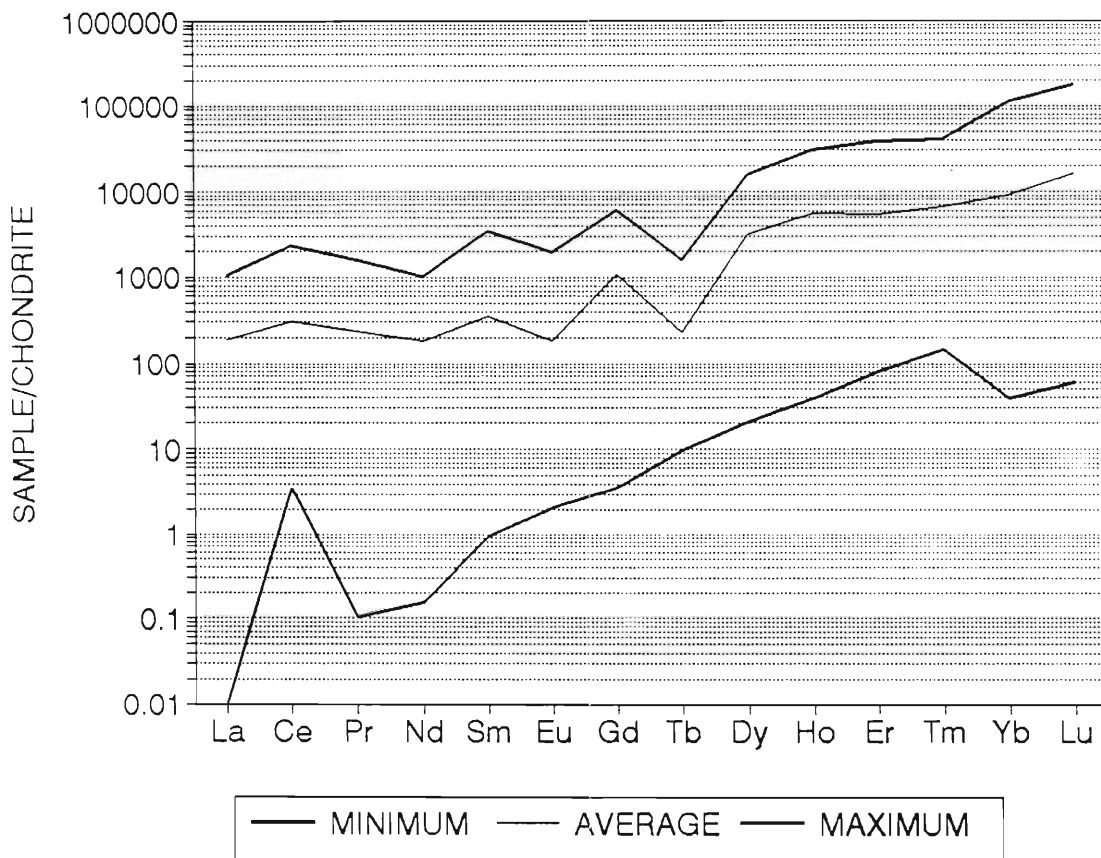


FIGURE 2.04: Chondrite normalised REE profiles of the average, minimum and maximum from the literature.



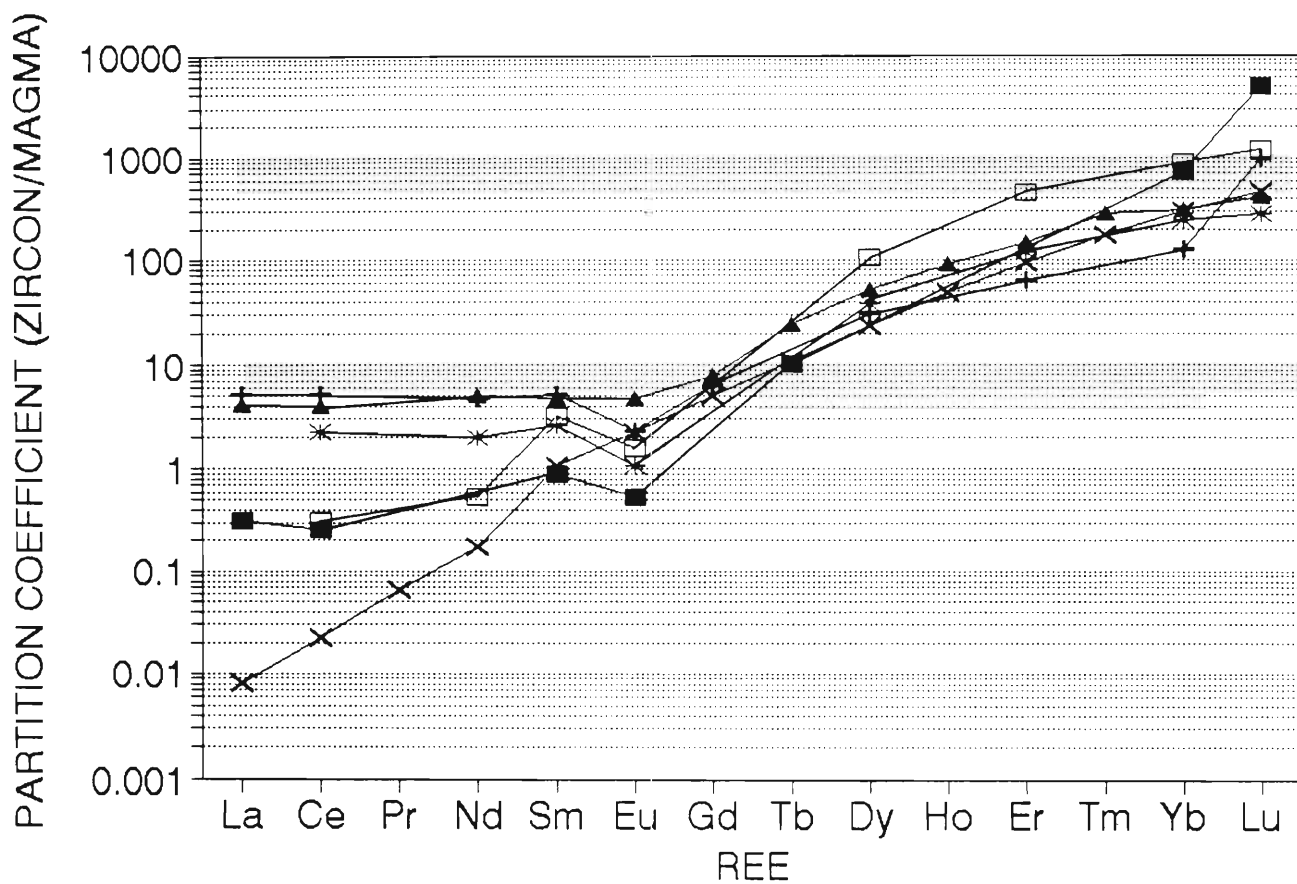


FIGURE 2.05: Partition coefficients for zircon/magma from the literature, see the text for details.

TABLE 2.02: Partition coefficients for zircon from andesites and diorites (Fujimaki, 1986).

Element	Augite-Hypersthene Andesite	Biotite-Hornblende-Quartz Diorite
La	3.11-5.25	1.14
Ce	3.49-5.14	1.17
Nd	3.80-4.77	1.38
Sm	4.72-5.16	2.03
Eu	4.23-2.39	0.85
Gd	6.77-6.41	6.01
Dy	63.4-31.4	44.9
Er	135-64.6	107
Yb	254-128	516
Lu	958-997	689

Murali *et al.* (1983) produced partition coefficient graphs for zircon for several types of rock including syenite and charnockite.

Watson (1980) experimentally obtained partition coefficients for a peralkaline felsic melt at 800°C and 2kbar pressure (Table 2.04).

**TABLE 2.03:** Zircon/matrix partition coefficients for rare earth elements for dacites and rhyolites from Nagasawa (1970); and the calculated and average literature values from Hinton and Upton (1991).

Element	Range	Average	Average <sup>*</sup>	Minimum Calculated <sup>*</sup>
La			4.1	0.01
Ce	2.3-7.4	4.2	4.0	0.02
Pr				0.64
Nd	2.0-6.5	3.6	5.0	0.18
Sm	2.6-6.5	4.3	4.7	1.06
Eu	1.1-5.2	3.4	4.7	2.30
Gd			7.9	5.01
Tb			24.4	10.90
Dy	38-54	48	52.0	23.70
Ho			88.5	48.60
Er	120-150	140	143	94
Tm			282	171
Yb	240-300	280	304	293
Lu	280-390	345	420	472
Ce <sup>4+</sup>				718

\*: Average and calculated from Hinton and Upton (1991).

**TABLE 2.04:** Experimentally derived partition coefficients from a peralkaline felsic melt (Watson, 1980).

Element	Range
La	1.4-2.1
Sm	26-40
Ho	340+
Lu	72-126

### Chondrite Normalised Profiles

All chondrite normalised profiles in this thesis are normalised to the C-1 chondrite values of Evensen *et al.* (1978), except for figures 3.05A and 3.05B which are normalised to the C-1 chondrite values of Taylor and McLennan (1981).

Due to the Oddo-Harkings effect even atomic numbered REE are more abundant than the previous and subsequent odd atomic numbered REE. For example Ce<sup>58</sup> is more abundant than La<sup>57</sup> and Pr<sup>59</sup>, and Pr<sup>59</sup> is less abundant than Nd<sup>60</sup> and so forth. To obtain a straight-line profile the concentrations of REE are normalised or divided by the chondrite REE concentrations which are presumed to represent the early unfractionated solar system. The REE normalised plots are called Masuda-Coryell diagrams after the original workers who proposed this plot. The diagrams indicate the degree of enrichment or depletion of the various REE above or below the chondrite value, thus reflecting processes after the fractionation of the earth.

Nagasawa (1970) was the first to quantify and calculate partition coefficients of the REE abundances of zircon. The results confirmed Deer *et al.*'s (1966) view that zircons concentrated REE. The zircons were found to be enriched in REE up to 4000 times that of the chondrite value for the

HREE. All subsequent analyses of zircon have indicated HREE enrichment. Nagasawa (1970) recognised the negative Eu anomaly in zircon but did not recognise a positive Ce anomaly because he did not analyse La and considered the LREE analyses to be contaminated. Terrestrial zircon commonly has negative Eu and positive Ce anomalies, while meteorite and lunar zircon only exhibit negative Eu anomalies (Ireland and Wlotzka, 1992).

Several REE profiles in the literature are discussed below to give an indication of the diversity of REE profiles found in zircon. Chondrite normalised REE profiles for several zircons in the literature are plotted in Figure 2.06.

Zircons from granodiorites showed positive Ce peaks, and negative Eu anomalies (Gromet and Silver, 1983). Chemical zoning of other accessory minerals indicates that during crystallization the REE content of the melt decreased.

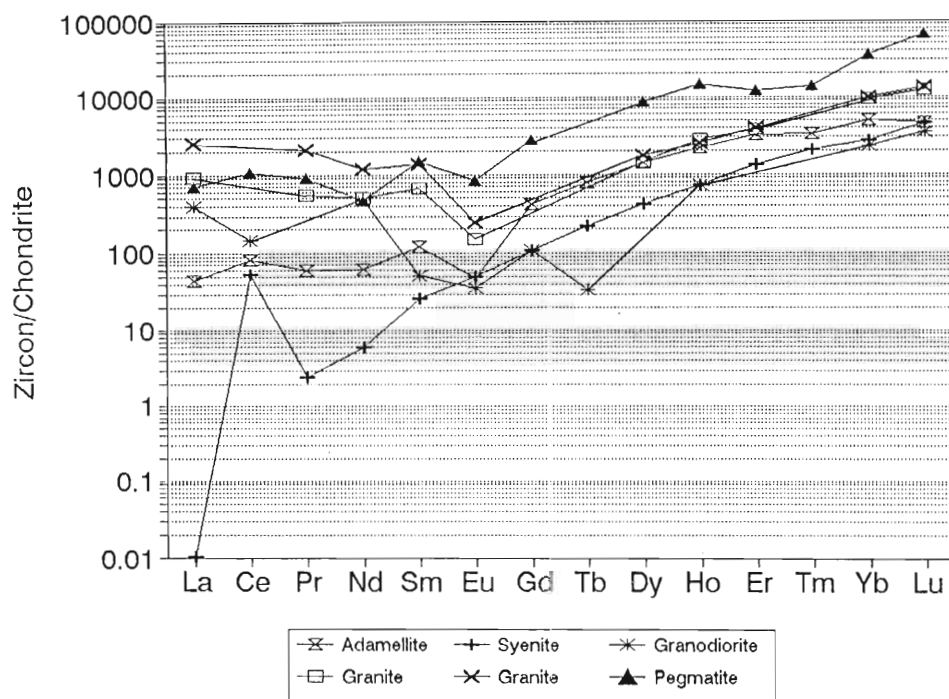


FIGURE 2.06: Chondrite normalised REE profiles for several zircons from the literature.

Sawka and Chappell (1988) analysed zircon from a granodiorite. The chondrite normalised diagrams are LREE and HREE enriched. No positive Ce anomalies are present and only minor Eu anomalies are evident.

Murali *et al.* (1983) analysed REE (La,Ce,Sm,Eu,Tb,Yb,Lu) for zircon from beach sands, syenites, nepheline syenites, and charnockites. All grains, excluding the zircon from the nepheline syenites and charnockites, have positive cerium anomalies. The nepheline syenite has a negative Ce anomaly. Negative Eu anomalies are evident in all the samples.

Gaudette *et al.* (1981) analysed brown and clear zircon. The brown zircons have a large positive Eu anomaly. The clear zircons have no Eu anomalies. The data is not published but the chondrite normalised curves are plotted.

Hinton and Upton (1991) analysed the REE from zircon from a syenite, a basaltic diatreme and a corundum-rich syenite xenolith. The zircons from the xenolith have very large positive Ce anomalies and small to no Eu anomalies. The zircons from the diatreme and the syenite have very positive Ce anomalies and no Eu anomalies.

Zircons from meteorites have abnormal REE profiles and three from Ireland and Wlotzka (1992) are plotted in Figure 2.07. In meteorites the zircon either have a negative Ce anomaly and a positive Eu anomaly with a HREE enrichment; or have profile that is close to horizontal with a negative Eu anomaly.

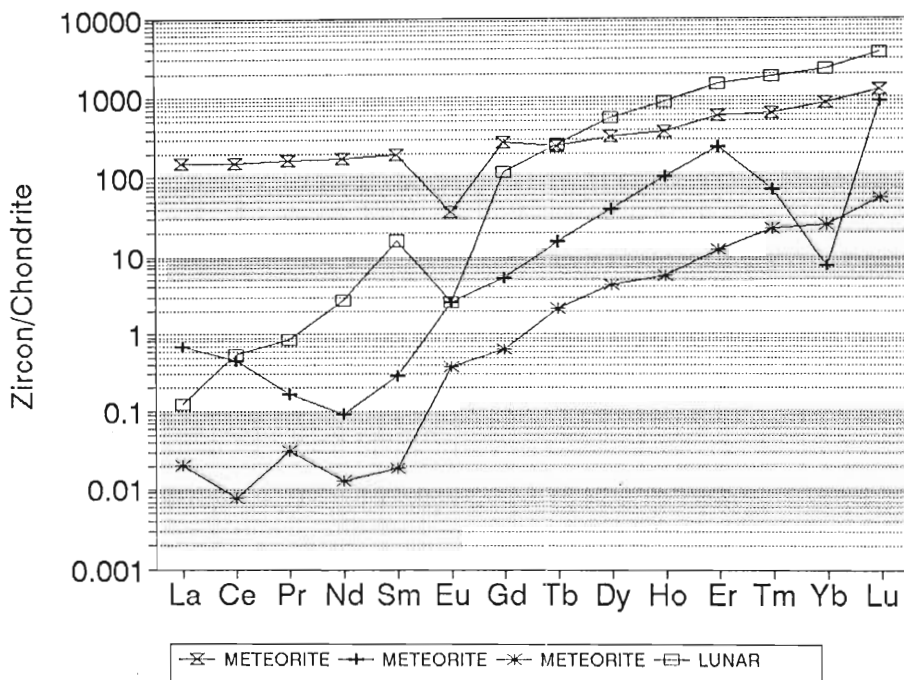


FIGURE 2.07: Chondrite normalised REE profiles for lunar and meteorite zircons. Data from Ireland and Wlotzka (1992).

In one case the meteorite zircon with HREE enrichment has a slightly positive Ce and Eu anomalies and a large negative Yb anomaly. The lunar zircon has a slightly positive Ce anomaly and a medium sized negative Eu anomaly. All the terrestrial zircons plotted are HREE enriched, have positive Ce anomalies and negative Eu anomalies of varying size, with one exception with no Eu anomaly.

### **Cerium Anomalies (Ce/Ce<sup>\*</sup>)**

Murali *et al.* (1983) were the first to notice positive Ce anomalies in zircon and attributed them to cerium having two common valencies, Ce<sup>3+</sup> and Ce<sup>4+</sup>, with Ce<sup>4+</sup> preferentially incorporated into zircon. Hinton and Upton (1991) calculated the zircon/melt partition coefficients for Ce<sup>3+</sup> and Ce<sup>4+</sup> of 0.022 and 718 respectively. Ce anomalies are therefore indicators of redox conditions in the source melts. The greater the oxidation state of the magma the lower the Ce<sup>3+</sup>/Ce<sup>4+</sup> value. Schreiber *et al.* (1980) calculated the ratio of the valencies of Ce and Fe in a basaltic melt and found that the Ce and Fe (and Eu) valence ratios compared to  $fO_2$  curves are approximately parallel. The abundance of Ce<sup>4+</sup> in basic magmas is very low, but Ce<sup>4+</sup> is preferentially incorporated into zircon because of the equivalent charge and size of Zr (0.84Å) and Ce ions (0.97Å). In a melt with oxidizing conditions the Ce<sup>4+</sup> will be incorporated into the zircon, and most of the Ce<sup>3+</sup> will be incorporated into other minerals. Most terrestrial zircons have Ce anomalies. An average Ce/((La+Pr)/2) or Ce/Ce<sup>\*</sup> of 2.22 was calculated from REE analyses in the literature with a range from 0.767 (meteorite) to 150.4 (syenite).

### **Eu Anomalies (Eu/Eu<sup>\*</sup>)**

Most terrestrial zircons have negative Eu anomalies with a calculated average of 0.185 and a range of 0.144 to 8.33. The Eu anomaly is usually an artifact of the magma in which the zircon grew due to the incorporation of Eu<sup>2+</sup> into plagioclase during crystal fractionation. Most rocks have negative Eu anomalies and this effects the REE concentrations in zircon. The partition coefficient of Eu from zircon is commonly equal to the Sm partition coefficient. In a few cases (eg. Fujimaki, 1986) the partition coefficient of Eu is lower than Sm and this may be due to a high Eu<sup>2+</sup>/Eu<sup>3+</sup> value in the source rock. The Eu<sup>2+</sup> does not fit into the zircon as well as Eu<sup>3+</sup>.

## **2.2.2 URANIUM AND THORIUM**

U, Th and Pb analyses in zircon are very common in the literature because zircon is the most common mineral used for U-Th-Pb dating. The lowest values for U and Th are found in Archaean greenstone terranes, meteorites and kimberlites. Clauoué-Long, *et al.* (1990) reported U and Th values for Archaean hydrothermal zircon in the Abitibi greenstone belt. For granodiorite the zircons have uranium values between 30ppm and 86ppm, and thorium values between 16ppm and 78ppm. In

auriferous veins U ranged from 19ppm to 75ppm, and Th from 9ppm to 41ppm. The lower end of the concentration range is dominated by zircons obtained from 4.5 Ga old chondrite meteorites, in which U values range between 0.58 and 54 ppm and with Th values between 0.051 and 16 ppm (Ireland and Wlotzka, 1992). Zircon from kimberlites had 7 to 23ppm U and 2 to 7ppm Th (Heaman *et al.*, 1990), carbonatites and nepheline syenites had U values between 56 and 571ppm and Th values between 28 and 58ppm.

The high end of the concentration range is dominated by metamict zircon from syenites and pegmatites. Deer *et al.* (1966) compiled several bulk analyses of zircon, the highest U value reported is from a quartz-sericite with 41000ppm U. A zircon from a granite pegmatite had 16000ppm U and 12800ppm Th.

Zircon with U between 250 and 930ppm and Th between 440 and 2800ppm from Bull's Run were analysed by Schutte (1966). The U/Th value ranged between 0.14 and 1.16.

### 2.2.3 U, Th AND THE REE IN MONAZITE

Monazite is an important mineral contaminant in the zircon concentrate and the zircon concentrate product and it is therefore necessary to review the literature on monazite. Monazite is a REE-phosphate with a general formula of  $(\text{LREE,Th})\text{PO}_4$ . Due to monazite being highly resistant, both chemically and mechanically, monazite is commonly found concentrated in alluvial and dune placers.

Rapp and Watson (1986) compiled the ranges and average of analysis in the literature. Their table is duplicated and modified in Table 2.05 with the REE calculated as ppm. The chondrite normalised profiles from Rapp and Watson (1986) is plotted in Figure 2.08. Figure 2.08 clearly shows that monazite is enriched in LREE with a La/Sm value (degree of LREE enrichment) of 8.4 compared to zircon with an average La/Sm value of 1.07. A total of 99.5% of the REE in monazite are composed of the elements La to Gd. Monazite commonly has a large negative Eu anomalies (average  $\text{Eu}/\text{Eu}^*$ : 0.04).

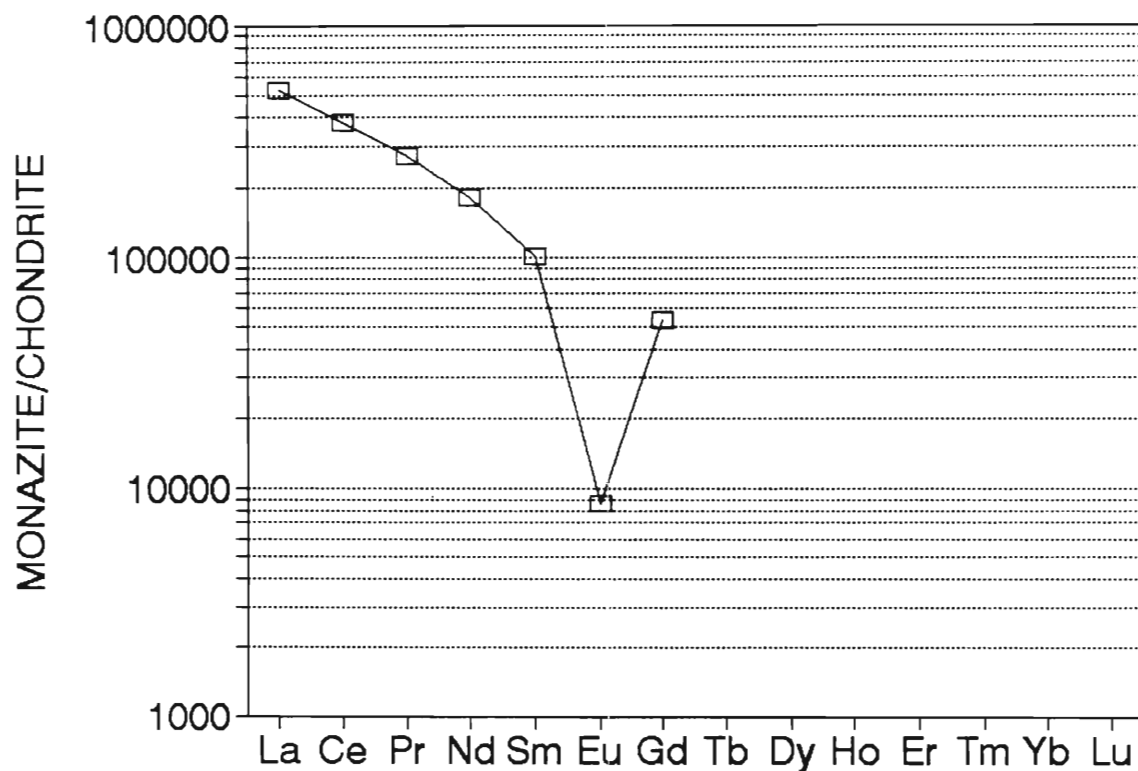
See Table 2.05 for monazite analyses reported by van Breemen *et al.* (1987) and Aleinikoff *et al.* (1979). The values that Aleinikoff *et al.* (1979) obtained for monazites from a granite and a paragneiss have the same concentrations as the RBM monazite product. The U analyses were 1235 and 2207ppm and the Th analyses were 49271 and 57609ppm, with a monazite from paragneiss with 3149ppm U and 53402ppm Th.

**TABLE 2.05:** Monazite composition. Data from Rapp and Watson (1986).

Oxide	Range(%)	Average(%)	Element	Range(ppm)	Average(ppm)
P <sub>2</sub> O <sub>3</sub>	20-30	27.5	--	---	----
SiO <sub>2</sub>	0.3-6.1	2.3	--	---	----
CaO	0-6	1.0	--	---	----
U <sub>3</sub> O <sub>8</sub>	0-4	0.5	U	0-33900	4200
			U	1100-3000 <sup>1</sup>	
			U	1235-3150 <sup>2</sup>	
			Pb	3480-9470 <sup>1</sup>	
ThO <sub>2</sub>	2-31	8.3	Th	17600-272400	72900
			Th	49270-57610 <sup>2</sup>	
Y <sub>2</sub> O <sub>3</sub>	0-5	1.2	Y	0-39400	9450
REE <sub>2</sub> O <sub>3</sub>	43-73	59.5	REE	372900-633000	516000
			La	---	130000
			Ce	---	243600
			Pr	---	26300
			Nd	---	86200
			Sm	---	15500
			Eu	---	500
			Gd	---	10800
			Tb-Lu	---	2600

1: Van Breemen *et al.* (1987), from a granite.

2: Aleinikoff *et al.* (1974), from granites and a paragneiss

**FIGURE 2.08:** The chondrite normalised REE profile of monazite. Data from Rapp and Watson (1986).

Several examples of opaque dark grey monazite, compared to the usual translucent yellow type, were identified in the zircon concentrate. According to Rosenblum and Mosier (1983) "dark monazites" contain more Eu (approximately 7-fold enrichment to 0.36wt %  $\text{Eu}_2\text{O}_3$ ), Si and Th and are derived from weakly metamorphosed carbonaceous shales or phyllites.

#### 2.2.4 Y AND REE IN XENOTIME.

Xenotime, a Y-REE phosphate, is commonly found as a solid solution substitution in zircon. REE analysis of the end member xenotime is rare in the literature, with the exception of Åmli (1975). The data from Åmli (1975) in Table 2.06 and the chondrite normalised REE profile in Figure 2.09 shows that xenotime is highly enriched in the HREE.

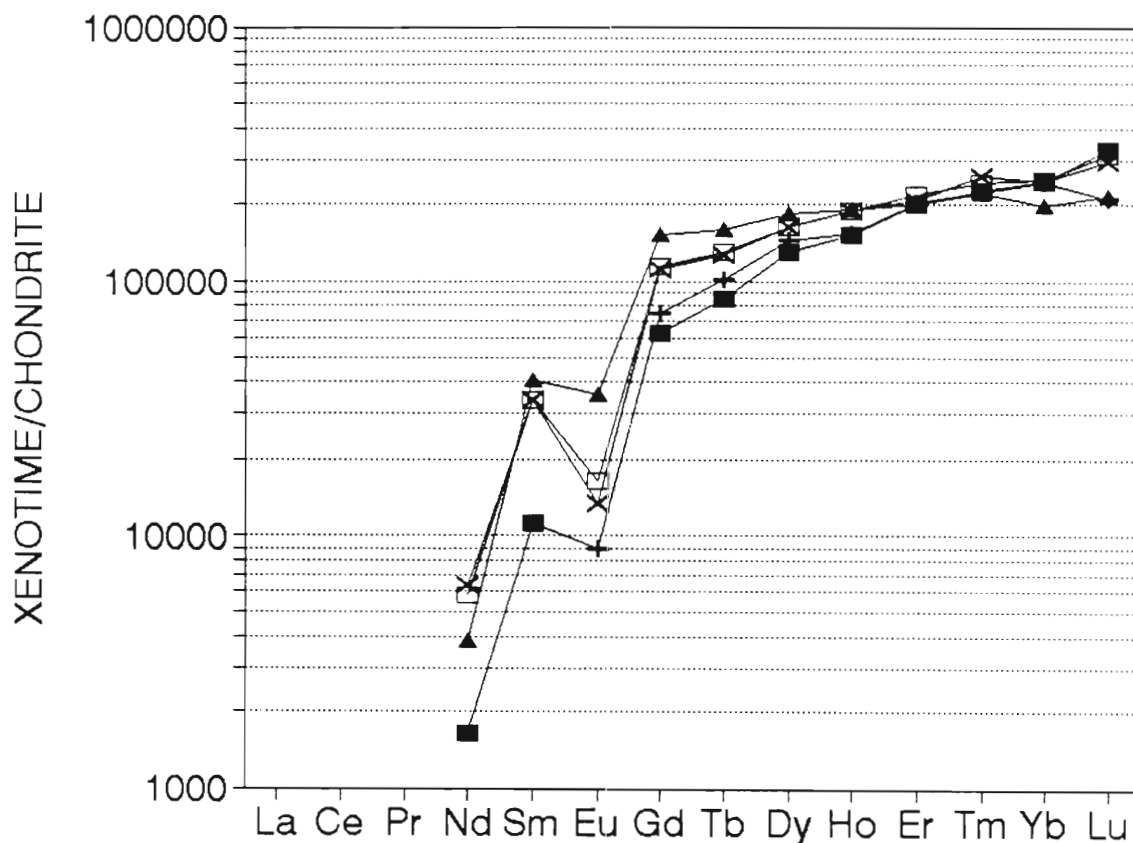


FIGURE 2.09: The chondrite normalised REE profile of xenotime. Data from Åmli (1975)



**TABLE 2.06:** Xenotime analyses from Åmli (1975).

Oxide	Range (%)	Average (%)	Element	Range (ppm)	Average(ppm)
P <sub>2</sub> O <sub>5</sub>	33.7-34.9	34.5			
Y <sub>2</sub> O <sub>3</sub>	42.5-47.4	45.3			
REE			La	-----	
			Ce	-----	
			Pr	-----	
			Nd	770-3000	1950
			Sm	1380-6380	3500
			Eu	520-3020	1320
			Gd	12660-40940	21230
			Tb	2870-9120	4750
			Dy	32880-61166	41600
			Ho	7590-11090	9670
			Er	29470-36470	32880
			Tm	4120-6570	5630
			Yb	25730-41270	36060
			Lu	3340-8350	5960

The REE curves in Mariano (1989) using the data of Rhône-Poulenc (1987) show profiles with a general positive slope from La to Tb, with a negative inflection of Yb and Lu, and a very large negative Eu anomaly. The profiles of the data from Hill (1976) are similar to the profiles of Åmli (1975).

## CHAPTER 3

### METHODS OF ANALYSIS

#### 3.1 INDUCTIVELY COUPLED PLASMA - MASS SPECTROMETER

Trace elements concentrations in zircon were determined using a VG-Plasmaquad inductively coupled plasma - mass spectrometer (ICP-MS). Initially indium with an atomic mass of 115 (In) was used as an internal standard. Later, due to mass calibration drift, rhenium with an atomic mass of 187 (Re) was added as a second internal standard to correct variations of drift with increasing mass away from In. In and Re were added to all samples so that the samples contained 50ppb concentration. Calibration curves were plotted using several rock standards that were included with each run (see end of Chapter 3). The main problem with ICP-MS analysis is the occurrence of chemical interferences due to the formation of oxides and the complexing of argon within the plasma. Therefore the atomic mass range of 40 to 57 and 70 to 77 cannot easily be analysed, with the exception of Ti. Initially Mg, Rb, Sr, Y, Nb, Ba, the REE, Ta, Pb, Th and U were analysed. In the later runs only Y, REE, Th and U were analysed. In a single run Zr and Hf were analysed with very dilute solutions. During trace element analyses ZrO and HfO peaks for each of the five isotopes of Zr and Hf are found 16 mass units higher up on the atomic mass spectrum. The ZrO peaks are at equivalent concentrations to cerium. The ZrO peaks fall in the palladium-silver-cadmium mass range and the HfO peaks fall in the iridium-platinum-gold mass range and may be used to calculate Zr/Hf ratios without the large dilutions required if Zr and Hf are directly analysed.

#### 3.2 SAMPLE PREPARATION

All zircon samples were fused with Lithium Meta-borate ( $\text{Li}(\text{BO}_3)$ ) flux. The sample and flux were weighed (1:10 ratio) into platinum crucibles and then placed over a bunsen burner to melt the flux. The flux and sample were mixed into a single bead in the platinum crucible and then placed in an oven at  $1000^\circ\text{C}$  for  $4\frac{1}{2}$  to 5 hours. The sample was then reheated over a bunsen-burner and cooled rapidly to form a glass bead. Samples which form opaque radial crystals will not dissolve. The bead usually cracks and is removed from the platinum crucible. The sample bead is placed in 2% nitric acid and dissolved. In and Re internal standards were then added. Two techniques of sample preparation were devised to enable the dissolution of small and large numbers of zircon.

### 3.2.1 LARGE BULK SAMPLES

Large bulk samples (0.080 to 0.110g) were scaled down from kilogramme samples of zircon concentrate with the aid of a brass micro-splitter. The large amount of flux used (10:1) enabled the sample and flux to coalesce into one large bead. Due to the bead's large size relative to the 10ml platinum crucible it was impossible to add the appropriate amount of nitric acid into the crucible to dissolve the bead. The beads were therefore placed into 100ml plastic bottles and 97.5ml of HNO<sub>3</sub>, 1ml of 5000ppb In HNO<sub>3</sub>, 0.504ml 9850ppb Re HNO<sub>3</sub> were added to the bottle. The resulting concentrations were a dilution of the sample of approximately 1000 with internal standards of 50ppb In and Re. Magnetic stirrer beads were placed in the bottles and the solutions were allowed to stir for 3 to 5 hours. Prior to analysis the samples were diluted by a factor of 10 by adding 2% HNO<sub>3</sub> with 50ppb Re and 50ppb In. The final dilution factor was approximately 10000.

Early samples that were prepared without the Re internal standard during dissolution (suffix D, L and M) had Re added to the samples prior to analysis (1ml of sample-2% HNO<sub>3</sub> liquid with 500ppb In was added to 9ml of HNO<sub>3</sub> with 55.56ppb Re). The resultant liquid had internal standards of 50ppb In and 50ppb Re.

The initial runs, designated D, L and M, were standardised using rock standards with 500ppb In and a dilution of 300. Due to the rock standards having an In internal standard ten times that of the samples the dilutions for the samples were divided by ten.

Sample runs T, TB and TC were run with rock standards with a dilution factor of 3000, and internal standards of In and Re at 50ppb concentrations. All sample analysis calculations were made with dilution factors of about 10000.

#### 3.1.2.1 DIFFICULTIES WITH BULK SAMPLE PREPARATIONS

1. Often the whole flux-sample bead or parts of the bead would adhere to the platinum crucible. To remove the bead involved repeatedly reheating and cooling until the bead cracked and it was then possible to remove the bead and place it in the plastic bottle for dissolving

2. If a perfect glass is not formed during reheating the resultant bead will only partially dissolve and flux-sample residue remains in the solution.

3. With repeated reheating the bead may explode, resulting in a loss of flux and sample.

### 3.2.2 100-GRAIN SAMPLES

One hundred grain samples weighing from 0.000950 to 0.003900g were hand-picked onto glass

slides and transferred to water-proof weighing-paper and their mass recorded using a microbalance. This enabled individual populations to be analysed. All samples were picked so that 200-300 grains were obtained. These samples were then divided into two portions and analysed separately as duplicate samples.

With such small samples the amount of flux is also very small. The molten flux has a very high surface tension and with such small amounts of flux it is impossible to form single sample-flux beads. The flux melts into many small separate beads and one medium sized bead containing the sample grains. The large bead cannot be rolled over the small beads to form a single composite bead.

Platinum wire with a small loop at one end was placed in the crucibles and used to "dab" at the small beads to form a single large bead at the end of the platinum wire loop. The beads, wire and crucible were then placed in the oven at 1000°C for 4½ to 5 hours. The beads were then reheated and cooled rapidly to form a glass.

Due to the small size of the samples the beads were dissolved in the platinum crucibles with 3 to 10ml of HNO<sub>3</sub>. The liquid was made up with 5ml of 2% HNO<sub>3</sub> with 100ppb In and 50ppb Re, and 5ml of 2% HNO<sub>3</sub> with 50ppb Re. The resultant liquid has 50ppb In and Re. Prior to using Rhenium as an internal standard 10ml of 2% HNO<sub>3</sub> with 50ppb In liquid was used. The average mass of the 100 grain samples was 0.001g. The samples were dissolved in 10ml of acid resulting in an average dilution factor of 10000.

The analyses of initial samples analysed in runs D, L and M had low HREE concentrations due to having only one internal standard. Only four of these single-grain samples had enough remaining sample-flux-liquid to add Re. The other samples with no remaining liquid could not be re-analysed with two internal standards. The dilution factors of these four samples were doubled by adding 3ml of 2% HNO<sub>3</sub> at 100ppb Re and 50ppb In to 3ml of sample liquid at 50ppb In. The resultant liquid had internal standard values of 50ppb In and Re.

### 3.2.2.1 DIFFICULTIES AND SOLUTIONS WITH 100-GRAIN PREPARATION

1. During initial experimentation with the platinum wire method the samples analysed showed a memory of the previous sample. For example previous monazite micro-beads resulted in an enrichment of the LREE in zircon analysed afterwards that were prepared with the same platinum wire. Reflective-light microscopy showed tiny beads of flux-sample on the platinum wire. Several methods of cleaning were experimented with to establish which method was the most efficient at dissolving the residue beads.

The most efficient method of cleaning the platinum wire was found to be heating up the wire over a bunsen-burner and then quenching the light-orange hot wire in cool water, followed by reheating and stirring in 10% HNO<sub>3</sub> for 4 to 5 hours. It must be noted that the platinum wires have

a life-span of about 10-15 sample preparations after which they develop many micro-cracks wherein flux-sample beads may remain undissolved after cleaning. These wires must not be used for further sample preparation.

2. Initially the samples were prepared in 4ml crucibles and transferred to 10ml crucibles before being placed in the oven. The sample often "climbed" the wire where the wire was in contact with the side of the platinum crucible when it was in the oven at 1000°C. Corrugated platinum wire was used so that minimum contact between the wire and the crucibles wall was obtained.

Later, when more 4ml crucibles became available, and 7mm magnetic stirrer bugs were obtained, the preparation, oven and dissolution steps were all carried out within 4ml crucibles.

### 3.3 ROCK STANDARDS

Eight rock standards were run with each analytical run to construct the working curves (Table 3.01).

**TABLE 3.01:** Summary of rock standards used to calibrate the ICP-MS zircon analyses.

Name	Rock Type	Source	
GH	Granite	CRPG	Centre de Recherches Petrographiques et Geochimiques.
JB-1	Basalt	GSJ	Geological Survey of Japan
DR-N	Diorite	ANRT	Association Nationale de la Recherche Technique, Paris
NIM-S	Syenite	MINTEK	
NIM-G	Granite	MINTEK	
NIM-D	Dunite	MINTEK	
NIM-P	Pyroxenite	MINTEK	
NIM-N	Norite	MINTEK	

Standard values for the rocks standards were taken from Govindaraju (1989).

### 3.4 SOURCE OF ZIRCON SAMPLES

The investigations, treatments and analyses of zircon were performed on two major samples of zircon. The first was zircon concentrate November 1991 (ZC-B91). Most of the experiments were performed on a non-magnetic product of ZC-B91 and is designated zircon concentrate NM or ZC-B91 NM. An Eriez magnetic separator was used to obtain a non-magnetic product, with all magnetic portions up to 2.24A removed. The second major sample was zircon concentrate product from August 1992 (ZCP-892). A zircon concentrate product from June 1992 was used for magnetic cleaning and is designated ZCP-692. Monazite was sampled from the monazite product of August 1991 (MP-891).

### 3.5 DESCRIPTION OF ANALYSES OF THE STARTING MATERIAL

Analyses of Y, REE, Th and U were performed on the source or starting samples (See Table 3.02).

**TABLE 3.02:** ICP-MS element results for the zircon source material ZC-B91 NM and ZCP-892, and the monazite bulk sample MP-891.

Description:	ZIRCON	ZIRCON	MONAZITE
Sample #:	ZC-B91	ZCP-892	MP-691
Y	1033.10	989.90	10001.25
La	10.22	47.95	73631.88
Ce	36.02	122.91	148377.61
Pr	4.13	15.01	18973.22
Nd	14.58	63.55	68831.82
Sm	9.69	23.60	13468.94
Eu	2.19	4.44	314.87
Gd	24.20	41.65	9206.89
Tb	8.99	14.01	914.38
Dy	89.80	126.43	2943.89
Ho	35.20	41.16	395.66
Er	142.69	194.24	658.01
Tm	27.59	39.42	45.89
Yb	244.75	371.59	295.77
Lu	50.28	67.09	35.20
Th	140.81	181.52	41221.76
U	311.62	381.03	2769.74
U/Th	2.21	2.10	0.07
U + Th	452.42	1.28	43991.51
La/Sm	0.66	1.28	3.44
Yb/Gd	12.52	11.04	0.04
Ce/Ce*	1.33	1.10	0.93
Eu/Eu*	0.42	0.43	0.08

Monazite is enriched in the light rare earth elements (LREE) and zircon is enriched in the heavy rare earth elements (HREE) (see Figure 3.01). A zircon sample that contains monazite will have elevated LREE levels. The La/Sm value is an indicator of the relative enrichment of LREE. ZC-B91 NM has a low La/Sm value of 0.66 compared to monazite from RBM which has a La/Sm value of 5.47. ZCP-892 has a La/Sm value of 1.28. The higher ratio suggests a contamination of the zircon concentrate product by monazite impurities. The zircon concentrate NM (Figure 3.02) and the monazite product (Figure 3.03) chondrite normalised profile are comparable to the average profiles found in the literature.

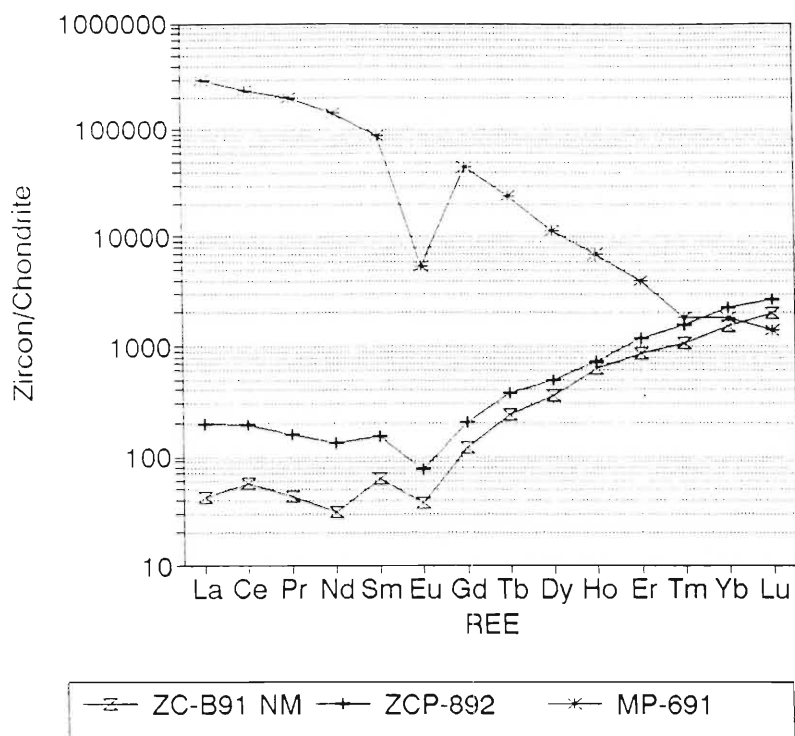


FIGURE 3.01: Chondrite normalised REE of the source zircon and monazite from RBM.

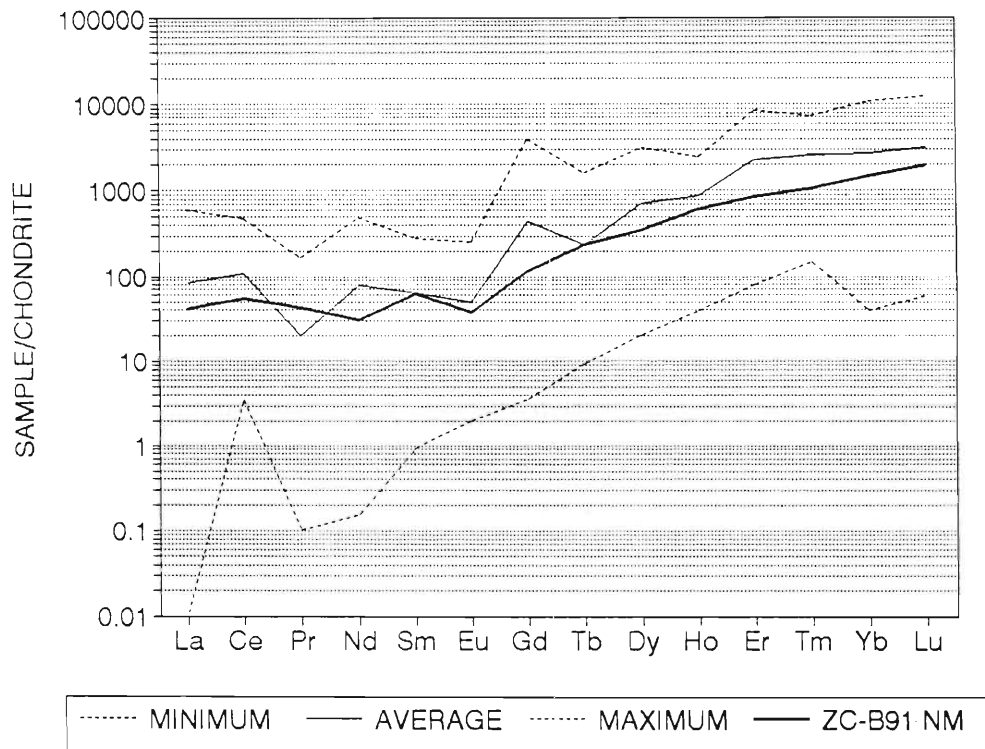


FIGURE 3.02: Chondrite normalised REE profile of ZC-B91 NM compared to minimum, maximum and average values from the literature mentioned in Chapter 2.

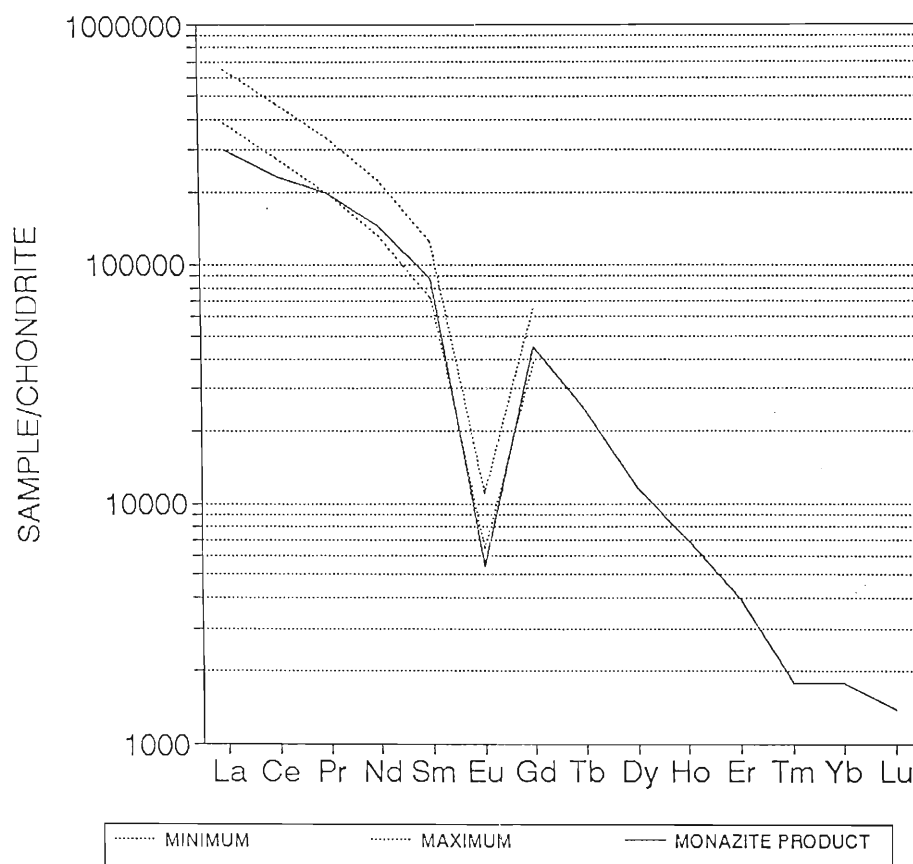


FIGURE 3.03: Chondrite normalised REE profile of MP-891 compared to the minimum and maximum values of Rapp and Watson (1986).

The calculation of the amount of monazite required to enrich the LREE of ZC-B91 to the LREE profile of ZCP-892 using La, Pr and Nd reveals a contamination of ZCP-892 by 0.051 to 0.071% monazite (average: 0.06%). The calculation is biased to a minimum value because ZS-B91 NM was considered to be a 100% monazite-free zircon product in the calculation, which may not be the case. The Yb/Gd value is an indicator of HREE enrichment, in the zircon and monazite samples. Monazite is depleted in HREE with a Yb/Gd value of 0.03 compared to the zircon concentrates with values between 11.04 and 12.52. The upward inflection of the monazite bulk products profile at Tm (Figure 3.01) is most likely due to a HREE contamination from zircon, xenotime or apatite impurities in the monazite sample.

ZC-B91 has a positive Ce anomaly ( $Ce/Ce^* = 1.33$ ) and a negative Eu anomaly ( $Eu/Eu^* = 0.42$ ). ZCP-892 is contaminated with LREE from monazite and therefore has only a small Ce anomaly (1.10) is evident and has a equivalent negative Eu anomaly (0.43). MP-891 has a slightly negative Ce anomaly (0.93) and a large negative Eu anomaly (0.08). Table 3.03 lists all the calculations pertaining to the REE of this thesis.



TABLE 3.03: Summary of REE Calculations.

---

**LREE enrichment from monazite calculation:**

$$\text{Percent monazite} = \left( \frac{[M]_{\text{ZIRCON SAMPLE}} - [M]_{\text{ZC-B91 NM}}}{[M]_{\text{MONAZITE}}} \right) \times 100$$

Where [M] is the concentration of La, Pr or Nd.

$$\text{Average Monazite Contamination} = (\underline{x}\% \text{ La} + \underline{y}\% \text{ Pr} + \underline{z}\% \text{ Nd}) \div 3$$

**Degree of LREE Enrichment:**

La/Sm

**Degree of HREE Enrichment:**

Yb/Gd

**Ce Anomaly (Ce/Ce\*) Calculation:**

$$\frac{\text{Ce}/(\text{La} + \text{Pr})}{2}$$

**Eu Anomaly (Eu/Eu\*) Calculation:**

$$\frac{\text{Eu}/(\text{Sm} + \text{Gd})}{2}$$


---

The zircon sample ZC-B91 NM has a U value of 311ppm and a Th value of 141ppm with a U+Th value of 452ppm and a U/Th value of 2.21.

The zircon sample ZCP-892 has a U value of 381ppm and a Th value of 182ppm with a U+Th value of 563ppm and a U/Th value of 2.10.

The monazite sample MP-691 has a U value of 2770.7ppm and a Th value of 41222ppm with a U+Th value of 43992ppm and a U/Th value of 0.07.

The lower U/Th value of ZCP-892 is due to the 0.028 to 0.036% monazite impurities which contribute between 11.5 to 14.8ppm Th and between 0.7 to 0.9ppm U.

### 3.6 A COMMENT ON DISCONTINUED ISOTOPES

The early sample runs included analyses of Rb, Sr, Nb, Ba, Ta and Pb. Mg, Zr and Hf were analysed in 100000 dilution samples. The results are summarised below to give an indication of the impurities and the Zr/Hf values.

The Pb results were erratic with large differences obtained for the different isotopes and little correlation between runs and duplicates. This is because the natural Pb isotope ratios differ from one sample to another, and are very different in the rock standards, as the isotopes are radiogenic decay products of U and Th. The lead results will therefore not be summarised.

The "ideal" zircon has 49.67% Zr. The results obtained on 8 samples ranged from 34.4 to 49.2%, with the average at 40.4%. The four 100-Grain samples that were analysed gave Zr values between 41.2 and 49.2% with an average at 46.0%. Deer *et al.* (1966) compiled values for Zr between 42 and 49.4%. The Zr analyses of the 100-grain samples can therefore be surmised to be correct.

The Hf concentrations range from 0.7% to 0.9% with an average of 0.83%, compared to 0.75 to 1.19% from Ring *et al.* (1981). The average for the 100-grain samples is 0.9%.

The Zr/Hf ranges from 48 to 54 with an average of 50. The Hf/(Hf+Zr) ranges between 1.82 and 2.06 with an average of 1.97. The Zr/Hf of Ring *et al.* (1981) for the RBM concentrate range from 40 to 64 and the Zr/Hf of Bull's Run (Schutte, 1966) range between 61 and 74.

Mg was analysed in dilute samples, the magnetically cleaned ZC NM had 0.0141% Mg and the starting material ZC had 0.236%. The washing and magnetic cleaning reduced the Mg concentration by 40%. The ZCP has a Mg value of 0.054% compared to the extracted magnetic fraction with a value of 1.436%. The bulbous frosted 100-grain samples have Mg concentrations between 0.204 and 0.254%. Clear D-type zircons that contained abundant inclusions contained 0.027% and 0.074% Mg. The sample with the higher concentration of Mg also contained higher Th and has an enriched LREE curve.

The average values for Nb and Ta for 6 samples is 11.61 and 2.02ppm respectively. The Nb concentrations ranged between 10.32 and 13.57ppm, and that of Ta ranged between 1.81 and 2.22ppm. The average Ba ranged between 28.7 and 44.7ppm, with an average of 39.5ppm. Sr ranged between 5.7 and 28.9ppm, with an average at 17.8ppm. Rb ranged between 1.3 and 10.3ppm, with an average at 5.4ppm.

The analyses of the aforementioned elements were discontinued due to them either having little application in the study or the results being unreliable, precision less than 5% was required for this project. Nb, Ta, Mg, Zr, Hf all had good reproducible results.

### 3.7 A NOTE ON THE REE, U and Th ICP-MS RESULTS

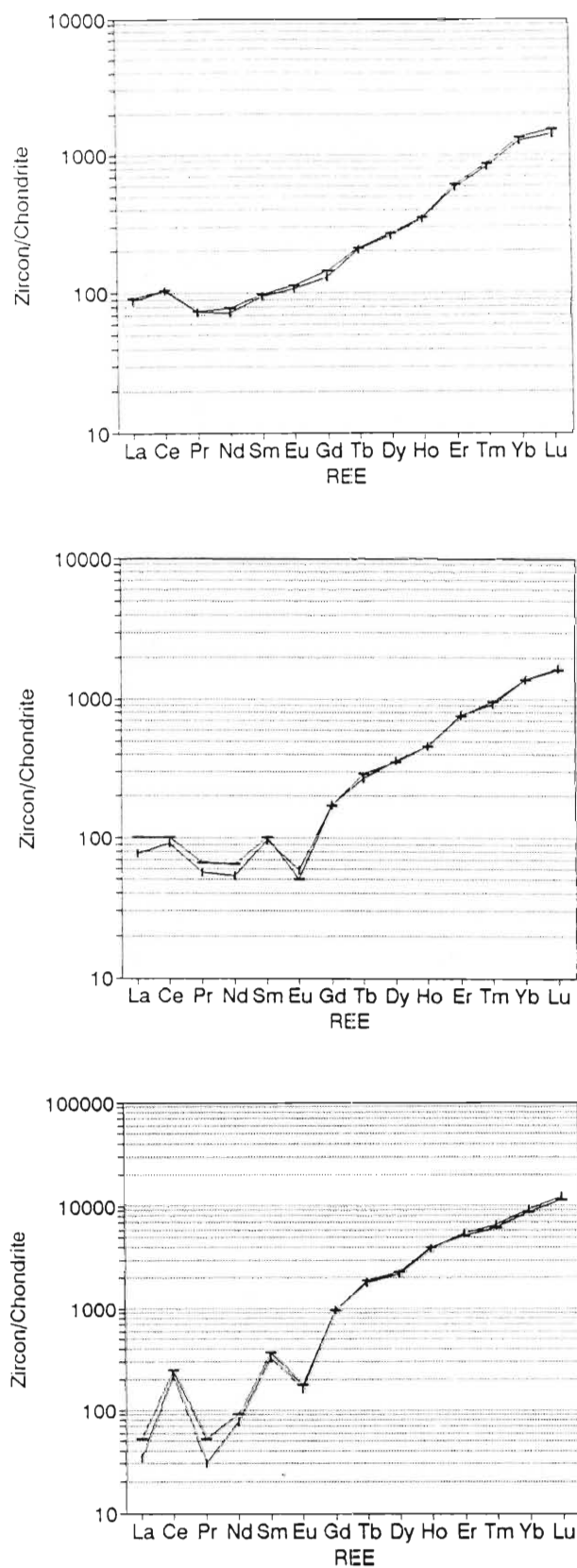
The precision of the ICP-MS analyses can be gauged by comparing duplicate analyses. Each analysis is an average of three consecutive runs (Table 3.04). The bulk samples BULLSRUN 1 and 2 from Bull's Run, prepared from two aliquots of ~5g crushed samples, were analysed with In and Re internal standards. The differences between the duplicates are below 5.5% with the exception of Nd, Gd, Lu, Th and U which range between 7.7% and 12.3% (Figure 3.04A). The bulk samples 125-250 1 and 2 from RBM were analysed with In internal standard, the differences between the duplicates are below 7% with the exception of Sm at 12.7% (Figure 3.04B). The average of the deviations between duplicate samples is 5.4% for BULLSRUN and 4.1% for sample 125-250.

TABLE 3.04: ICP-MS element results for duplicate samples.

Type:	BULK SAMPLE			100-GRAIN SAMPLE		
Sample #:	BULLSRUN			BULBOUS		
Duplicate:	1	2	Percent Difference	1	2	Percent Difference
Y	667.80	659.48	1.3	7174.76	6538.99	9.7
La	21.38	22.24	3.9	8.27	12.82	35.5
Ce	66.42	66.67	0.4	139.20	156.74	11.2
Pr	7.03	7.13	1.4	2.88	5.04	42.8
Nd	33.85	36.94	8.4	36.59	43.63	16.1
Sm	14.53	15.24	4.7	50.88	57.12	10.9
Eu	6.28	6.62	5.2	9.43	10.30	8.5
Gd	26.69	29.66	10.0	200.54	194.02	3.4
Tb	7.70	7.97	3.4	67.76	71.36	5.0
Dy	66.17	69.34	4.6	555.46	584.60	5.0
Ho	19.47	20.18	3.6	219.04	224.32	2.4
Er	97.58	102.37	4.7	922.66	867.56	6.4
Tm	21.27	22.27	4.5	171.36	161.62	6.0
Yb	210.14	222.44	5.5	1554.90	1437.25	8.2
Lu	36.52	39.55	7.7	316.23	293.40	7.8
Th	664.52	758.06	12.3	781.10	678.62	15.1
U	174.55	196.20	11.0	1158.20	1420.45	18.5

Type:	BULK SAMPLE		
Sample #:	125-250		
Duplicate:	1	2	Percent Difference
Y	963.981	909.454	6.0
La	65.497	63.21	3.6
Ce	149.792	140.062	6.9
Pr	17.883	17.406	2.7
Nd	64.122	62.227	3.0
Sm	20.459	18.148	12.7
Eu	3.684	3.916	5.9
Gd	37.586	36.553	2.8
Tb	10.699	10.305	3.8
Dy	92.048	94.861	3.0
Ho	25.989	26.706	2.7
Er	133.724	133.578	0.1
Tm	27.394	27.549	0.6
Yb	240.921	227.738	5.8
Lu	47.47	44.546	6.6
Th	174.676	178.634	2.2
U	270.213	274.896	1.7



**FIGURE 3.04:** Chondrite normalised REE profiles demonstrating precision of bulk samples: (A) BULLSRUN, (B) 125-250; and 100-grain sample (C) BULBOUS.

The only 100-grain sample, BULBOUS, successfully duplicated was run with In standard. The duplicates represent halves of a -250 grain handpicked sample, which had highly pitted and rounded grains so differences in chemistry due to heterogeneity may be possible. The grains may also contain xenotime substitution. The deviation between the duplicates is between 10.9 and 42.8% for the LREE and 2.4 and 8.2% for the HREE (Figure 3.04C). The average deviation for all the elements is 12.5%. Due to the pitted nature of the grains they resemble detrital monazite, but because only 125 grains were analysed in each duplicate, if 1 grain in BULBOUS were a monazite the La, Pr and Nd would be enriched by approximately 550ppm. Even if these data reflect poor precision in LREE between 100-grain samples, the shapes of the REE profiles are sufficiently similar to allow meaningful interpretation of either aliquot.

D.H. Cornell (*pers. comm.*) analysed the standard samples JB-1 and W-1 under similar conditions to ascertain the accuracy of the ICP-MS (Table 3.05, Figures 3.05A and 3.05B). The REE, Y, Th and U profiles in Figures 3.05A and 3.05B are normalised to the C-1 chondrite values of Taylor and McLennan (1981). Y and Tm show large deviations compared to the standard values. The standard Tm values of Govindaraju (1989) may be incorrect due to the small amount of data available. Several REE deviate by 10 to 15% but there is an overall good accuracy, and the REE profiles show reasonable correspondence if Tm and Y are omitted.

**TABLE 3.05:** ICP-MS element results for rock standards compared to the standard values of Govindaraju (1989).

	JB-1 Literature (ppm)	JB-1 ICP-MS (ppm)	Percent Difference	W-1 Literature (ppm)	W-1 ICP-MS (ppm)	Percent Difference
Y	24	19.788	17.6	26	19.171	26.3
La	38	34.463	9.3	11	10.146	7.8
Ce	67	59.229	11.6	23.5	21.513	8.5
Pr	7.5	6.759	9.9	3.2	2.994	6.4
Nd	27	24.305	10.0	14.6	12.658	13.3
Sm	5	4.985	0.3	3.68	3.440	6.5
Eu	1.52	1.452	4.5	1.12	1.119	0.1
Gd	4.7	4.353	7.4	4.01	3.425	14.6
Tb	0.76	0.699	8.0	0.63	0.611	3.0
Dy	4	3.555	11.1	3.99	3.419	14.3
Ho	0.7	0.685	2.1	0.81	0.725	10.5
Er	2.2	1.988	9.7	2.3	2.108	8.4
Tm	0.35	0.267	23.7	0.34	0.267	21.5
Yb	2.1	1.801	14.2	2.03	1.988	2.1
Lu	0.31	0.260	16.1	0.317	0.282	11.2
Th	9.2	8.168	11.2	2.4	2.368	1.3
U	1.7	1.555	8.5	0.57	0.551	3.3

Calibration lines show good fits with correlation coefficients ranging from 0.909 to 0.927 for Eu and with all the rest with one isotope or more above 0.988 (Figure 3.06A-C). Pr, La and Er have correlation coefficients of 0.999 or greater. Twenty of the 29 isotopes analysed have calibration line correlation coefficients of 0.99 or greater.

The precision of Y, REE, Th and U data is acceptable, the comparison of individual runs, duplicate pairs and standards all show average deviations below 5%. Some larger deviations are evident, are usually due to known analytical problems. Certain deviations were found to originate from carbon build-up in the vacuum gauge, remedied by cleaning. Other areas of error were found to involve dirty cones, sample input-pump failures and mass calibration shifts. The focusing of the lens stack can result in large differences in data from opposite ends of the spectrum due to changes in sensitivity with mass. This was remedied using  $^{115}\text{In}$  and  $^{187}\text{Re}$  double internal standards.

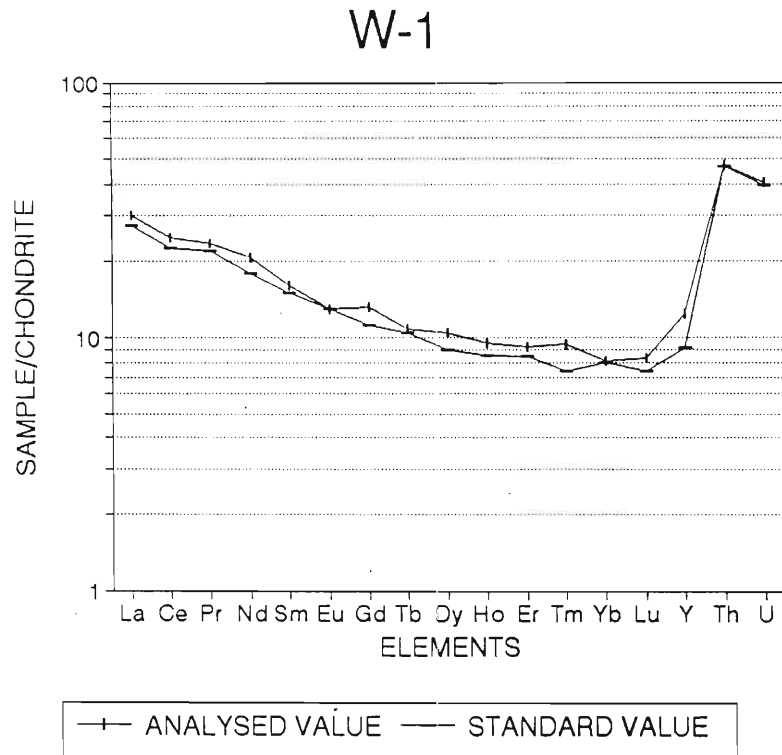
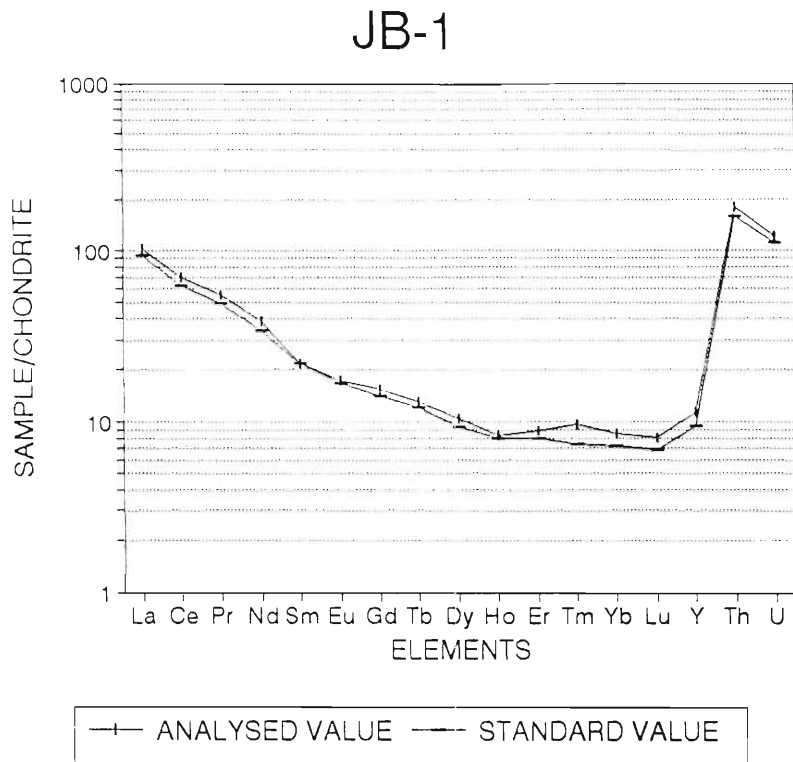


**FIGURE 3.05:** Chondrite normalised REE profiles of standards demonstrating accuracy, ICP-MS values and standard values from Govindaraju (1989): A) JB-1; B) W-1.

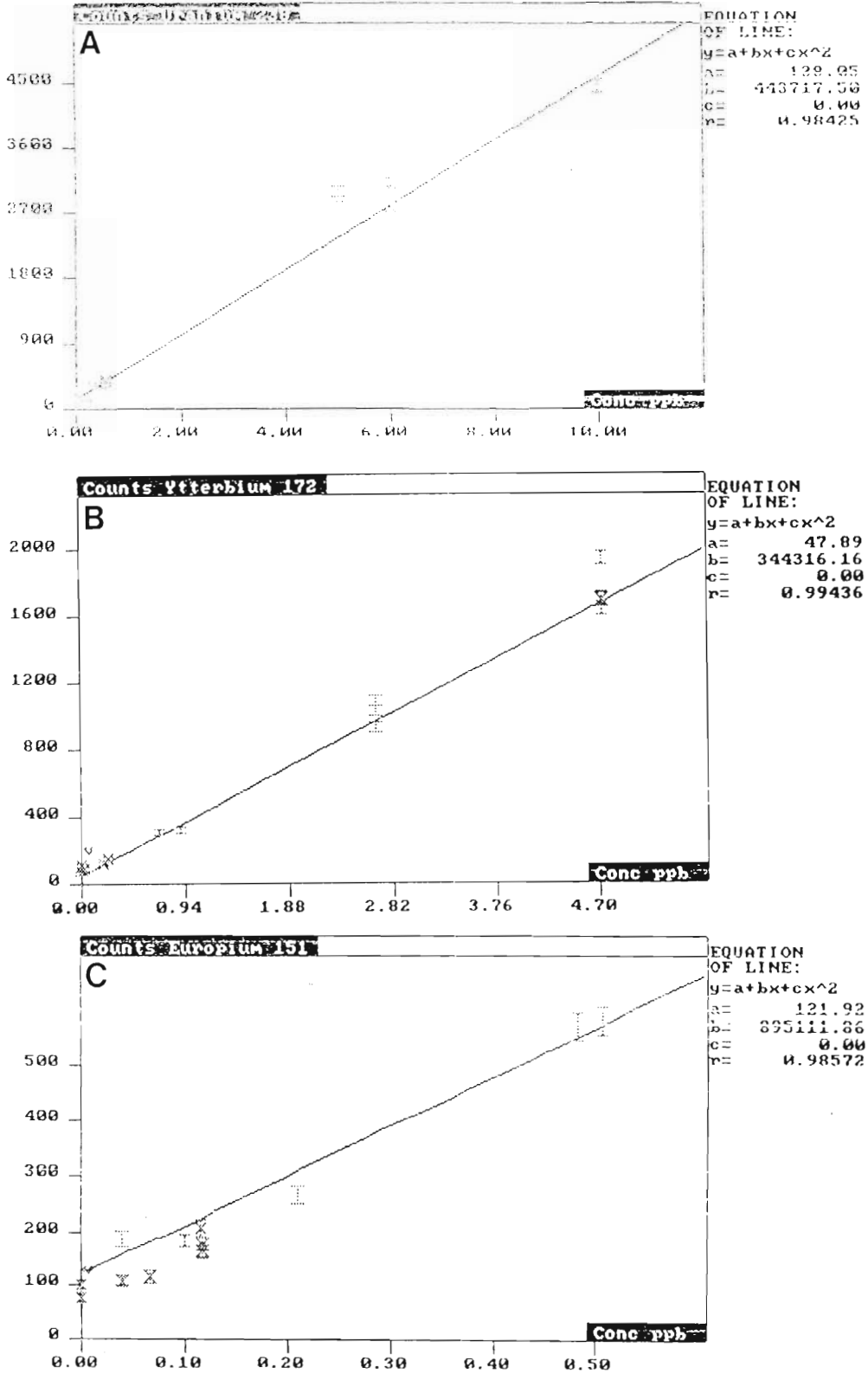


FIGURE 3.06: Calibration curves for three isotopes analysed on the ICP-MS, (A)  $^{238}\text{U}$ , (B)  $^{172}\text{Yt}$ , (C)  $^{151}\text{Eu}$ .



## CHAPTER 4

### GENERAL ATTRIBUTES OF THE ZIRCON CONCENTRATE

Several attributes of zircon from the RBM zircon concentrate were studied to assist in the interpretation of the U and Th reduction experiments. These included detailed point counting, identification of inclusions and fillings within zircon, identification of the types of zoning and the mapping of the distribution of U in individual grains.

#### 4.1 POINT COUNTING

Multiple factor point counting (ie. counting more than one attribute at each point) is a practical method of acquiring a detailed description of the bulk zircon concentrates. The relative amounts of crystal types, degrees of abrasion, crystal colour (metamict, coloured or clear), and number of inclusions are important in understanding the zircon concentrate and the experimental results.

Multiple factor point counting was performed on three sieve size fractions from 0.15kg of ZS-B91 NM, which were sieved for 1½ hours on a sieve shaker, namely <90µm, 90µm-125µm and 125µm-250µm. The less than 90µm fraction was 12.4% of the bulk, the 90µm-125µm was 63.8%, and the 125µm-250µm fraction was 23.8%.

The point counting was done by placing the sample on fine lined graph paper. The vertical lines were scanned using a low power binocular microscope. Only grains lying on the lines were investigated for the characteristics noted below. A computer programme was written in Borland's C++ (v2.0) program language for data recording and reduction. Each of the following attributes was noted for each grain:

1. **Colour and transparency?:**
  - Metamict
  - Coloured
  - Clear
2. **If metamict, was it?:**
  - Murky White
  - Red
  - Brown
  - White
3. **Degree of Elongation (L:B)?:**
  - <1.5 : 1
  - <3 to ≥1.5 : 1
  - ≥3 : 1
4. **Type of crystal form (Pupin's typology)?:**
  - ROUNDED
  - SINGLE
  - MULTIPLE
  - G1
  - UPPER P

LOWER P  
D  
COMPLEX S  
SIMPLE S

5. Number of Inclusions:

0 inclusions  
1-5 inclusions  
>5 inclusions  
Unable to ascertain.

The attributes of three hundred grains from each sieve fraction were recorded. Non-zircon grains in the samples were ignored. The data was imported into and manipulated in a spreadsheet. A summary of some of the comparisons is listed below.

#### 4.1.1 COLOUR DISTRIBUTION OF ZIRCON.

The bulk sample contains 5.9% metamict, 11.2% coloured and 82.9% clear grains. Coloured grains are defined as grains that are clear and transparent but exhibit pink to red to purple colour. Coloured zircon is indistinguishable from non-coloured zircon in high magnification transmitted light microscopy (ie. > x100), and low-powered reflective microscopy (x30) with grains on a white background is the optimum method. Metamict zircons were those zircons that were opaque or nearly opaque and exhibited colours ranging from black, grey, white, cream, brown to red brown. Crystal type proportions for each size fraction in the bulk sample is graphically shown in Figure 4.01. Table 4.01 is a summary of the zircon colour results and distributions.

**TABLE 4.01:** Colour point counting results.

Sample	Metamict	Coloured	Clear	Total
Bulk Sample	5.87%	11.19%	82.94%	100.00%
<b>Contributions of each size fraction to Bulk Sample:</b>				
<90 $\mu$ m sieve fraction	0.12%	1.23%	11.03%	12.38%
90 $\mu$ m to 125 $\mu$ m sieve fraction	3.02%	8.20%	52.62%	63.84%
>125 $\mu$ m sieve fraction	2.73%	1.77%	19.29%	23.79%
<b>Colour distribution within each size fraction:</b>				
<90 $\mu$ m sieve fraction	0.99%	9.91%	89.09%	100.00%
90 $\mu$ m to 125 $\mu$ m sieve fraction	4.73%	12.84%	82.44%	100.00%
>125 $\mu$ m sieve fraction	11.48%	7.43%	81.09%	100.00%

The > 125 $\mu$ m sieve fraction contributes nearly 50% of the metamict grains but only constitutes 24% of the bulk sample by mass. The less than 90 $\mu$ m sieve fraction has only 1% metamict grains compared to the 11.5% of the largest size fraction. The large sieve fraction is therefore expected to have a higher U and Th concentration

#### 4.1.2 DISTRIBUTION OF CRYSTAL TYPES.

The crystal types (ie. the relative development of the different crystal forms) were counted

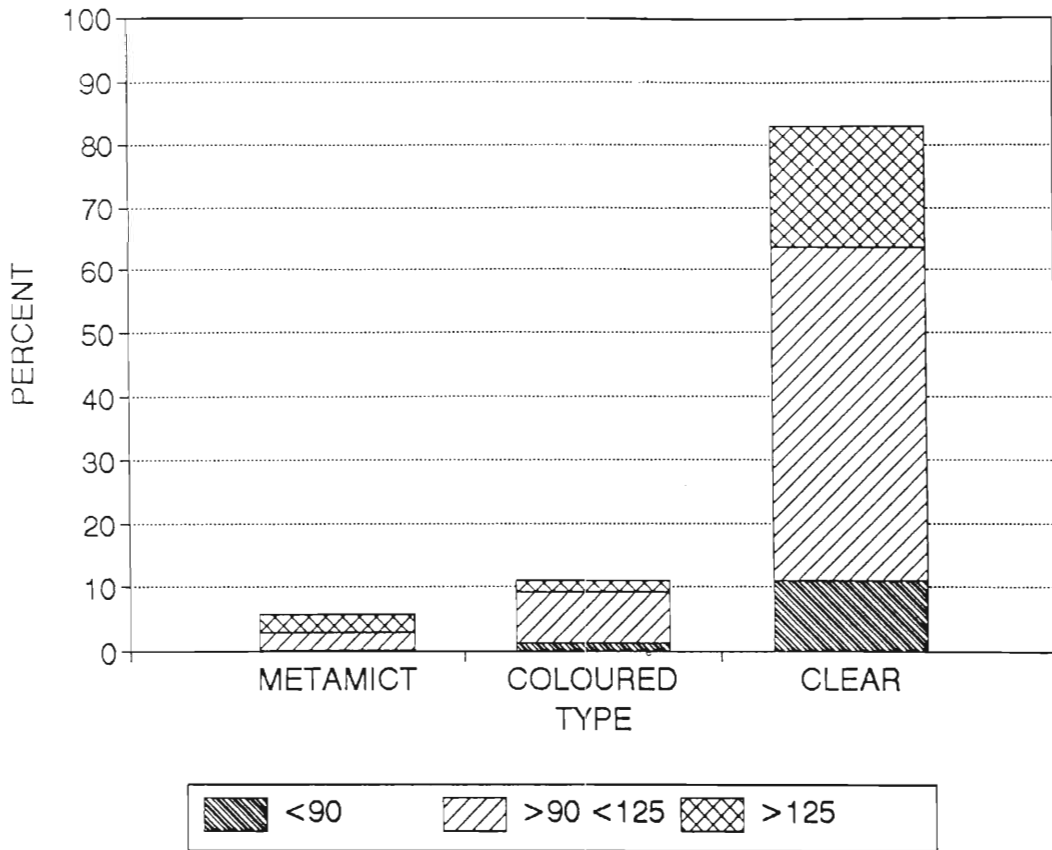


FIGURE 4.01: Distribution of crystal type with size.

using nine categories based on the simplified version of Pupin's (1980) classification scheme (see Section 2.1.4). Only 41% of grains from the bulk sample could be categorized into 6 identifiable crystal type groups, while the remaining 59% fell into the Rounded, Single and Multiple categories (See Table 4.02).

TABLE 4.02: Distribution of crystal types in the bulk and size fractions.

Sample	G1	UP	LP	D	CS	SS	UNIDENTIFIED
<b>Contribution of each crystal type to bulk sample (% of bulk):</b>							
Bulk Sample	2.8	4.3	4.4	18.9	3.0	7.4	59.2%
<b>Percentage of each crystal group (calculated to 100% of identified pairs):</b>							
Bulk Sample	6.9	10.6	10.8	46.4	7.4	18.1	

D-type zircon is the most abundant identifiable crystal type, contributing 19% of the bulk sample and 46% of identifiable crystal types. The second most common variety of zircon is the Simple S type contributing 7% to the bulk sample and 18% of the identifiable crystal types. If the SIMPLE S, the LOWER P, and D type zircon represent high temperature zircon according to Pupin (1980) 75% of the identifiable zircon are derived from high temperature (>750°C) rocks. The 59% of zircon crystals that could not be classified as crystal types were divided up as ROUNDED 26.4%, SINGLE

faced 17.0% and MULTIPLE faced 15.9%. The less than 90 $\mu$ m sieve fraction contained the least unidentified grains with 62% of the grains being identifiable, and the middle and large fractions contained the most unidentifiable grains with only 35% and 43% of the grains being identifiable in the respective size fractions. The increased abrasion in the larger size fractions can be explained by the fact that grains less than 150 $\mu$ m are abraded to a lesser degree in the wind environment (Kuenen, 1960).

#### 4.1.3 COMPARISON OF CRYSTAL TYPE TO COLOUR OF THE CRYSTAL.

Comparing the crystal colour (ie. metamict, coloured or clear) to the crystal type (see Table 4.03 and Figure 4.02) the COMPLEX S type zircon has the highest proportion of metamict grains. The unidentified classes and the two P transition groups contained the highest proportion of coloured zircon.

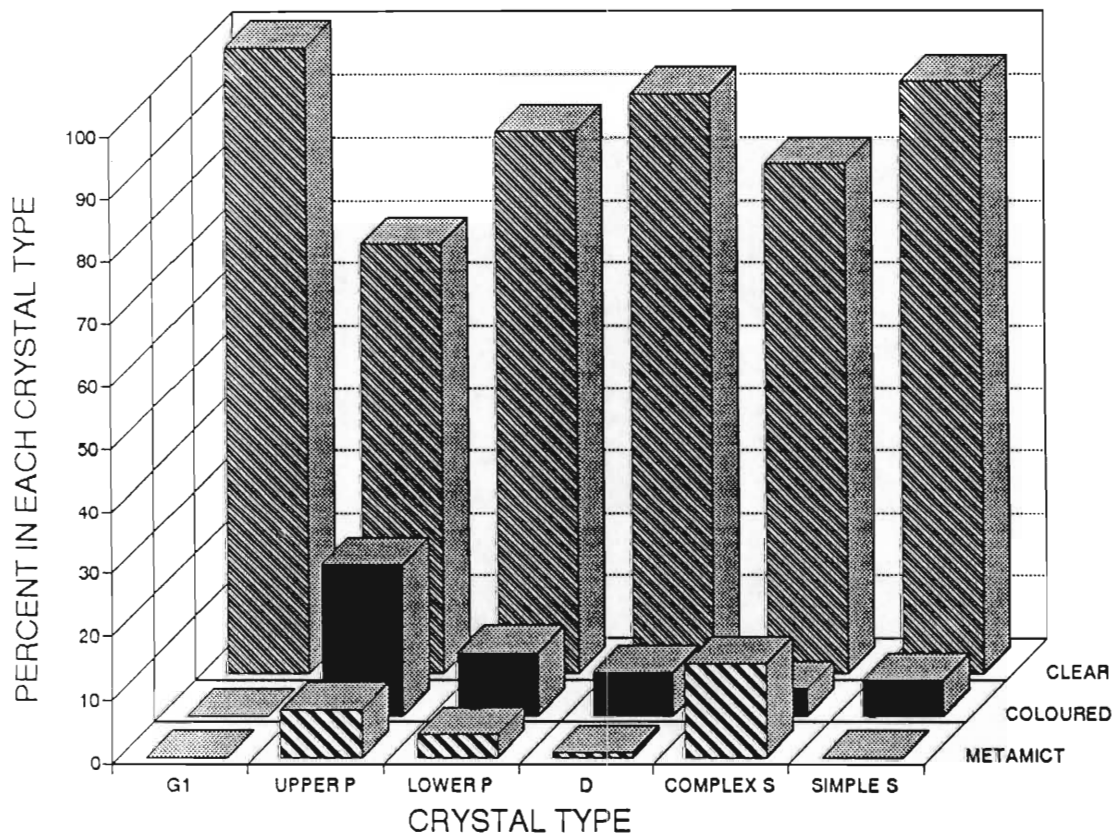


FIGURE 4.02: Comparison of crystal type to colour, each zircon type calculated to 100%.

**TABLE 4.03:** The distribution of colour in each crystal type group.

Crystal Type	Metamict	Coloured	Clear
G1	0%	0%	100%
UPPER P	7%	24%	69%
LOWER P	4%	10%	87%
D	1%	7%	93%
COMPLEX S	15%	4%	81%
SIMPLE S	0%	6%	94%
MULTIPLE	10%	12%	78%
SINGLE	7%	15%	77%
ROUNDED	8%	13%	79%

#### 4.1.4 ELONGATION COMPARED TO SIEVE FRACTION AND CRYSTAL STATE

The sieving of a sample containing a high proportion of elongate grains is biased because the elongate grains will be collected in the sieves with larger apertures than the grain width.

The point counting data in Table 4.04 shows that 55.4% of the sample has a Length/Breadth ratio of less than 1.5. This high fraction of grains with low elongation is due to the large number of grains that have been broken. Most grains in the bulk sample are terminated by a pyramid at one end and a fractured prism at the other. The <90 $\mu\text{m}$  fraction is the least abraded or broken and has the highest proportion of elongate grains (41%). The other two fractions both have less than 10% grains with an elongation ratio of >3. This shows that the average width of a large proportion of the elongate grains is smaller than the mesh size of the 90 $\mu\text{m}$  and 125 $\mu\text{m}$  sieves. A biased result would only be obtained if a sieve with smaller mesh size than the average width of elongate grains in the <90 $\mu\text{m}$  size fraction were used.

**TABLE 4.04:** Length/Breadth ratios distributions in the bulk and size fractions.

Sample	Length/Breadth elongation ratio		
	<1.5	1.5-3.0	>3.0
Bulk Sample	55.4%	31.4%	13.4%
<b>Distribution within each size group:</b>			
<90 $\mu\text{m}$ sieve fraction	31.7%	27.7%	40.6%
90-125 $\mu\text{m}$ sieve fraction	64.2%	26.4%	9.5%
>125 $\mu\text{m}$ sieve fraction	43.9%	46.6%	9.5%
<b>Distribution by crystal colour:</b>			
Metamict zircon	68%	24%	8%
Coloured zircon	60%	33%	8%
Clear zircon	46%	35%	19%

#### 4.1.5 DISTRIBUTION PATTERNS OF INCLUSIONS IN ZIRCON.

A simple correlation exists between the number of inclusions and the average size of the samples (See Table 4.05 and Figure 4.03). Only 3% of the grains in the smallest size fraction contain more than 5 inclusions. In the largest size fraction a total of 81% of the grains contain greater than 5 inclusions. Therefore the larger the grains the more inclusions it is likely to hold.

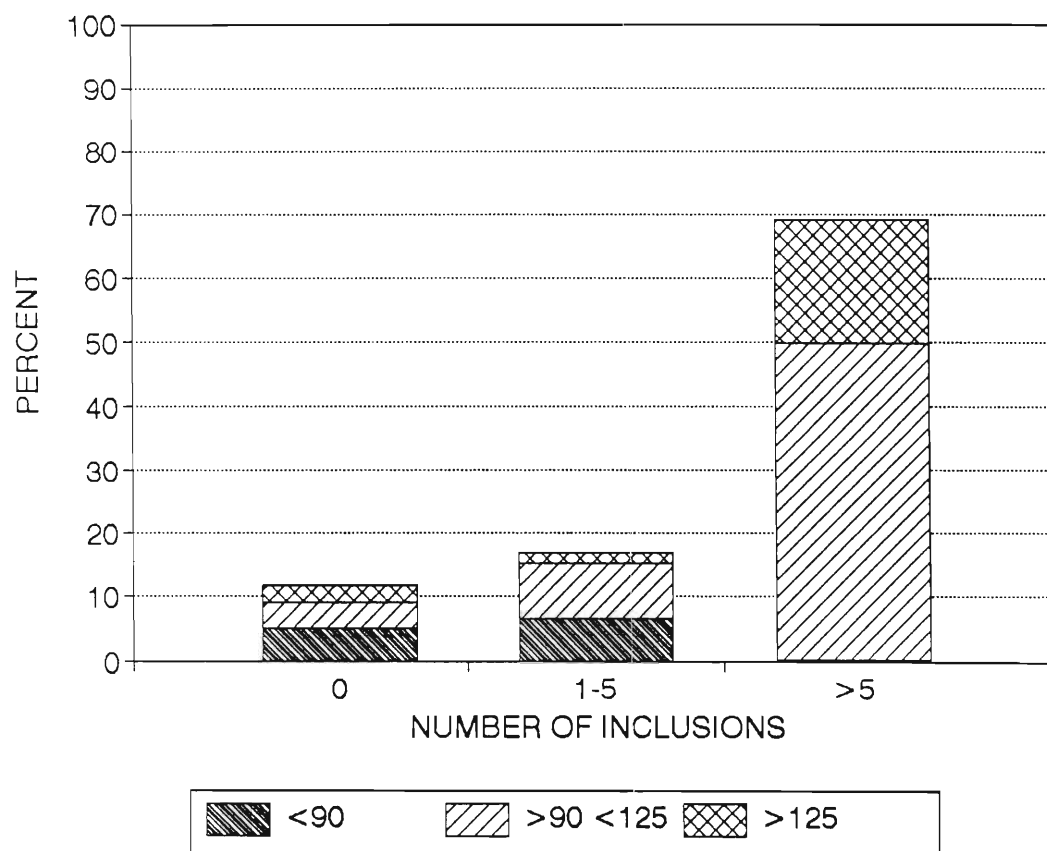
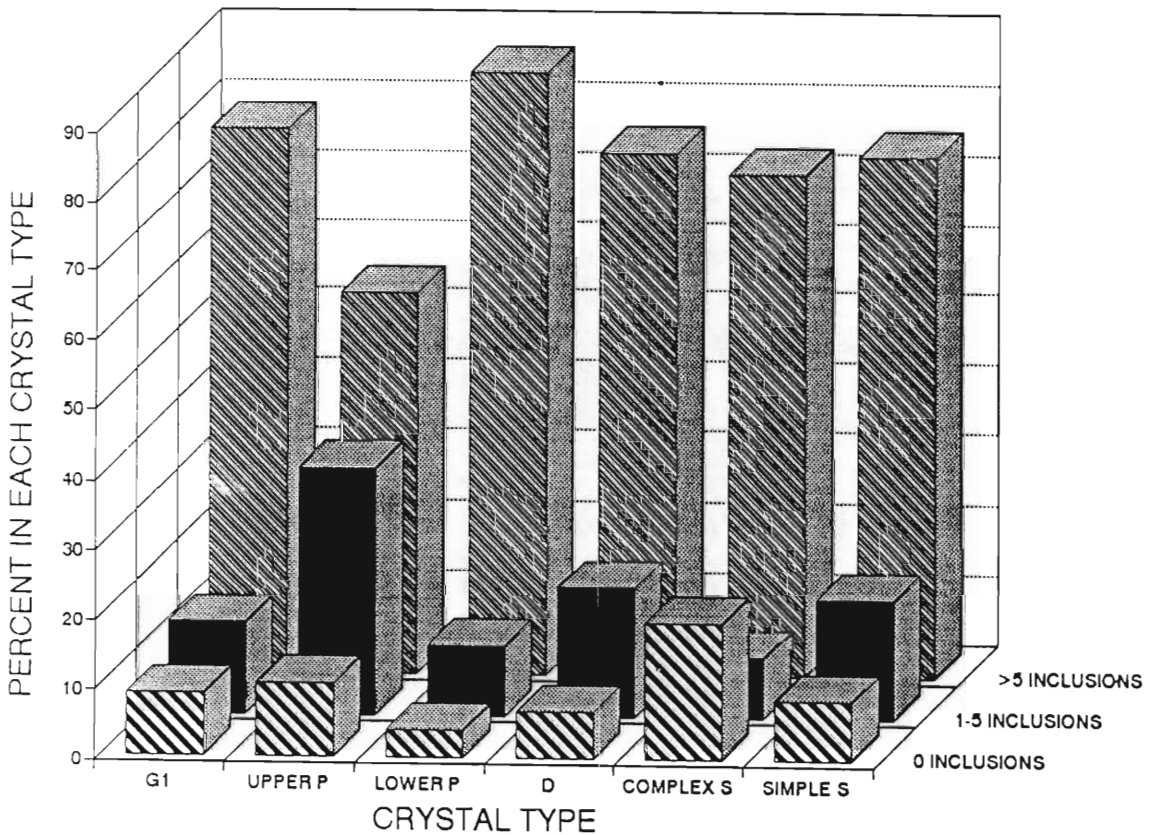


FIGURE 4.03: Distribution of the number of inclusions with size.

**TABLE 4.05:** Distribution of the number of inclusions within the bulk sample and sieve fractions (Excluding grains where inclusions could not be counted due either to frosted surface or opacity).

Sample	Number of Inclusions		
	0	1-5	>5
Bulk Sample	12%	18%	71%
<b>Distribution within each size group:</b>			
<90µm sieve fraction	42%	55%	3%
90-125µm sieve fraction	7%	14%	79%
>125µm sieve fraction	11%	7%	81%

See Table 4.06 and Figure 4.04 for the distributions of amount of inclusions within each crystal type. The COMPLEX S type zircons contain the least inclusions (19% with no inclusions) compared to LOWER P type which has the most inclusions (86% have greater than 5 inclusions).



**FIGURE 4.04:** Comparison of crystal type with the number of inclusions in each type (each type calculated to 100%).

The **ROUNDED**, **SINGLE** and **MULTIPLE** groups all have high proportions of grains with few or no inclusions. This may be due to grains with inclusions being more susceptible to breaking. The fractured terminations of broken grains often show inclusions protruding from surface of the break. Such inclusions are likely to be removed by weathering, being less resistant to attack than zircon.

**TABLE 4.06:** Distribution of the number of inclusions compared to crystal type.

Sample	Number of Inclusions		
	0	1-5	>5
<b>Distribution within each crystal type:</b>			
G1	9%	13%	78%
UPPER P	10%	35%	54%
LOWER P	4%	10%	86%
D	7%	19%	75%
COMPLEX S	19%	9%	72%
SIMPLE S	8%	17%	75%
MULTIPLE	13%	18%	69%
SINGLE	12%	15%	73%
ROUNDED	18%	18%	64%

#### 4.1.6 DISCUSSION OF POINT COUNTING

The diversity of attributes of zircon in the zircon concentrate is clearly illustrated by multi-factor point counting. The data shows several trends that were expected, for example: the increase of roundness and the decrease of elongation with increasing size of metamict zircon. Trends that were unexpected include the decrease in the quantity of metamict zircons with size. The data is useful to describe the zircon concentrate and is very useful in explaining experimental results.

Other attributes which were not counted, for example the presence of zoning or SEM point counting of the types of inclusions, would also be useful in understanding the distribution of impurities within the zircon concentrate.

#### 4.2 BACKSCATTERED ELECTRON IMAGERY

The Scanning Electron Microscope (SEM) focuses a beam of electrons onto the surface of a sample under vacuum, producing various interactions which result in several types of emission which can be recorded or produced as images. Two major types of interaction occur, the first is an *inelastic interaction* termed secondary electron (SE) emission, and the second is an *elastic interaction* or backscattered electron (BSE) emission. See Lloyd (1987) for a review of backscattered electron imagery techniques. The SE emission shows up irregularities of the surface of the sample and is used mainly to produce images of outer shape or relief. The BSE are scattered by elastic interactions within the sample and their intensity depends on the density and to a lesser extent the relief of the sample. To obtain images related to composition, BSE imagery is performed on smooth surfaces of



polished samples to eliminate topographic effects.

BSE images record information on the variations in mean atomic number ( $Z$ ) or density contrast within the polished section. With higher mean  $Z$ -number and density the backscattered intensity increases. Therefore in multi-phase samples with different density in each phase, the phases produce different BSE intensities.

#### 4.2.1 BSE METHOD AND RESULTS

A Hitachi-S520 SEM was used to obtain BSE images. The BSE photomicrographs were taken with at 15kV with an objective aperture of 200. All SEM photomicrographs have scales in the bottom right-hand corners.

Density contrast within zircon was identified in several samples. In several samples concentric oscillatory zoning was evident and in others sector zoning with oscillatory growth zoning is also present this is due to changes in chemical composition and/or density. Another useful effect of BSE is to differentiate inclusions, for example the zircon in Plate 4.01 (SEM 120813) contains three unidentified inclusions of at least two compositions. Further BSE images of inclusions within zircon are presented in Section 4.3 and zoning in Section 6.1.

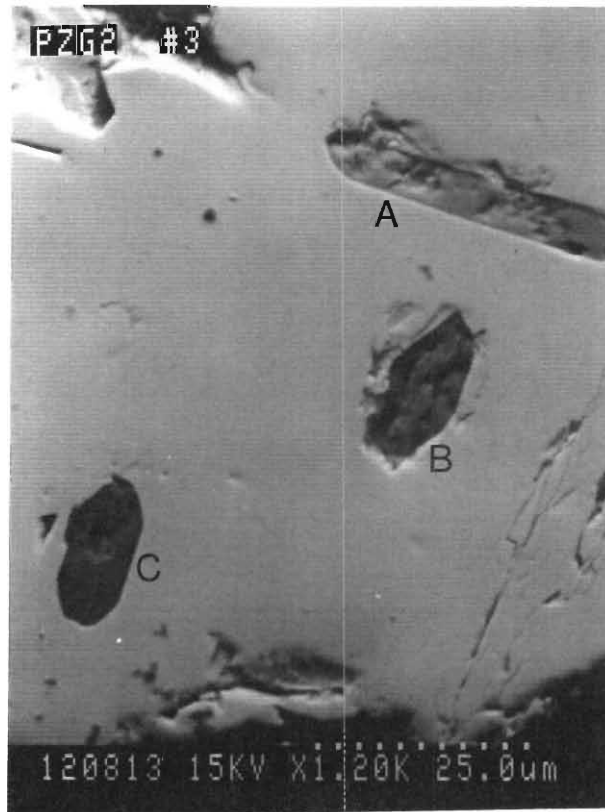


**PLATE 4.01:** SEM BSE image of a zircon containing three inclusions (SEM 120813): (A) Apatite, (B) Alkali feldspar, and (C) Albite. The scale is shown at the bottom of the photograph.

### 4.3 INCLUSIONS IN ZIRCON

It is important to identify the inclusions in the zircon grains to obtain an indication of the range and contribution of trace elements from the inclusions to the bulk sample.

#### 4.3.1 LITERATURE ON INCLUSIONS IN ZIRCON

A major difficulty in a literature review of inclusions in zircon is that inclusions are usually only identified if the zircons were believed to be of metamorphic or hydrothermal origin. In cases where zircon is thought to be of igneous origin the existence of inclusions is admitted but further information concerning their identity or composition are not furnished by the authors. Table 4.07 lists the inclusions identified in the literature and their respective chemical formulae, and a few examples are given below.

Claué-Long *et al.* (1992) reported that zircon from veins in the Archean Abitibi quartz diorite batholith contain inclusions of quartz, gold, tourmaline, muscovite, dolomite, auriferous pyrite, albite, K-feldspar, apatite and scheelite. Chernyshev *et al.* (1987) identified nepheline, Ca-feldspar, apatite, and sphene in zircons from carbonatites. Rimsaite (1981) identified uraninite, uranothorite, quartz, apatite, feldspar and galena inclusions. Fractures in zircons that were annealed contained uranyl bearing aggregates, Fe-oxides, Fe-arsenides, galena and REE-bearing compounds.

Rubin *et al.* (1989) reported inclusions of thorite, Fe-oxides, coffinite, cerfluorite, changbaitte, columbite, xenotime and yttrifluorite

**TABLE 4.07:** Minerals identified as inclusions in zircon in the literature.

Mineral Name	Mineral Formula
Quartz	SiO <sub>2</sub>
Tourmaline	Na(Mg, Fe, Mn, Li, Al) <sub>3</sub> Al <sub>6</sub> [Si <sub>6</sub> O <sub>18</sub> ](BO <sub>3</sub> ) <sub>3</sub> (OH, F) <sub>4</sub>
Muscovite	K <sub>2</sub> Al <sub>4</sub> [Si <sub>6</sub> Al <sub>2</sub> O <sub>20</sub> ](OH, F) <sub>4</sub>
Dolomite	CaMg(CO <sub>3</sub> ) <sub>2</sub>
Fe-oxides	Fe <sub>2</sub> O <sub>3</sub> or Fe <sub>3</sub> O <sub>4</sub>
Pyrite	FeS <sub>2</sub>
K-feldspar	(K, Na)[AlSi <sub>3</sub> O <sub>8</sub> ]
Plagioclase	Na[AlSi <sub>3</sub> O <sub>8</sub> ]-Ca[Al <sub>2</sub> Si <sub>2</sub> O <sub>8</sub> ]
Apatite	Ca <sub>5</sub> (PO <sub>4</sub> ) <sub>3</sub> (OH, F, Cl)
Sphene	CaTi[SiO <sub>4</sub> ](O, OH, F)
Galena	PbS <sub>2</sub>
Scheelite	CaWO <sub>4</sub>
Nepheline	Na <sub>3</sub> (Na, K)[Al <sub>4</sub> Si <sub>4</sub> O <sub>16</sub> ]
Xenotime	(Y, HREE)PO <sub>4</sub>
Thorite	ThSiO <sub>4</sub>
Uraniothorite	(U, Th)SiO <sub>4</sub>
Uraninite	UO <sub>2</sub>
Coffinite	U(SiO <sub>4</sub> ) <sub>1-x</sub> (OH) <sub>4x</sub>
Columbite	(Fe, Mn)Nb <sub>2</sub> O <sub>3</sub>
Bastnasite	(Ce, La)CO <sub>3</sub> F
Cerfluorite	(LREE)F <sub>3</sub>
Changbaitte	PbNb <sub>2</sub> O <sub>6</sub>
Yttrifluorite	YF <sub>3</sub>

\*: HREE = Heavy Rare Earth Element; LREE = Light Rare Earth Element

### 4.3.2 METHOD AND RESULTS

Zircons that contained inclusions (Plate 4.02) were hand-mounted and carefully polished until the inclusions were exposed. During polishing zircon grains are easily cracked, extreme care must be exercised when polishing and only very fine abrasives with gentle hand-polishing will yield satisfactory results. The inclusions were then identified and semi-quantitatively analysed using a Kevex X-ray energy dispersive spectrometer attached to a Jeol-35 Scanning Electron Microscope. Due to the low kV used (15kV) the peak Fe at the top end of the spectrum is suppressed relative to the mid-range elements, while Na and Mg peaks are lowered due to absorption by the beryllium counter window.

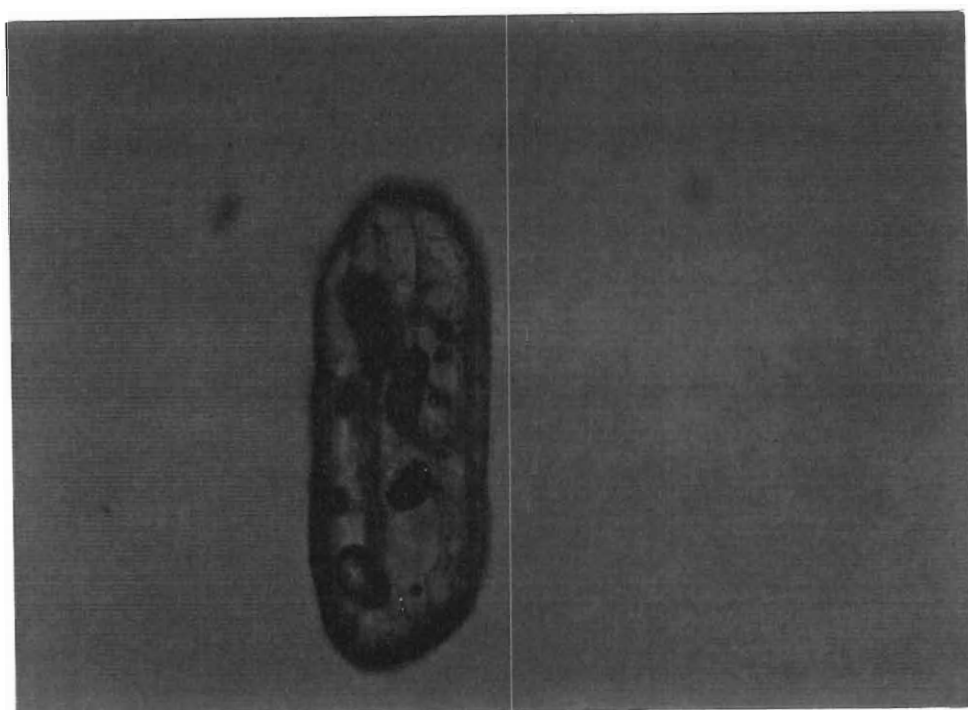


**PLATE 4.02:** A 150 $\mu$ m long zircon containing multiple inclusions.

Table 4.08 lists the minerals identified as inclusions in RBM zircon. The most common inclusion is the Fe-Ti oxide, ilmenite. Two types were identified, one with no Mn peak (Figure 4.05A) and ilmenite with small Mn peaks (Figure 4.05B), about 7% MnO. The work of Hugo (1993) and Arran (1993), on trace elements and provenance of ilmenite from northern Natal, may be a useful indicator of provenance for zircon that contain different varieties of ilmenite.

Clear to slightly coloured inclusions, elongated parallel to the zircon *c*-axis or at 45° to the *c*-axis and parallel to growth zoning, in large elongate zircon were identified as zircon. The forms {100}, {110} and {101} could be recognized with transmitted light microscopy.

Red transparent inclusions in a rounded zircon with a L/B ratio of 1 were identified as the

Ca-phosphate, apatite (Figure 4.05C).

A bipyramidal zircon contained more than 8 inclusions ranging from Fe-sulphide (Pyrite?) (Figure 4.05D) to pure silica and biotite (Figure 4.05E).

In several cases where an inclusion intersected the grain surface or a pit separated an inclusion from the surface, alumino-silicates were identified surrounding ilmenite (Figure 4.05F). Several inclusions were found to be alumino-silicate filled pits with constricted openings to the grain surface. These alumina-silicates commonly contained small Cr peaks, and some also contained small K peaks. A rounded semi-metamict zircon contained Fe-poor biotite (phlogopitic biotite) with low to no Na. Several of the grains contained biotite (Figure 4.05E). Zircons are commonly associated with biotite in granites or gneisses, for example Aleinikoff (1983) found that zircon was the most abundant inclusion in biotite compared to the other minerals in a granite.

**TABLE 4.08:** List of minerals identified as inclusions in RBM zircon.

Inclusion	Impurities
Alumino-silicates	Al, Mg, K
Clay + Fe-staining	Al, Mg, K, Fe
Ilmenite	Fe, Ti
Ilmenite + Mn	Fe, Ti, (Mn)
Zircon	-----
Amphibole	Mg, Ca, Al, Fe, Na, (Ti), (K)
Alkali Feldspar	K, Al
Albite	Ca, K, Al
Apatite	Ca, P
Pyrite	Fe, S
Sphene	Ca, Ti
Biotite	Fe, Al, K, Mg, Na, Ti
Phlogopite	Mg, Al, Fe, (Ti)
Muscovite or Illite	Al, K, Fe

Plate 4.03 (SEM 120818) is a BSE image of a metamict grain. The grain contains numerous unidentified inclusions. Plate 4.04 (SEM 120800) shows an unidentified elongate inclusion within a zircon.

#### 4.4 FILLINGS

Numerous zircons from the zircon concentrate contain red or grey fillings in shallow concave indentations, in open pits or pits with constricted mouths as shown in Plate 4.05 (SEM 120828), Plate 4.06 (SEM 120849) and Plate 4.07 (SEM 150517). The concave rounded pits in the zircon originate from intergrowths of zircon with other minerals or inclusions within zircon which intersect the surface. Due to the greater resistance of zircon to mechanical and chemical attack the minerals in the pits are preferentially removed during the weathering process. Plate 4.08 (SEM 120805) is a BSE image of a unidentified inclusion in zircon that intersects the surface. The inclusion has a rounded shape and shows weathering near the surface.

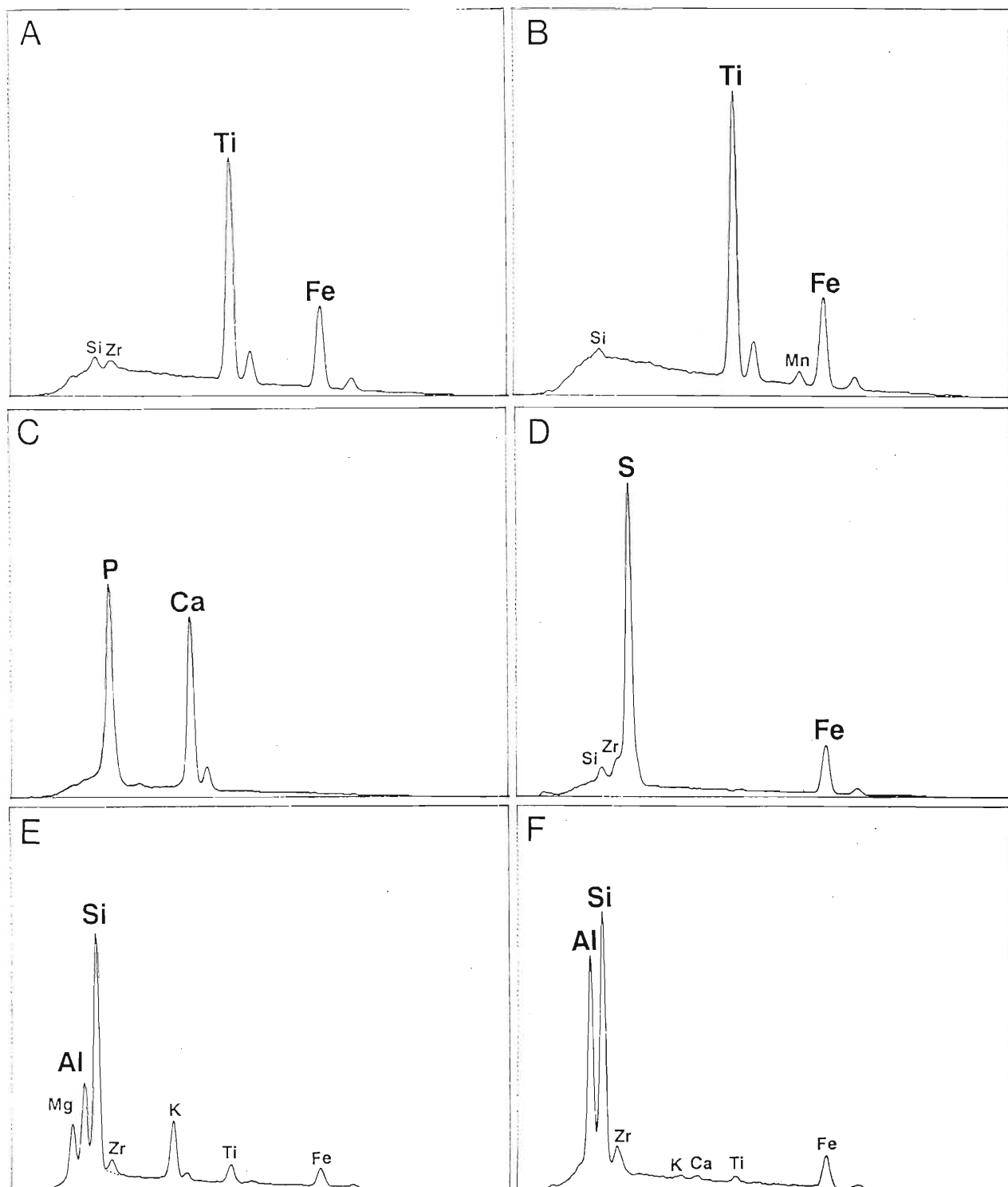


FIGURE 4.05: X-ray EDS spectrums for 6 types of inclusion in zircon: A) Ilmenite; B) Mn-Ilmenite; C) Apatite; D) Pyrite; E) Biotite; F) Alumina-silicate (Clay).

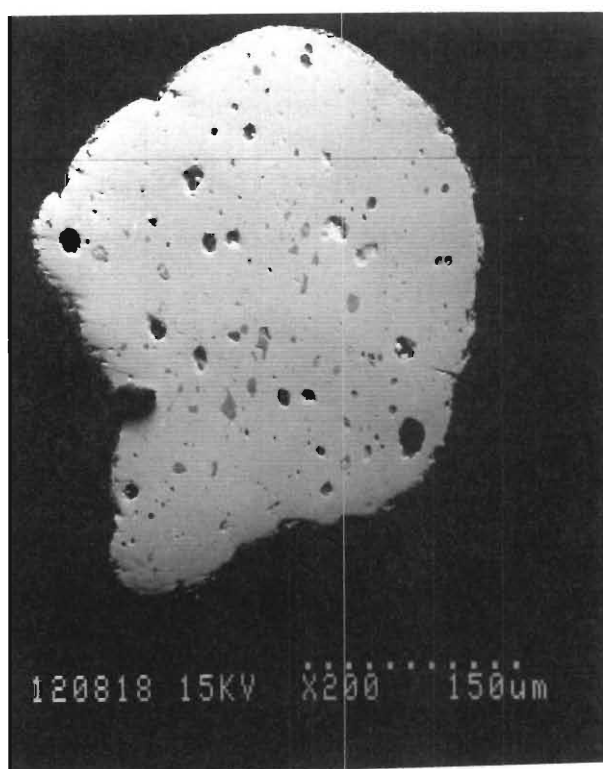


PLATE 4.03: SEM BSE image of a metamict zircon polished thin section containing numerous inclusions.

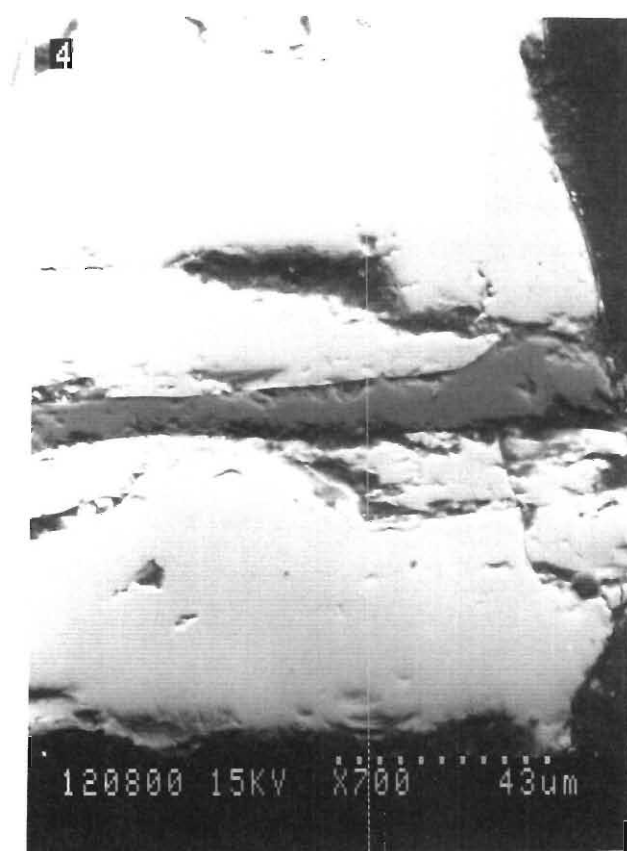


PLATE 4.04: SEM BSE image of a zircon containing an unidentified inclusion.



PLATE 4.05: SEM photomicrograph of a clay-filled open-mouthed pit in a zircon. Note the cracks in the surface coating over the clay-filling (SEM 120828).

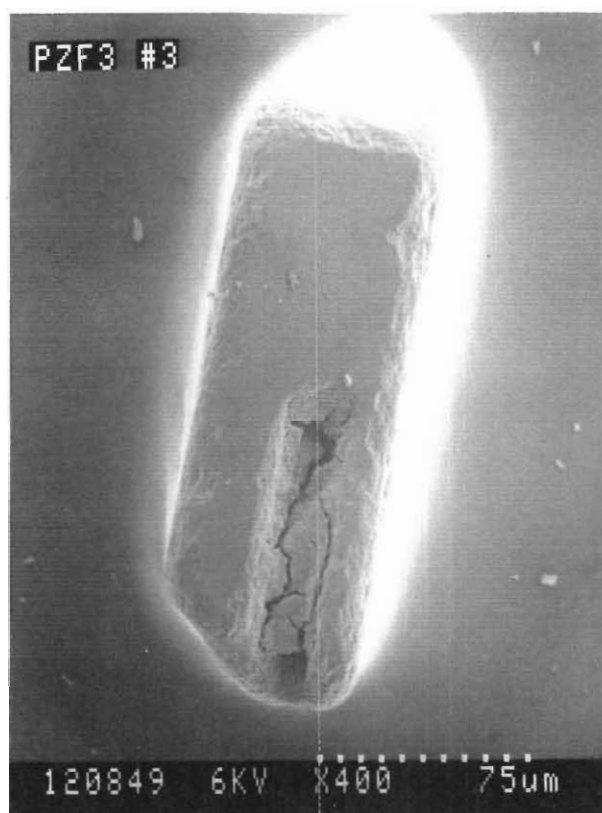
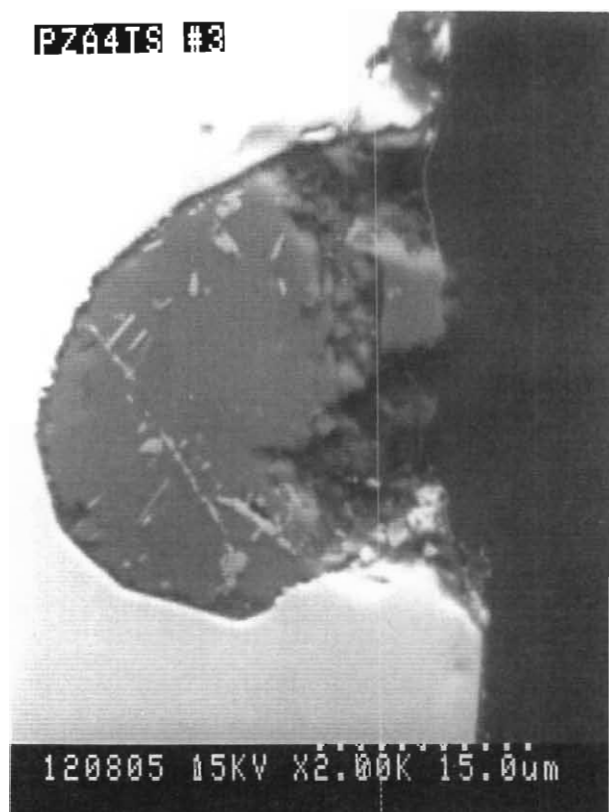


PLATE 4.06: SEM photomicrograph of a D-type zircon with a large open pit filled with clay and covered by a coating which contains numerous pits (SEM 120849).



**PLATE 4.07:** SEM photomicrograph of an elongate S24-type zircon with a clay-filled pit with a constricted mouth (SEM 150517).



**PLATE 4.08:** SEM BSE image showing a section through an inclusion that intersects the surface of the zircon grain (SEM 120805).



#### 4.4.1 LITERATURE ON GRAIN COATINGS

The most widely accepted explanation for the origin of the clay fillings in zircon is the infiltration of airborne dust into the sediments followed by the mechanical infiltration of dust particles into the dune or alluvial deposit and onto the grains. Walker (1979) observed that clay coatings are rare in beach deposits, but are common in associated dune deposits. Rain water is the prime mode for the infiltration of the clay into the pits in grains in aeolian or alluvial sediments. In Libya, Walker (1979) observed that the grains in areas of higher rainfall had higher levels of surficial clay. When the grains are later moved by the wind clay tends to be abraded from the surfaces, but remains in the indentations and pits.

The origin of the iron pigment found coating the grains, including the clay fillings in the pits, is believed to be the breakdown of iron bearing minerals and clays within the sediments. The iron pigment is deposited as amorphous ferric hydrate or fine crystalline goethite. Both limonite and goethite are metastable and will convert to hematite with time (Langmuir, 1971). The durability of the iron pigment and clay coatings depends on the number and size of the indentations and the size of the grains. Finer grains tend not to be abraded and thus retain their coatings for longer periods than the larger grains (Walker, 1979; Kuenen, 1960).

#### 4.4.2 METHOD AND RESULTS

Grains with open pits containing material varying from red, through brown and grey to black were mounted in Petropoxy 154 with the pits upward. The pit and indentation fillings were then semi-quantitatively analysed with the SEM. They all showed alumino-silicate spectra with iron peaks (Figure 4.05F). The pits are thus filled with clay that is stained with limonite or hematite. The clay platelets within the pits can be clearly recognized in Plates 4.09 (SEM 150518 close-up of SEM 150517) and in the cross-section of a pit in Plate 4.10 (SEM 120809).

Removal of clay from the pits is difficult, especially in pits with constricted openings. Several washing experiments were completed on grains with fillings or red iron coatings. Grains were washed in boiling 10% nitric for 1 hour followed by cleaning in a ultra-sonic bath. Plate 4.11A shows the zircon grain before washing with an iron-stained clay-filled pit and Plate 4.11B shows the grain after treatment, note that some of the clay remains in the open pit but the red iron coating is entirely removed. HF treatment (described in Chapter 6) removed the clay fillings from all the grains, including the pits with constricted openings (See Plate 6.07).

Point counting of magnetic zircon fractions indicates that the iron-filled or iron-coated clay-filled indentations cause the stained grains to report in the magnetic fractions on Frantz Magnetic Separators.

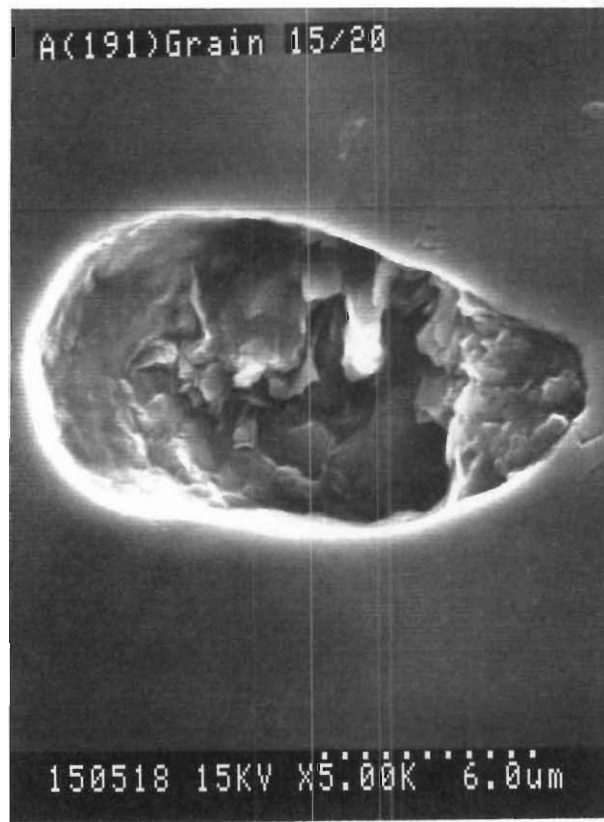


PLATE 4.09: SEM photomicrograph close-up of a pit filled with clay platelets (SEM 150518 close-up of Plate 4.07).

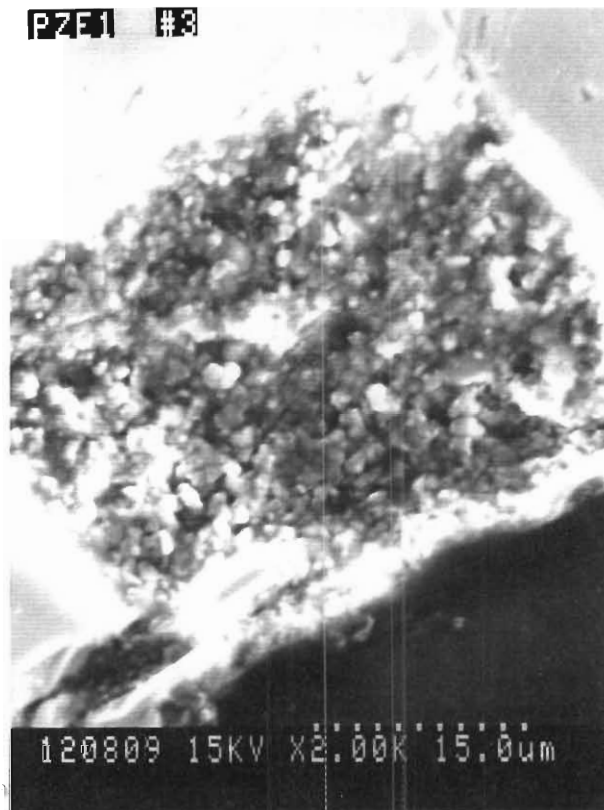
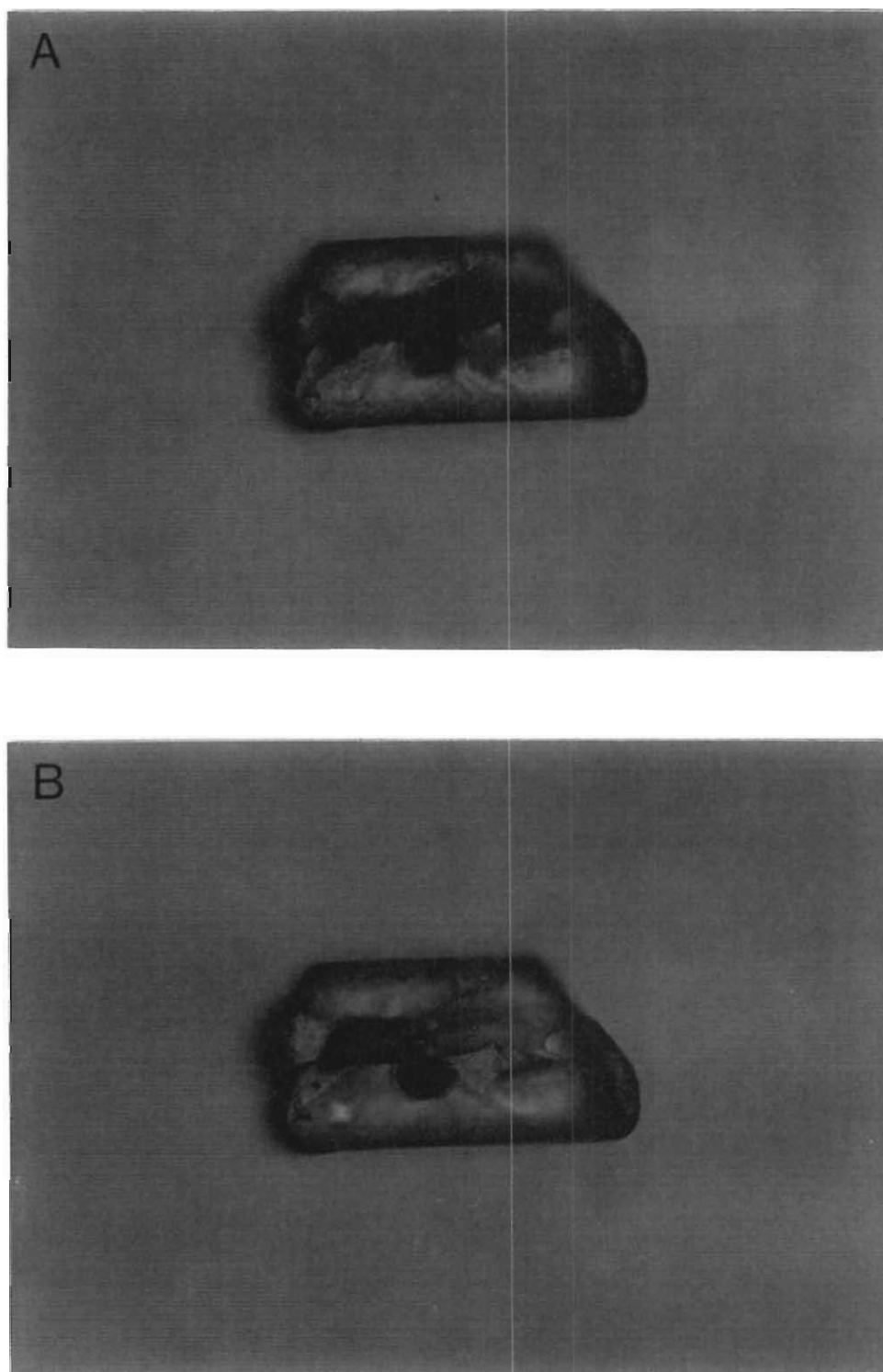


PLATE 4.10: SEM photomicrograph of a cross-section of a clay-filled pit (SEM 120809).



**PLATE 4.11:** The iron-coated clay filling in a pit in a 100 $\mu$ m zircon grain before washing (A); and after washing in acid in a ultrasonic bath (B).

## 4.5 ZONING

Several types of zoning or overgrowths are recognized in the zircon concentrate. Several zircons have clear overgrowths on partially metamict cores. The most common type of zoning found in the zircon product is fine oscillatory zoning. A detailed examination of zoning within zircon is important if the impurities in the concentrate are to be understood. Zoning is an important factor controlling the distribution of impurities within the zircon structure, as described below.

### 4.5.1 LITERATURE ON ZONING IN ZIRCON

#### Sector zoning in zircon

Sector zoning is produced by different growth zones having different compositions (Figure 4.06A). Caruba and Turco (1971) classify the pyramid  $\{211\}$  face of zircon as S-forms (stepped faces) using Hartman and Perdok's (1955) model of crystal growth. S-faces are more likely to adsorb foreign elements due to the large number of attachment sites on resulting on the stepped structure of the growth surface. Fission track mapping of zircon from RBM indicates that a large proportion of the zircon grains contain high uranium in the pyramids.

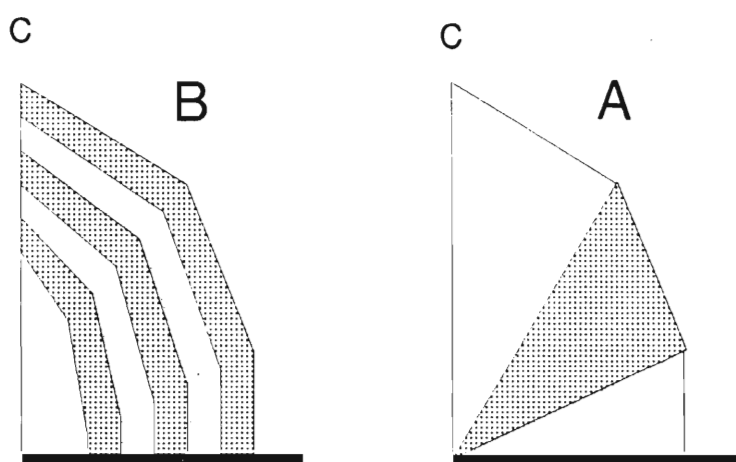


**FIGURE 4.06:** A) Sector zoning; B) Oscillatory zoning superimposed on sector zoning.

The F-forms (flat faces) are  $\{100\}$ ,  $\{110\}$  and  $\{101\}$  according to Caruba and Turco (1971). F-faces have less attachments at the growth surface and are therefore expected to include fewer foreign elements (Chernov, 1984). The  $\{100\}$ -faces are an exception to this rule and contain higher proportions of foreign elements (Vavra, 1990). Fission track mapping of uranium distribution has

shown that the {110}-growth sectors have far lower concentrations of uranium than their adjoining sectors (Carpéna *et al.*, 1987), and also lower concentrations of Y and Hf (Hoffman and Long, 1984)

The {110} sectors observed by cathodoluminescence are consistently brighter than others, while {100} sectors are consistently darker (Vavra 1990). Sommerauer (1974) states that this brightness is related to a low total concentration of foreign elements. This is contrary to the literature compiled by Marshall (1988) which states that Si, Mn, V, Hf, Y, Dy, Gd, Sm and Eu impurities in zircon may be activators of cathodoluminescence when excited by electrons (eg. Leverenz, 1968; Ono, 1976; Marfunin, 1979). Mariano (1978) describes zircon as having an intrinsic broad luminescence emission-band at 590nm with superimposed  $Dy^{3+}$  and  $Eu^{2+/3+}$  line spectra and possibly other line spectra from the other REE. The relative intensity of cathodoluminescence depends on the quantity and types of activators and quenchers relative to the intrinsic emission spectrum. Therefore the brightness is not only related to low concentrations of foreign elements as stated by Sommerauer (1974), but may be related to high concentrations of activators (eg.  $Dy^{3+}$ ). The various explanations for the differences of brightness in {100} and {110} must therefore be viewed with caution.

#### **Oscillatory growth zoning in zircon.**

Oscillatory zoning (Figure 4.06B) is common in igneous zircons (Silver and Deutsch 1963; Pidgeon and Aftalion 1978). Oscillatory zoning in zircon represent growth bands alternately depleted and enriched in U, Th, REE and other trace elements (Chakoumakos *et al.*, 1987; Köppel and Sommerauer 1974). The bands are identified by transmitted light microscopy, cathodoluminescence (Fielding 1970; Ono 1976; Clark *et al.* 1979) backscattered electron (BSE) SEM images (Sinha *et al.* (1992), HF acid etching and optical or SEM microscopy (van Breemen *et al.*, 1987) and images of the SIMS ion probe (Jackman *et al.*, 1987). Pidgeon (1992) states that the mechanism that produces oscillatory zoning in zircon is not yet understood. It is suggested that zircon continually crystallizes in a cooling magma with zonation produced by chemical changes in the magma as it crystallizes (Silver and Deutsch, 1963). A zircon core from early stage magma will generally be relatively depleted in trace elements, while the rim will be enriched in trace elements such as Hf, U, Th, Y, REE and P, concentrated in late stage magma. Fine micron scale oscillatory zoning is however difficult to explain by such an evolution model. Fujimaki (1986) stated the uniform distribution of euhedral to subhedral zircon grains in an andesite groundmass are strong evidence that zircon is a groundmass liquidus phase, and not a mesostasis phase, in other words zircon forms in the early stage of magmatic crystallization.

Oscillatory zoning may arise without the intervention of externally imposed changes in the state of the magma from which crystals grow (Ortoleva, 1990). Changes of pressure, temperature or composition of the melt are not required to produce zoning if there is solid solution components

available to the growing crystal. Zircon, as described in Chapter 2, has two solid solution series: zircon-xenotime and zircon-hafnon. *Autonomous oscillatory zoning* develops through kinetic feedback loops associated with the chemical kinetics of crystal growth, according to Ortoleva (1990) the possible source of feedback for generic crystal growth is the concept of "*autocatalytic surface attachment*". A solid solution consists of end member formula units (eg. A (Zr,Si: Zircon) and B (Y, P: Xenotime)). An A-rich surface favours the addition of A units over the addition of B formula units on an A-rich surface. A-formula units continue to be deposited on the growing crystal until the melt near the growing crystal becomes so depleted in A-formula units, while B-formula units become relatively enriched that deposition switches to B-formula units.

The contacts between alternating zones in zircon, and in other minerals, are sharp which indicates a sudden change in crystal growth. A possible application of the autonomous feedback mechanism in zircon is found in the relation of element concentrations in the melt, the partition coefficients of zircon and the diffusion rates of Zr, Hf, REE, Y, P, Th and U in melts. Most melts are enriched in LREE and depleted in HREE, on the other hand zircon prefers to incorporate HREE. The diffusion rates of large ions (REE) and highly charged ions (such as Zr,Hf) are very slow in magma. The result is a depletion in Zr and Hf near the growing zircon crystal face. Crystal growth therefore switches to Y and P accompanied by lower levels of Zr and Hf. When the Y and P is depleted and the Zr and Hf enriched to the point where the mode of growth will switch back the advancing crystal face switches to Zr- and Hf-rich growth. Xenotime may have higher partition coefficients for Y and the HREE than zircon, REE profiles of co-existing xenotime and zircon in the Dartmoor granite show xenotime to be several orders of magnitude more enriched in HREE than zircon (Ward *et al.*, 1992). Xenotime growth therefore leads to the depletion of Y and the HREE near the crystal-magma interface. This depletion will result in HREE-Y-depleted growth when the growth returns to zircon. The Y-rich zones have brighter cathodoluminescence emissions than the Hf- and Zr- rich areas according to Hoffman and Long (1984). It appears that zircon does not switch from zircon growth to xenotime growth, but only partially switches to xenotime growth with accompanying but reduced zircon growth. Zircon oscillatory zoning appears to be a variation of the autonomous feedback mechanism envisaged by Ortoleva (1990).

Few workers, excluding Romans *et al.* (1975) and Hoffman and Long (1984), realize the significance of xenotime-zircon substitution in the zoning of zircon. The literature contains many references to the zoning of trace elements in zircon.

Romans *et al.* (1975) analysed xenotime-rich zones in zircon and found enrichment of Y, P and HREE. The zones were still predominately zircon but were depleted in Zr and Si. The data of Hansmann and Oberli (1991), Hinton and Upton (1991), Wayne and Sinha (1992), and Sinha *et al.* (1992) all indicate a decrease in zircon components (Zr, Hf or Si) when there was an increase in xenotime components (Y, HREE, or P). Chakoumakos *et al.* (1987) reported sympathetic

relationships between U and Th and xenotime components Y and P in zoned zircon. Jackman *et al.* (1987) reported both sympathetic and antipathetic trends of Y with U and Th.

Nearly all the detailed analyses of the distribution of zircon and xenotime components in zircon indicate that zoning is essentially a result of increased xenotime substitution in the growing zircon. The detail to note is the increase in U and Th with increased Y or P substitution.

The aforementioned literature shows that oscillatory zoning results in the alternating depletion and enrichment of uranium, thorium and REE. Zoned zircon is considered to be relatively unstable (Sommerauer, 1974). The trace elements (U, Th, REE) distort the lattice (Köppel and Sommerauer 1974; Sommerauer 1974) making it relatively unstable and susceptible to recrystallisation "at relatively low temperatures" by removing the contaminants and homogenizing the oscillatory zones into unzoned patches (Pidgeon 1992). Analyses of zoned and homogenized or partially homogenized unzoned portions show large decreases in uranium and thorium in the unzoned patches (Pidgeon 1992). Sets of approximately 10 bands were analysed by ion microprobe, giving an average composition of the oscillatory zones. The oscillatory zoned results were compared to unzoned portions that cross-cutted the zoning (Table 4.09). The unzoned regions were considered by Pidgeon to be recrystallized zoned zircon.

**TABLE 4.09:** Analyses (ppm) of zoned and unzoned portions of single zircons analysed by ion microprobe (Pidgeon, 1992).

Uranium			Thorium		
Zoned	Unzoned	Reduction Factor	Zoned	Unzoned	Reduction Factor
931	381	2.4	1906	513	3.7
953	491	1.9	1291	115	11.2
993	286	3.5	1441	114	12.6
852	285	3.0	1225	138	8.9
AVERAGE:		2.7			9.1

The average reduction of U during natural homogenization of zoning is a factor of 2.7 and thorium is reduced by a factor of 9.1. Metamict grains are therefore not the only zircons that may act as open systems. Oscillatory zoned zircons under the right conditions may also act as open systems when the alternating bands re-equilibrate. Pidgeon (1992) did not consider the possibility of xenotime substitution. Xenotime has higher U and HREE partition coefficients than zircon under the same conditions, the U-rich bands of Pidgeon (1992) may be U-rich xenotime substitution. High temperatures may expel the xenotime impurities from the zircon lattice.

A review of Y, REE and P data of zircons from the literature leads to the conclusion that all or nearly all zoning, both sector and oscillatory zoning, is derived from or accompanied by the increased substitution of xenotime into the zircon structure. If this is true it has important repercussions for cathodoluminescence studies of internal morphology, and is an important consideration in understanding the distribution of trace elements in zircon. Impurities of P, Y, HREE and possibly U and Th may all be coupled to xenotime substitution.

## 4.5.2 CATHODOLUMINESCENCE

### 4.5.2.1 LITERATURE ON CATHODOLUMINESCENCE IN ZIRCON

For general reviews on cathodoluminescence see Nickel (1978) and Marshall (1988).

Mariano (*pers. comm.*) stated that  $Dy^{3+}$  was the prime activator of cathodoluminescence (CL) in zircon, with other REE such as  $Eu^{2+}$  and  $Eu^{3+}$  also contributing. With wavelength analysers Mariano (*pers. comm.*) is able to differentiate between the two Eu valence states and obtain a qualitative ratio of  $Eu^{3+}$  to  $Eu^{2+}$ . This ratio could be a useful provenance tool. Marshall (1988) reviewed the literature on the activators of cathodoluminescence in zircon. Hanchar (*pers. comm.*) has doped zircon with Dy and observed the same cathodoluminescence emission as he observed in natural zircons. He is presently studying the correlations of other REE cathodoluminescence emitters, stating that zones of different ages in zircon he has studied under SHRIMP ion microprobe emit different wavelengths of cathodoluminescence CL emission.

### 4.5.2.2 METHOD AND RESULTS

Cathodoluminescence emission of zircon was performed on a Cambridge Image Technology Cold Luminescence Model 8200 Mk II mounted on a Nikon Transmitted Light microscope at Randse Afrikaanse Universiteit (RAU). The x10 objective and the small area photograph aperture were used to record the emissions. The kV was set between 9 and 25 (average: 18) with a gun current between 200 and 500  $\mu A$ . Due to the weak emission of zircon long exposure periods were required, between 1 and 10 minutes with an average of 3½ minutes. The grains in the field of view were surrounded by areas of non-luminescing epoxy. To reduce overexposure photographs were underexposed. The grains were mounted on glass slides in Petropoxy 154 with their *c*-axes parallel to the surface; then they were polished until half the grain had been removed. The Petropoxy 154 epoxy was found to be inappropriate for cathodoluminescence work because it burned when placed under the electron gun for long periods. The results were not affected by the burning of the epoxy though the vacuum may have fluctuated due to gases produced.

Two major types of emission were noted. The first is bright yellow-green to yellow, and the second is low intensity dark blue.

The grain in Plate 4.12 has three major zones of luminescence; a bright luminescing outer core and a non-luminescing inner core and overgrowth. The pyramid of the core shows crystal faces (101) and (211), while the pyramids of the overgrowth show only the (100) face. This type of imaging is a powerful tool for provenance studies. The image not only records the final crystal morphology but also the changes in morphology during the growth of the crystal. The image could be used as a



"fingerprint" of the parent rock as most of its zircon should show similar patterns. The growth history of the grain in Plate 4.12 can be described in terms of 4 phases.

1) Growth of core with (100) and (101) faces with no luminescing impurities.

2) The incorporation of cathodoluminescing trace elements increases as the crystal growth continued with oscillatory zoning. The (100) growth sector has higher luminescence.

3) The growth continued and as the available impurities increased the (211) growth sector became the dominant growth zone.

4) The growth of (211) was terminated at a peak of impurity incorporation. Growth reverted to (101) dominance with low impurities and no luminescence.

The interpretation of the transition between phase (3) to (4), according to Vavra (1990), is due to a increase in zircon-saturation. The (101) and (100) overgrowth may be a late-stage growth when the residual magma became enriched in Zr.

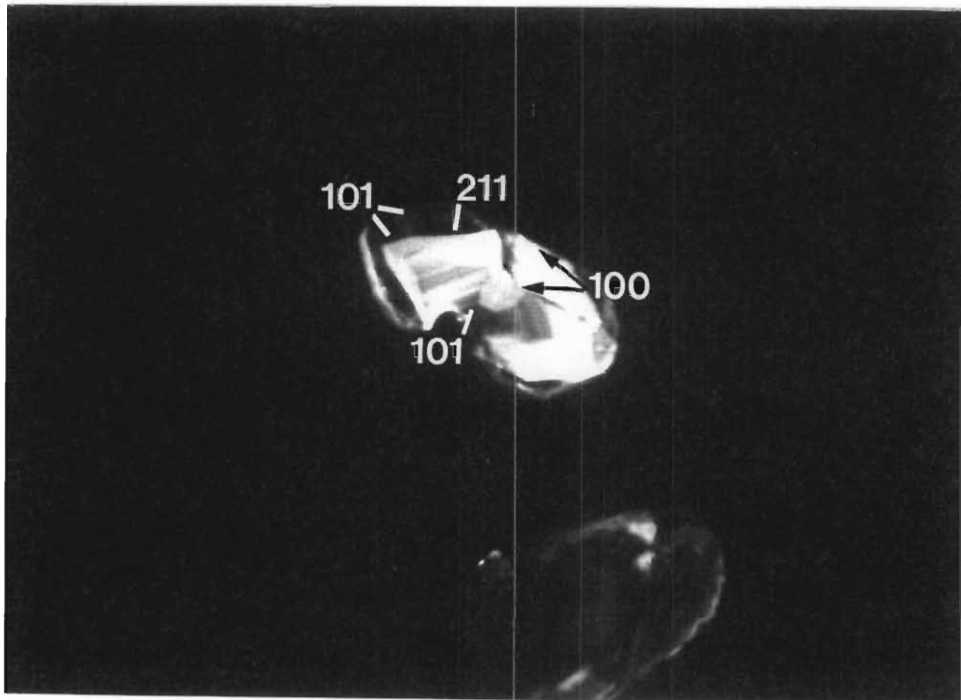


**PLATE 4.12:** Cathodoluminescence emission of a 110- $\mu\text{m}$  zircon with crystal growth zones (100), (101) and (211) identified, a zircon grain with a complex history.

The zircon in Plate 4.13 shows both similar, and different, growth trends to the zircon in Plate 4.12. The grain start growth with (101) and (100) faces, it changes to a (211) and (100) followed by a phase where the (101) face begins to return and finally reverts to (211) and (100) dominated growth.

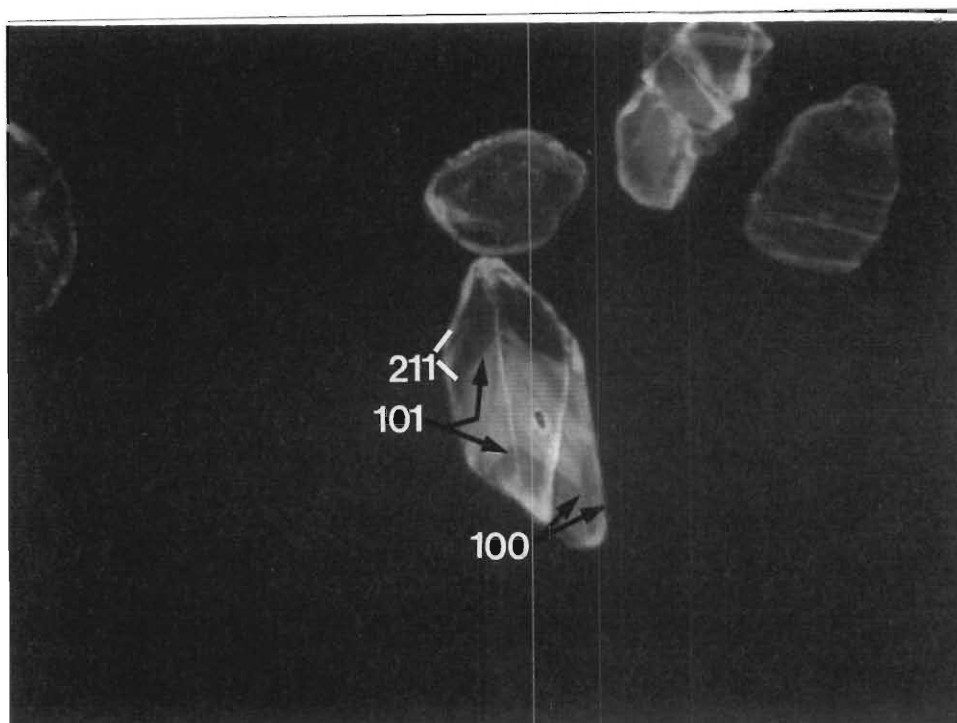


**PLATE 4.13:** Cathodoluminescence emissions of a 120µm zircon showing a complex growth history.

Oscillatory zoning, sector zoning and a variety of zircons with different growth histories were identified in other zircons with cathodoluminescence (Plate 4.14 and Plate 4.15)

The identification of the growth "fingerprint" of zircons is method of correlating source rocks to the detrital zircons in the coastal dunes. Hanchar (1992) suggested that internal zoning, and the nature of inherited cores could be used as to correlate detrital zircon to their parent rocks. The numerous types of internal zoning in RBM zircon indicates numerous parent rocks.

A comparison of zoning between rocks in the Mhlatuze and Tugela river catchments and the dunes was beyond the scope of this project, but this type of work would be most beneficial for exploration and in understanding the provenance of the zircons from the coastal dunes.

Obtaining a full knowledge of the distribution of elements indicated by the zoning recorded in zircon by cathodoluminescence and by transmitted light microscopy requires detailed electron or ion microprobe work. The substitution of xenotime into the zircon lattice is a prime contributor of Y, HREE and P in zircon.

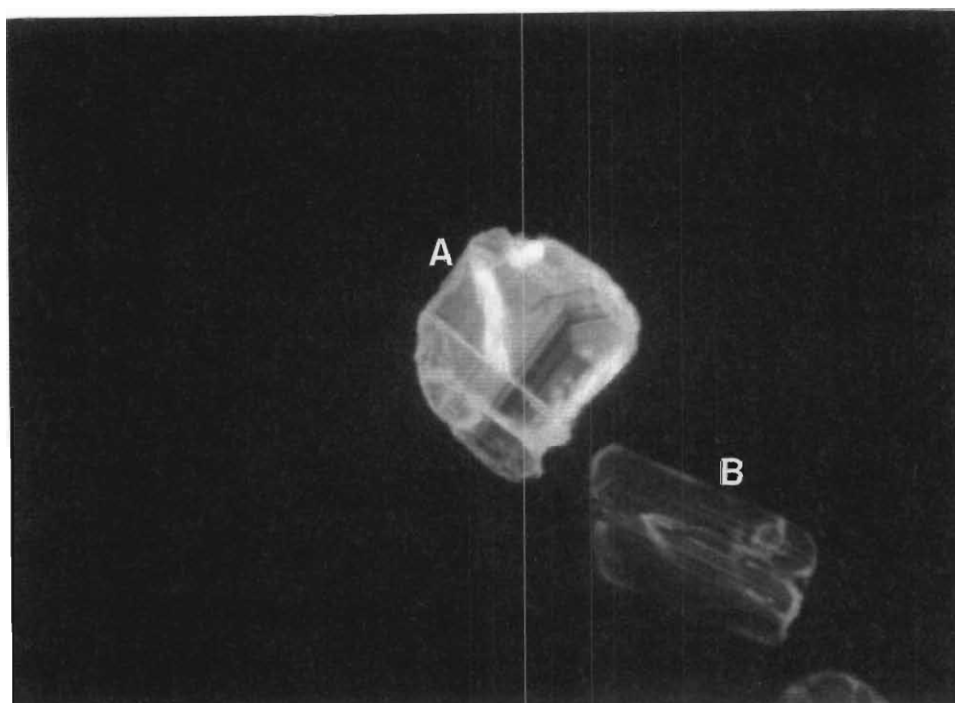


**PLATE 4.14:** Two zircons with different origins: A) a fragment of an oscillatory growth zoned zircon; B) A fragment of a narrowly oscillatory zoned zircon.

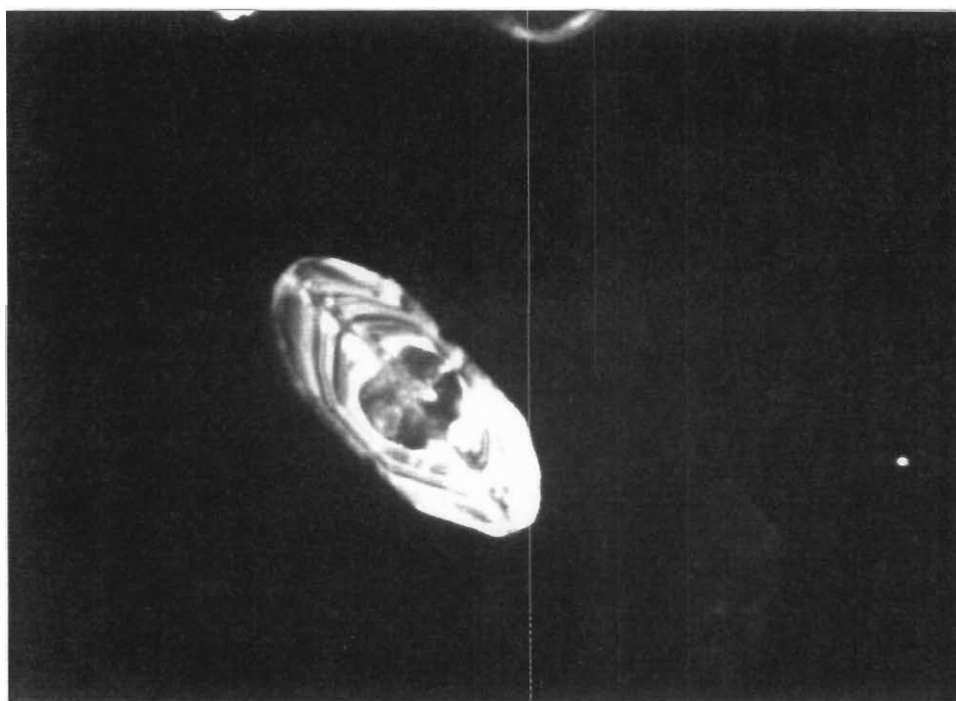


**PLATE 4.15:** An oscillatory zoned zircon.

## 4.6 COLOUR

Eighty-eight percent of the transparent grains in the bulk sample ZC-B91 NM were colourless with the remainder having a pink to purple hue. The bulk sample contains 6% translucent or opaque grains which are semi-metamict, metamict and grains with misty swirls in the interior. The opaque grains range from white through light grey, dark grey, pale yellow, pale brown, red brown, dark red brown, dark brown to black with fewer blue or green grains. Several grains have red to brown opaque cores or rims.

## 4.7 FISSION TRACKS

### 4.7.1 LITERATURE ON NEUTRON-INDUCED FISSION TRACK ANALYSIS

Neutron-induced fission track analysis is the primary method of recording the distribution of U and also Th in polished thin sections. A qualitative approach was used as the distribution and not the quantity of U in the zircons was required. Fission of U or Th is induced by neutron bombardment of the U- or Th-bearing samples in a nuclear reactor. Usually  $^{235}\text{U}$  undergoes fission but if the sample is placed in the fast neutron flux, compared to the thermal neutron flux,  $^{238}\text{U}$  and  $^{232}\text{Th}$  will also undergo fission. Neutron-induced fission only occurs in the reactor, therefore the recording of the fission tracks must also occur in the reactor. The highly charged fragments resulting from neutron-induced fission are ejected from their *in situ* sites. Approximately 50% of the fragments enter the detector and are recorded as fission tracks. The fission tracks in the recorders result from damage caused by charge repulsion by the highly charged fission fragments.

Two types of recorders are commonly used. The first is plastic foils, such as Kodak CA 80-15 cellulose nitrate film or Makrofol E polycarbonate, which are placed on the polished samples and record the fission tracks (Fleischer *et al.* 1965). The second type of recorder used is high purity muscovite sheets (Price and Walker, 1963). The advantage of mica sheets over plastic foil is that mica sheets do not record the passage of  $\alpha$ -particles and have a higher thermal fading temperature. Fission tracks in plastic foil anneal at temperatures of about 80°C compared to those in mica at about 450°C (Thiel *et al.* 1979). Temperatures in reactors may reach 80°C and therefore the use of plastic foils may contain several inherent errors. The fission tracks on the mica sheets are exposed by etching the sheets after irradiation in 40-48% HF for 3-4 hours.

The mapping of the distribution of U within the zircons was essential to determine the methods that should be used to reduce the U and Th. The literature contains several references to U enrichment in the rims and pyramids of zircon (see Section 4.5.1) and several papers deal with the mapping of the distribution of U in zircon by neutron-induced fission track analysis. For example

Clark *et al.* (1979) mapped the U distribution from zircons from a "rapakivi" granite. Three of the four grains mapped show U enriched rims. Grauert *et al.* (1974) reported 90% of the zircon mapped by fission track radiography from a metaquartzite had an enrichment of U in the rim and in cracks, with several having complex U distributions and few showing sector zoning with enrichments in the pyramids.

#### 4.7.2 METHOD OF FISSION TRACK ANALYSIS

The fission track radiography method that was used to map the uranium microdistributions in individual zircon grains is described in Price and Walker (1963), Thiel *et al.* (1979) and Burnett and Woodlum (1983).

The zircons were mounted on a grid system with their *c*-axis parallel to the plane of the glass plates (12mm x 12mm x 1mm) in Petropoxy 154. The grains were then carefully polished by hand until half of each grain had been removed. High purity muscovite plates (with very low uranium values) were cut to size and marked with a grid to facilitate correlation between the fission tracks and the zircon grains following irradiation. The mica was placed over the polished section and held in place by heat-shrinking plastic-wrap over the slide.

The slides were photographed to record the position of the grains on the grid. This facilitated the correlation of the fission tracks to their grains. The slides were then placed in cadmium capsules (13mm x 40mm) and sent to the reactor where the samples were irradiated.

Due to many different concentrations of U in grains in the bulk sample no single neutron flux can accommodate the suspected wide range of uranium compositions in the grains of the bulk sample. A flux of  $2 \times 10^{13}$  neutrons.cm<sup>-2</sup> in the fast neutron portion of the Palindaba reactor was chosen. The flux was not measured in the site of the samples, but the flux in the neighbouring positions were measured at  $2.02 \times 10^{13}$  and  $2.09 \times 10^{13}$  N.cm<sup>-2</sup>, giving an average flux of  $2.07 \times 10^{13}$  N.cm<sup>-2</sup>. The samples were placed in the reactor for 2 hours. The high flux and long period of neutron bombardment resulted in over exposure of fission tracks in the metamict uranium-rich zircons, but optimum fission track concentrations in the mid-range uranium zircons. The samples were allowed a period of three months after irradiation to lose their induced radioactivity.

The mica sheets were detached from the glass slides and the fission tracks on the irradiated mica sheets were exposed by etching. Experimentation showed that sufficient exposure of the tracks in glass-etching fluid (Glass Crafts Etching Fluid) after 2 days. The fission tracks were photographed at x100 magnification with transmitted light and correlated with the previous photomicrographs of the zircon grains.

### 4.7.3 RESULTS

A large portion of the zircons have high concentrations of U in the rims and pyramids (See Plate 4.16).

Plate 4.17 is a grain with four phases of growth (a-d). The grain has a U-poor core (phase a) with a rim which is U-rich (phase b). A medium rich U phase (phase c) grew over the U-rich core rim which is overgrown by a U-poor zircon (phase d).

Plate 4.18 is a zircon with two phases (A & B). A U-rich core/early phase that is metamict when viewed in transmitted light microscopy (phase A) and a clear rim and pyramid which are low U overgrowths (phase B). This type of zoning may result from two processes.

1) The grain grows in a U-rich igneous melt with later growth of a U-poor phase on the older zircon template from late igneous crystallizing or metamorphic U-poor fluid.

2) The zircon grows in a melt with high diffusion rates so all growth is U-rich (ie. the melt around the growing zircon is not depleted) and during the last stages of crystallization when diffusion rates are drastically reduced (or U has been incorporated into other accessory minerals) and there is an enrichment of Zr, new growth of zircon occurs.

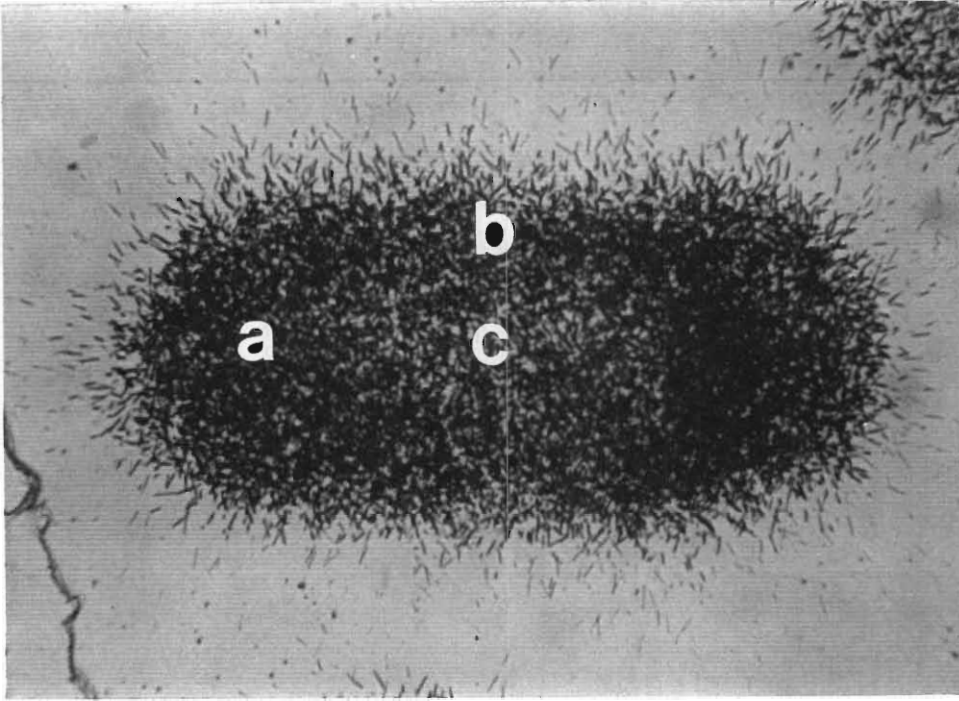
Zr is an incompatible element in most minerals and is found enriched in the residual melts of peralkaline liquids between the larger crystals. Evidence for this late-stage enrichment of Zr was found by Nicholls and Carmichael (1969) where the residual Zr (1800ppm) was not incorporated into zircon but formed a Zr-rich intergranular glass.

The U-distribution map in Plate 4.19 shows sector zoned enrichment of U in the pyramidal growth zones. This form of enrichment is the most common in both U-poor (Plate 4.19) and U-rich grains (Plate 4.20).

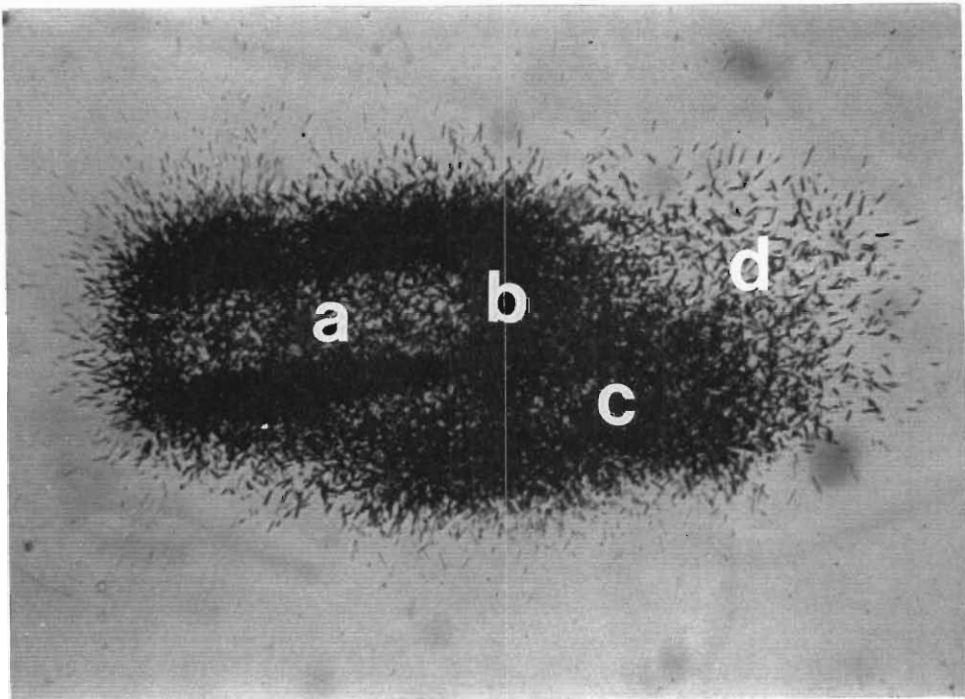
In some melts U is enriched in the residual melts and the final growth of zircon is U-rich. Zircons with U-rich rims are common and the U-enrichment of the rims may also be superimposed on U-rich sector growth zoning (Plate 4.16).

Plate 4.21 shows a zircon with U-rich pyramid sector zoning and also with an U-rich inclusion in a U-poor core. The inclusion in the core (Plate 4.22) appears to be speckled and there appears to be a rim of radiation damage in the zircon surrounding the inclusion. Several radial cracks emanating from the inclusion in the core are clearly evident.

The fission track results confirm that U is preferentially enriched in the rims and pyramids of the zircon. The partial dissolution or abrasion of zircon will remove the outermost portions of the grains and are therefore considered suitable techniques for reducing the U and Th concentrations of the bulk zircon samples.



**PLATE 4.16:** Fission track distribution of U in a zircon, with enrichment of U in the pyramids (A) and rims (B) relative to the core (C).



**PLATE 4.17:** Fission track distribution of U in a grain with 4 (A-B) different growth zones, each with different uranium concentrations.

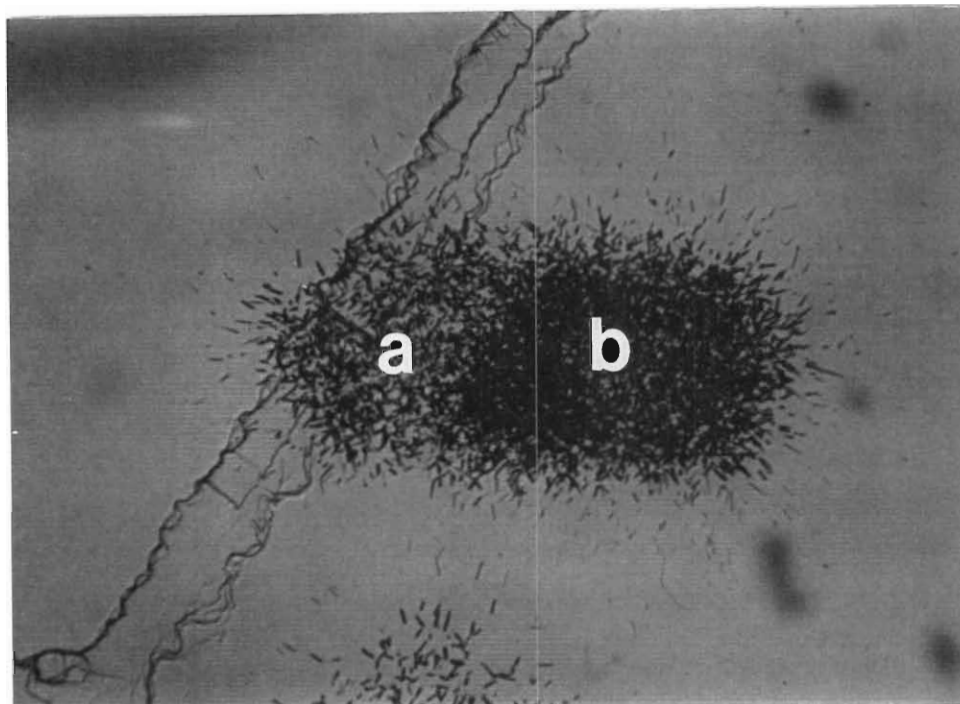


**PLATE 4.18:** Fission track distribution of U in a zircon with a U-poor overgrowth (A) compared to the U-rich core (B).

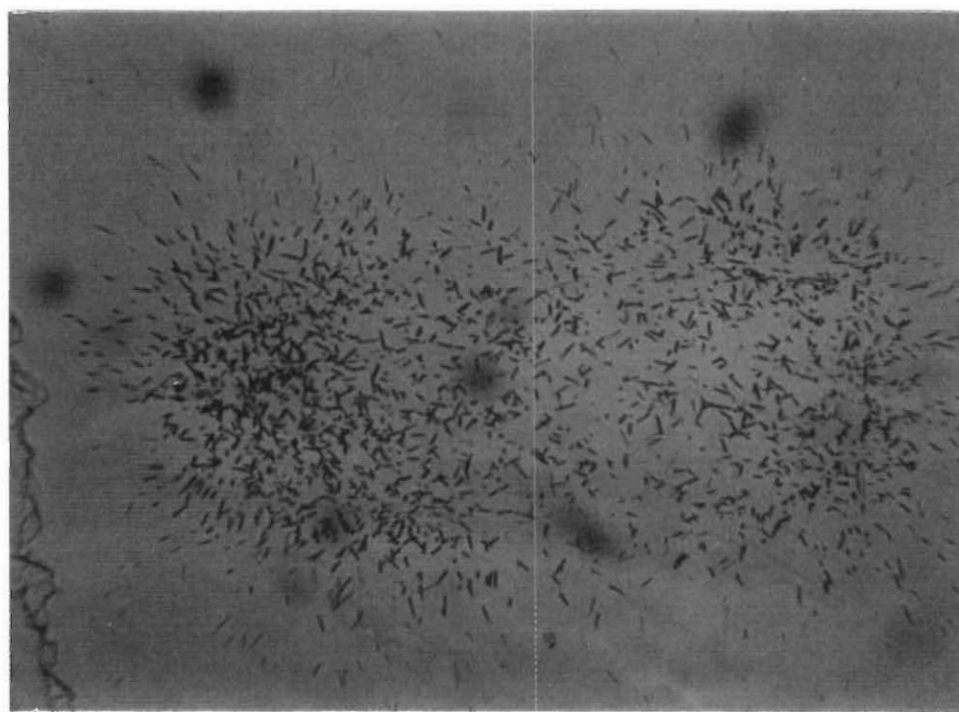


**PLATE 4.19:** Fission track distribution of U in a zircon with U-rich pyramids.



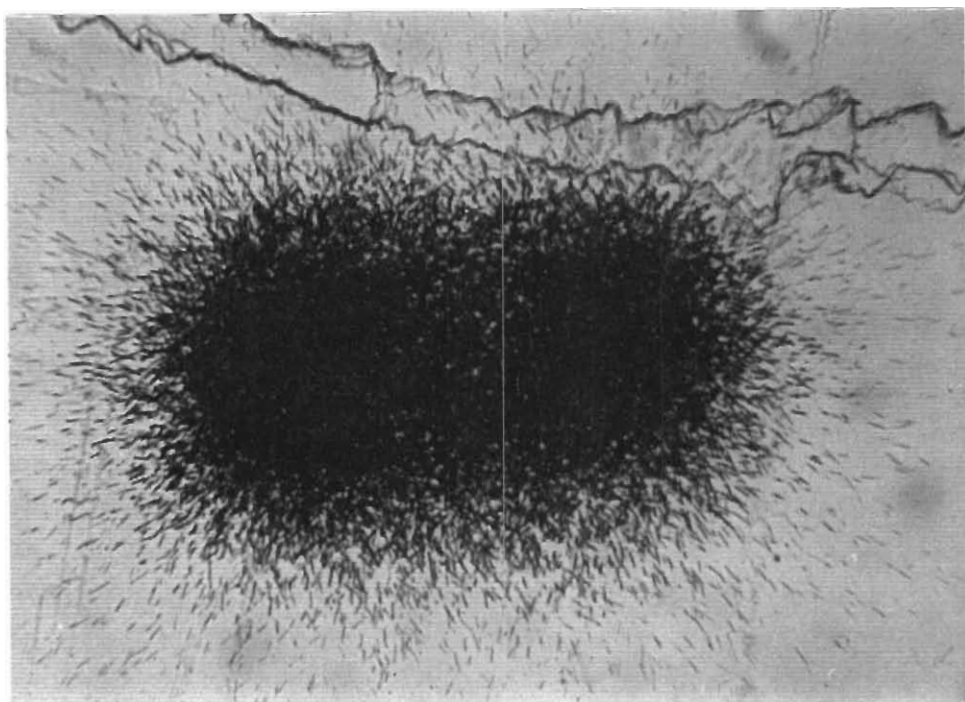


**PLATE 4.20:** Fission track distribution of U in a zircon with U-rich pyramids.

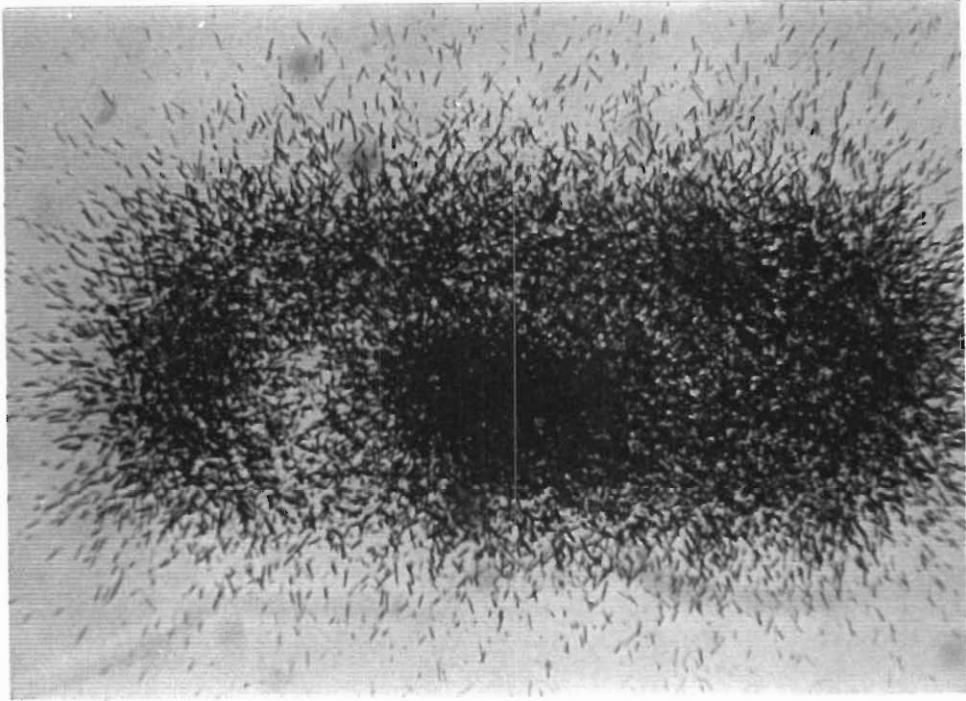


**PLATE 4.21:** Fission track distribution of U in a zircon with a U-rich non-zircon (uraninite?) inclusion within a U-poor core with a U-rich overgrowth.

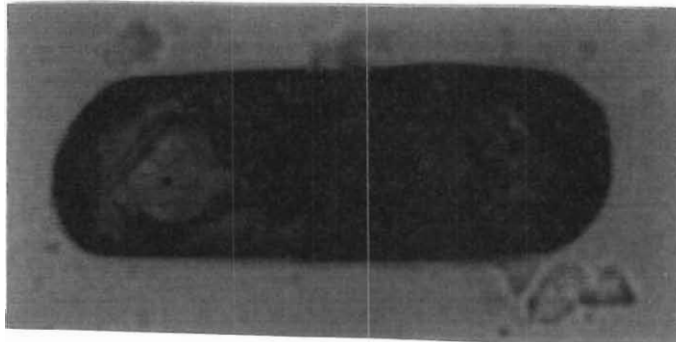


**PLATE 4.22:** Transmitted light photomicrograph of the zircon in Plate 4.21 before it was polished.

#### 4.8 DENSITY MEASUREMENT

Following the technique developed and outlined by Hughes and Birnie (1980) of measuring non-magnetic micro-grains using magnetic liquid and a Frantz Isodynamic magnet separator Electromagnet, a density measuring apparatus was designed and built.

The composition of magnetic fluids range from water to high temperature oils that have colloiddally suspended 100Å-sized magnetite particles. The magnetic fluid EMG 909 was obtained from the Ferrofluidics Corporation, Massachusetts, USA. The fluid is manufactured with 3-15% magnetite, 6-30% oil soluble dispersant and 55-91% carrier fluid. When a magnetic field is applied to the fluid the fluids apparent density changes. Particles with densities that are lower than the apparent density float to the surface. Density of particles from 0.8 to 21.5 g.cm<sup>-3</sup> can be measured. Because the correlation of the ampage and the apparent density of the magnetic fluid is linear, a plot of ampage to apparent density may used to determine the density of micro-particles.

A large electromagnet with moveable magnetic poles and adjustable ampage was repaired and modified. A low-magnification aluminium binocular microscope was built on top of the electromagnet. The ampage controller was inaccurate. Two potentiometers were added to the circuit to enable fine adjustments of the ampage. The ampage was read with a ammeter to one decimal place of a μA. The configuration was set up so zircon (S.G. 4.67) appeared on the surface at 100μA, midway in the 0-200μA readable range.

The ampage was increased until the grains broke through the surface (ie. the "first appearance" of the zircon was noted), this measurement was then recorded and repeated 10 times. The highest and lowest recordings were disregarded and an average was taken of the remaining recordings. The first appearance of a grain on the surface was considered the only method of taking reliable recordings.

The calibration of the instrument done using equal sized micro-pieces of quartz (S.G. 2.65), andalusite (S.G. 3.18), fluospar (S.G. 3.18), topaz (S.G. 3.53), molybdenite (S.G. 4.7) and cerussite (S.G. 6.57). The calibration curve (Figure 4.07) has a correlation coefficient of 0.994.

The density of several zircons were recorded. A zircon with equivalent shape to the micro-pieces used to calibrate the system had an average reading of 106.4μA or a density of 4.77g.cm<sup>-3</sup> (SD 2.0μA). Other clear elongate zircons gave average results between 84.0μA (SD 1.6μA) and 93.2μA (SD 1.8μA). The lower values yielded densities of between 3.8g.cm<sup>-3</sup> and 4.2g.cm<sup>-3</sup>. These low values are probably erroneous. Errors may arise due to their assorted shapes, elongation and "luminesce" of zircon in the oil. The zircons glow red in the liquid making it difficult to detect their "first appearance".

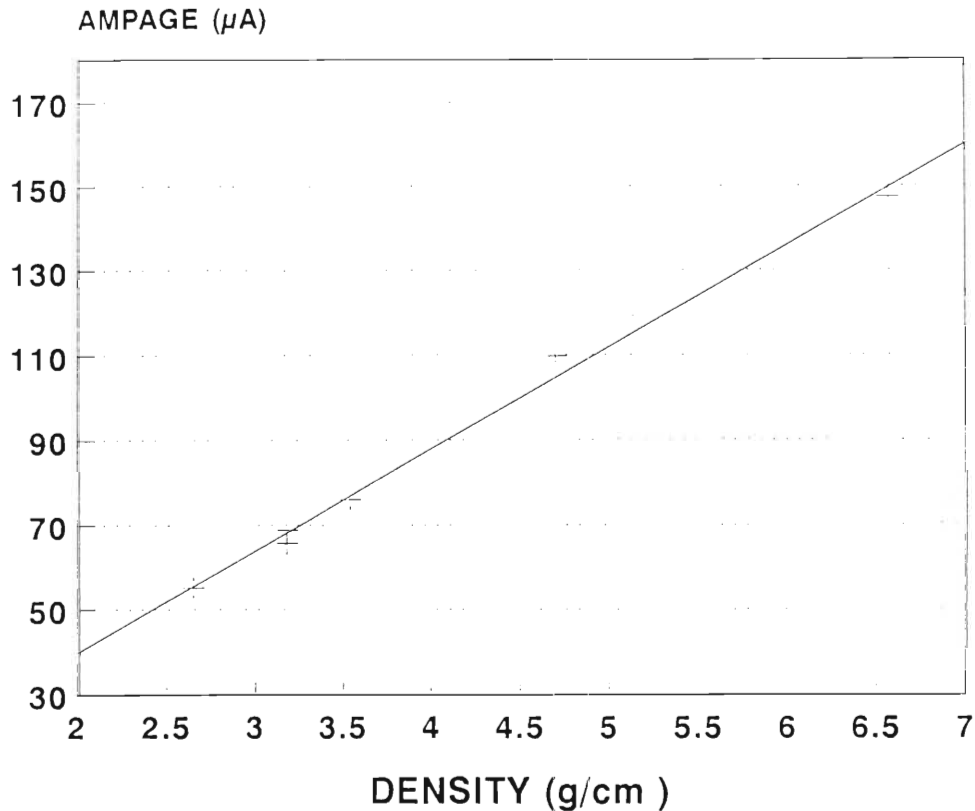


**FIGURE 4.07:** Calibration curve for the magnetic fluid micro-particle density measuring apparatus.

#### 4.8.1 PROBLEMS WITH MAGNETIC FLUID DENSITY MEASURING TECHNIQUE

Certain difficulties were encountered during experimentation with the magnetic liquid. To obtain comparable results use:

- 1) Equal sized containers (ID: 5mm, OD: 7mm, Depth: 8mm) and equal amounts of magnetic liquid (0.06ml in this study).
- 2) Containers that must be in the same position for every recording.
- 3) First appearance of the grains on the surface, several methods of recording a grains density were experimented with and the only satisfactory method was recording of the ampage when the grain first broke the surface.
- 4) Glass containers that are positioned at a slight angle so the grains will break the surface at the same position.
- 5) Use a circular fluorescent tube as a light source. The liquid is opaque black and has a very low surface reflectivity. Several light sources were experimented with, all of which proved unsatisfactory. The surface changes from concave upward to convex upward with increasing strength of the magnetic field. This results in a change in the position of the reflected light on the surface of

of the magnetic field. This results in a change in the position of the reflected light on the surface of the magnetic liquid. The light is also broken into bands of black and white on the surface, if a grain appears in a black band or a very bright white band it may not be observed until the ampere is increased.

6) Use equal shape and size particles. The calibration curves were satisfactory but the recording of "first appearance" of the zircons were unsatisfactory. The shape of the zircon is believed to be an important factor in the erratic recordings obtained for different shaped zircon.

Further refinement of the experimental procedure may overcome the difficulties encountered with zircon. Circular fluorescent tubes may overcome the light source problem, or the adaption of the apparatus to record the density when the grain lifts off the bottom of the glass container. A light source was used close to the sample appears to interfere with the magnetic field. This method of density measurement holds a lot of potential if these basic problems can be overcome.

## CHAPTER 5

### ANALYSIS OF INDIVIDUAL ZIRCON GROUPS

The trace element concentrations in individual zircons were analysed for two reasons:

- 1) To obtain data on the distribution of trace elements between the individual zircons; and
- 2) To perform a preliminary provenance study on the zircon concentrate.

Ten individual zircon samples were handpicked (200-320 zircons per duplicate pair, or 200-250 per single analysis) using crystal morphology or crystal state as the criterion for each group. The method of analysis is summarised in Chapter 3.

Four clear types, one frosted and five metamict zircon samples were successfully analysed. Several duplicate pairs were lost during preparation. Both the large D-type and S-type duplicates failed to dissolve in the 2% nitric acid after dissolution. The results of several more samples, analysed before Re was used as an internal standard, were considered erroneous and several of these samples were re-analysed using two internal standards.

#### 5.1 CLEAR AND COLOURED ZIRCON

Three types of clear zircon were handpicked and analysed (Table 5.01). The three types were, according to Pupin's (1980) and the simplified version of Pupin's morphological classification scheme, D, P4; and a set of coloured D and LOWER P type according to the simplified version of Pupin's classification scheme. Two inclusion-bearing samples of D type zircon with L/B values of 2 to 5 are also included to show the effect of inclusions on the REE profiles.

##### 5.1.1 D-TYPE ZIRCON

220 Fine grained D-type zircons (sample #: CLEAR D), with Length/Breadth values of five or greater and with a maximum breadth of 60µm, were analysed as a single sample. The REE profile (Figure 5.01) exhibits no cerium anomaly ( $Ce/Ce^*$ : 0.98) but contains a large negative Eu anomaly ( $Eu/Eu^*$ : 0.36). The U and Th concentrations are low with U at 216ppm and Th at 111ppm with a U/Th value of 1.96. The LREE concentrations in this D-type zircon are the highest of the clear zircon types.

##### 5.1.2 P4-TYPE ZIRCON

200 Tabular P4-type zircon (sample #: CLEAR P4), with L/B values of 2 to 3 and Breadth/Intermediate values of 4 or greater, were analysed as one sample (Table 5.01). The REE

TABLE 5.01: Y, REE, U and Th concentrations in clear zircon.

Description:	Clear D Elongate	Clear P4 Tabular	Pink Coloured	Clear D Inclusions	Clear D Inclusions
Sample #:	CLEARD	CLEARP4	COLOURED	DINCL-1	D-INCL-2
Y	975.86	1057.59	870.85	-----	884.28
La	20.74	6.35	2.49	4.50	187.79
Ce	44.66	23.69	22.71	32.08	561.73
Pr	5.58	1.91	0.90	1.19	86.76
Nd	21.35	7.79	7.38	7.30	370.33
Sm	11.84	6.98	9.53	3.49	71.29
Eu	2.11	0.88	1.48	0.60	1.25
Gd	25.75	20.85	29.45	17.46	37.23
Tb	10.26	8.89	9.39	6.14	6.97
Dy	92.91	89.68	87.94	57.05	57.42
Ho	37.38	36.23	28.24	23.43	24.85
Er	145.33	143.72	134.05	100.20	100.74
Tm	26.32	25.46	25.98	19.77	18.64
Yb	232.82	244.71	231.63	163.50	171.12
Lu	44.47	47.10	43.75	32.35	32.30
Th	110.48	123.08	182.13	62.73	263.41
U	216.34	250.13	294.05	111.74	132.59
U/Th	1.96	2.03	1.61	1.78	0.50
U+Th	326.83	373.21	476.17	174.47	396.00
La/Sm	1.10	0.57	0.16	0.81	1.66
Yb/Gd	11.19	14.53	9.73	11.59	5.69
Ce/Ce*	0.98	1.62	3.65	3.28	1.06
Eu/Eu*	0.36	0.21	0.25	0.19	0.07

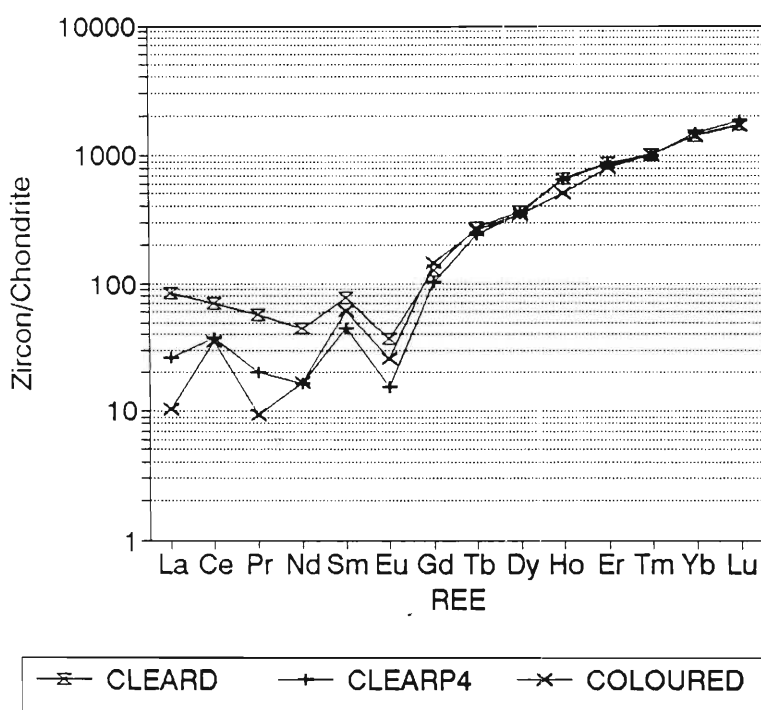


FIGURE 5.01: Chondrite normalised REE profile for D-type zircon, tabular P4-type and coloured D- and P-types.

profile in Figure 5.01 exhibits a relatively small positive Ce anomaly ( $Ce/Ce^*$ : 1.62) and a large negative Eu anomaly ( $Eu/Eu^*$ : 0.21). The U and Th values of these tabular zircon are mid-range with U at 250ppm and Th at 123ppm with a U/Th ratio of 2.03. The Y concentration is the highest of the clear zircons with a value of 1058ppm.

### 5.1.3 COLOURED D- & P-TYPE ZIRCON

The analyses of 230 grains of pink coloured D- and P-type (COLOURED) show a REE profile (Figure 5.01) with a large positive Ce anomaly (3.65) and a large negative Eu anomaly of 0.25. The coloured zircon has the largest positive Ce anomaly second only to the bulbous frosted zircon grains (see below). The sample has a very low La/Sm values (degree of LREE enrichment) of 0.57. The sample has a high U value of 294ppm which is similar to the U concentration in bulk ZC-B91 NM, and a high Th value of 182ppm. The relatively high Th, concentration results in a low U/Th of 1.61. The absence of LREE enrichment excludes monazite inclusions as a source of the Th because monazite is a LREE-rich mineral which would enrich the LREE of the sample as well as the Th.

### 5.1.4 INCLUSIONS IN MEDIUM L/B D-TYPE ZIRCON

Two samples of clear zircons of medium sized D-type zircon with abundant inclusions (predominately ilmenite in the first sample and miscellaneous inclusions in the second sample) were analysed with run L which was run with In as the only internal standard which resulted in the REE, Th and U having low values.

The features to note in the profile of DINCL-1 (Figure 5.02) are the large positive Ce anomaly (3.27) and the large negative Eu anomaly (0.19). The second sample, DINCL-2, has a very different LREE profile compared to DINCL-1. The miscellaneous inclusions have enriched the LREE in the second sample. The REE abundances obtained by subtracting DINCL-1 from DINCL-2 shows a large LREE content in the inclusions, and little or undiscernible HREEs. The U/Th value for DINCL-2 is 0.50 compared to 1.78 for DINCL-1. The LREE and Th enrichment indicates that a large portion of the inclusions within the sample are monazite, apatite or thorite.

Both CLEAR and DINCL-1 are D-type zircon with a difference in breadth and a difference in L/B values. A large positive Ce anomaly is evident in the chondrite normalised profile of DINCL-1, which is absent from the profile of CLEAR. This indicates that at least two source rocks contributed D-type zircon, one rock with a high  $Ce^{4+}/Ce^{3+}$  and one rock with a  $Ce^{4+}/Ce^{3+}$  value of 1 or less.



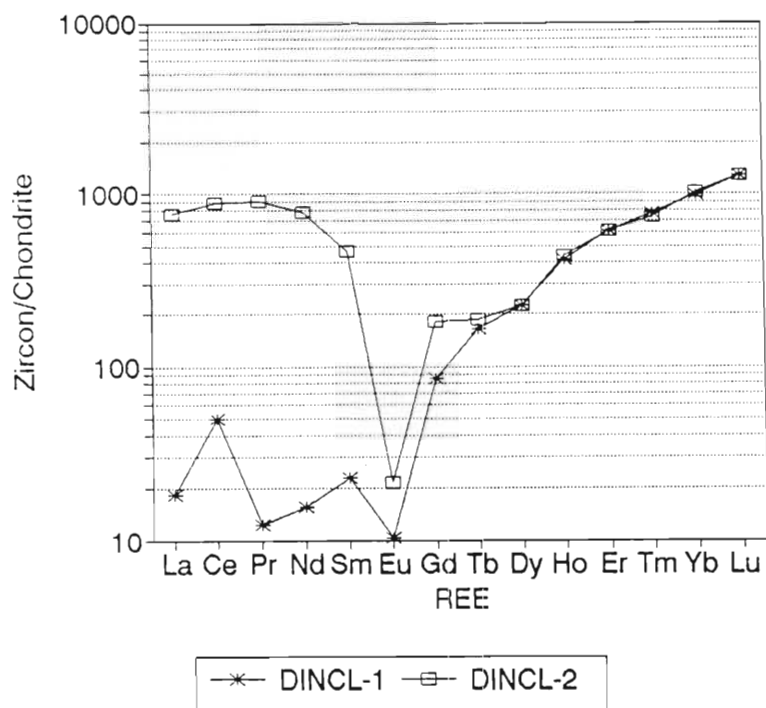


**FIGURE 5.02:** Comparison of chondrite normalised REE profiles of large D-type zircon containing ilmenite (DINCL-1) and miscellaneous inclusions (DINCL-2).

## 5.2 BULBOUS FROSTED ZIRCON

Duplicate samples of frosted bulbous zircons (BULBOUS-1 & BULBOUS-2) were analysed (Table 5.02). The REE profiles of these translucent zircons show very large positive Ce anomalies with  $Ce/Ce'$  of 4.69 and 6.85, and large negative Eu anomalies with  $Eu/Eu'$  of 0.25 and 0.27 (Figure 5.03). The U and Th values are very high with U values of 1158 to 1421ppm and Th values of 679 to 781ppm with a U/Th values of 1.48 and 2.09. The Y concentrations are also very high with concentrations of 6539 and 7175ppm, suggesting a xenotime substitution.

The La/Sm value, an indicator of LREE enrichment, is very low with a range from 0.10 to 0.14. The high thorium concentrations are therefore not derived from monazite contamination which would also contribute LREE to the sample.

Bulbous frosted grains with high U and Th values were also noted by Grauert *et al.* (1974): the pitted and frosted surface and cracks in the zircon grains, in a quartzite which had been intruded by a pegmatite, showed large accumulations of U. The bulbous rounded grains from the coastal dunes of northern Natal may therefore also represent zircon which have been through more than one sedimentary cycle.

TABLE 5.02: Y, REE, U and Th concentrations in bulbous frosted zircon.

Description:	Bulbous Frosted	Bulbous Frosted
Sample #:	BULBOUS-1	BULBOUS-2
Y	7174.76	6538.99
La	8.27	12.82
Ce	139.20	156.74
Pr	2.88	5.04
Nd	36.59	43.63
Sm	50.88	57.12
Eu	9.43	10.30
Gd	200.54	194.02
Tb	67.76	71.36
Dy	555.46	584.60
Ho	219.04	224.32
Er	922.66	867.56
Tm	171.36	161.62
Yb	1554.90	1437.25
Lu	316.23	293.40
Th	781.10	678.62
U	1158.20	1420.45
U/Th	1.48	2.09
U+Th	1939.30	2099.07
La/Sm	0.10	0.14
Yb/Gd	9.59	9.17
Ce/Ce*	6.85	4.70
Eu/Eu*	0.25	0.27

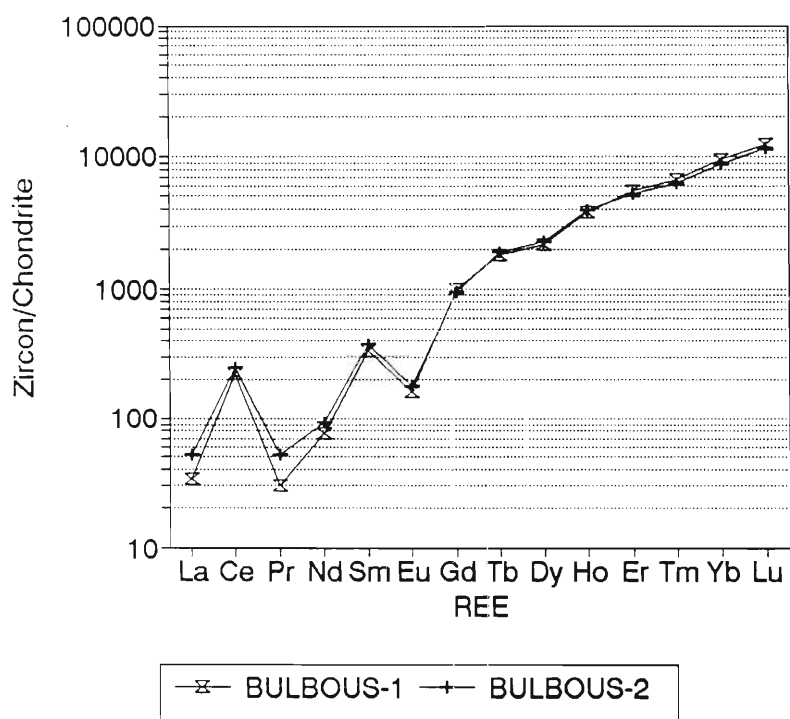


FIGURE 5.03: Chondrite normalised REE profiles of the bulbous frosted zircon with high U and Th concentrations.

### 5.3 METAMICT ZIRCON

Approximately 250 grains of opaque yellow brown (YELLOW), opaque pale brown (PALEBROWN), opaque grey D-type (GREYD-1 & GREYD-2), opaque red brown (REDBROWN) and Bull's Run opaque grey (BULLSRUN-1 & BULLSRUN-2) metamict zircon were analysed by ICP-MS (see Table 5.03 and Table 5.04). The metamict zircons are all enriched in Y, the REE, Th and U compared to the clear grain samples and the bulk zircon concentrates. The Bull's Run zircons have very low Y, REE, Th and U concentrations compared to the metamict zircon from the dunes, the Bull's Run zircon also have a very low U/Th value of 0.26.

The REE chondrite normalised profiles in Figure 5.04 and Figure 5.05 have somewhat erratic profiles. The most striking features of the five metamict zircon profiles are:

- 1) A wide range of LREE profiles;
- 2) The absence of Ce anomalies (excluding REDBROWN & YELLOW);
- 3) Small negative Eu anomalies;
- 4) Low HREE/LREE relative to the other zircons.

The REDBROWN sample has a slight negative Ce anomaly ( $Ce/Ce^*$ : 0.84) and the YELLOW sample has a slight positive Ce anomaly ( $Ce/Ce^*$ : 1.33). The other three samples have no prominent Ce anomalies.

Murali *et al.* (1983) found three distinct groups of zircon (Table 5.05) from nepheline syenites, charnockites, carbonatites and detrital zircons from southern India, using the Ce and Eu anomalies and the degree of HREE enrichment. The survey of the literature indicates another two variants and several rock types may be added to the three types of Murali *et al.* (1983). The individual zircons and their rock types are included in the figure for comparison.

The metamict zircon from the dunes north of Richards Bay according to the above classification, have weak HREE-enrichment, no prominent Eu anomalies and no prominent Ce anomalies; and therefore are grouped in a sub-group between TYPE 2 and TYPE 3. The source rocks for these zircons from the literature are pegmatites, migmatites, carbonatites, granodiorites and basanites. The REDBROWN and YELLOW zircon may also be included in group one which are derived from syenites, nepheline syenites, granites and mafic rocks. The BULLSRUN-1 and BULLSRUN-2 samples are both classed as TYPE 3 which are derived from carbonatites or pegmatites. Bull's Run is in fact a syenite and nepheline-syenite gneiss with minor carbonatite and microsyenite intrusives (Scogings and Forster, 1989).

TABLE 5.03: Y, REE, U and Th concentrations in metamict zircon.

Description:	Yellow Metamict	Pale Metamict	Grey D Metamict	Grey D Metamict	Red Brown Metamict
Sample #:	YELLOW	PALEBROWN	GREYD-1	GREYD-2	REDBROWN
Y	20525.22	20938.30	9753.36	17363.20	17446.13
La	106.31	966.79	625.29	2882.45	2513.04
Ce	752.21	2501.22	1524.34	7040.64	4354.90
Pr	129.60	316.58	218.46	891.72	584.93
Nd	790.61	1388.39	992.22	3509.80	2467.02
Sm	856.75	914.43	442.14	1049.66	1057.62
Eu	284.04	294.24	163.60	275.89	287.42
Gd	1401.07	1424.92	646.20	1402.57	1123.79
Tb	443.18	445.39	207.61	416.54	374.57
Dy	3033.80	2972.61	1540.53	3044.97	2505.00
Ho	616.75	615.97	346.32	683.61	697.22
Er	2422.22	2408.57	1512.40	2916.33	2250.49
Tm	431.03	432.91	291.03	567.65	366.87
Yb	3360.63	3344.32	2521.30	4878.05	2864.87
Lu	568.15	557.43	464.89	877.69	522.53
Th	3949.96	4780.96	2683.67	4883.61	2413.19
U	4884.19	4489.57	5180.68	11004.08	3746.17
U/Th	1.24	0.94	1.93	2.25	1.55
U+Th	8834.15	9270.53	7864.35	15887.69	6159.36
La/Sm	0.08	0.67	0.89	1.73	1.49
Yb/Gd	2.97	2.90	4.83	4.30	3.15
Ce/Ce*	1.33	1.08	0.99	1.05	0.84
Eu/Eu*	0.79	0.79	0.93	0.70	0.80

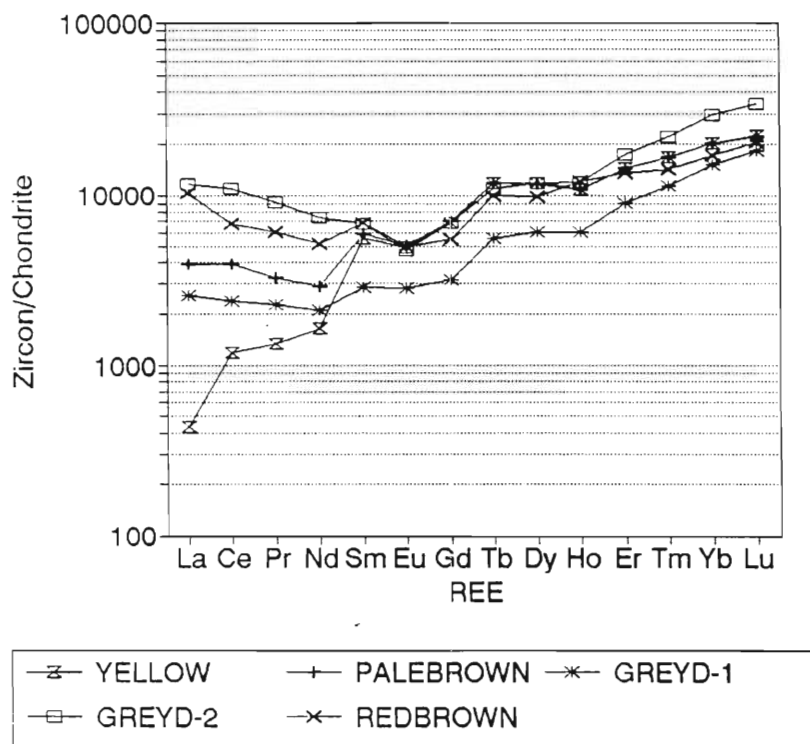


FIGURE 5.04: Chondrite normalised REE profiles of the metamict zircon.

TABLE 5.04: Y, REE, U and Th concentrations in the metamict zircon from Bull's Run.

Description:	Bull's Run Metamict	Bull's Run Metamict
Sample #:	BULLSRUN-1	BULLSRUN-2
Y	667.80	659.48
La	21.38	22.24
Ce	66.42	66.67
Pr	7.03	7.13
Nd	33.85	36.94
Sm	14.53	15.24
Eu	6.28	6.62
Gd	26.69	29.66
Tb	7.70	7.97
Dy	66.17	69.34
Ho	19.47	20.18
Er	97.58	102.37
Tm	21.27	22.27
Yb	210.14	222.44
Lu	36.52	39.55
Th	664.52	758.06
U	174.55	196.20
U/Th	0.26	0.26
U+Th	839.06	954.26
La/Sm	0.93	0.92
Yb/Gd	9.74	9.28
Ce/Ce*	1.30	1.27
Eu/Eu*	0.96	0.93

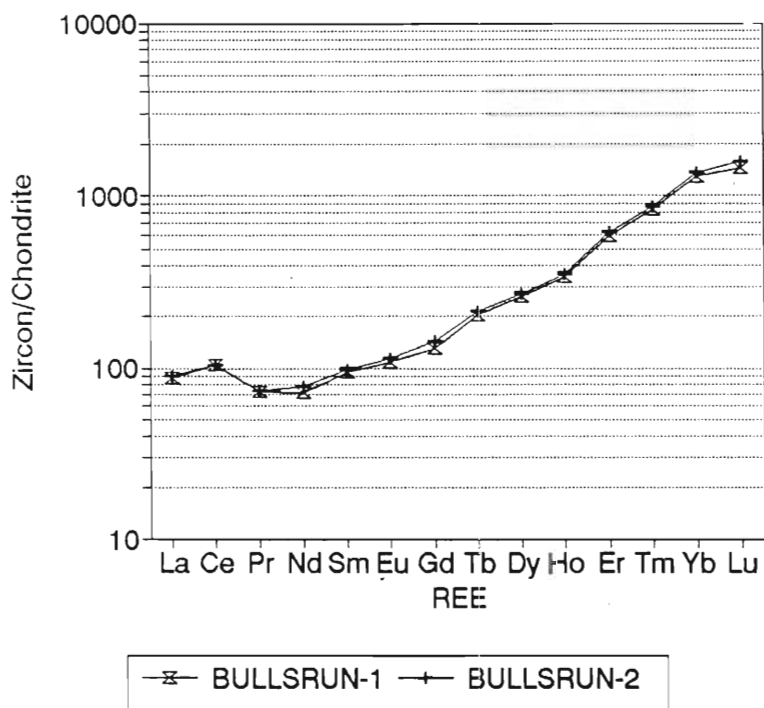


FIGURE 5.05: Chondrite normalised REE profiles of the metamict zircon from Bull's Run.

**TABLE 5.05:** Cerium, Europium anomalies and HREE concentrations in zircon and their related source rocks. A classification scheme developed by Murali *et al.* (1983). (N=Neutral, +=Positive, -=Negative).

TYPE	Ce/Ce <sup>+</sup>			Eu/Eu <sup>+</sup>			HREE-enrichment			Rock Source <sup>1</sup>
	N	+	-	N	+	-	Poor	Mid	Rich	
<b>Murali <i>et al.</i> (1983):</b>										
TYPE 1	-	*	*	-	-	*	-	*	-	NEPHELINE SYENITE, SYENITE
TYPE 2	*	-	-	-	-	*	*	-	-	MIGMATITES, CHARNOCKITES
TYPE 3	*	-	-	*	-	-	-	*	*	CARBONATITE, PEGMATITE
<b>Extended from the literature:</b>										
TYPE 1	-	*	*	-	-	*	-	*	-	ADAMELLITE, GRANOPHYRE, ANORTHOCLASE, ANDESITE, DIORITE
TYPE 1-2	-	*	*	-	-	*	*	-	-	GRANODIORITE
TYPE 2-1	*	*	-	-	-	*	-	*	-	PEGMATITE
TYPE 2	*	-	-	-	-	*	*	-	-	GRANODIORITE, METEORITE
TYPE 3	*	-	-	*	-	-	-	*	*	METEORITE, BASANITE
TYPE 4	-	*	-	-	-	*	-	-	*	SYENITE, ANOTHOCLASE
TYPE 5	GEMS			-	-	*	*	-	*	PEGMATITE
YELLOW	-	*	-	*	-	*	-	*	-	TYPE 2-3
PALE	*	-	-	*	-	*	*	-	-	TYPE 3
GREYD-1	*	-	-	*	-	*	*	-	-	TYPE 3-2
GREYD-2	*	-	-	*	-	*	*	-	-	TYPE 3-2
RED	*	-	-	*	-	*	*	-	-	TYPE 3-2
BULL-1	-	*	-	*	-	*	*	-	-	TYPE 3-1
BULL-2	-	*	-	*	-	*	*	-	-	TYPE 3-1
BULB-1	-	*	-	-	-	*	-	*	-	TYPE 1
BULB-2	-	*	-	-	-	*	-	*	-	TYPE 1
CLEAR	*	-	-	-	-	*	*	-	-	TYPE 2
CLEARP4	-	*	-	-	-	*	-	*	-	TYPE 1-(4)
COLOURED	-	*	-	-	-	*	-	*	-	TYPE 1-(4)
DINCL-1	-	*	-	-	-	*	-	*	-	TYPE 1-(4)

1: HREE enrichment is defined as POOR (Lu/La)<sub>CN</sub> is 4-15, MID if 15-585 and HIGH if >585

2: In TYPES 4 and 5 the (Lu/La)<sub>CN</sub> is between 2080 and 51400; and in TYPE 4 the (Ce/Ce<sup>+</sup>) is between 10 and 150.

The LREE profiles of the metamict zircon range from La/Sm of 0.08 (YELLOW) to 1.73 (GREYD-2), with BULLSRUN-1/2 at 0.93. The difference between the two grey metamict samples (GREYD-1/2) is difficult to interpret. But *dark monazite*, a Eu-rich variety of monazite, that is opaque grey and has a euhedral form were identified with a Kevex X-ray energy spectrometer attached to a Jeol-35 Scanning Electron Microscope. These *dark monazites* may have been mistaken for zircon when GREYD-2 was hand-picked. GREYD-2 has nearly double the LREE, Y and U+Th of GREYD-1 and therefore monazite may be contaminating one of the above samples. Y values of the metamict zircons, excluding the Bull's Run zircon, are enriched more than 20-fold over the clear zircons and bulk samples.

The metamict zircons have low U/Th values (excl. GREYD-2) with an average ratio of 1.24 compared to the bulk ZC-B91 NM with a U/Th of 2.21 and the bulk ZCP-892 with a U/Th value of 2.10 and the individual clear zircon with an average U/Th value of 1.87.

Many papers have been written on the process and effect of metamictisation (eg. Holland and Gottfried, 1955; Farges and Calas, 1991; Woodhead *et al.*, 1991). Metamictization is characterised by a large decrease in density, refractive index, and birefringence of the crystalline zircon (Holland and Gottfried, 1955), through damage produced by the  $\alpha$ -decay of U and Th.

The displacement, distortion or tilting of  $\text{SiO}_4$  tetrahedra occurs during metamictization of zircon (Farges and Calas, 1991) with few, if any, undisplaced  $\text{ZrO}_4$  tetrahedra remaining in their original positions (Woodhead *et al.*, 1991). Yada *et al.* (1987) viewed fission tracks and point defects in zircon with a high magnification SEM. Diameters of individual fission tracks (voids in the crystal formed by charge-repulsion from the movement of highly charged fragments) range from 15 to 40Å. The progressive damage by an increase in the number of fission tracks results in the destruction of the structure of zircon. Eventually, with time, the disrupted structure is replaced by an amorphous silica structure which is stabilised by the incorporation of  $\text{H}_2\text{O}$ .

Metamict zircon analysed by Farges and Calas (1991) have U values ranging from 1800 to 72800ppm, and Th values ranging between 440 to 92700ppm. The U/Th values have a large range, ranging from 0.79 to 112.5. Metamict zircon is rarely analysed for REE in the literature, but Exley (1980) analysed Y-, REE- and Th-rich zircons from the Skye epigranite and granophyre by electron microprobe. Values obtained for:

Y ranged from 5100 to 32300ppm,  
Ce ranged from 300 to 2000ppm,  
Gd ranged from 600 to 2600ppm,  
Yb ranged from 1400 to 4100ppm, and  
Th values ranging from 1200 to 17300ppm.

Törnroos (1982) analysed metamict zircon from pegmatites in Mozambique with low U values between 90 and 350ppm and Th values between 970 and 1930ppm, and with very low U/Th values between 0.07 and 0.25. The Mozambique metamict zircon contained xenotime and therefore have Y values from 1340ppm up to 27900ppm with an average of 11500ppm for 9 samples. For comparison the average concentration of trace elements obtained for the metamict zircon from the RBM product are:

Y ranged from 9523 to 20681ppm,  
Ce ranges from 760 to 4355ppm,  
Gd from 704 to 1609ppm,  
Yb from 2507 to 4847ppm,  
U from 3746 to 11004ppm and  
Th from 2413 to 4883ppm.

The sampling of 200 to 350 metamict grains for ICP-MS analysis involves the inherent problem of grains that appear the same but are in fact derived from different provenances. Euhedral metamict crystals are rare in the RBM concentrate, so a large portion of the grains picked were rounded or were fragments of larger grains. In a single rock type the range of U and Th values may be very large in metamict zircon of a single type.

The point counting in Chapter 4 showed that metamict zircon constituted 5.9% of the zircon bulk sample. Calculating the U and Th contribution of the 5.9% of metamict zircon, using the average U and Th value, suggest that nearly 100% of the both U and Th in the bulk samples U is contributed by metamict zircon, which is improbable. The 5.9% metamict zircon point counted includes lighter coloured or misty-translucent metamict zircon which were not analysed, and contribute the majority of metamict grains. The grey type zircon is very rare within the bulk sample and therefore, even though highly enriched in trace elements, does not contribute much U and Th to the bulk sample.

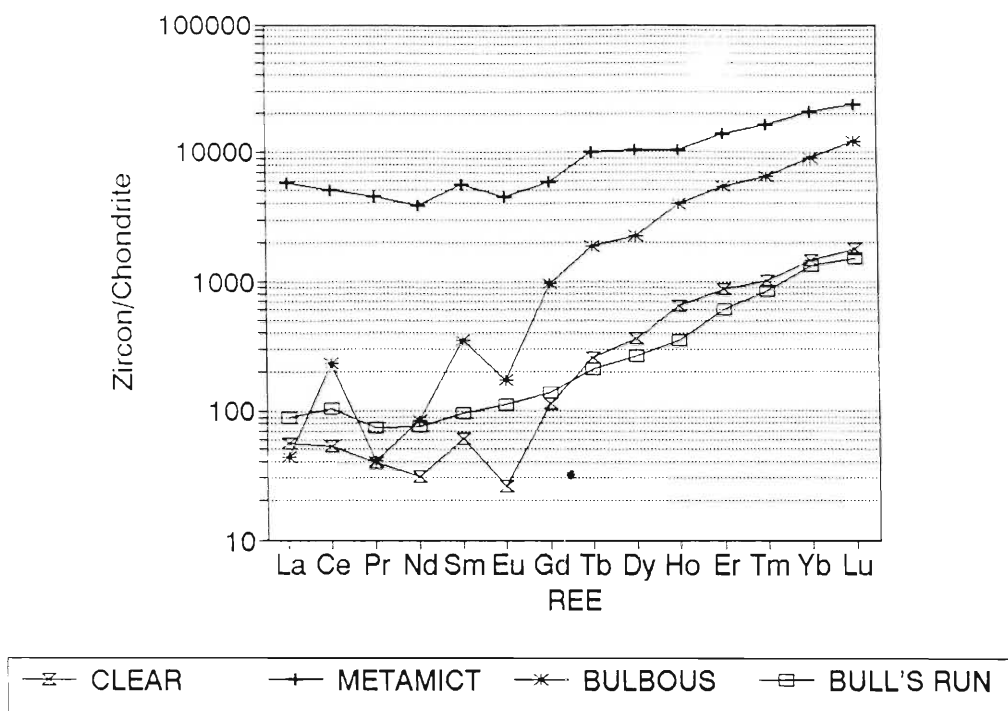
#### 5.4 SUMMARY OF THE ANALYSES OF INDIVIDUAL ZIRCONS

Figure 5.06 and Table 5.06 summarise the average of the analyses obtained for the clear, metamict and bulbous zircon. The metamict zircons are the most U-, Th- and REE-rich, followed by the bulbous frosted zircon.

**TABLE 5.06:** Summary of the average Y, REE, U and Th concentrations in clear, frosted bulbous, metamict and Bull's Run zircon.

Description:	Average Clear	Average Metamict	Average Bulbous	Average Bull's Run
Y	1016.72	17205.24	6856.88	663.64
La	13.54	1418.77	10.54	21.81
Ce	34.17	3234.66	147.97	66.55
Pr	3.74	428.26	3.96	7.08
Nd	14.57	1829.61	40.11	35.39
Sm	9.41	864.12	54.00	14.88
Eu	1.50	261.04	9.86	6.45
Gd	23.30	1199.71	197.28	28.18
Tb	9.57	377.46	69.56	7.83
Dy	91.30	2619.34	570.03	67.76
Ho	36.80	591.97	221.68	19.83
Er	144.52	2302.00	895.11	99.97
Tm	25.89	417.90	166.49	21.77
Yb	238.76	3393.83	1496.08	216.29
Lu	45.78	598.14	304.81	38.04
Th	116.78	3742.28	729.86	711.29
U	233.24	5860.94	1289.32	185.37
U/Th	1.87	1.58	1.79	0.26
U+Th	337.67	9603.21	2019.18	896.66
La/Sm	0.61	0.97	0.12	0.92
Yb/Gd	11.82	3.63	9.38	9.51
Ce/Ce*	2.09	1.06	5.77	1.28
Eu/Eu*	0.27	0.80	0.26	0.95





**FIGURE 5.06:** Chondrite normalised REE profiles of the average values for the clear zircon, metamict zircon, bulbous zircon and Bull's Run zircon.

At the other end of the REE range the clear zircons have the lowest LREE concentrations, and the Bull's Run grey and white opaque zircon have the lowest HREE concentrations.

The frosted bulbous zircon have the most prominent Ce anomaly ( $Ce/Ce^*$ : 5.77), and both the clear and frosted zircon have the largest negative Eu anomalies ( $Eu/Eu^*$ : 0.26-0.27).

The enrichment of U and Th in the frosted zircon appears to have been accompanied by the enrichment of the zircon in the HREE and Y, possibly related to xenotime end-member. The large Ce anomaly may also be related to the addition of Ce from a source with a high oxygen fugacity (ie. high  $Ce^{4+}/Ce^{3+}$ ), and high (Zr), U, Th and REE: possibly a pegmatitic or syenitic source fluids. The metamict zircons grew in rocks with high zircon/melt partition coefficients and/or high concentrations of U, Th, Y and REE.

### 5.5 PRELIMINARY PROVENANCE STUDY

A preliminary provenance study using the REE concentrations in the zircon and the partition coefficients in the literature was performed. Several notable difficulties are apparent, including the scarcity of REE data for the potential source rocks, lack of reliable partition coefficient data in the literature and other complications concerning magmatic crystallization. The results of the calculations are listed below.

Chondrite normalised rare earth profiles for three areas inland from Richards Bay are available in the literature, these are plotted in Figure 5.07. The large Tugela catchment and river basin drains a large area with numerous sources for zircon, and is most likely the principal source region for zircon in the heavy mineral dune placers. The abundance and source of zircon in the Cretaceous sedimentary wedge under and north of Richards Bay is unknown, but through repeated reworking from several marine regressions and transgressions it may hold large concentrations of heavy minerals. The contribution of these heavy minerals to the Pleistocene and Holocene sediments is at present unknown. Due to the limited scope of this provenance study only the rocks inland from Richards Bay will be considered.

The Lebombo rhyolites (Erlank, 1984 and Harris and Erlank, 1992) are plotted in Figure 5.07A. The Lebombo rhyolites are acid volcanics with a north-south extension of 600km, with the southern termination NW of Richards Bay. The Wangu Gneiss and biotite dykes within the Wangu Gneiss NW of Eshowe and Ngoye aegirine granite gneiss E of Eshowe (Scogings, 1989) are plotted in Figure 5.07B and Bull's Run gneissose carbonatites NW of Eshowe (Scogings and Forster, 1989) are plotted in Figure 5.07C.

The Wangu granitoid gneisses have very high zirconium concentrations between 450 and 3730ppm and the Ngoye gneiss has 840ppm Zr (Scogings, 1989). These rocks may contribute detectable amounts of zircon to the coastal plain. Both these bodies are drained by the Mhlatuze river (See Figure 1.01) which has its mouth in the harbour of Richards Bay.

The important points concerning the Lebombo rhyolite REE profile are the small Eu anomalies and the change in slope between the LREE and the HREE, with the LREE having the steeper slope. The  $Eu/Eu'$  of the Lebombo rhyolites is 0.71, which is high compared to other rhyolites worldwide which have an average of 0.23 (range: 0.03-0.49) (Barberi *et al.*, 1975; Davies and Macdonald, 1987; Govindaraju, 1989). The Wangu and Ngoye gneisses both have smooth profiles with a gradual change in slope and large  $Eu/Eu'$  values. The biotite dykes on the other hand have minor Eu anomalies.

Due to the scarcity of REE data from northern Natal the average REE profiles for several rocks types worldwide are plotted in Figure 5.08. Average REE profiles from granulite gneisses and amphibole gneisses compiled by Weaver and Tarney (1981) are plotted in figure 5.08A. The profiles from 6 granites in Finland with a progressive increase in differentiation are plotted in Figure 5.08B from Petersen (1980) and 4 granites in southern England with progressive changes from differentiation is plotted in Figure 5.08C (Ward *et al.*, 1992). The figures in parentheses in the legends of Figures 5.08B and C are the Zr concentrations in the samples from which the REE were obtained.

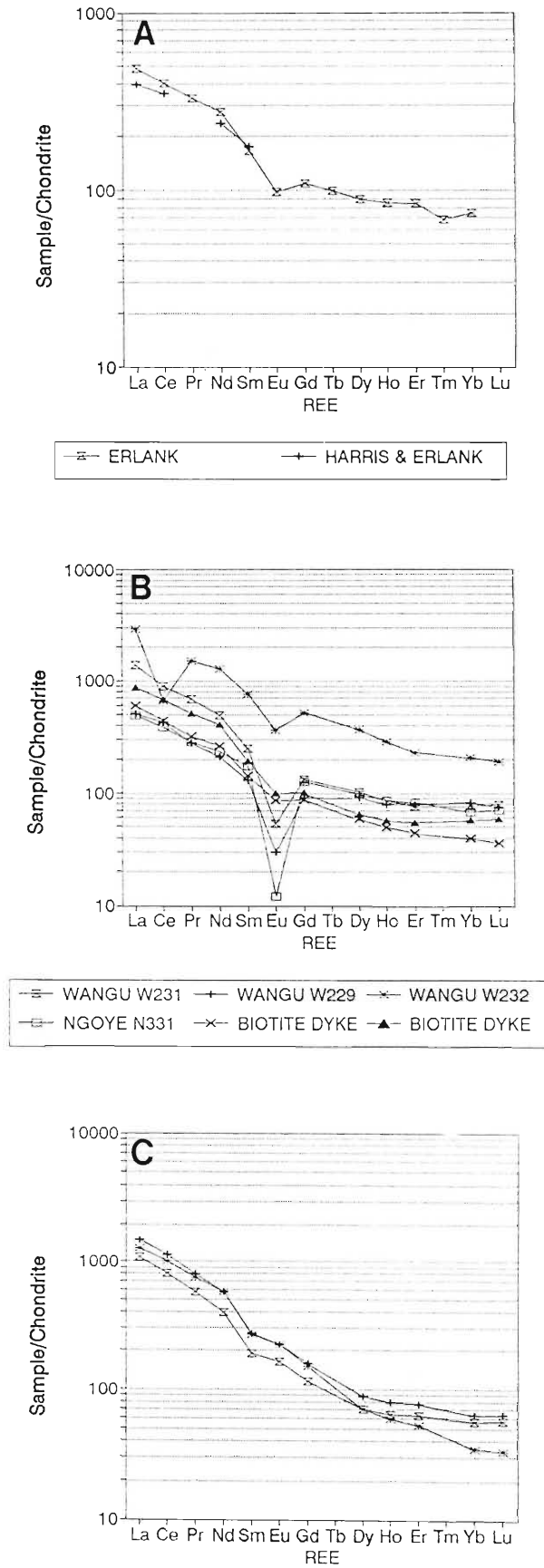


**FIGURE 5.07:** Chondrite normalised REE profiles of: A) Lebombo Rhyolite (Erlank, 1984 and Harris and Erlank, 1992); B) Wangu gneisses and biotite dykes and Ngoye gneiss (Scoggings, 1989); C) Bull's Run Carbonatites (Scoggings and Forster, 1989).

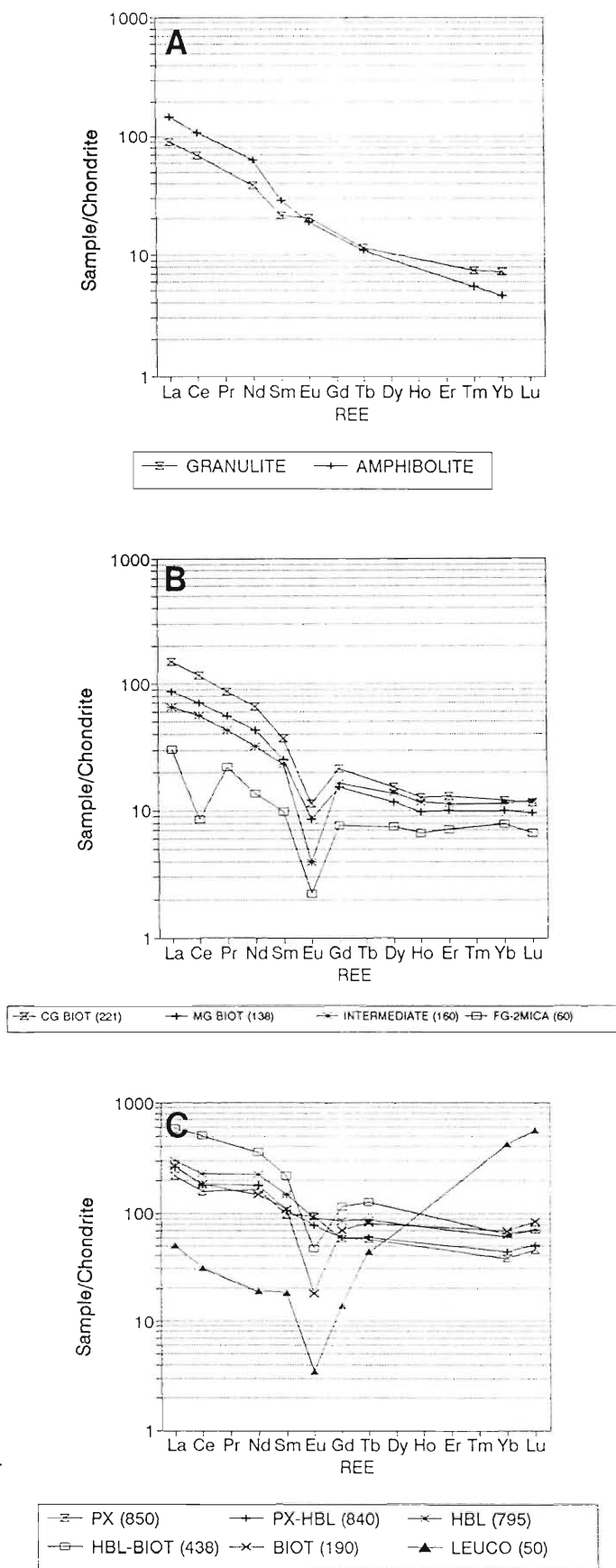


FIGURE 5.08: Chondrite normalised REE profiles of: A) Average granulite and amphibole gneiss (Weaver and Tarney, 1981); B) Granite fractionation series, pyroxene granite to leucogranite (Petersen, 1980); C) Granite fractionation series (Ward *et al.* 1992).

Several difficulties exist in deriving or calculating the REE profiles of source rocks from the REE profiles of zircon. Firstly the REE data of potential source rocks in the interior of northern Natal is scarce. Secondly, the partition coefficient data is often unreliable due to the lack of knowledge of the crystallization history of the parent magma. The data rarely covers the whole range of REE. Thirdly, complications arising from fractionation during magmatic crystallization make application of the method difficult. Ward *et al.* (1992), Yurimoto *et al.* (1990) and Petersen (1980) studied the implications of early crystallization and fractionation of accessory minerals on the trace elements of the evolving magma. Both showed that the early fractionation of LREE into monazite, HREE into apatite, zircon and xenotime, and Eu into plagioclase and K-feldspar resulted in an enrichment in REE in the initial cumulates and depleted the residual melt in the REE. The partition coefficients of REE into the various minerals in the melt from Ward *et al.* (1992) is duplicated in Figure 5.09. From the figure it can clearly be seen that the HREE concentrations are controlled by the crystallization and fractionation of apatite, zircon and xenotime; and the LREE by monazite and apatite. The ratio of minerals that have grown, and the ratio of minerals that are presently growing effect the REEs available to be partitioned into each of the accessory minerals. Petersen (1980) reported a 17-fold decrease in Zr between the early and late granite phases, with a massive zircon growth period in the middle phase of fractionation (0.07wt% of bulk rock), prior to the hornblende-biotite and biotite phase of crystallization (See Figure 5.08B). Ward *et al.* (1992) reported a reduction in Zr from 155-221ppm in the early granite to 60-66ppm in the late granite.

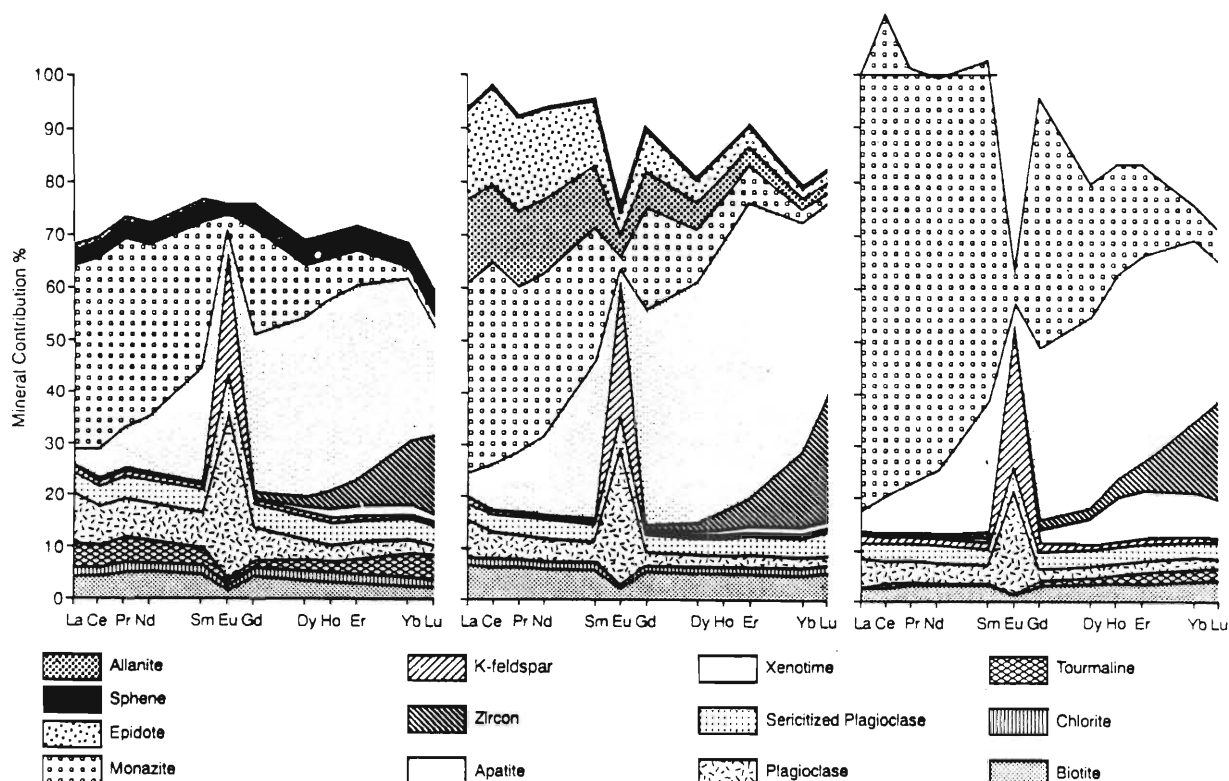


FIGURE 5.09: The partitioning of REE between major and accessory minerals in the coarse grained megacrystic biotite Dartmoor granite (From Ward *et al.*, 1992).

The amount of REE that is available for incorporation into the growing zircon is dependent on the previous crystallization of monazite, apatite, xenotime and zircon. The partition coefficients of REE between various melts and the zircon were reported by Ward *et al.* (1992) for the early and middle periods of granite crystallization. The middle period has higher partition coefficient (average La to Eu: 40) relative to the early period (average La to Eu: 18). Yurimoto *et al.* (1990) related the discontinuities in REE profiles, especially for Nd and Sm in highly silicic melts, to the fractionation of monazite.

The large differences in partition coefficients and REE concentrations possible in single magmatic bodies makes the application of calculating source rocks from the detrital zircons REE profiles tentative at best. The REE profiles of source rocks were calculated for three individual zircons, the D, P4 and COLOURED zircon analyses. The calculations for metamict zircons were not performed for all the available partition coefficients because it was considered that the metamict zircon is more likely to have been altered, and no partition coefficients work on metamict zircon is available in the literature. The zircon/whole rock and zircon/groundmass partition coefficients that are listed in Chapter 2 were used to calculate the profiles.

Calculating the REE profile of a source rock requires REE data of the zircon and reliable partition coefficients of zircon to groundmass for several rocks. The REE data of the source rock is derived from the following equation:

$$k_M = [M]_{\text{zircon}}/[M]_{\text{magma}}$$

Where  $k_M$  is the partition coefficient for element M, and  $[M]$  is the concentration of element M in the zircon and the magma from which the zircon grew. Therefore the concentration of element M in a magma or whole rock can be calculated from the concentration of element M in the zircon from which it originated by the following equation:

$$[M]_{\text{magma}} = [M]_{\text{zircon}}/k_M$$

The average mineral/groundmass partition coefficients for dacites from Nagasawa (1970) give flat LREE profiles, with a change in slope, from positive to negative at Sm (Figure 5.10A). Nagasawa (1970) did not analyse La, so the LREE slope may be similar to the Sm-Nd slope with the negative Ce-Nd slope being derived from a positive Ce anomaly in the zircon. The slope for the D-type zircon (excluding LREE & Sm) is the most uneven. The P4 and COLOURED zircon both have gentle Sm-Eu-HREE profiles. The Nd to Sm slopes are anomalous in these profiles due to the low Sm/Nd values of the dacites. The Sm/Nd values of the zircons from the literature range from 0.1 to 16.1 with an average of 0.83 if the metamict zircons are included. The three RBM zircons have Sm/Nd ratios of 1.71 to 3.72. The calculated profiles from partition coefficients with low Sm/Nd values therefore result in the anomalous Sm behaviour. In Nagasawa (1970) one granite from which zircon was removed has a low Sm/Nd value of 0.58 and the zircon from this granite has a corresponding low

Sm/Nd value of 1.97; while the second granite has a higher Sm/Nd value of 0.83 and the zircon from this granite has a corresponding high Sm/Nd value of 4.84. A review of Sm and Nd values of zircon shows a general increase in the Sm/Nd value from andesite, dacite, diorite and granodiorite through granophyre, granite and basanite to syenite and pegmatite. The use of Sm/Nd values in zircon as a crude provenance indicator is untested but due to the large range of Sm anomalies produced by partition coefficient calculations the Sm/Nd values may be a good provenance indicator. The Sm/Nd value of the D type zircon falls in the adamellite-granite-basanite range, while the P4 and COLOURED zircon falls in the granite-pegmatite range. The bulbous frosted zircon falls in the syenite-basanite range. Yurimoto *et al.* (1990) devised a model in which as the fractionation process progresses the melt becomes depleted in LREE and slightly enriched in HREE due to the fractionation of monazite. The result is a discontinuous REE pattern with the kink between Nd and Sm. The crystallization of garnet and/or zircon will further complicate the profile by changing the HREE in the residual melt. The upward inflection of the Nd to Sm slope may therefore only be the record of monazite fractionation and an individual igneous body could therefore have more than one Sm/Nd value depending on the spatial distribution of monazite fractionation.

In Figure 5.10B Nagasawa's (1970) zircon/whole rock partition coefficients for granites give rather smooth surfaces for all three samples (excluding Sm and Eu for D-type and COLOURED-type), with the P4 type having a very smooth profile.

Murali *et al.*'s (1983) partition coefficients, which were estimated from the plots for acid charnockites result in smooth profiles with downward inflections for La and Lu (Figure 5.10C). Sm and Eu do not show any anomalous behaviour in the D-type zircon. The Ce in all the samples may show slight to large anomalies if the La to Sm tieline is considered to be the true LREE profile. If this is the case the LREE of P4 and COLOUR have flat profiles and the HREE have negative slopes: an unlikely source profile.

Watson's (1980) experimental partition coefficients for a felsic melt result in a very low value U-shaped profile (Figure 5.10D). The U-shape is an unlikely profile and the low Lu partition coefficient is most likely erroneous.

Fujimaki's (1986) partition coefficients for andesites and diorites produce profiles that are very erratic in nature (Figure 5.10E).

Hinton and Upton's (1991) average partition coefficients from the literature give erratic profiles with staggered LREE to HREE profiles (with Ce and Sm positive peaks and Eu and Tm negative anomalies) (Figure 5.10F). Hinton and Upton (1991) calculated the theoretical partition coefficients for zircon with the ionic radius and charge as the criteria. The profiles from these partition coefficients give smooth REE-rich profiles (Figure 5.10G). The D-type zircon has a very smooth La to Eu profile, with an upward inflection of the HREE and a small Eu anomaly. This profile has a very similar shape to the profile for the Lebombo rhyolites, but the Lebombo concentration is lower by an order of magnitude.

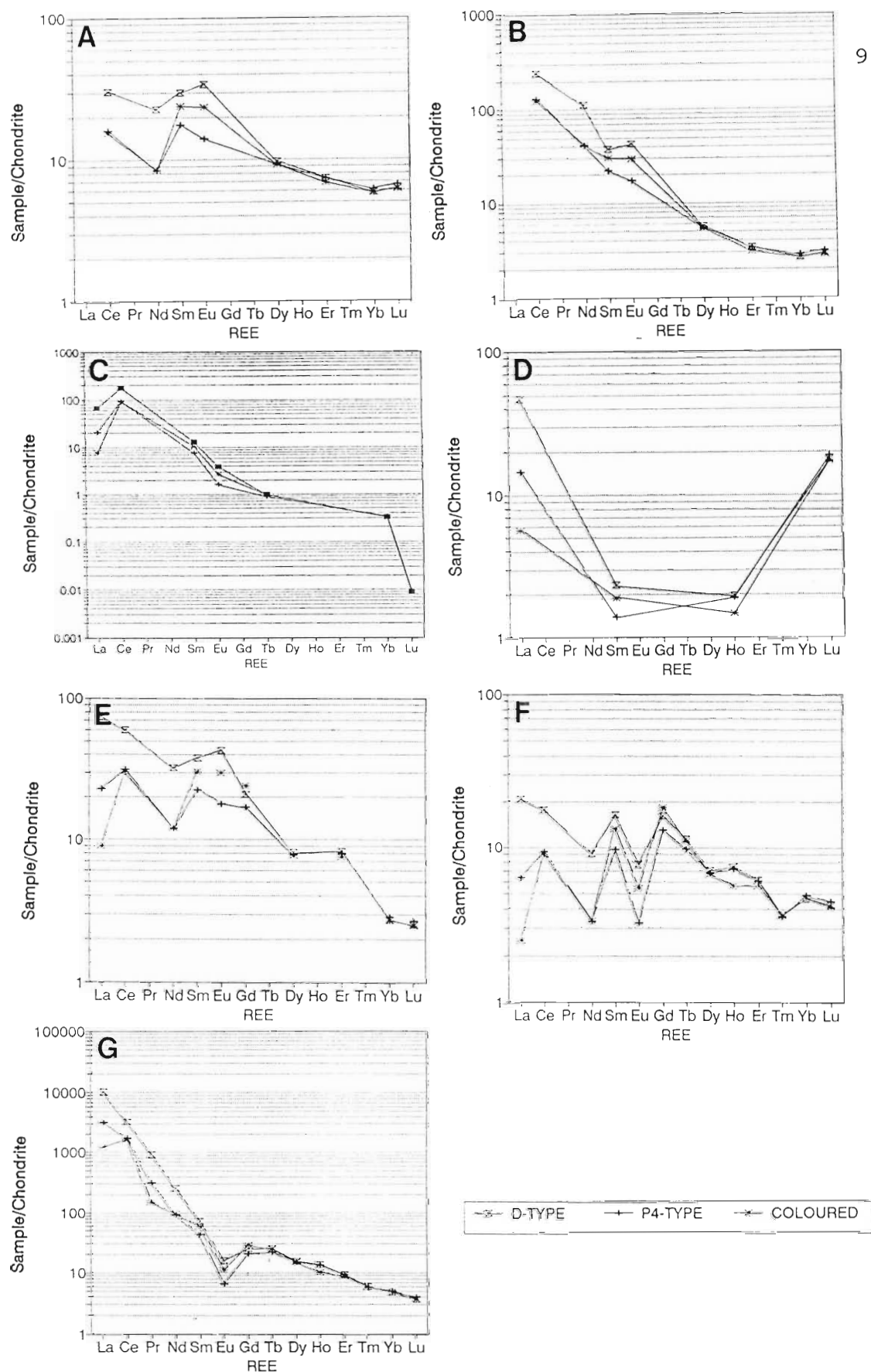


**FIGURE 5.10:** The chondrite normalised calculated REE profiles of source rocks for the D, P4 and COLOURED zircon with partition coefficients from: A) Dacites (Nagasawa, 1970); B) Granites (Nagasawa, 1970); C) Charnockite (Murali *et al.*, 1983); D) Felsic melt (Watson, 1980); E) Andesites and Diorites (Fujimaki, 1986); F) Average of the literature (Hinton & Upton, 1991); G) Calculated theoretical values (Hinton & Upton, 1991).



The partition coefficient profile of zircon is similar to that of garnet. Irving and Frey (1978) reported partition coefficients of garnet, from kimberlite through the transition phases to rhyolite. In the case of garnet the degree of HREE partition coefficients increase with approximately the same slope from kimberlite through hawaiite to dacite, rhyodacite and rhyolite. The partition coefficient profiles of the LREE follow the same trend except that the La/Sm value for the rhyolite/rhyodacites are approximately 1 compared to much lower values for the other rock types. The negative Eu anomaly is non-existent in the basic rocks and steadily increases from dacite through rhyodacite to rhyolite. If zircon is presumed to follow this trend then La/Sm may be used as an indicator of the acidity of the parent magma. The clear D-type zircon has a La/Sm value of approximately 1 which would correspond to a rhyolite/rhyodacite origin, while the P4 and coloured varieties have much lower LREE enrichments of 0.57 and 0.16 respectively.

None of the calculated profiles have large negative Eu anomalies, with the exception of Hinton and Upton's (1991) theoretical partition coefficients, which are common in granites and rhyolites. The Lebombo rhyolites have very small Eu anomalies and may be the source for some of the zircon. The best results for the D-type zircon were obtained from Nagasawa's (1970) average granite and Hinton and Upton's theoretical partition coefficients. The later compares favourably with the profile of the Lebombo rhyolites. Vavra (1990) and Pupin (1980) both considered D-type zircons to be derived from rhyolites so it appears that the D-type may be partially derived from the Lebombo rhyolites. None of the partition coefficient calculated profiles are as enriched as the average rhyolite. This indicates that the partition coefficients in the literature trend towards the high side.

All three zircons have smooth-sloped calculated profiles with low Eu negative anomalies from the partition coefficients from granites in Nagasawa (1970). The average REE profiles from granulite and amphibole gneiss do not have prominent Eu anomalies, and may therefore contribute zircons of metamorphic origin with low Eu anomalies.

From the comparison of  $Ce/Ce^*$ ,  $Eu/Eu^*$  and the degree of HREE enrichment in Table 5.05, the metamict zircons appear to be derived from migmatites, carbonatites and pegmatites. The clear zircons appear to be derived from syenites, granites, granophyres, migmatites and possibly some less acidic rocks as well. The Bull's Run zircon have a carbonatite, syenite or pegmatite signature; which is the signature that is expected. The bulbous frosted zircons have syenite and nepheline syenite signatures, as well as those of granite and granophyre. This may confirm the hypothesis that the bulbous-rounded frosted zircons with high U values have the same origins as those envisaged by Grauert *et al.* (1974): mechanically abraded zircons in a quartzite were enriched in U during the intrusion of the sedimentary rock by pegmatites.

Comparison of Sm/Nd values places the clear D type zircon in the adamellite-granite-basanite group, and the P4 and COLOURED zircon in the granite-pegmatite range.

Morphology is a potential indicator of provenance. The potential sources of D-type zircon are dealt with in detail in Section 2.1. The P4 type zircon can be derived from monzogranites, sub-alkaline series granites, subsolvus granites and are very common in leucogranodiorites and hypersolvus granites according to Pupin (1980). The fact that no {211}-forms are present, and the {110}-forms are present, correspond to a melt with low zircon-supersaturation with low concentrations of elements which substitute for Zr in zircon in the melt (Vavra, 1990). It must be stressed that this evaluation of Vavra's (1990), on zircon surface morphology, only reflects the final growth of zircon and therefore the magmatic conditions in the final period of growth. Cathodoluminescence studies of polished sections will give a more comprehensive history of the source magma (see Section 4.5.2). The D and P coloured variety are derived from sources similar to the aforementioned D and P4 types.

The chondrite normalised REE profiles using the theoretical values of Hinton and Upton (1991) and Nagasawa (1970) suggested that the clear types are most likely derived from granitic or rhyolitic rock types. The Wangu and Ngoye gneisses have more prominent Eu anomalies, and only have a small gentle upward inflection of the HREE profiles compared to the calculated profiles. The biotite dykes have small Eu anomalies and gentle slopes, but do not outcrop over large areas, and are therefore unlikely to supply large quantities of zircon.

The best method of provenance study on the large scale appears to be cathodoluminescence or backscattered secondary electron imagery. Firstly, the method can be applied to abraded grains with some success, and is therefore an improvement on the general crystal morphological studies because it includes a more genetic approach, ie. it includes the history of the zircons growth and not just the final stage of growth (see Section 4.5.2). Secondly the method is simple, cheap and fast. REE modelling appears to be a more subsidiary tool in large provenance studies. REE modelling will only be effective when a more comprehensive trace element data set is available for the Tugela River and Mhlatuze River catchments.

## CHAPTER 6

### EXPERIMENTAL REDUCTION OF U & Th

Several experiments were undertaken with the aim of reducing the U and Th values of the zircon concentrate (ZC) and the zircon concentrate product (ZCP). The objective was to obtain a (U + Th) value for the zircon concentrate product of 400ppm or less. The six methods of reduction used were partial dissolution by acid, abrasion, partial dissolution by acid followed by air abrasion, removal of the low and high density zircons, removal of large and small zircon, and the removal of magnetic zircons.

#### 6.1 PARTIAL DISSOLUTION

Numerous authors have studied the solubility of zircon in different fluid compositions and at different temperatures and pressures.

##### 6.1.1 ALKALINE LEACHING LITERATURE

Stevens and Corron (1948) stated that zircon can be corroded by acid and they also conclude that zircon will react, alter or dissolve in alkaline environments. Maurice (1949) disagreed and noted that zircon is stable in alkaline aqueous solutions at 400°C. Caroll (1953) stated that waters rich in calcium bicarbonate or sodium bicarbonate may be able to dissolve zircon. Zircon in laterites rich in alkaline elements were corroded or leached at surface temperatures and pressures.

Alderton *et al.* (1980), King and Kerrich (1987) and Rubin *et al.* (1989) all show that Zr mobility in rocks can be attributed to the presence of F-rich fluids of late magmatic or hydrothermal origin. Rubin *et al.* (1989) showed that hydrothermal zircon growth is related to fluorite growth. The solubility and mobility of zirconium is related to F concentration and the "aluminosity" of the fluid and rock through which the fluids migrate. Alderton *et al.* (1980) also showed that extreme mobilisation of Zr took place during the tourmalinization of a granite.

Wayne and Sinha (1992) related zircon dissolution and reprecipitation during 600°C metamorphism to HF acid fugacity. The rate of dissolution depends on temperature, pressure, fluid-rock ratio, strain state and the zircons mechanical and chemical response to metamorphism.

Sinha *et al.* (1992) reported 47% U loss and 51% Pb loss from clear zircon after 720 hours

in 2M NaCl at 600°C and 6kb. Clear zircon after 200 hours with the same experimental conditions lost 40% of the U and 33% of the Pb. Metamict zircon lost 51% of the U and 87% of the Pb. The experiment was repeated with 2% HNO<sub>3</sub> which was less effective and after 720 hours only 12% of the U and 32% of Pb was lost.

### 6.1.2 ACID AND PRESSURE LEACHING LITERATURE

Several papers in the literature are devoted to synthetic hydrothermal treatment performed on zircon in laboratories.

Saxena (1966) completely recrystallized cyrtolite in a hydrothermal annealing experiment at a temperature of 600°C and a pressure of 2kbar for 168 hours. If a fluid is present and recrystallization of zircon occurs there will be lead and uranium loss.

Pidgeon (1992) found examples of clear growth zoned zircon that had been partially recrystallized to unzoned zircon under moderate metamorphic conditions with substantial losses in lead and uranium.

Pidgeon *et al.* (1966) treated zircon in 2m NaCl at 500°C and 1kbar fluid pressure resulting in 61% lead loss and an insignificant loss of uranium.

Hansen & Friderichsen (1989) leached clear zircon containing 300ppm U in water (containing: 161ppm Ca, 2.2ppm Mg and 7.1ppm K) at 180°C for 600 hours with a reported resultant loss of 17% of the U and 15% of the Pb. Sinha *et al.* (1992) reported clear zircon developing surface pits and that extensive U and Pb loss can occur over relatively short periods (720h) at 600°C and 6 kbars.

Maslenikov & Kotov (1991) treated metamict zircon in 2M NaCl at 300°C and washed the grains in 15% HNO<sub>3</sub> at 80°C, resulting in a 9% loss of U and a 9% loss of Pb. When the samples were washed in 15% HNO<sub>3</sub> at 200°C the loss increased to 74% of the U and 98% loss of Pb. When leached at 600°C and washed at 200°C losses were 25% of the U and 96% of the Pb. After leaching at 300°C and washing at 200°C losses were 86% Pb and 55% U. The losses are accompanied by regeneration of the amorphous metamict zircon to crystalline zircon. Preliminary results using Na<sub>2</sub>CO<sub>4</sub> as the fluid medium show that sodium carbonate is far more effective than NaCl in reducing U and Pb in metamict zircon (Maslenikov *pers. comm.* 1991). U and Th reduction in a hydrothermal environment with the clear zircon concentrate from RBM has been completed at the Precambrian Institute in St. Petersburg, Russia. Structural transformation during the hydrothermal experiments have been measured by high temperature X-ray powder diffraction. The results will be submitted as a report to RBM.

Several workers have treated zircons with a variety of acids at different temperatures and pressures. Tilton (1960) reports zircon losing 15% Pb after 15 minutes in boiling 1:1 aqua regia. Steiger & Wasserburg (1966) recorded 2% Pb loss after 20 minutes in 35% HNO<sub>3</sub> at 80°C, followed

by 20 minutes in 10% HCl at 80°C and 20 minutes in 35% HNO<sub>3</sub> at 80°C. Chernyshev *et al.* (1987) treated zircon with 48% HF at 150°C for 18 hours, followed by 18 hours in 6N HCl at 210°C. Fragmented grains which were cemented by Th-rich cement broke up. When 1.6% of the zircon had dissolved, 20-30% of the U, Th and Pb entered the solution. If 10% of the zircon was dissolved 60-75% of the U, Th and Pb was removed. Finally, when 28% of the zircon was dissolved 75-80% of the U, Th and Pb was removed.

Tole (1985) treated 1g samples of cyrtolite (amorphous zircon milled down to 250µm-500µm) in pH 5 HCl-NH<sub>4</sub>OH fluid at 25°C, 60°C and 80°C from 42 minutes to 1507 hours. Initially high U values were recorded which decreased and leveled off with time in some of the samples, but other samples showed haphazard trends. Zirconium was not detected in the fluid, while silica was detected in increasing amounts with time in the fluid. This may corroborate the proposal of Woodhead *et al.* (1991) who considered that Zr ions are displaced and SiO<sub>2</sub> is displaced or tilted in position during metamictisation. The silica tetrahedra then forms a weakened silica structure which is prone to dissolution. Crystalline zircon was reported by Tole (1985) not to go into solution.

Acid treatment, especially using HF acid, is clearly the most effective and rapid method of reducing U and Th in zircon. However, the industrial use of HF is probably an unacceptable safety and environmental hazard. Hydrothermal methods involve long lengths of time and high pressures which may not be economically viable. Hydrothermal treatment on the clear zircon from RBM has been arranged, but the results are not, as yet, available.

### 6.1.3 EXPERIMENTAL LEACHING METHOD

Three leaching experiments using different acids and mixtures were performed at the Richards Bay Minerals laboratories. All the acid treatments were performed within a CEM microwave in 100ml teflon bombs.

Acids used were as follows:

1. 10ml of 48% Hydrofluoric with 0.5g of zircon (HF)
2. 5ml of 48% Hydrofluoric, 3ml 37% Hydrochloric, 2ml 65% Nitric with 0.5g of zircon (HF-*aqua regia* or HF AR).
3. 10ml of 65% Nitric with 0.5g of zircon (NITRIC)

Duplicate 0.5g samples of zircon concentrate NM were placed with 10ml of each acid in the teflon bombs and heated for 20 minutes at a pressure of 1205 N.m<sup>-2</sup>. Calculated temperature vs pressure curves at the RBM laboratories were poorly constrained but indicate temperatures of, or greater, than 150°C. The teflon bombs were slowly rotated within the oven with no mechanism of stirring. Under a binocular microscope the NITRIC samples exhibited no apparent to minor

dissolution surface textures. The HF and HF AR treatments showed dissolution features including an overall whitening of grains due to extensive pitting from the acid dissolution. Analyses of all three products for Y, REE, Th and U was performed with an ICP-MS. The results are tabulated on Table 6.01 and see Figure 6.01 for a comparison of the U and Th values. The leachates were not analysed, but U and Th values for the leachate were calculated from the values of the starting material and the treated product.

**TABLE 6.01:** Y, REE, Th and U results for the acid dissolution and air abrasion experiments.

Description: Sample #:	SOURCE ZC-B91 NM	ABRASION 4 ZCP-892	HF ZC-B91 NM	HF AB ZC-B91 NM	HF-AR ZC-B91 NM	HF-AR AB ZC-B91 NM
Y	1033.10	916.61	890.12	958.15	878.28	996.98
La	10.22	15.60	8.93	3.93	5.01	8.57
Ce	36.02	53.93	30.66	20.58	23.46	30.32
Pr	4.13	5.06	1.85	0.96	1.27	2.38
Nd	14.58	21.25	9.17	2.23	6.12	8.45
Sm	9.69	9.06	5.89	1.68	3.02	3.18
Eu	2.19	2.56	0.74	1.02	1.07	0.58
Gd	24.20	26.97	16.89	15.56	20.30	19.58
Tb	8.99	9.07	8.13	7.44	7.79	8.53
Dy	89.80	87.00	80.42	70.82	77.47	80.60
Ho	35.20	31.10	31.89	28.98	32.88	31.80
Er	142.69	132.63	124.36	109.46	132.23	128.90
Tm	27.59	25.58	25.10	23.95	25.17	23.04
Yb	244.75	231.15	233.03	216.28	241.86	218.07
Lu	50.28	45.69	47.38	42.57	48.33	44.78
Th	140.81	145.36	125.62	110.74	125.53	124.78
U	311.62	323.25	238.73	221.01	264.85	258.46
U/Th	2.21	2.22	1.90	2.00	2.11	2.07
U+Th	452.42	468.62	364.34	331.75	390.37	383.23
La/Sm	0.66	1.08	0.95	1.48	1.04	1.70
Yb/Gd	12.52	10.61	17.07	17.21	14.74	13.78
Ce/Ce*	1.33	1.45	1.72	2.48	2.18	1.59
Eu/Eu*	0.42	0.46	0.21	0.41	0.31	0.17

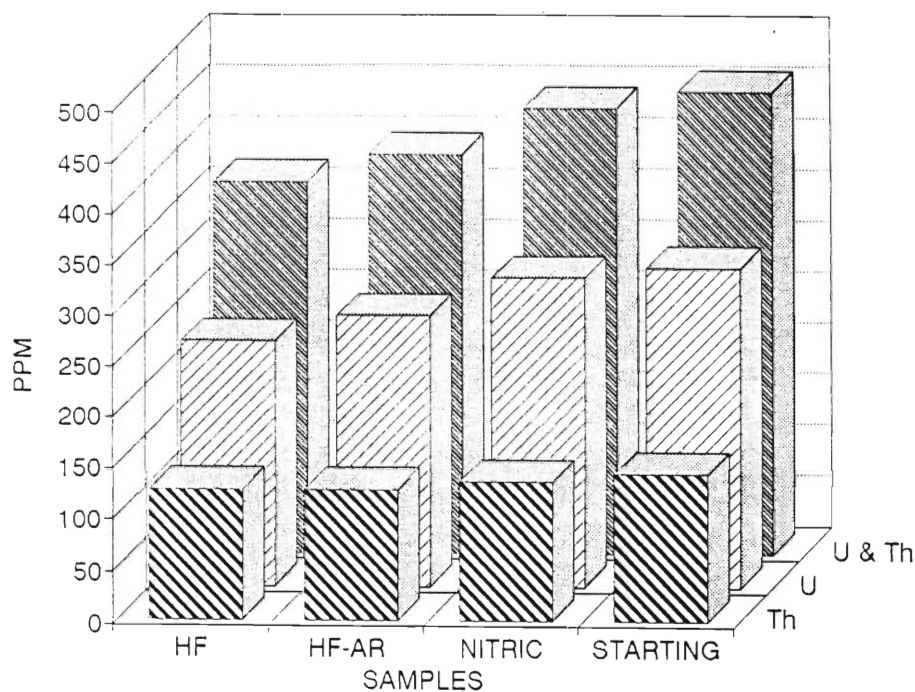


**FIGURE 6.01:** Comparison of U and Th concentrations in the starting material and the three acid dissolution experiments.

#### 6.1.4 LEACHING RESULTS

The NITRIC dissolution reduced the starting U concentration by 9.3ppm and Th by 7.9ppm. The HF AR dissolution resulted in a reduction of the U by 46.77ppm (15.01%) and the Th by 15.3ppm (10.9%) with a mass loss of about 6%. This is a very efficient means of reducing the U and Th concentrations. The dissolved material has calculated concentrations of U of 1044ppm and Th of 380ppm (U/Th: 2.75). The HF dissolution resulted in a reduction of the U by 72.9ppm (23%) and the Th by 15.2ppm (11%) with a mass loss of 16%. The dissolved material has calculated concentrations of U of 694ppm and Th of 221ppm.

The pure NITRIC treatment is not considered an efficient method of reducing U and Th. In HF and HF AR treatments U is removed to a greater degree than Th. The difference in Th reduction between the HF and HF AR leachings is negligible. The dissolved material from the HF AR leaching has far higher values for U and Th than the HF leaching, which suggests that in addition to the dissolution of the high U and Th domains the HF is also dissolving low U and Th material.

The REE profiles for the leaching experiments are plotted in Figure 6.02. The REE profiles are a useful tool in understanding the effects of dissolution. The HREE are reduced by 0 and 17ppm,

results not noticeable on the logarithmic chondrite normalised profiles. The HF leached product has the greatest reduction of LREE. The LREE, excluding Ce, show losses between 25 and 53% with an average of 42%. In comparison Ce is only reduced by 11%, while the HREE losses are between 0% and 26% with an average of 10.6%. The Ce positive and the Pr negative anomalies become more prominent with acid leaching. The La, Pr and Nd values are lowest in the *aqua regia* leaching product. The La/Sm value is 0.29 for the *aqua regia* leach product.

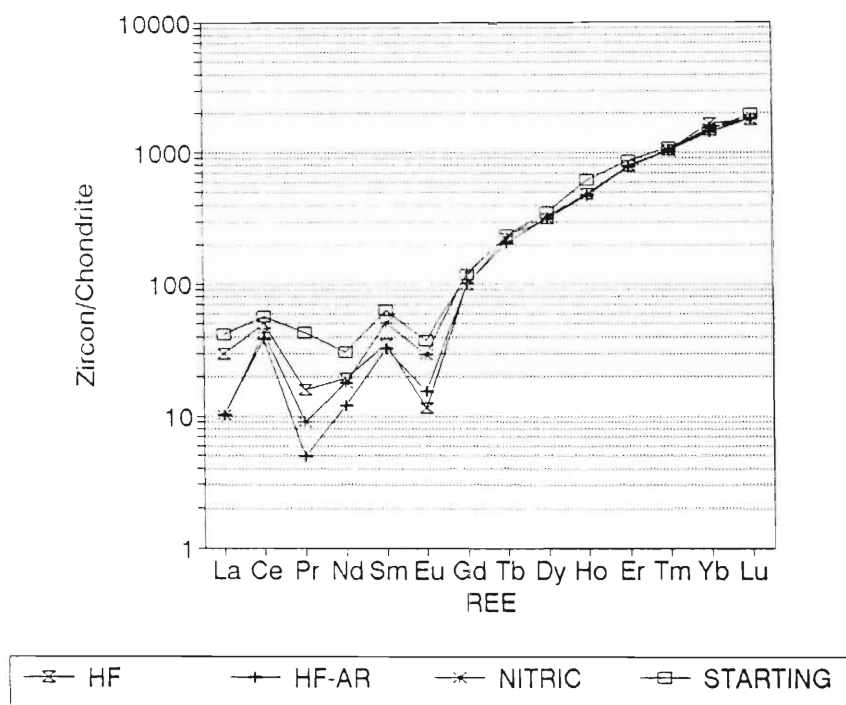


**FIGURE 6.02:** Chondrite normalised REE profiles of the starting material and the three acid dissolution products.

### 6.1.5 SEM PHOTOGRAPHS OF EXPERIMENTALLY LEACHED ZIRCON

SEM photomicrographs of the HF leached zircons show several different textures related to dissolution.

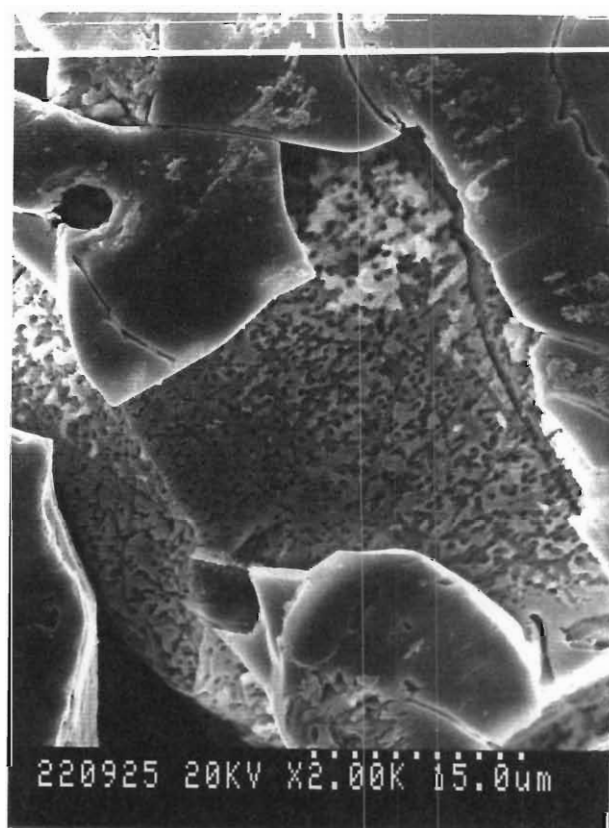
Plate 6.01 (SEM 220925) shows a close-up of a zircons surface. The outer rim shows no dissolution except along cracks. Below the unpitted surface two severely pitted remnant layers are evident above a less pitted layer.

Plate 6.02 (SEM 220914) shows a grain that has been dissolved with the preferential loss of certain zones within the zircon. This is also apparent in the magnified portion of Plate 6.02 in Plate 6.03 (SEM 220909) and the close-up Plate 6.04 (SEM 220926). In Chapter 4 the reasons for the zoning are explained. The alternating zones of the oscillatory zoned zircons are low impurity zircon followed by high impurity zircon. The high impurity zircon will be very enriched in U compared to the low impurity zircon. The high U zones will have a higher degree of metamictisation which results



in a zone that is more susceptible to chemical attack than the neighbouring zones.

Plate 6.05 (SEM 220911) is a close-up showing a sponge-like severely dissolved surface. Plate 6.06 (SEM 220912) is a S18-S19 zircon according to Pupin's (1980) classification which shows increased dissolution along the traces where abrasion has occurred in the past. Plate 6.07 (SEM 220910) shows the surface of a zircon grain and a smooth bottomed surface pit that is now empty. In the unleached zircon these pits are usually filled with clay minerals and iron coatings that are difficult, and sometimes impossible, to remove by low-concentration acid washing, acid washing in ultra-sonic baths or by acid boiling. The HF treatment has removed all the filling from the surface pit.



**PLATE 6.01:** A SEM photomicrograph close-up of HF-pitted zircon, with a resistant rim.(SEM 220925).

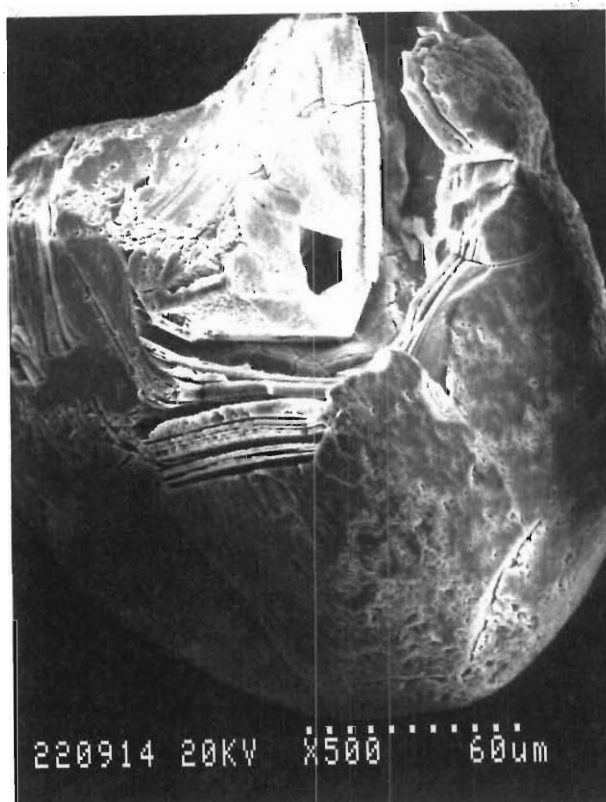


**PLATE 6.02:** A SEM photomicrograph showing the preferential loss along alternating zones in the interior of a zircon from HF dissolution (SEM 220914).

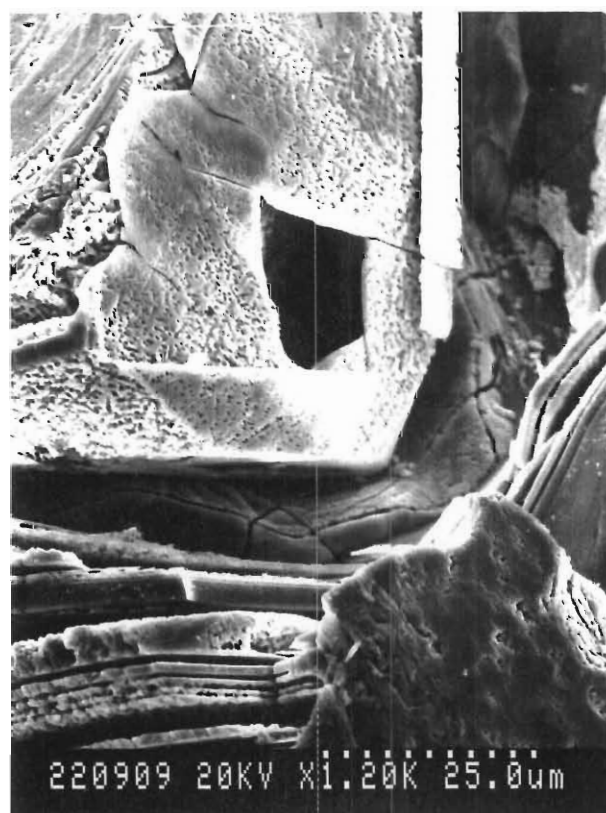


**PLATE 6.03:** A SEM close-up of PLATE 6.02 clearly showing the dissolution along alternating zones (SEM 220909).

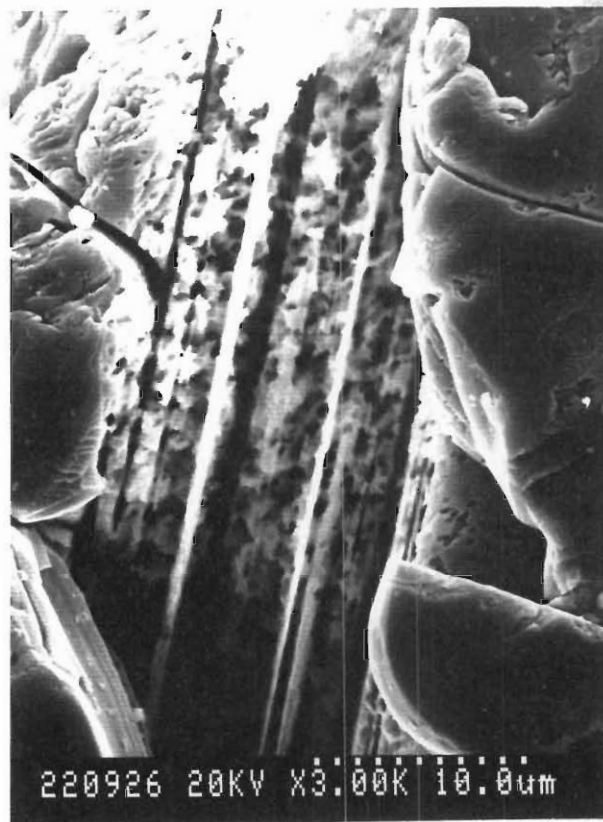


PLATE 6.04: A SEM photomicrograph of the interior of a zircon showing the preferential dissolution of alternating zones (SEM 220926).

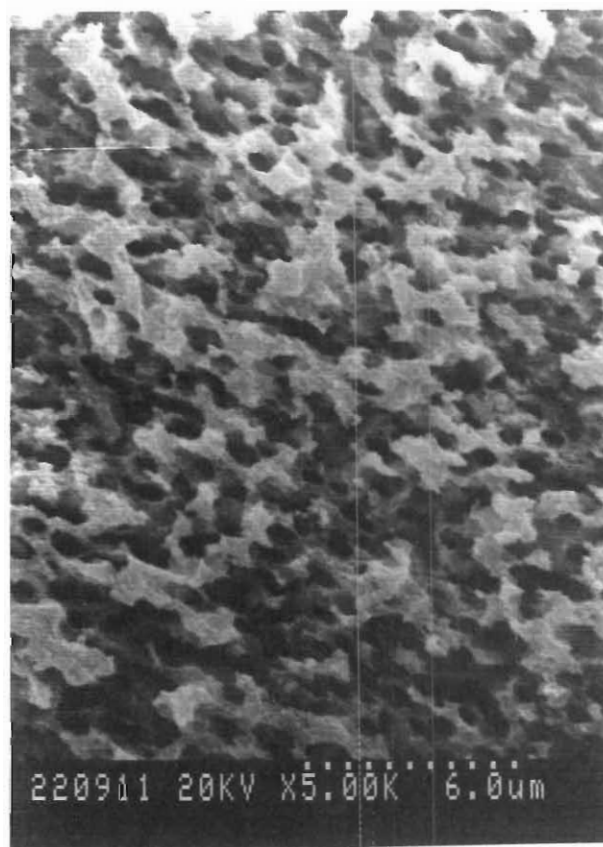


PLATE 6.05: A SEM photomicrograph of the pitted surface of a zircon after HF dissolution (SEM 220911).

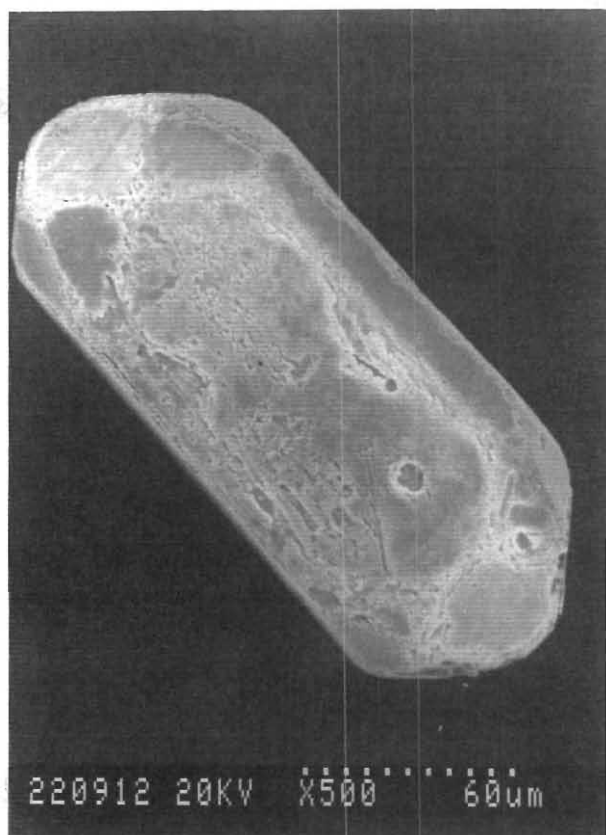


PLATE 6.06: A SEM photomicrograph of a S18-S19 zircon which shows increased dissolution along the traces where abrasion has occurred in the past (SEM 220912).

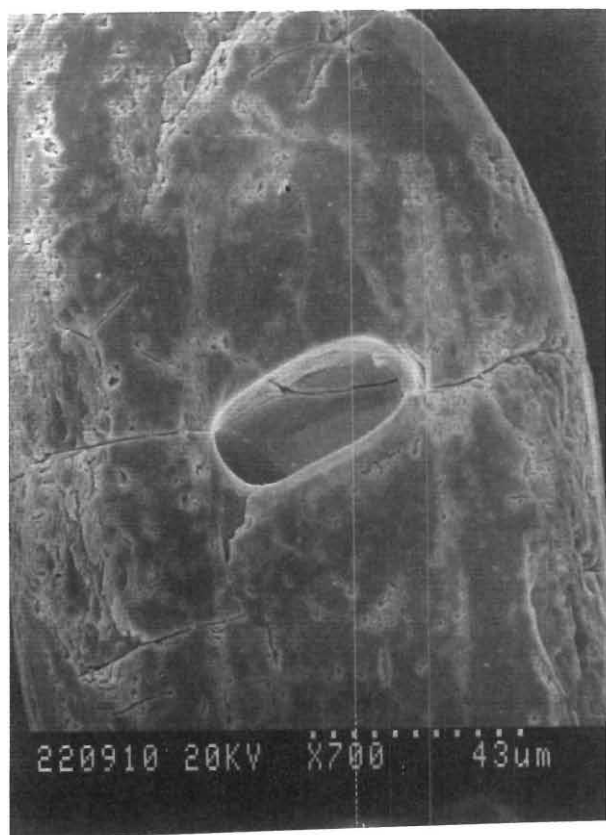


PLATE 6.07: A SEM photomicrograph showing the smooth-empty pit the was most likely filled with clay before HF partial dissolution (SEM 220910).

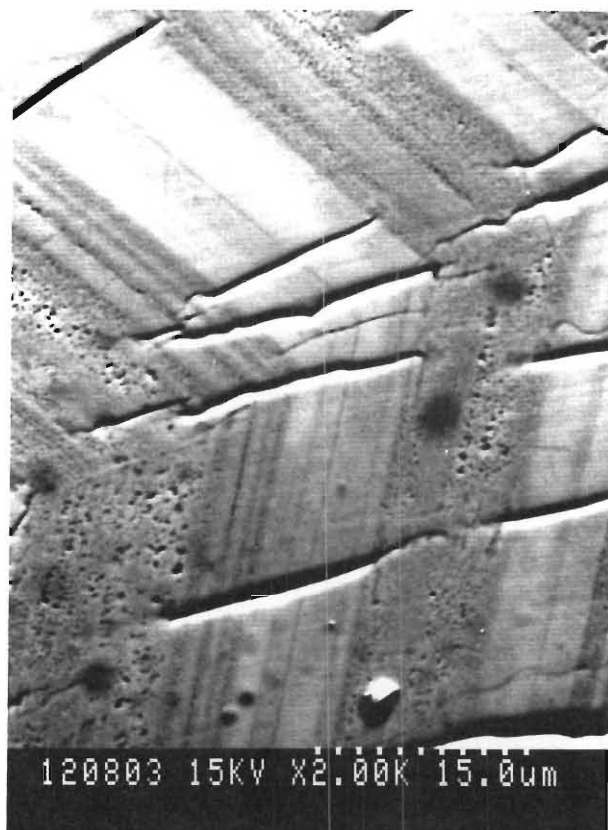


PLATE 6.08: A SEM photomicrograph of a naturally leached zircon. The darker zones show preferential leaching compared to the light zones (SEM 120803).

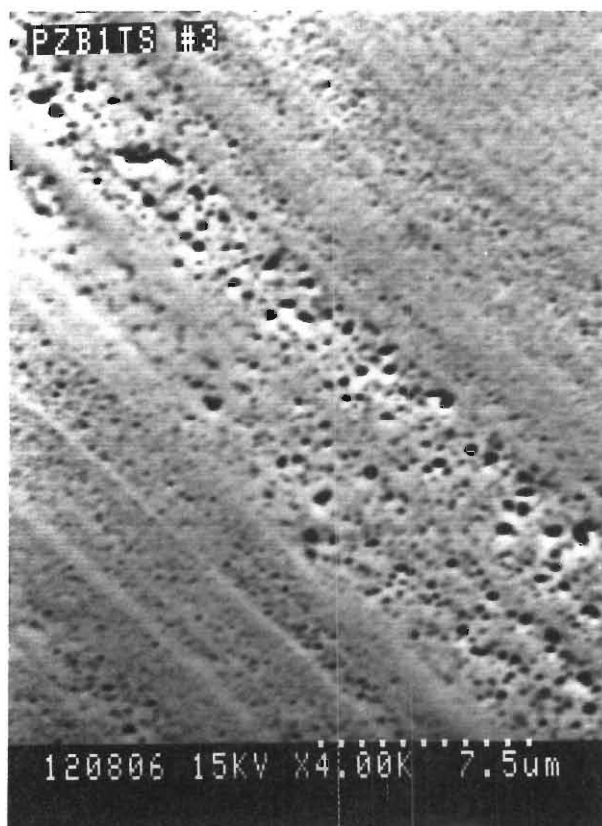
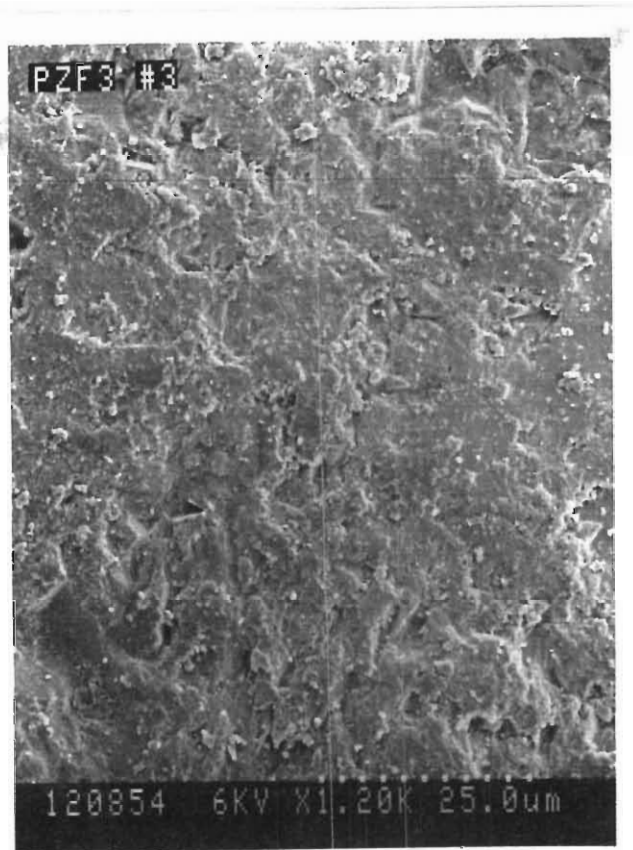
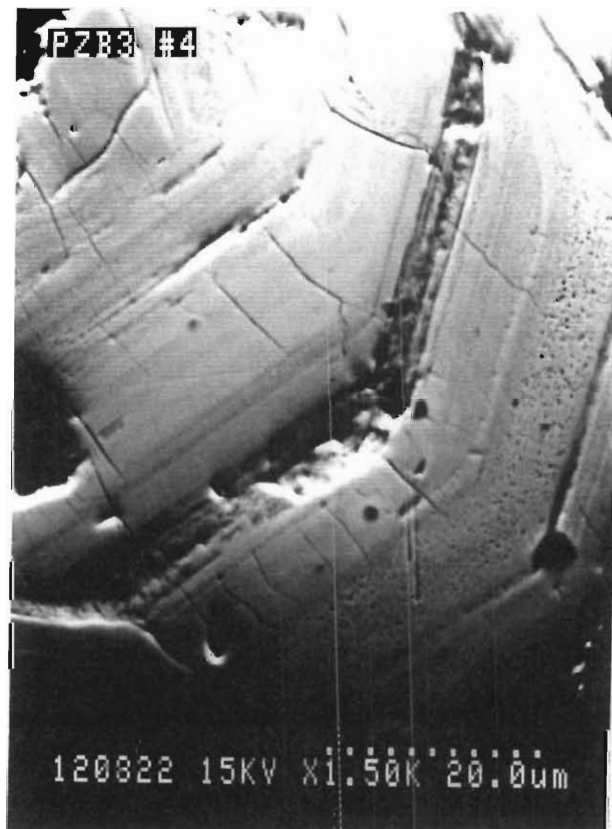


PLATE 6.09: A SEM photomicrograph of naturally leaching in metamict zircon (SEM 120806).



**PLATE 6.10:** A SEM photomicrograph of the naturally pitted surface of the grain in Plate 6.07 and 6.08 (SEM 120854).



**PLATE 6.11:** A SEM photomicrograph of pitting in alternating zones superimposed on the sector growth zones of a metamict zircon (SEM 120822).

### 6.1.6 SEM EVIDENCE FOR NATURAL LEACHING OF ZIRCON

One hundred and fifty unleached natural zircons were mounted in epoxy and polished to reveal the cores of the grains. Backscattered electron imagery (BSE) with a Hitachi-30 SEM was used to identify differences in atomic density related to the chemical composition of different zones and inclusions in zircon. The BSE image shows the difference of atomic density and atomic mass ( $Z$ ) with varying shades of grey. The higher the density or the average atomic mass ( $Z$ ), the lighter the shade of grey. The more metamict zones have higher  $Z$  but lower density which therefore show up as a lighter shade of grey.

In metamict and partially metamict zircon the preferential loss of material in alternating zones was apparent. Plate 6.08 (SEM 120803) and Plate 6.09 (SEM 120806) clearly show pitting in alternating zones (from 0.4 to 4.7  $\mu\text{m}$  wide). The surface of this zircon also exhibited pitting which is apparent in Plate 6.10. The semi-metamict sector zoned zircon in Plate 6.11 (SEM 120822) also shows several zones with pits. An interesting feature in Plate 6.08 is the radial expansion cracks in the less-ductile less-metamict zones. These cracks result from expansion during metamictisation of the more metamict amorphous and ductile zones (pitted). The proof for increased elasticity in the pitted zones is proven by the fact that even though stress originates from the expanded zones in the core of the grain, the incompetent pitted zones do not crack. The competent zones further from the core crack, due to stress from the sum of stress of all the expansion in zones below that particular zone.

The natural pitting and the expansion cracks act as conduits and assisted the dissolution of the zircon during the experiments. The metamict zircons therefore have increased solubility and will be preferentially dissolved. Zircon that crystallized under non-equilibrium conditions will have growth oscillatory zoning (which is unstable according to Pidgeon (1992)). The alternating concentration or depletion of U and Th in successive layers increases the metamictisation of the enriched zones. Acid leaching will attack and preferentially dissolve the weakened partially metamict U- and Th-rich zones.

Chakoumakos *et al.* (1987) and Wayne and Sinha (1992) both identified expansion cracks in clear oscillatory zoned zircon. BSE imagery indicated that the light high  $Z$ -number zones expanded and the dark low  $Z$ -number zones cracked. The BSE imagery results of Wayne and Sinha (1992) are opposite to the results obtained above. The difference may be explained either by the fact that in metamict zircon the zones with the highest damage and therefore lowest density were the zones that expanded; or the numerous pits are adding a topographic effect resulting in a darker image.

## 6.2 ABRASION EXPERIMENTS

The efficiency of abrasion in reducing U and Th in zircon depends on the quantity of metamict and cyrtolite zircon grains, which are softer than clear crystalline zircon, and the distribution of U and Th within the clear zircon grains. The fission track mapping of individual zircons from the RBM product show a clear trend of U enrichment in the rims and pyramid faces (See Chapter 4). The removal of the rims and pyramids by abrasion will result in a small loss of mass with a corresponding large loss in U and Th.

### 6.2.1 ABRASION EXPERIMENTS IN THE LITERATURE

Air abrasion mills remove surface material from zircon by percussive impact between the grains and with the mill wall. In some cases emery or diamond is used to coat the walls to increase the abrasion potential of the walls. The literature describes several techniques of grinding and polishing for the production of spheres (eg. Krogh, 1982a; Aleinikoff *et al.*, 1990; Paranto and Patton, 1981).

Krogh (1982a) designed an air abrasion technique to abrade the softer U- and Pb-rich surface areas and remove the softer metamict grains and cracked grains (See Table 6.02 for parameters). The apparatus is designed for abrading very small samples of between 0.5 and 100mg zircon. Krogh (1982a) specifies two techniques of abrasion. The first technique used the impact of grains with the abrasion mill walls to remove the outer layers. The surfaces of the grains processed by this technique tended to be chipped. The velocity of the air, which is controlled by air pressure and the number of air inlets and outlets, determines if the grains break or polish. In most cases all pre-cracked grains were removed from the sample. A second method was devised by Krogh (1982a) to reduce the chipping effect and create a more polished grain surface. Small samples of zircon were mixed with pyrite and placed in the air abrasion mill. The grains of the product of this technique are shiny and elliptical. Archaean zircons after abrasion had similar or less uranium than the unabraded zircon. Krogh (1982a) reports 12 to 54% reductions of common lead in samples abraded in an air abrasion mill.

Aleinikoff *et al.* (1990) used an abrasion chamber similar to that developed by Krogh (1982a). Very few grains were broken during abrasion without a pyrite abrasive. Grains with elongation ratios of 5 to 6 only had their tips and edges rounded. The elongate grains became lozenge shaped during abrasion and the rounded grains became spheres.

Corfu and Ayres (1984) used Krogh's (1982a) air abrasion technique on zircons from hornblendites, granodiorites and felsic dykes. In samples from the hornblendite the U values increase from 579 to 966ppm, an increase of 67% with abrasion. A sample of brown zircon from the felsic



dyke shows a 28% increase in U from 819 to 1047ppm. In the case of the granodiorite the clear zircon's U level decreased by 36% from 123 to 79ppm following air abrasion. Those zircon grains which showed an increase had U enriched cores. Fission track mapping of the zircons from the northern Natal coast, showed that several grains exhibit enriched cores or have inclusions enriched in U. The overall success of abrasion on a heterogeneous zircon product depends on the predominance of rim enriched over core enriched grains.

The effect of abrasion described in the literature depends on the history of the rock from which the zircons originated. The zircon from an individual igneous rock unit will either have U enriched rims, have an earlier U enriched core, a homogeneous or an oscillatory/sector zoned distributions of U. Individual igneous rock units rarely have a mixed population of zircon. The RBM deposit of detrital zircon has a diverse provenance. From fission track work it emerged that the zircon grains are enriched in U and Th in the rims and pyramid growth zones.

**TABLE 6.02:** Parameters of abrasion methods described in the literature.

NAME	DIMENSIONS Depth & Diameter	AIR PRESSURE (kPa)	MASS (mg)	TIME (m)
Krogh (1982a)	0.7-3.8	13.8-69.0	30-50	VAR.
Aleinikoff et al.(1990)	1.5-5.0	13.8-20.7	2-20	5-45

## 6.2.2 NATURAL ABRASION IN THE LITERATURE

In aeolian environments small grains usually show little evidence of abrasion features. Aeolian abrasion experiments show that abrasion decreases rapidly with decreasing grain size and is insignificant in grains below 150 $\mu$ m (Kuenen, 1960).

Percussion marks due to collision and the structure of quartz are a microtexture regarded by Margolis and Krinsley (1971) to be indicative of aeolian abrasion. They duplicated this feature with a silt abrasion experiment. A 35cm long 12cm circular plastic wind tunnel was used with wind velocities of 8 to 32 km/h. The grains were adhered to the chamber walls. Suspended abrasive coarse silt (less than 62 $\mu$ m) moved around the outside of the chamber abrading the quartz grains. After 2 hours the grains developed similar surface features to abraded desert sand grains.

## 6.2.3 ABRASION METHODS

From the literature survey of abrasion of zircons and the results obtained by fission track analysis, abrasion seemed a potential method for reducing the U and Th values of zircon. Three types of abrasion apparatus were used and evaluated:

- 1) Slow Tumbler (liquid) (30rpm) (see Plate 6.12)
- 2) Fast Attrition Cell (liquid) (300rpm) (see Plate 6.13)
- 3) Air Abrasion Mill (air) (100-200kPa) (see Plate 6.14)

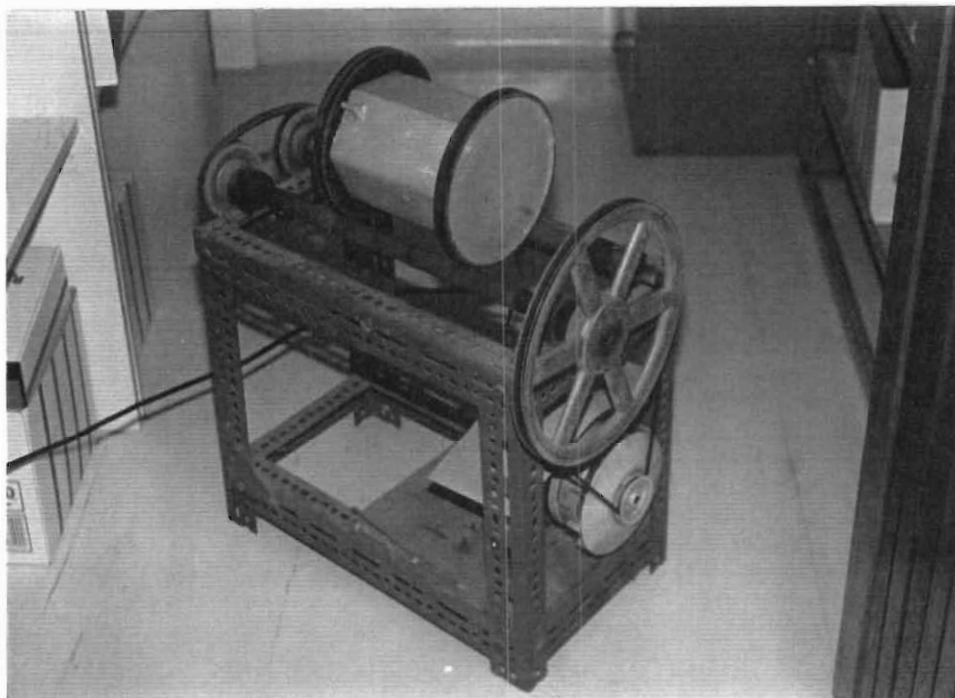


PLATE 6.12: The slow-speed tumbler used in the wet abrasion experiments.

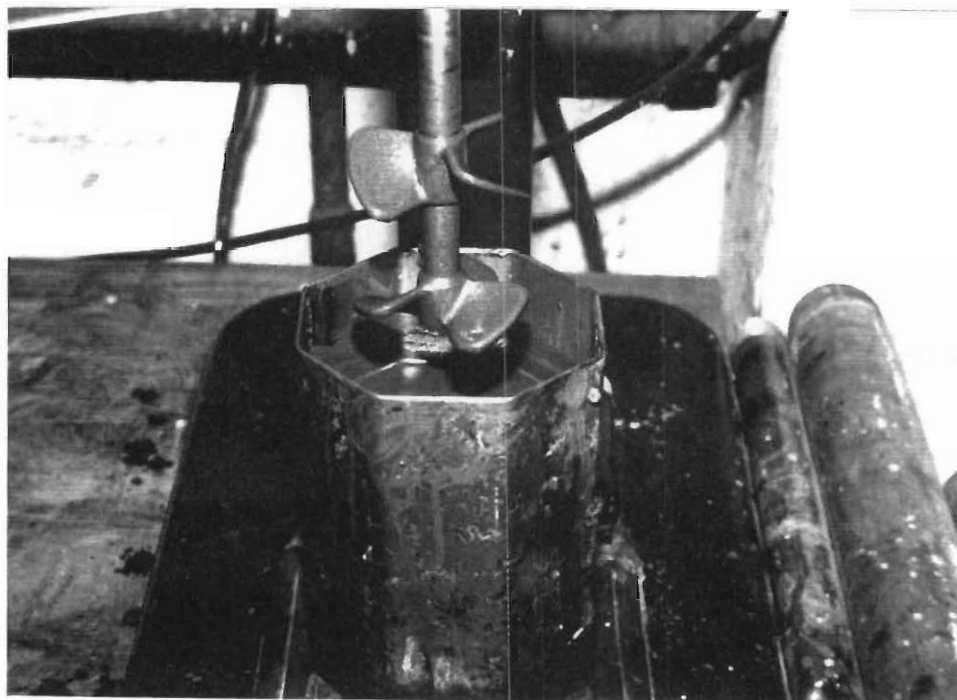
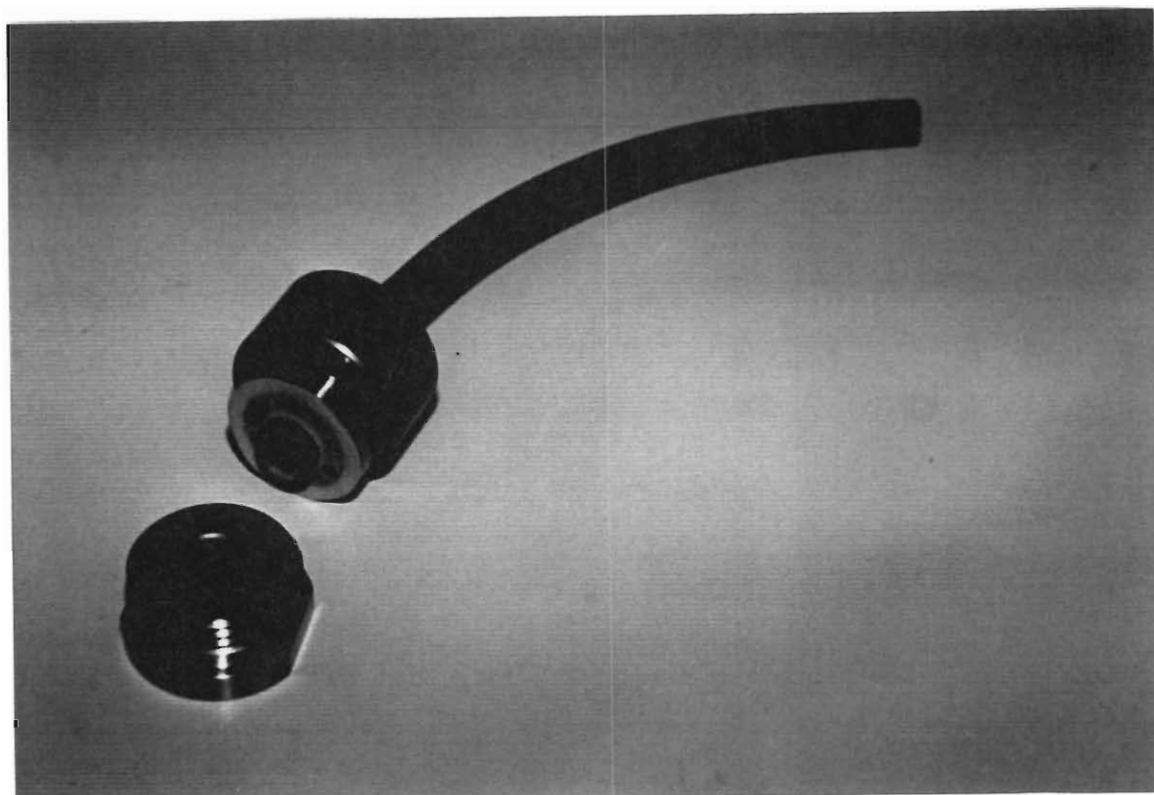


PLATE 6.13: The high-speed attrition-cell used in the wet abrasion experiments.



**PLATE 6.14:** The air-abrasion mill used in the air abrasion experiments. Designed after Krogh (1982a).

#### **6.2.3.1 SLOW TUMBLER (LIQUID)**

A tumbler was repaired and run at 30rpm. The tumbling chamber was hexagonal with a diameter of 14cm and a length of 20cm. The chamber was lined with hard rubber. One kilogram of RBM zircon concentrate and half a litre of water were placed in the chamber to form a slurry. The volume ratio of zircon to water was 1 : 2.3, and the mass ratio zircon to water was 1 : 0.5. A sample was taken after 67 hours (120600 revolutions) and again at 125 hours (225000 revolutions). The grains were examined under a low power binocular microscope and the grains showed no sign of increased abrasion. Effective tumbling thus probably requires very long periods.

#### **6.2.3.2 FAST ATTRITION CELL (LIQUID)**

A hexagonal chamber made of stainless steel was used as the chamber. The propellers rotated at 300rpm. The two propellers are fitted so that they oppose one another resulting in a turbulent action. The first experiment involved 1300g of zircon concentrate product mixed into a slurry with 700ml of water. The volume ratio was 1 : 2.5 and the mass ratio was 1 : 0.54. The sample was stirred for 5 hours and 15 minutes (94500 revolutions). Samples were extracted every hour. The samples exhibited no increase in abrasion features under the binocular microscope.

To increase the abrasion potential of the attrition cell a slurry of 0.700kg of zircon concentrate product and 0.750kg of #400 grain polishing corundum were mixed into a slurry with 700ml of water. The result was a slurry with a volume ratio of 1 : 1.3 : 4.7 respectively and a mass ratio of 1 : 1.1 : 1 respectively. The sample was stirred for 8 hours or 144000 revolutions. The corundum with lower

density and smaller grain size than the zircon was then separated from the zircon using a superpanner. No increase in abrasion textures were apparent when the product was viewed under a low power binocular microscope.

The starting material, zircon concentrated product, has a U concentration of 381ppm and Th concentration of 182ppm. The abraded product has a U concentration of 348ppm and a Th concentration of 274ppm. The increase of 92.44ppm in Th is difficult to explain. One possibility is that the density separation concentrated monazite in the analysed sample.

### 6.3.3.3 AIR ABRASION

Air abrasion (Plate 6.14 and Plate 6.15) was performed in an air abrasion mill with the same parameters as the mill designed by Krogh (1982a) to reduce discordance in dating zircon. Air abrasion is more effective than water or fluid abrasion due to the momentum of the grains being more significant in a low density regime. Another important factor contributing to abrasion in an air medium is the high spin rate of the entrained grains resulting in glancing blows of high energy when grains collide with one another and with the chamber's walls. Chepil (1945) observed spin rates of grains of 200 to 1000 revolutions per second (rps); and White (1982) reported mean spin rates of 350 to 400 rps in wind.

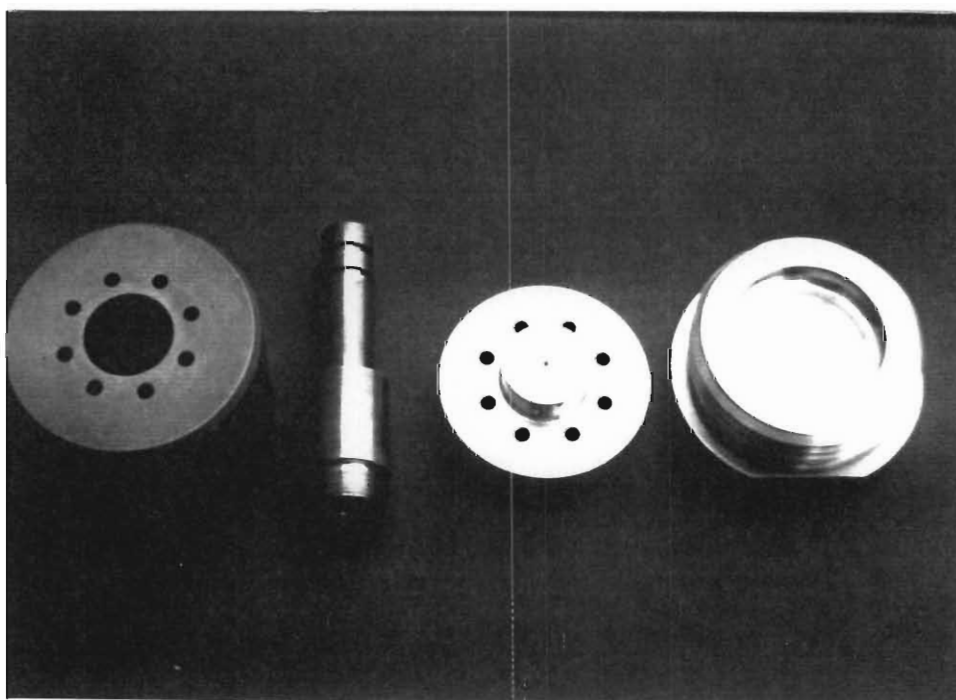


**PLATE 6.15:** The components of the air abrasion mill, made to the same parameters as the mill used by Krogh (1982a) for decreasing the discordance of dated zircons.

An air compressor with an air pressure regulator was connected to the mill. Teflon filters with a grid size of 0.015mm were used in all the air abrasion experiments. All the zircon/monazite fragments less than 0.015mm (15 $\mu$ m) were therefore exhausted from the abrasion mill. Aleinikoff *et al.* (1990) found that the exhausted dust from air abrasion is usually less than 2 $\mu$ m in diameter. The pressure was regulated, with an error of 10 kPa, between 100 kPa and 200kPa, and was applied from 10 to 60 minutes for the various experiments. The amount of abrasion is dependent on the mass of the sample, the pressure of the air supply (which is directly related to the velocity of the air in the abrasion chamber), and the relative hardness of the grains within the chamber. A pressure which is too high or a sudden increase in the supplied air pressure results, in the shattering of grains. To reduce the shattering of the grains the pressure was gradually increased to the required level.

After initial experimentation with pressures, sample size and time, six samples were abraded (Table 6.03).

**TABLE 6.03:** Air abrasion experiment parameters and mass losses.

SAMPLE #	STARTING MATERIAL	MASS (mg)	TIME (m)	PRESSURE (kPa)	MASS LOSS (%)
1	ZCP	74.703	45	100-110	5.4
2	ZCP	56.409	45	100-110	5.6
3A	ZCP	81.140	60	180-200	60.5
3B	ZCP	81.359	60	180-200	99
4	ZCP	85.294	54	140-150	13.8
5	ZC(HF)	130.057	20	180-200	6.3
6	ZC(HF AR)	125.969	20	180-200	4.7

The metamict zircons within the samples that had been acid leached were found to be brittle when hand-picked for SEM-imagery. The grains often shattered when gripped lightly with tweezers. These samples were abraded to establish if the high U grains that had been attacked by the acid, preferentially broke down compared to the crystalline zircon.

#### 6.2.4 AIR ABRASION RESULTS

Abrasion samples #4, #5 and #6 were analysed for trace elements on the ICP-MS (See Table 6.01). Sample #3A failed to dissolve during the preparation for ICP-MS analysis and #3B was lost during abrasion.

Sample #4 was from the zircon concentrate product. The starting zircon was analysed and has U and Th values of 381ppm and 182ppm respectively. Calculations from the LREE profiles show that the sample contains a minimum of 0.03% monazite. Sample #4 was abraded with a mass loss of 13.8% and the U was reduced by 15% and Th by 20%.

Calculations from the LREE show that, of the 13.8% removed by abrasion, 0.026% of the abraded material was monazite. The RBM monazite product has U and Th concentrations of 2770ppm and 41222ppm respectively. The removal of the monazite results in a 11ppm loss of Th and

a 0.7ppm loss of U.

The remaining material that was removed by abrasion has a calculated concentrations of 738ppm U and 330ppm Th. The high U and less high Th values indicate that there was significant abrasion of metamict zircons and U enriched rims.

Dana and Harlbut (1959) show that resistance to abrasion in a air medium increases with hardness. Crystalline zircon has a Moh hardness of 7.5. Metamict zircon has a lower hardness due to its amorphous state and monazite has a Moh hardness of 5. Micro-indentation hardness for clear zircon is 841 to 1468 kg.mm<sup>-2</sup> and metamict zircon is 485 to 841 kg.mm<sup>-2</sup> according to Speer 1980). Therefore monazite and the metamict grains are abraded to a greater degree than crystalline zircon. From the data of Dana and Harlbut (1959), zircon has a relative resistance to abrasion of 8.2 and monazite 5.9. Clear zircon is therefore 1.4 times (resistance to abrasion<sub>zircon</sub>/resistance to abrasion<sub>monazite</sub>) more resistant to abrasion than monazite. Due to the equivalent size and density of zircon and monazite the differences in momentum are negligible.

The calculated U/Th value of material removed in the air abrasion experiment #4 is 1.6, which is lower than the 2.1 of the starting material and clearly demonstrates the removal of monazite which has a U/Th value of 0.07. The zircon concentrate product has a U/Th value of 2.10, and with the removal of the monazite the abraded products ratio increases to 2.22. Calculating the ratio of the abraded material, less the 0.026% monazite, gives a high U/Th value of 2.23. The abraded material, less the monazite, has a U/Th equivalent to the clear zircon product of 2.23. The REE profile of the abraded ZCP (Figure 6.03) is similar to the profile of the zircon concentrate NM profile in Figure 6.02.

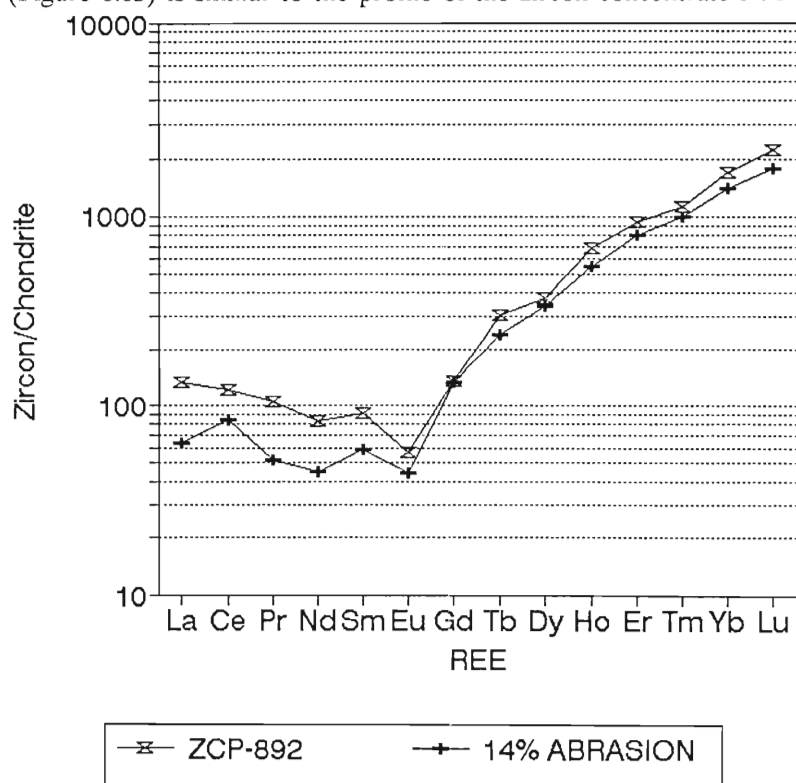


**FIGURE 6.03:** Chondrite normalised REE profiles of the starting material ZCP and the abraded product.

Abrasion experiments #5 and #6 were performed on acid leached zircon of the zircon concentrate (Table 6.01). Table 6.04 summarises the U and Th losses for the acid dissolution and air abrasion experiments. Sample #5 was leached in concentrated HF which resulted in a loss of 73ppm U and 15ppm Th accompanied by a 16% loss of mass (see Figure 6.04). Abrasion removed a further 6.3% mass of the acid leached product with a resultant total mass loss of 21.3%. The material removed by the acid has calculated concentrations of 694ppm U and 221ppm Th with a U/Th value of 3.14. The leached product has U and Th values of 239ppm and 126ppm respectively. The samples were air abraded removing a further 18ppm U and 15ppm Th. The 6.3% material removed by air abrasion has calculated concentrations of 502ppm U and 347ppm Th with a U/Th value of 1.45.

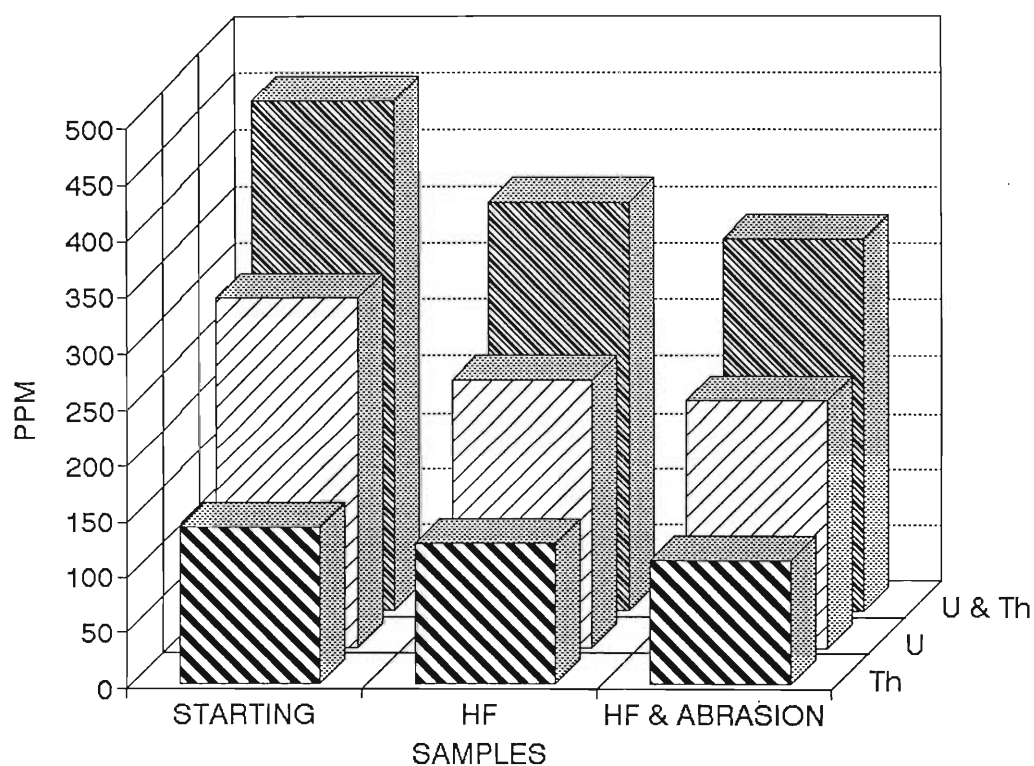


**FIGURE 6.04:** Comparison of U and Th concentrations in the starting material, HF acid treated material and the abraded and HF acid treated material.

TABLE 6.04: Air abrasion results for the acid leached zircon.

Sample #	Treatment Type	Mass Loss(%)	Element loss		U(ppm)	Th(ppm)
			U(%)	Th(%)		
5	Non-Treated	--	--	--	312	141
5	HF-Leaching	16	23	11	239	126
5	Removed Material	--	--	--	694	221
5	Air Abrasion	6	29	21	221	111
5	Removed Material	--	--	--	502	347
5	Sum of Treatments	21	29	21	221	111
5	Total Removed Material	--	--	--	654	254
6	HF-AR Leaching	6	23	11	265	126
6	Removed Material	--	--	--	1044	380
6	Air Abrasion	6	29	21	259	125
6	Removed Material	--	--	--	394	141
6	Sum of Treatments	12	29	21	259	125
6	Total Removed Material	--	--	--	895	352

Sample #6 had 25% less material abraded from the grains than sample #5 due to the greater dissolution effect and resultant decrease in grain strength of sample #5. The concentrated HF-*aqua regia* acid treated sample resulted in the loss of 47ppm U and 15ppm Th with an accompanying mass loss of 6% (see Figure 6.05). The material removed by the acid leaching has calculated concentrations of 1044ppm U and 380ppm Th with a U/Th value of 2.75. The leached product has U and Th values of 265ppm and 126ppm respectively. Air abrasion removed a further 6ppm U and 0.75ppm Th. The 4.7% material removed by air abrasion has calculated concentrations of 394ppm for U and 141ppm for Th with a U/Th value of 2.80.

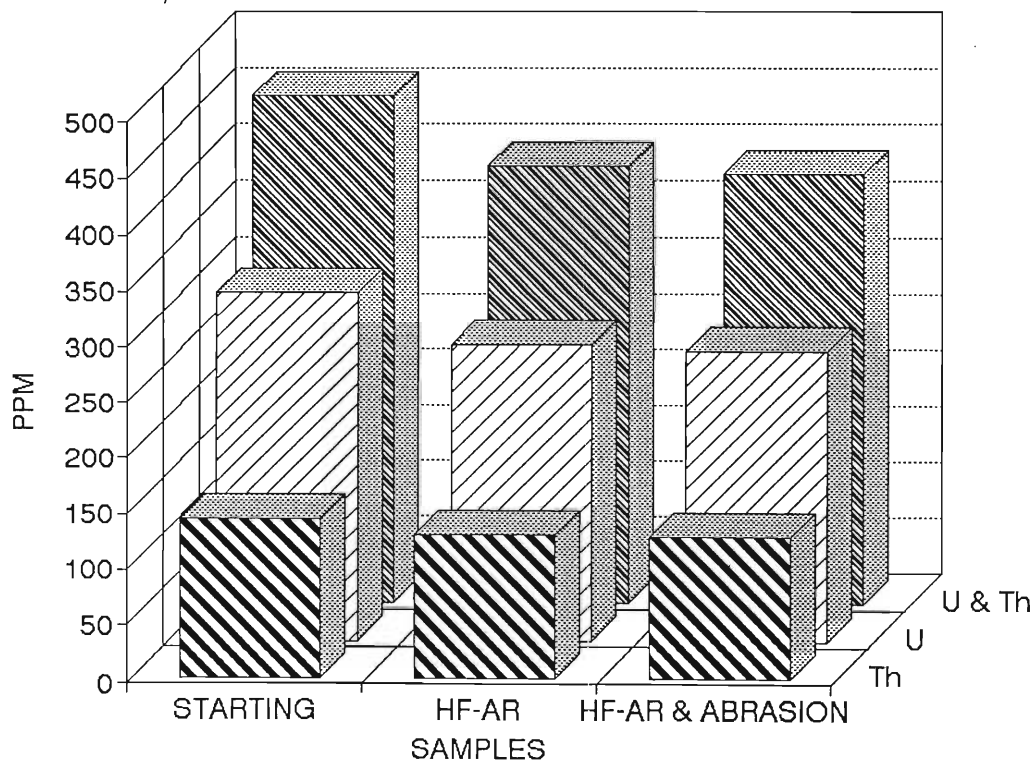


FIGURE 6.05: Comparison of U and Th concentrations in the starting material, HF-AR acid treated material and the abraded and HF-AR acid treated material.



Figures 6.06, 6.07 and 6.08 are plots of element loss corrected for mass loss. Figure 6.06 shows the effect of HF acid dissolution and the effect of abrasion of the partially dissolved product.

The acid dissolution results in a large reduction of Pr, Nd, Sm, Eu and smaller losses of Y, Th and U. U is lost to a greater degree than Th. The abrasion results in large losses of LREE with a positive Ce anomaly, the Ce anomaly is evidence for the Ce/Ce' anomaly common in zircon. The Y is not decreased at all, and Th is decreased to a greater extent than the U. The profiles indicate an initial loss of Y- and U-rich zircon by acid dissolution followed by the loss of monazite by abrasion. The profile would be obtained by partially dissolving the metamict zircon (U-, Y- and LREE- rich compared to the clear zircon) and the U-rich zones of the clear zircon.

HF-*aqua regia* partial dissolution (Figure 6.07) has a different effect on the trace elements of the zircon concentrate. The initial acid dissolution profile is similar to the final HF + air abrasion profile in Figure 6.06. The HF-*aqua regia* may dissolve monazite or metamict zircon with greater efficiency than HF. Though the Y-Th-U profile is similar to the HF dissolution profile. The effect of abrasion on the LREE profile of the HF-*aqua regia* partially dissolved product is difficult to explain: La, Ce, Pr, Nd and Y are all enriched compared to the dissolution product. The air abrasion effect on the profile of the zircon concentrate product (Figure 6.08) can be explained by the fact that at least 75% of the LREE in ZCP are derived from monazite. Monazite is abraded to a greater degree than zircon. 14% mass loss by abrasion would remove most of the monazite.

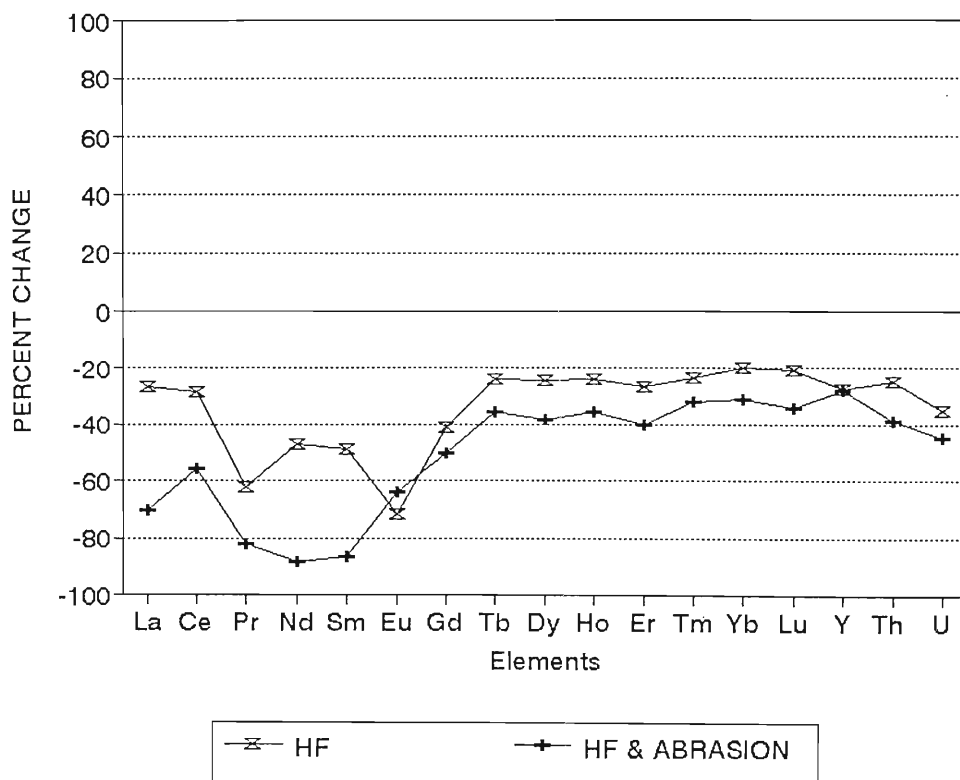


FIGURE 6.06: Element loss profile corrected for mass loss of the HF acid treated and air abraded products.

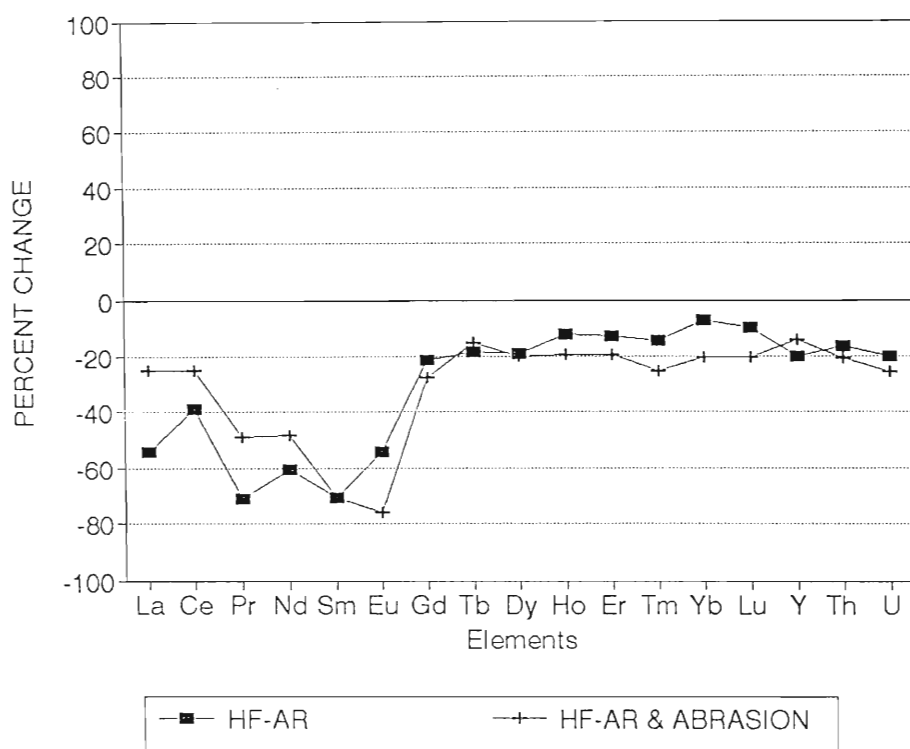


FIGURE 6.07: Element loss profile corrected for mass loss of the HF-AR acid treated and air abraded products.

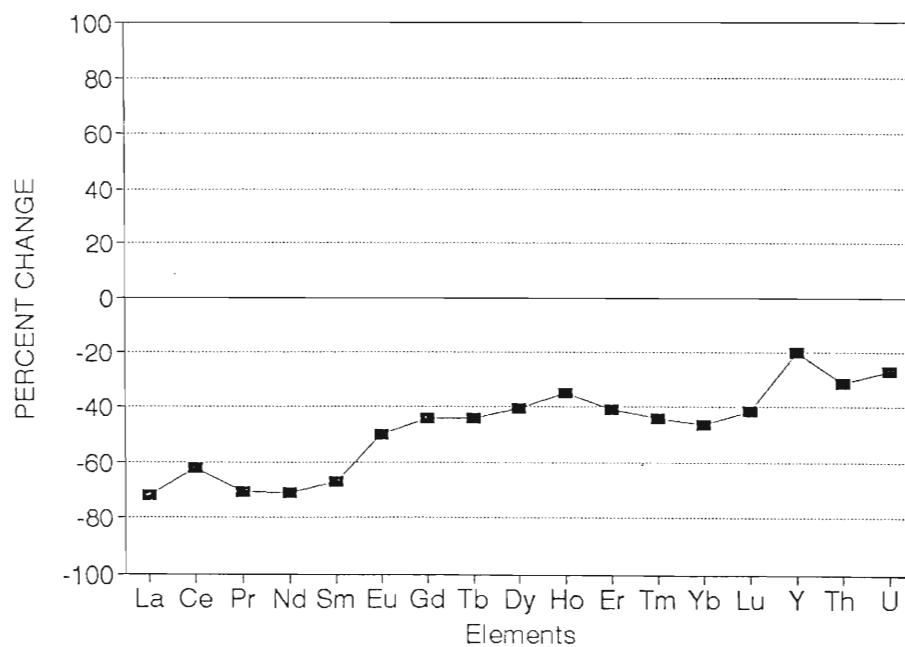


FIGURE 6.08: Element loss profile corrected for mass loss of the air abraded product.

Sinha *et al.* (1992) analysed alternating zones in a zircon that were identified by differences in brightness by BSE imagery. Two type of zones are evident, Hf-U rich zones and Th-Y-HREE rich zones. The Hf-U rich zones has 1.4 to 2 times the concentration of U and Hf than the Th-Y-HREE rich zones. The Th-Y-HREE rich zones have enrichments of 4 to 6 times the Th, Y and HREE concentrations of the U-Hf rich zones. The location of the LREE is not specified.

The dissolution appears to remove U-Y rich zones and the abrasion Th-U zones which is not easily explained by the literature on trace element zoning in zircon. The corresponding loss of LREEs, Y and U by dissolution and increased loss of LREE and Th by abrasion may be explained by loss of metamict and monazite respectively. The resistance of Y to abrasion is difficult to explain, other than by the enrichment of Y in the cores of zircon.

### 6.2.5 SEM INVESTIGATION OF ABRASION

SEM photomicrographs of the abraded grains show the grain's pyramids to be rounded, for example Plate 6.16 (SEM 220917), an elongate grain showing abrasion features on the pyramids and prismatic faces that result in a lozenge shape (Plate 6.17 (SEM 220923)). The less elongate grains, for example in Plate 6.18 (SEM 220916), are abraded to spheres and show no evidence of prismatic or pyramidal faces. Plate 6.19 (SEM 220918) shows a parallel abrasion-ridges-texture, which is a feature indicative of air abrasion percussion marks, commonly found in deserts and in large dune cordons. Plate 6.20 (SEM 280818) shows a naturally abraded metamict zircon. The traces and pyramid are abraded and the prism faces are untouched. Note the parallel percussion marks.

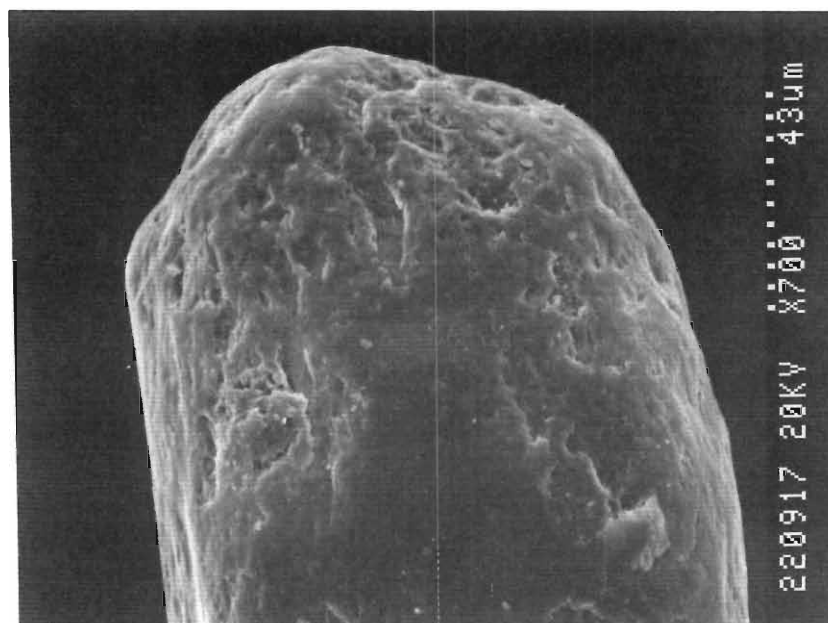


**PLATE 6.16:** A SEM photomicrograph of an experimental air abraded pyramid of a zircon (SEM 220917).

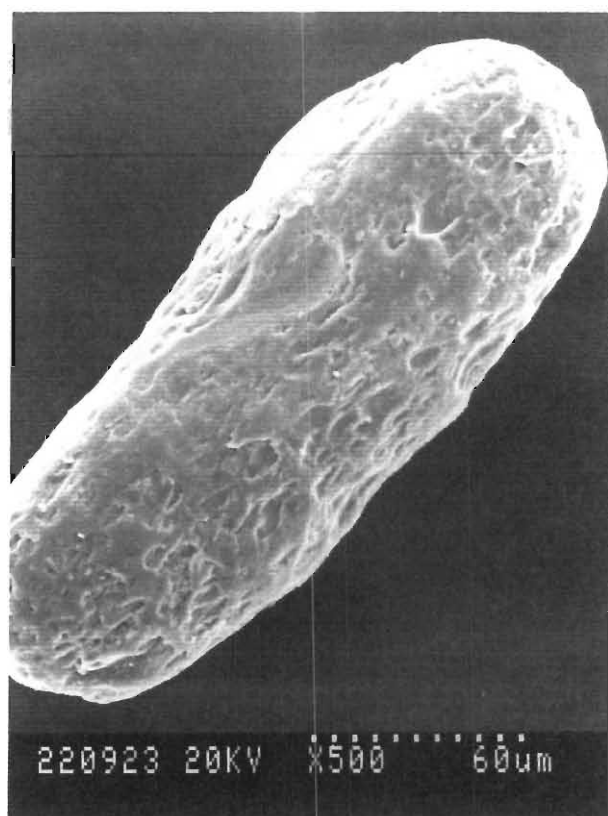


**PLATE 6.17:** A SEM photomicrograph of an experimentally air abraded zircon showing the lozenge shape, indicative of air abraded elongate zircons (SEM 220923).

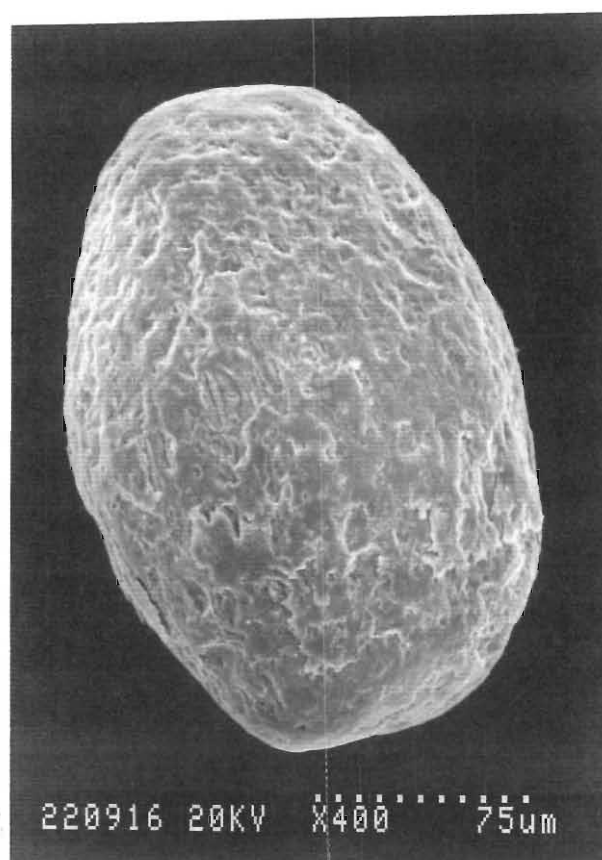


**PLATE 6.18:** A SEM photomicrograph of an experimentally air abraded zircon showing the spherical shape, indicative of air abraded grains with low L/B values (SEM 220916).

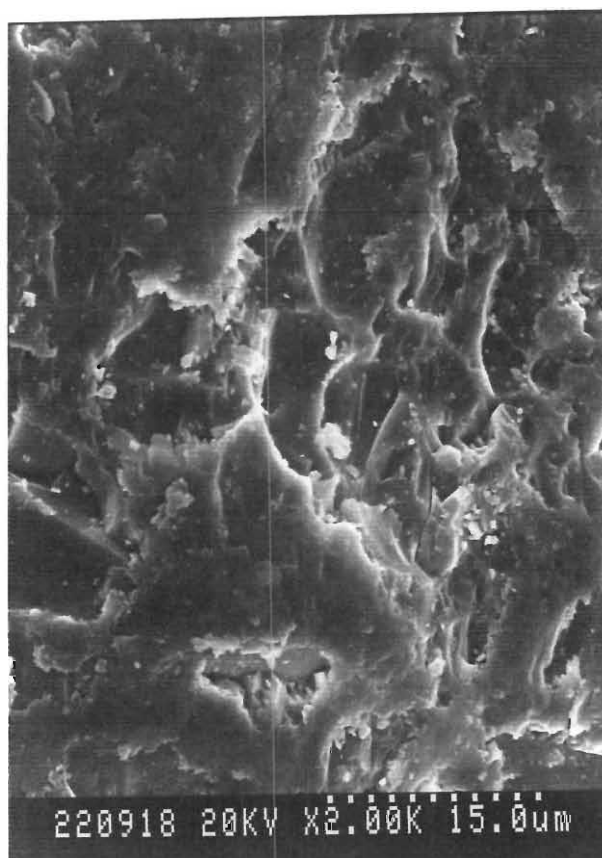


**PLATE 6.19:** A close-up SEM photomicrograph of the surface of an experimentally air abraded zircon. Note the percussion marks. (SEM 220918).

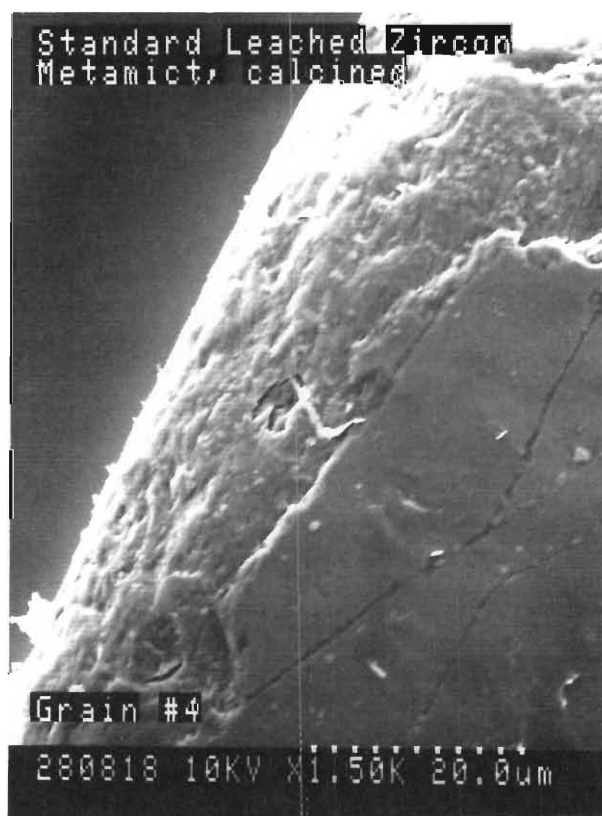


**PLATE 6.20:** A close-up SEM photomicrograph of the surface of a naturally abraded metamict zircon (SEM 280818). Note the parallel ridges of percussion marks.

### 6.2.6 DISCUSSION OF AIR ABRASION RESULTS

Air abrasion is an efficient means of reducing U and Th. In Sample #4 the concentrations of U and Th were reduced by 15% and 20% respectively with a mass loss of 14%. The greater efficiency of sample #4 is possibly due to the higher portion of magnetic material present within the zircon concentrate product sample, with 381ppm U and 182ppm Th compared to the zircon concentrate NM. The magnetic material has higher concentrations of monazite and metamict zircon. Abrasion preferentially removes the grains of lower hardness, ie. the magnetic monazite and metamict zircon are removed.

The results indicate that HF acid leaching (#5) started to remove lower U- and Th-zircon, but the treatment decreased the structural strength of the remaining zircon that was enriched in U and Th. Compared to the acid leaching of #6 the removed material of #5 has far lower U and Th concentrations which may indicate that monazite was removed preferentially by HF-*aqua regia*. In the case of #5, abrasion removed U- and Th- rich material, which may be the less abrasion resistant monazite, which was not dissolved by the acid treatment. The material removed by the abrasion of sample #6 has a low Th concentration due to the monazite contaminant being removed by the acid treatment. The abrasion of sample #6 was inefficient, with an insignificant reduction of U+Th accompanied by a mass loss of 6%.

The sum of U and Th of the material removed by the combined acid treatments and air abrasion show that the 12% of zircon removed in sample #6 has a far higher U+Th concentration than sample #5. The HF acid treatment removed zircon that had low U and Th concentration as well as zircon with high U and Th concentration. The U+Th values show that the treatment of #5 is successful in decreasing the U and Th well below the required 400ppm U+Th.

### 6.3 SEPARATION BASED ON DENSITY AND SHAPE

The density of zircon ranges from 3.8 to 4.67g.cm<sup>-3</sup>. The substitution of phases such as hafnon (HfSiO<sub>4</sub>) with a density of 6.97g.cm<sup>-3</sup>, thorite (ThSiO<sub>4</sub>) with a density of 6.70g.cm<sup>-3</sup> and coffinite (U(SiO<sub>4</sub>)<sub>1-x</sub>(OH)<sub>4x</sub>) with a density of 7.16g.cm<sup>-3</sup>, will all increase the density of zircon. The density of zircon is reduced during the metamictization process, starting with 4.6 to 4.71g.cm<sup>-3</sup> for normal zircon and decreasing to between 3.9 to 4.2g.cm<sup>-3</sup> for metamict zircon. Monazite has a density between 4.8 and 5.5g.cm<sup>-3</sup>. A high density separate will contain zircon with U- or Th-rich substituted phases and monazite. A low density zircon separate will contain metamict zircon.

### 6.3.1 DENSITY SEPARATION METHOD

A superpanner (Plate 6.21) was utilised to separate the bulk zircon concentrate product into low density (first zircon to be removed), middlings, and the high density (the last zircon to be removed) fractions. The superpanner is an automated "gold-diggers" pan. A variable speed electric motor turns an adjustable cam. The rotating cam knocks the pan backwards and forwards. The pan is pushed against the cam by an adjustable spring. The pan is also pulled left and right by adjustable wires. The resulting motion of the pan follows an elliptical path. The water flow is supplied at regulated rate at the top end of the pan, and is removed by a venturi vacuum pump at the bottom end of the pan. The dip of the pan is also adjustable and is the chief adjustment used during operation after the pan has been set in motion. The lower the dip of the pan the lower the density of grains collected at the top end of the pan. The lights were removed with the water at the bottom of the pan into a vacuum flask. With suitable experimentation the superpanner can be adjusted to separate particular densities.

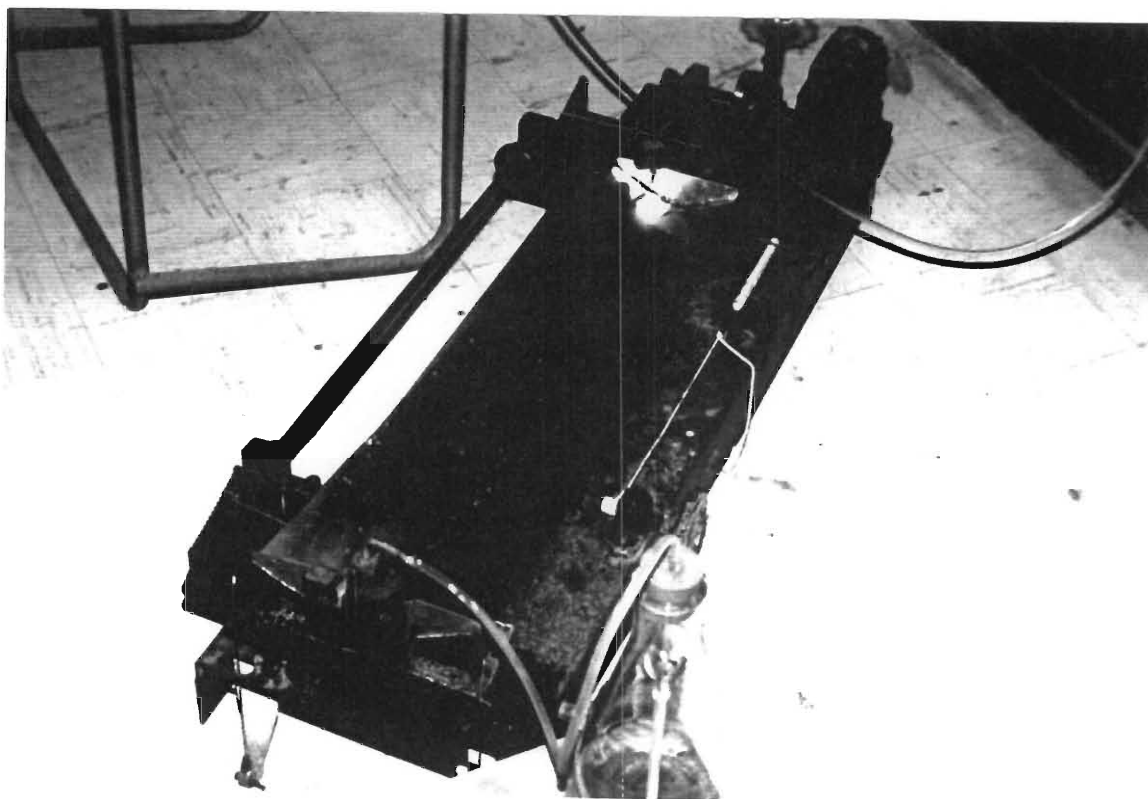


**PLATE 6.21:** The superpanner used for separation of high and low density separates.

The "lights" on inspection are more coarse grained and darker than the middlings, and the "heavies" are fine-grained and lighter coloured than the middlings.

The unsuccessful liquid abrasion zircon products were separated into three portions, "lights" (5.24%), middlings (88.26%) and "heavies" (6.50%). The three portions, as well as a bulk abraded sample and a bulk non-abraded sample, were then analysed using the ICP-MS.

### 6.3.2 SUPERPANNER RESULTS

The source sample ZCP and the separates were analysed by ICP-MS (see Table 6.05). The low density fraction has lower U and Th values, 64 ppm less U and 19ppm less Th than ZCP. The high density fraction has lower U and much higher Th concentration, 27ppm less U and 177ppm more Th (Figure 6.09) than ZCP.

**TABLE 6.05:** Y, REE, Th and U results for the starting, high density and low density material separated on the superpanner.

Description: Sample #:	STARTING ZCP-892	LOW DENSITY ZCP-892	HIGH DENSITY ZCP-892
Y	989.90	1032.58	1010.05
La	47.95	26.56	369.43
Ce	122.91	68.20	721.42
Pr	15.01	8.34	92.39
Nd	63.55	35.65	330.19
Sm	23.60	18.40	63.95
Eu	4.44	5.70	2.68
Gd	41.65	30.81	59.22
Tb	14.01	11.64	12.48
Dy	126.43	100.47	98.87
Ho	41.16	37.81	36.66
Er	194.24	146.15	145.84
Tm	39.42	27.41	27.41
Yb	371.59	248.10	243.78
Lu	67.09	49.41	50.47
Th	181.52	161.88	358.75
U	381.03	317.34	354.06
U/Th	2.10	1.96	0.99
U+Th	1.28	479.22	712.81
La/Sm	11.04	0.91	3.64
Yb/Gd	1.10	9.96	5.09
Ce/Ce*	0.43	1.10	0.92
Eu/Eu*	0.50	0.73	0.13



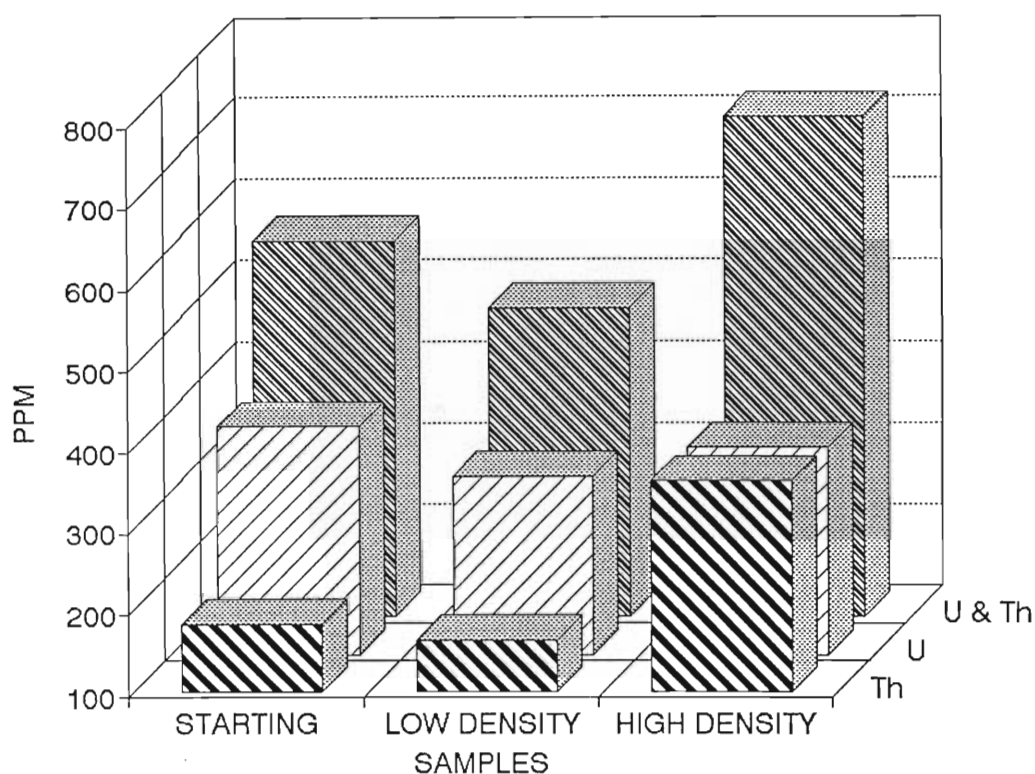


**FIGURE 6.09:** Comparison of U and Th concentrations in the starting material, the high density and low density separates.

The REE profiles (Figure 6.10) show a steep enriched La to Sm LREE profile which illustrates a high monazite contamination in the high density fraction. A minimum monazite content calculated from the enrichment of LREE is 0.5%. The monazite therefore contributes 149ppm Th and 12ppm U to the heavy fraction. The remaining material in the high density fraction after the removal of the 0.5% monazite has 209ppm Th and 342ppm U. An explanation for the lower U in the heavy fraction is that the high density fraction forms a large fraction of the bulk sample (6.5%), and is therefore "flooded" with clear zircon with  $4.67\text{g}\cdot\text{cm}^{-3}$ , which generally have low U and Th concentrations.

The removal of approximately 5% of the high or low density material from the bulk sample increases or reduces the Th by only a few ppm. The removal of the low density portion results in an increase in U and Th of the product, with 385ppm U and 183ppm Th. The removal of the high density material results in a product with 383ppm U and 169ppm Th. The removal of the magnetic fraction is a far more effective and efficient method which reduces the U and Th values of the zircon concentrate to 312ppm U and 141ppm Th.

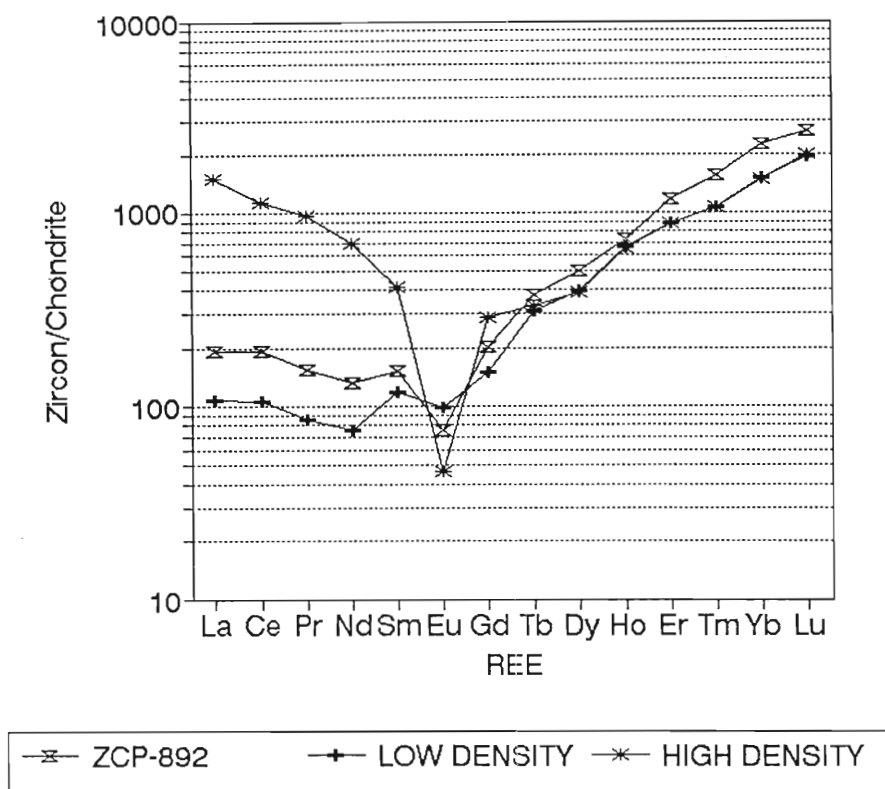


**FIGURE 6.10:** Chondrite normalised REE profiles of the starting material and the high and low density separates.

Cornell and Pietersen (1992) separated high density (4.7%) and low density (1.7%) zircon from a zircon concentrate product. The samples and the source were analysed by XRF for CaO, Fe<sub>2</sub>O<sub>3</sub> and P<sub>2</sub>O<sub>5</sub>. The high density sample had 3.5 times less CaO and 5.5 times less Fe<sub>2</sub>O<sub>3</sub> than the bulk sample. The P<sub>2</sub>O<sub>5</sub> was 1.5 times higher in the high density sample. The low density material had 1.5 times higher CaO and 2 times more Fe<sub>2</sub>O<sub>3</sub>, and slightly lower P<sub>2</sub>O<sub>5</sub>. The high P<sub>2</sub>O<sub>5</sub> in the high density sample is evidence for monazite contamination.

The samples were later analysed for U and Th by ICP-MS. The high density sample was analysed as 92040T and 92041T, and the low density sample was analysed as 92118T and 92119T. The samples 92040T and 92041T had In values of 25% of what they should be. As a result, the trace element concentrations were analysed with Re as the only internal standard. The high density sample (4.7%) has 286ppm U and 376ppm Th. The low density (1.7%) fraction has 283ppm U and 153ppm Th.

The removal of the 4.7% high density fraction results in an increase in the U to 385ppm and decrease in the Th to 172ppm in the bulk sample.

Density separation is not considered a viable method of reducing uranium in the bulk sample. The effect of the removal of smaller fractions was not assessed, but involves the difficulty of obtaining a good density separate that is not contaminated with the medium density fraction. By reducing the size of the high density fraction from 6.5% to 4.7% the U content of the high density fraction decreases by 20% and the Th content increases by 5%.

## 6.4 SIZE CLASSIFICATION AND SIEVING

### 6.4.1 ZIRCON GRAIN SIZE LITERATURE

Grauert *et al.* (1974) separated and analysed zircon size fractions from migmatized gneisses. The zircon was heterogeneously zoned with up to three phases of growth. The less than 40 $\mu$ m zircon size fraction had 642ppm U and increased through 866, 890, 973, 1163 to 1342 in the greater than 150 $\mu$ m size fraction. The U-poor overgrowths in the small size fraction constituted 50% of the grains, while in the larger size fraction the overgrowths were only 20% of the total volume.

Aleinikoff (1983) analysed zircons from the Sherman Granite. Zircons were analysed according to their size and within which minerals they were enclosed. Trace elements in the small zircon grain fraction was found to be 55% of the U, 78% of the Th and 51% of the Pb of the large grain fraction. The highest uranium was found in the large air abraded grains, ie. the cores are enriched in uranium. The zircon was liberated from mineral separates of plagioclase, quartz, K-feldspar, biotite and hornblende (See Table 6.06).

**TABLE 6.06:** The U, Th and Pb results of two size fractions of zircon classified by the mineral from which they were extracted (Aleinikoff, 1983).

Mineral	Size	U(ppm)	Th(ppm)	Pb(ppm)
Bulk	(large)	2188	531	339
	(small)	1206	415	211
Plagioclase	(large)	1254	344	238
	(small)	1267	467	259
Quartz	(large)	2505	710	258
	(small)	1383	459	251
K-feldspar	(large)	1475	528	347
	(small)	1378	474	326
Biotite	(large)	1590	418	224
	(small)	1100	396	172
Hornblende	(large)	1954	494	268
	(small)	1270	518	244

Biotite yielded the most zircons and K-feldspar yielded the least zircon. Several attributes of the zircon were also related to the host mineral of the zircon. In a series from hornblende-biotite-quartz-plagioclase-K-feldspar the zircon had progressively less U-rich dark cores, fewer inclusions, brighter colours, more clear grains and greater elongation ratios (L/B). This may be useful information in understanding provenance. A single rock may contain several typologically and chemically different zircon populations depending on the mineralogy of the rock unit.

Aleinikoff and Stoeser (1989) reported the analyses for different size fractions of zircon from metaluminous to peralkaline granites in Saudi Arabia. The level of uranium increased by less than a factor of two, with decreasing grain size for all the zircon samples except for two uranium-rich zircon samples (1600-5585ppm), which have a reversed trend.

Schärer and Allègre (1983) analysed zircons from the Palung granite in the Himalayas. Biotite granite and porphyritic granite were sampled. U and Pb values decreased with grain length and size. In the porphyritic granite the largest grains had U and Pb values of 2613ppm and 272ppm respectively. This is compared to the smallest fraction having U and Pb values of 234ppm and 18.9ppm respectively. The U concentration in the smallest fraction is 9% of the value in the largest fraction. In the biotite granite the U values decrease from the largest (395-1211ppm) to the smallest (42.9ppm).

Gaudette *et al.* (1981) sieved non-magnetic zircons into ASTM size fractions. No regular trend was evident, though in elongate zircons (brown and clear) the larger grains are richer in uranium, while the rounded zircons (brown and clear) generally have lower uranium in the larger grains.

Barth *et al.* (1989) classified the zircon populations of tonalites, quartz diorites and granite gneisses of northern Italy according to morphological character and size, and analysed the grains for U, Th and Pb. A general trend of U increasing with decreasing size is evident. S-type zircons with widths between 130 and 160 $\mu\text{m}$  had 610 to 680ppm U; the smaller G-types with widths of between 110 and 150 $\mu\text{m}$ , 40 and 110 $\mu\text{m}$  and 30 and 70 $\mu\text{m}$  have uranium values of 1760ppm, 2240ppm and 2540ppm respectively.

Bossart *et al.* (1986) characterises "exotic" S-type zircons by size. The uranium concentrations increase with a decrease in size. The size differences are small and the grains are said to contain "exotic" features.

Van Breemen *et al.* (1987) produced results for the Hanbury granite in Canada for two size fractions:

Size Fraction	U (ppm)	Pb (ppm)
> 105 $\mu\text{m}$	661	222
74-105 $\mu\text{m}$	1526	478

In other samples from gneisses no trend is obvious, though the number of directly comparable samples is few. In a mylonitic granulite grade granitic-gneiss the largest and smallest fractions have the highest U concentrations, with the mid range having 25% less U.

Frost *et al.* (1990) analysed zircons from fayalite monzonites in the USA. The middle size range has the highest uranium values. Henjes-Kunst *et al.* (1988) analysed uranothorite zircons and pure zircons from granites in the Greek islands. All the uranothorite zircons show a large increase in uranium with decreasing size. The normal zircons show no systematic trends with decreasing grain size.

Wayne and Sinha (1992) analysed the size fractions from the least magnetic zircon fractions obtained from their Frantz Isodynamic magnetic separator. The samples were from grey and pink gneisses and daughter mylonites in the USA. The grey gneiss zircon had consistent U concentrations with decreasing size. The uranium values in the mylonite zircon increased by a factor of 2.5 with

decreasing size. Zircons from the pink gneisses were divided into zircons with metamorphic overgrowths and those without overgrowths. The overgrown zircons have 3 to 6 times the U concentrations of the zircons without the overgrowths. The U concentrations in the zircons with U-rich overgrowths steadily increase with decreasing size. The small grains presumably have larger proportions of U-rich overgrowth compared to core material. The zircons in the pink gneisses were corroded and 50% of the grains have overgrowths. The overgrowths grew in a fluorite-rich unit where zirconium was mobile when metamorphic fluids migrated through the rock. The dissolution and reprecipitation of zircon is believed to be related to variations in HF fugacity. The overgrowths are richer in Hf, Th, U, Y, REE, and poorer in Fe and Zr. The larger grain rims are less enriched in the above elements. The rims are thought to contain small amounts of xenotime.

To summarise, most zircon populations studied in the literature seem to have higher U in the smaller fractions. This is because the outer layers of the zircon are usually U-enriched, and in smaller grains the U-rich outer zones make up a greater volume proportion of the total grain. However several cases have reversed or no systematic trends.

#### 6.4.2 SIEVING METHOD

A 0.149Kg sample of zircon concentrate (ZC-B91) was sieved for 1 hour 30 minutes using 90 $\mu$ m, 125 $\mu$ m and 250 $\mu$ m sieves. The less than 90 $\mu$ m fraction (12.4%) and the greater than 125 $\mu$ m and less than 250 $\mu$ m fraction (23.6%) were analysed by ICP-MS. The zircon types, inclusions, typologies and elongation ratios were point counted for each size fraction (see Chapter 4). The greater than 250 $\mu$ m fraction contained only 8 grains of bulbous translucent and metamict zircon. Obtaining reliable sieving results with zircon is difficult due to the tendency of grains with high elongation ratios (Length/Breadth), to be retained by the sieves with larger diameters than the average width of the zircon.

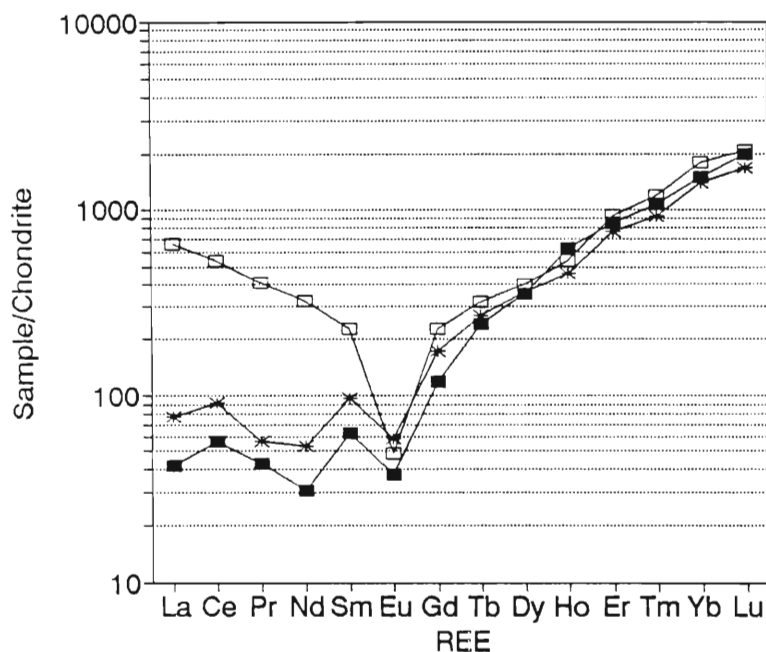
#### 6.4.3 SIEVING RESULTS

The trace element results are listed in Table 6.07 and are shown graphically in Figure 6.14 compared to the zircon concentrate product. The bulk zircon concentrate was not analysed but should have equivalent or greater U and Th concentrations than the zircon concentrate product (ZCP-892). A further complication is that the U results for analysis run T were 22% lower than the better constrained analyzes runs TC and X. To compare the results the U values for the grain size fraction have been calculated to the analyses of the run X values. The results are 314ppm U and 132ppm Th

for the 125 to 250 $\mu$ m fraction, and 390ppm U and 243ppm Th for the less than 90 $\mu$ m size fraction.

**TABLE 6.07:** Y, REE, Th and U results for the size fractions.

Description:	BULK	125-250	125-250	<90	<90
Sample #:	ZC-B91 NM	DUPLICATE 1	DUPLICATE 2	DUPLICATE 1	DUPLICATE 2
Y	1033.10	858.59	880.39	1012.06	1039.07
La	10.22	18.86	24.77	163.20	184.03
Ce	36.02	57.85	64.21	343.02	402.83
Pr	4.13	5.42	6.42	39.57	46.62
Nd	14.58	25.28	30.57	153.79	176.32
Sm	9.69	14.92	15.52	35.29	38.62
Eu	2.19	3.41	2.90	2.85	2.37
Gd	24.20	35.42	35.22	46.62	47.37
Tb	8.99	10.00	10.85	11.94	11.99
Dy	89.80	92.00	90.46	101.77	103.85
Ho	35.20	26.06	26.02	30.56	31.40
Er	142.69	127.69	126.36	156.65	154.98
Tm	27.59	23.72	24.70	30.46	30.53
Yb	244.75	229.41	228.95	296.32	289.74
Lu	50.28	42.29	41.50	52.73	52.26
Th	140.81	125.81	138.56	245.56	240.58
U	311.62	231.35	259.81	303.77	307.95
U/Th	2.21	1.84	1.88	1.24	1.28
U+Th	452.42	357.16	398.37	549.33	548.53
La/Sm	0.66	0.80	1.00	2.91	3.00
Yb/Gd	12.52	8.02	8.04	7.87	7.57
Ce/Ce*	1.33	1.36	1.20	1.00	1.02
Eu/Eu*	0.42	0.43	0.37	0.21	0.17



—■— ZC-B91      —\*— 0.125-0.250mm      —□— <0.090mm

**FIGURE 6.11:** Chondrite normalised REE profiles of ZC-B91, the <90 $\mu$ m and >125 $\mu$ m size fractions.

The greater than 125 $\mu\text{m}$  fraction has at least 3ppm more U and 9ppm less Th than the ZC-B91 NM. The less than 90 $\mu\text{m}$  fraction has at least 79ppm more U and 102ppm more Th than the starting material. Compared to the ZCP-892 the >125 $\mu\text{m}$  fraction has 67ppm less U and 49ppm less Th. The <90 $\mu\text{m}$  fraction has 9ppm more U and 62ppm more Th.

Calculations using La, Pr and Nd from the REE profiles (Table 6.07 and Figure 6.11) show that the less than 90 $\mu\text{m}$  fraction is contaminated with a minimum of 0.21% monazite. The larger fraction is more enriched in LREE when compared to the source sample which may indicate slight monazite contamination or higher values due to metamict zircon.

The removal of the 12.4% <90 $\mu\text{m}$  fraction will result in a small decrease in U and Th (U+Th: 425ppm). The removal of the 23.6% >125 fraction will result in an increase in U and Th.

The distribution of U is comparable to the distribution of U by grain size in the literature. The middlings fraction has more U than either the large fraction or the small fraction, but the small fraction has 76ppm more U compared to the larger fraction.

The larger grains are also more prone to natural abrasion in the wind medium, and are therefore more likely to have their U-rich rims removed or reduced in volume. 57% and 65% of the two larger fractions are rounded or broken compared to only 38% of the small fraction. The highest quantity of metamict grains is found in the 125 to 250 $\mu\text{m}$  fraction, though by mass proportion most of the metamict grains in the bulk sample are found in the middlings.

## 6.5 MAGNETIC SEPARATION

Removal of magnetic zircon from a zircon sample is a common procedure used to remove discordant zircon and improve the dating accuracy of a sample. This is because the more altered zircon grains (ie. the U-Th-Pb isotopic system is more likely to be disturbed) have a greater tendency of absorbing iron.

### 6.5.1 MAGNETIC ZIRCON LITERATURE

The uranium content of the non-magnetic portion of Aleinikoff's (1983) zircon decreased from 1206ppm in the bulk sample to 780ppm: a 35% decrease.

Gaudette *et al.* (1981) separated the bulk zircons of the Potsdam Sandstone (USA) into magnetic fractions on a Frantz Magnetic Separator. The concentrations decreased from 915ppm U and 141ppm Pb, in the most magnetic, to 370ppm U and 67ppm Pb in the non-magnetics.

Krogh (1982b) used high gradient magnetic fields to remove paramagnetic zircon. The

paramagnetic zircon, which had already been abraded, had much higher uranium than the bulk samples. The Archaean zircon which had enrichments of iron in the U-rich areas produced larger quantities of paramagnetic zircon than younger or less altered zircon. The Archaean age of the zircon has resulted in the grain having high U decay-induced damage over a long period. This has resulted in a higher probability of iron being supplied to the zircon and a longer period of iron absorption.

Aleinikoff and Stoesser (1989) analysed and compared non-magnetic and very magnetic zircon. The very magnetic zircon had 1232ppm U compared to 916ppm U in the non-magnetic zircon. The lower magnetic fractions of zircon are also enriched in U compared to the non-magnetics.

## 6.5.2 METHOD OF THE FIRST MAGNETIC SEPARATION

Removal of magnetic fractions from the zircon products was considered a potential method of reducing U and Th, as well as other trace elements. Two types of magnetic separators were used: a Frantz Isodynamic Magnetic Separator and a stronger Eriez Magnetic Separator.

The amperage setting on the magnetic separators is directly proportional to the strength of the magnetic field. The higher the amperage the stronger the magnetic field. Low amperage, weak magnetic field settings will remove the grains in the sample with the highest magnetic susceptibility, ie. the most magnetic grains.

The increase of amperage in increments therefore removes grains that are of less and less magnetic susceptibility in each consecutive pass.

The starting zircon concentrate was magnetically cleaned on the Eriez magnetic cleaner at the maximum amperage setting of 2.24A to produce the non-magnetic zircon concentrate (zircon concentrate NM or ZC NM). The bulk sample was passed twice through the Frantz or Eriez, followed by each fraction being re-passed through the separator to remove non-magnetic or less magnetic entrained grains in each magnetic fraction. The non-magnetics, from a magnetic fraction that had been passed through the magnetic separator a second time, were then included in the next lower magnetic fraction, and passed through the magnetic separator at the next higher amperage increment until all fractions had been through the magnetic separator.

The 1.7A magnetic fraction from ZC was removed using the Eriez magnetic separator. The 1.7A magnetic fraction was sub-divided on the Frantz magnetic separator into fractions at 0.3A intervals, starting at 0.1A and ending at 1.69A, with a forward slope of 15° and a side tilt of 10°. Only 15.14% of the 1.7A Eriez magnetic fraction was magnetically separated on the Frantz. The distribution is shown graphically in Figure 6.12. Three hundred grains from the 0.7A and 1.0A fractions were point counted. The results are tabulated in Table 6.08.



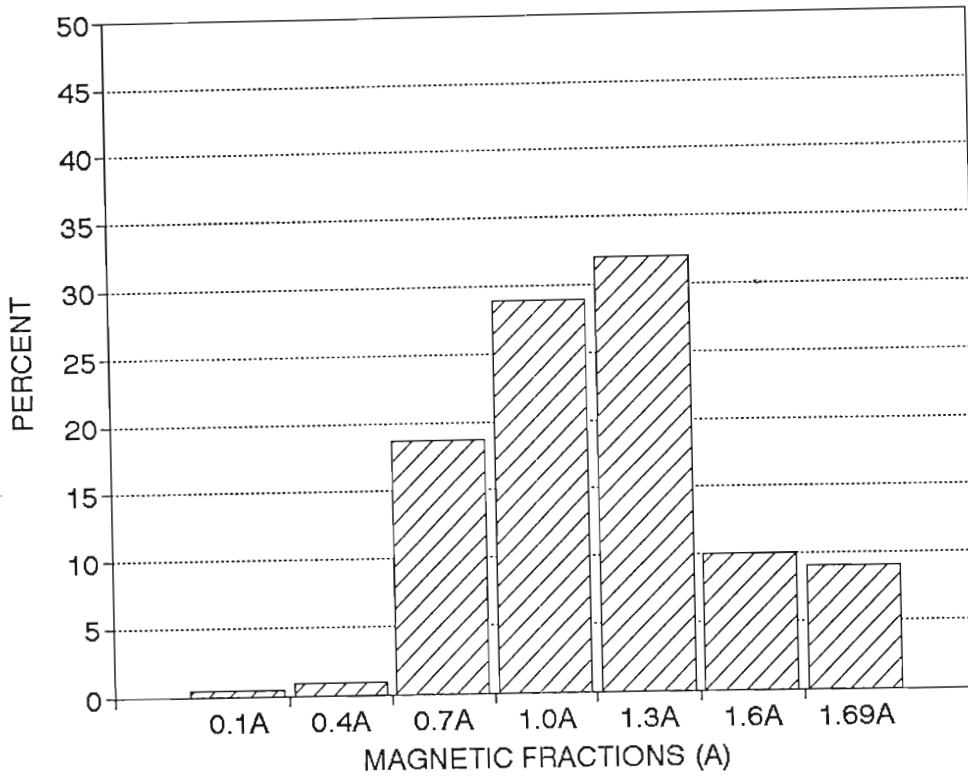


FIGURE 6.12: Distribution of mass magnetic fractions of the 1.7A magnetic fraction of ZC-B91.

TABLE 6.08: Point counting of the 0.7A and 1.0A magnetic fractions.

Magnetic Fractions:	0.7A	1.0A
Mass Percent:	0.05	0.08
"Green Minerals"	7	1
Ilmenite	1	0
Rutile	0	0
Monazite	25	2
Sphene	0	1
Others	1	1
Clear Zircon	1	4
Clear Zircon + Inclusions	6	11
Clear Zircon + Ilmenite	39	50
Brown Metamict	7	10
Red Metamict	2	2
White & Grey Metamict	6	7
Coloured Zircon	5	11
Percent Total:	100	100

The magnetics from 0.442kg of the ZC were removed on the Eriez Magnetic Separator. A total of 3.69% of the sample was removed as magnetics at 1.6A (3.16%), 2.0A (0.33%) and 2.24A (0.19%). The 1.6A fraction was further sub-divided into 0.3A fractions starting at 0.4A on the Frantz Magnetic Separator with a 15° forward slope and a side tilt of 10° (Figure 6.13). Only 14.1% of the 1.6A Eriez magnetic fraction was magnetic on the Frantz magnetic separator. All the magnetic fractions were point counted (300 grains each) to ascertain their constituents (Table 6.09).

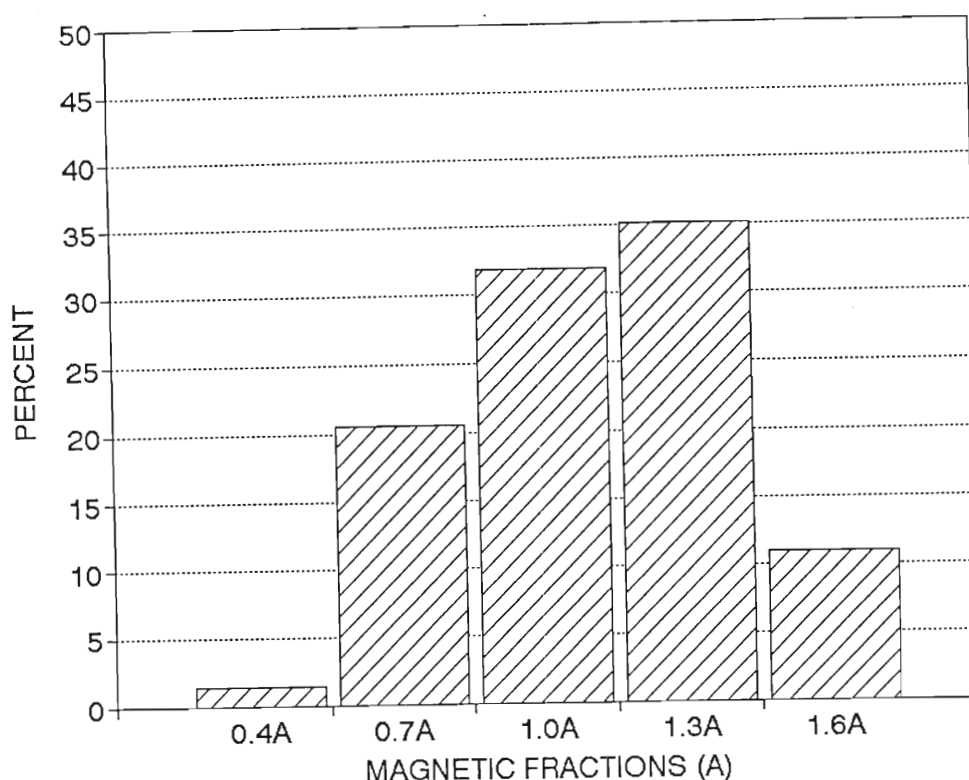


FIGURE 6.13: Distribution of by mass of the 1.6A Eriez magnetic fraction into 0.3A fractions on the Frantz.

TABLE 6.09: Point counting results for the magnetic fractions of ZC (Percent).

Magnetic Fractions:	0.4A	0.7A	1.0A	1.3A	1.6A	>1.6A
Mass Percent:	0.011	0.102	0.108	0.070	0.153	2.717
Green Minerals	9	43	6	0	0	0
Ilmenite	5	2	0	0	0	0
Rutile	0	0	0	0	0	1
Monazite	9	12	10	8	7	1
Sphene	4	2	0	1	0	0
Others	10	1	2	1	0	1
Clear Zircon	3	0	1	0	0	7
Clear Zircon + Inclusions	13	9	14	10	10	27
Clear Zircon + Ilmenite	25	12	30	28	29	24
Brown Metamict	8	5	10	24	24	5
Red Metamict	0	0	2	8	7	1
White & Grey Metamict	5	8	16	13	18	10
Coloured Zircon	9	6	9	7	5	23
Percent Total:	100	100	100	100	100	100

The 1.6A (Eriez) magnetic fraction of the zircon concentrate (ZC-B91) has five major constituents. In the high magnetic fraction the "green mineral" category has high values, totalling 0.0513% of the total sample and 1.6% of the magnetics. The "green minerals" were identified by SEM as Zn-spinel (Gahnite), spinel, tremolite, hornblende, augite, Cr-Diopside, other clinopyroxenes and epidote. Approximately 25 to 30% of each magnetic fraction is clear zircon with magnetic ilmenite inclusions totalling 0.76% of the whole sample and 23.9% of the total magnetic fraction. Metamict zircon forms a major fraction of the magnetics, ranging between 13 and 49% of any one magnetic fraction, totalling 0.58% of the total sample and 18.6% of the total magnetic fraction. Monazite is a less major constituent totalling 0.41% of the total sample, and 13.1% of the magnetics. Clear zircon

with non-ilmenite inclusions and/or iron stained clay fillings constitute the largest fraction of the total magnetic fraction, totaling 0.78% of the whole sample and 24.7% of the total magnetic fraction.

### 6.5.3 RESULTS OF THE FIRST MAGNETIC EXPERIMENT

The 0.7A magnetic fraction (ie. greater than 0.4A and less than and equal to 0.7A) was analysed for Y, REE, Th and U (Table 6.10 and Figure 6.14). The proportions of trace elements, compared to the source ZC-B91 NM from ICP-MS analysis run T are 37 to 51 times the bulk non-magnetic value of Th, and 1.4 to 1.8 times the bulk non-magnetic value of U.

**TABLE 6.10:** Y, REE, Th and U results for the source material and the magnetic fractions.

Description: Sample #:	STARTING ZCP-892	STARTING ZC-B91 NM	1.7A MAGNETIC ZCP-892	0.7A MAGNETIC ZC-B91 NM
Y	989.90	1033.10	5629.75	1579.47
La	47.95	10.22	12340.75	9196.29
Ce	122.91	36.02	24663.08	18154.56
Pr	15.01	4.13	3004.13	2280.63
Nd	63.55	14.58	9831.75	7421.53
Sm	23.60	9.69	1944.63	1415.72
Eu	4.44	2.19	135.92	56.50
Gd	41.65	24.20	1322.95	866.60
Tb	14.01	8.99	195.17	101.72
Dy	126.43	89.80	945.71	355.99
Ho	41.16	35.20	166.65	50.84
Er	194.24	142.69	595.10	145.43
Tm	39.42	27.59	107.08	22.22
Yb	371.59	244.75	861.69	170.74
Lu	67.09	50.28	142.59	30.14
Th	181.52	140.81	8014.26	6100.13
U	381.03	311.62	1170.53	430.49
U/Th	2.10	2.21	0.15	0.07
U+Th	1.28	452.42	9184.79	6530.62
La/Sm	11.04	0.66	3.98	4.08
Yb/Gd	1.10	12.52	0.82	0.25
Ce/Ce*	0.43	1.33	0.95	0.93
Eu/Eu*	0.50	0.42	0.25	0.15

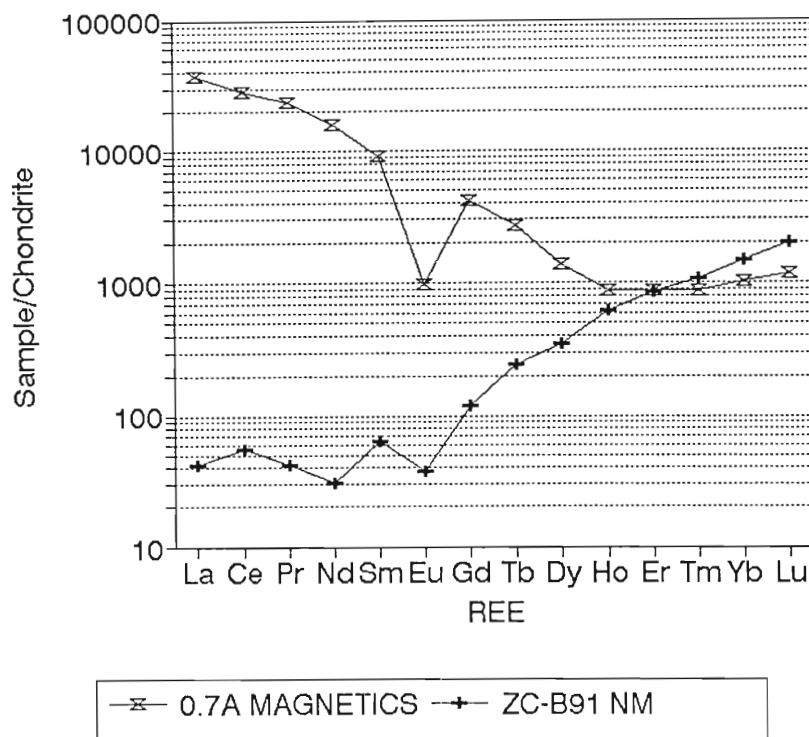


**FIGURE 6.14:** Chondrite normalised profiles of 0.7A magnetic fraction and the non-magnetic ZC-B91.

Point counting gave a monazite proportion of 12% in the 0.7A magnetic fraction. The point counted monazite content agrees with the monazite content calculated from the LREE enrichment. Calculating the monazite contamination from the LREE La, Pr and Nd (Table 6.10 and Figure 6.14) in the 0.7A magnetic fraction yields a 11.8% monazite contamination.

The effect of removing the 11.8% monazite from the magnetic fraction, results in a calculated 0.7A-magnetic product with 118ppm U and 1401ppm Th. A possible explanation for the high Th value is zircon only constitutes 40% of the 0.7A magnetic fraction, pyroxenes and other green minerals, which may contribute Th, constitutes the other 43% of the sample. Another unknown factor in the above calculation of monazite removal is the variability of U and Th concentration in monazite compared to the magnetic susceptibility of monazite. The U and Th concentration in the 0.7A fraction may be greater than the concentrations found in the bulk monazite sample that was analysed.

#### 6.5.4 METHOD OF THE SECOND MAGNETIC EXPERIMENT

The magnetic fraction from a zircon concentrate product sample, of March 1992, of 199.07g (ZCP-392) was separated on the Frantz Magnetic Separator at a 1.4A setting with a forward slope of 15° and a side tilt of 10°. The magnetic fraction constitutes 0.236% of the bulk sample. The non-zircons within the magnetic fraction were identified by scanning electron microscope (SEM) semi-

quantitative analysis (Table 6.11). The percentages quoted in Table 6.10 are estimates of modal proportion obtained from the identification of 310 hand-picked grains by SEM and are not quantitative results. The sample was not a 100% random sample.

**TABLE 6.11:** Non-zircon SEM identified minerals in the 1.4A magnetic fraction and their approximate proportions (Cornell and Pietersen, 1992).

Mineral	Percent	Mineral Formula
Clinopyroxene	40	$\text{Ca}(\text{Mg,Fe})\text{Si}_2\text{O}_6$
Sphene	12	$\text{CaTiSiO}_4$
Epidote	6	$\text{Ca}_2\text{FeAlSi}_3\text{O}_{12}(\text{OH})$
Hornblende	4	$\text{Ca}_2(\text{Mg,Fe})_5\text{AlSi}_7\text{O}_{22}(\text{OH})_2$
Plagioclase	3	$(\text{CaNa})\text{AlSi}_3\text{O}_8$
Apatite	3	$\text{Ca}_5(\text{PO}_4)_3(\text{OH})$
Monazite	6	$(\text{Ce,La,Th})\text{PO}_4$
Other Silicates	20	
Spinel and oxides	6	
Total	100	

### 6.5.5 RESULTS OF THE SECOND MAGNETIC EXPERIMENT

Cornell and Pietersen (1992) analysed the bulk zircon concentrate product and the 1.4A magnetic fraction (0.236%) by XRF. The magnetic fraction has 72 times more CaO, 56 times more  $\text{Fe}_2\text{O}_3$  and 14 times more  $\text{P}_2\text{O}_5$  than the bulk sample.

The samples were analysed for Y, REE, Th and U by ICP-MS as part of analysis run T (Table 6.10). The concentration of U from the magnetic fraction is 3.5 to 4.5 times larger and the Th concentrations is 34 to 53 times larger than the bulk starting material. The U concentration can be re-calculated from the results obtained from analysis run TC for the magnetic fraction. The calculated concentrations are 1300 and 1700ppm U and 6150 and 9600ppm Th for the magnetic fraction. The high Y, LREE and Th values are evidence for a large monazite constituent. The REE profile (Figure 6.15) has a steep La to Sm slope which illustrates the monazite contamination.

Calculation from the LREE concentrations indicates that the magnetic fraction has approximately 15.5% monazite compared to the 6% approximation identified by SEM. The  $\text{P}_2\text{O}_5$  of the magnetic fraction, analysed by XRF, is only 2%. 15.5% Monazite which has 27.5%  $\text{P}_2\text{O}_5$  (Rapp and Watson, 1986) would contribute approximately 4.3%  $\text{P}_2\text{O}_5$ . A 2%  $\text{P}_2\text{O}_5$  concentrate in the sample would require a 7% monazite content. The LREE concentrations may also have contributions from other rare REE-oxides that were identified by SEM. The inconsistencies between the LREE calculation and the  $\text{P}_2\text{O}_5$  calculation are difficult to explain. One possibility is the supply of LREE by clinopyroxenes which have enriched LREE profiles. La, Ce and Nd values for the clinopyroxene ferrohedenbergite from a rhyolite are reported by Michael (1988) to range between 385 and 720ppm.

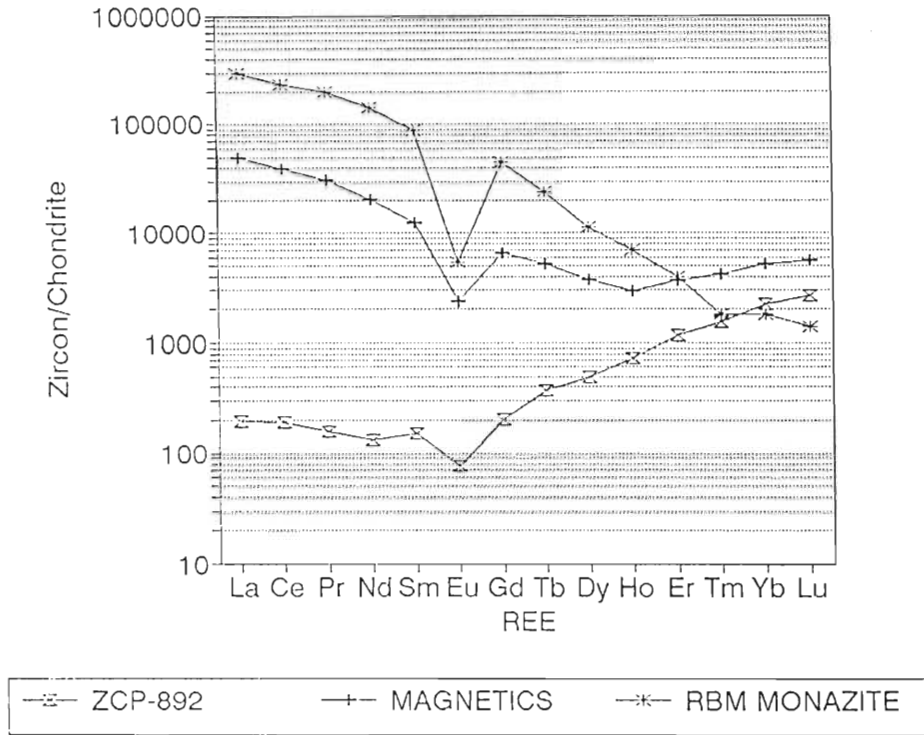


**FIGURE 6.15:** Chondrite normalised profiles of ZCP-892, the magnetic fraction of ZCP-892 and the RBM monazite MP-691.

The non-magnetic fraction of the zircon concentrate product was not analysed. The removal of the magnetic fraction from the zircon concentrate product results in a calculated 3ppm reduction in U and a 19ppm reduction in Th. The size of the magnetic fraction of the zircon concentrate product, only 0.24% of the bulk sample, is small compared to the size of the magnetic fraction of the zircon concentrate (ZC) of 0.44%. The difference in magnetic fraction size is due to the zircon concentrate product's magnetic fraction containing all the magnetics up to 1.4A, while the zircon concentrate has all the magnetics up to 1.69A removed. The ZCP at RBM undergoes increased magnetic cleaning in the zircon plant.

### 6.6 EFFECT OF PROVENANCE ON U AND Th

A detailed provenance study of the RBM zircon was beyond the aims and scope of this project. A detailed provenance study and the study of spatially different heavy mineral deposits has large potential in reducing U and Th. An understanding of the importance of such studies can be obtained from a review of provenance with an emphasis on U and Th.

The RBM product comprises numerous different zircon types. The types show differences in crystal typology, size, trace element impurities and inclusions. The rocks from which the zircons

originated are diverse in chemistry and zircon type. The river basins which supply the northern Natal north coast drain the interior which include: (1) the basement rocks of granite, gneisses and a few syenites and basic igneous rocks; (2) Karoo and earlier cover which includes (A) large sedimentary sequences with distant igneous sources rocks; (B) basaltic volcanic rocks which contain very little zircon; and (C) Late Karoo and Cretaceous basalts and rhyolites (3) a large Tertiary and Cretaceous sedimentary wedge which is overlain by the RBM deposit. The RBM deposit is situated in Holocene dunes and Pleistocene beach sequences (Fockema, 1986).

The deposit includes zircon with low U and Th values, as well as zircon with medium to high values (See Chapter 5). To lower the U and Th values the product can be blended with a concentrate of zircons with very low U and Th values. The result would be a product with mean U and Th values of the two concentrates. The Richards Bay Minerals product contains approximately 17% D-type zircon which contributes 11.8% of the bulk products uranium. The D-type of zircon from RBM has a U value of 216ppm and Th value of 110ppm. These values are very low when compared to the bulk analyzes of the best magnetically cleaned zircon concentrate with a U value of 311ppm and a Th value of 140ppm. By blending the magnetic cleaned zircon concentrate one to one with D-type zircon a product would be obtained with 264ppm U and 125ppm Th (U+Th: 389ppm).

D-type zircon according to Pupin (1980) and Vavra (1990) are common in trachytes or rhyolites, as well as other high temperature igneous rocks. The Lebombo Rhyolites found north of Richards Bay and extending to the border of Tanzania and Mozambique are potential suppliers of D-type zircon to the Cretaceous, Tertiary, Pleistocene and present-day sediments. An investigation of the dunes north of Richards Bay and in Mozambique may result in the discovery of zircon deposits with increased amounts of low uranium D-type zircons. Tertiary and Cretaceous sediments below the Pleistocene sediments have several transgressive and regressive coastlines. Buried heavy mineral placer deposits, such as Eneabba in western Australia, may be present in the sedimentary wedge. The input of sediments and zircon from the rhyolites into such a sedimentary wedge may be sufficient in these buried placers to justify the mining of low U zircon.

## 6.7 CONCLUSION ON U AND Th REDUCTION REDUCTION METHODS

The comparison of the U+Th results are plotted for all the treated samples and source materials in Figure 6.16. The acid treatments are considered extreme methods economically, but are efficient in reducing the magnetic cleaned zircon concentrate from a U+Th value of 452ppm to below 400ppm. HF partial dissolution reduces the U+Th to 364ppm with a mass loss of 16% and HF-*aqua regia* dissolution reduces the U+Th to 390ppm with a mass loss of 6%.

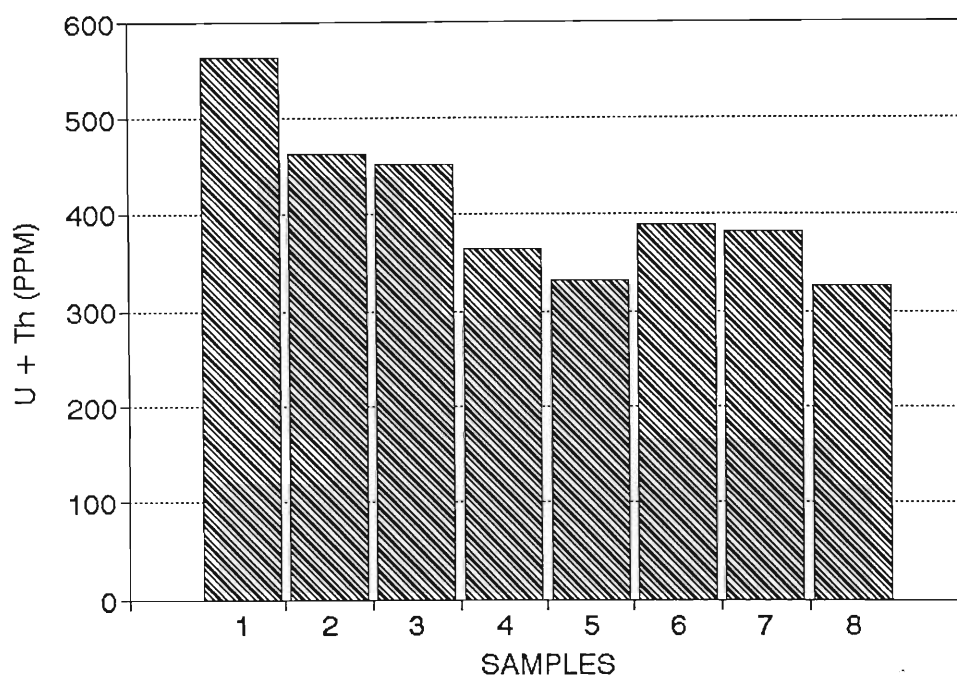


**FIGURE 6.16:** Comparison of U + Th concentrations of starting material and the treated products: (1) ZCP-892, (2) ZCP ABRADED, (3) ZC-B91 NM, (4) ZC HF DISSOLUTION, (5) ZC HF DISSOLUTION & ABRASION, (6) ZC HF-*AQUA REGIA* DISSOLUTION, (7) ZC HF-*AQUA REGIA* DISSOLUTION & ABRASION, (8) LOWEST (100% D-TYPE).

Air abrasion is the most economically viable method of reducing U and Th. A 14% mass loss results in a reduction of the U + Th from 563ppm to 463ppm, but not below the required 400ppm level. The problem with the air abrasion in the experiments performed is the fact that the zircon concentrate product still contains 0.24% magnetics at 1.4A on the Frantz magnetic separator. The abrasion may therefore remove a large portion of the magnetic material which would be easier to remove by a magnetic cleaning process. The magnetic material will have a large proportion of the U and Th rich metamict zircon and monazite. On the other hand magnetic cleaning of the air abraded sample may further reduce the U + Th of the sample, and possibly reduce the U + Th below 400ppm. The lowest values obtained in this study are from the samples that were air abraded after acid treatment.

The abraded HF treated material has a U + Th value of 332ppm with a 21% mass loss, and the abraded *aqua regia* 383ppm for a 11% mass loss. The D-type zircon in the zircon concentrate is considered to have the lowest U + Th value of the more abundant zircon. The U + Th for the D-type zircon can be considered as the cut-off point for reducing uranium and thorium. The U + Th value is 327ppm. The sample that was treated in HF and abraded in the air abrasion mill has a U + Th value of 332ppm which is close to the concentration in the D-type zircon.

The effect of acid treatment on abraded zircon grains was not determined. The percussion marks formed during abrasion resulted in an increase in the surface area and should increase the



effect and rate of zircon dissolution in acid. Further studies involving incremental increases in mass loss both, by abrasion and acid treatment, should be undertaken to establish the most efficient levels of treatment, the most efficient combinations of treatment, and to ascertain the point after which increased mass loss does not increase the U and Th loss.

## CHAPTER 7

### CONCLUSIONS AND SUGGESTIONS FOR FURTHER WORK

This study was successful in mapping the distribution of U and Th in zircons and determining potential methods of reducing U and Th in the zircon concentrate from RBM. In conclusion the following points are made:

- 1) ICP-MS analysis determined the rare earth elements, Y, Th and U concentrations in both bulk and 100 grain samples with sufficient precision and accuracy. A precision of 5% or less was found to be suitable for the applications in this thesis, enabling the visual comparison of chondrite normalised REE profiles.
- 2) The light rare earth element concentrations may be used to estimate the proportion of monazite impurity within zircon concentrate. The source of LREE in the zircon concentrate other than zircon is predominantly monazite, with small contributions from LREE-oxides and silicates such as clinopyroxene.
- 3) A simplified version of Pupin's (1980) classification scheme was successfully applied to the zircon concentrate. The most abundant morphological type is the D-type group, abundant in high temperature igneous rocks that chill rapidly such as rhyolites.
- 4) The zircon grains contain numerous mineral inclusions which contribute small amounts of Ti, Fe, Mn, Ca, P, Mg, Al, S, K and Na to the bulk zircon concentrate.
- 5) The zircon of Richards Bay Minerals display several types of zoning which has significance to U and Th distribution. The grain rims and zones of pyramid face growth are enriched in U and Th compared to the core regions of zircon grains.
- 6) Analyses of individual zircon groups indicate a wide range of REE, Y, U and Th concentrations. U ranges from 216 to 11004ppm and Th from 111 to 4883ppm.
- 7) REE provenance modelling of clear zircon was inconclusive, but suggests a rhyolitic or granitic provenance. The REE profiles for metamict zircon exhibit attributes common to pegmatites, migmatites and carbonatites. The attributes of the REE profiles of the clear zircon indicate nepheline syenitic, syenitic or granitic signatures.

- 8) Acid dissolution with HF or HF *aqua regia* was successful in reducing the U+Th level from 452ppm to below 400ppm with negligible mass loss. The HF acid dissolution is considered, both practically and economically, an extreme method of reducing U+Th. Leaching with acids of other than HF did not produce significant results.
- 9) Abrasion of zircon in a liquid medium resulted in insignificant changes in U and Th.
- 10) Abrasion in a air medium reduced U+Th from 563ppm to 463ppm with a low mass loss. The method may be an economical viable means of reducing U and Th, but requires further experimentation to ascertain the effect of intense magnetic cleaning prior to abrasion and to ascertain the optimum (U+Th)/mass loss ratio.
- 11) Abrasion following HF and HF AR acid partial dissolution reduced the U+Th from 452ppm to 332 and 383ppm respectively. The effect of acid dissolution following air abrasion on U+Th values was not investigated and is considered an important avenue of further research.
- 12) Intense magnetic cleaning, density separation and size fractioning yielded minor reductions in U+Th.
- 13) Further research in zircon provenance is required, but preliminary results show a diversity of parent rocks. Low U+Th zircons may conceivably be present in the Cretaceous sedimentary wedge with a large proportion of low U+Th zircons from the Lebombo rhyolites in northern Natal. A blending of low U+Th zircon with the present product would result in significant reduction of U and Th.

The above conclusions show that U+Th may be reduced below the 400ppm level by several methods and combinations of methods. Future work should concentrate on optimizing the methods experimented within this study. A second worthwhile avenue of research would involve a detailed zircon provenance study of the interior of Natal with a view to locating the provenance of low U+Th zircons. Detailed studies of zircon and the sedimentary facies present in the Cretaceous sedimentary wedge may also yield fruitful results. A detailed study of inclusions, zoning and inherited cores would be useful in planning strategies for the reduction of many impurities including Ti, Fe, Mn, Ca, P, Mg, Al, S, K and Na.

## REFERENCES

- Ahrens, L.H. and Erlank, A.J. (1969) Hafnium, Section B-O, *Handbook of Geochemistry II/5*. Springer-Verlag, New York.
- Alderton, D.H.M., Pearce, J.A., and Potts, P.J. (1980) Rare earth element mobility during granite alteration: evidence from southwest England. *Earth Planet. Sci. Lett.*, **49**, 149-165.
- Aleinikoff, J.N. (1983) U-Th-Pb systematics of zircon inclusions in rock-forming minerals: A study of Armoring against isotopic loss using the Sherman granite of Colorado-Wyoming, USA. *Contrib. Mineral. Petrol.*, **83**, 259-269.
- Aleinikoff, J.N., and Stoesser, D.B. (1989) Contrasting zircon morphology and U-Pb systematics in peralkaline and metaluminous post-orogenic granite complexes of the Arabian Shield, Kingdom of Saudi Arabia. *Chem. Geol.*, **79**, 241-258.
- Aleinikoff, J.N., Winegarden, D.L., and Walter, M. (1990) U-Pb ages of zircon rims: A new analytical method using the air-abrasion technique. *Chem. Geol.*, **80**, 351-363.
- Aleinikoff, J.N., Zartman, R.E., and Lyons, J.B. (1979) U-Th-Pb geochronology of the Massabesic gneiss and granite Near Milford, South-Central New Hampshire: New evidence for Avalonian Basement and Taconic and Alleghian disturbances in Eastern New England. *Contrib. Mineral. Petrol.*, **71**, 1-11.
- Åmli, R. (1975) Mineralogy and rare earth geochemistry of apatite and xenotime from the Gloserheia granite pegmatite, Froland, southern Norway. *Am. Min.*, **60**, 607-620.
- Arran, T. (1993) *Heavy mineral provenance in the Tugela valley*. MSc in prep, University of Natal, Durban.
- Ayuso, R.A., Arth, J.G., Sinha, A.K., Carlson, J., and Wones, D.R. (1984) Comparative geochronology in the reversely zoned plutons of Bottle Lake Complex, Maine: U-Pb on zircons and Rb-Sr on whole rocks. *Contrib. Mineral. Petrol.*, **88**, 113-125.
- Barberi, F., Ferrara, G., Santacroce, R., Treuil, M., and Varet, J. (1975) A transitional basalt-pantellerite sequence of fractional crystallisation, the Boina Centre, (Afar Rift, Ethiopia). *J. Petrol.*, **16**, 22-56.
- Barth, S., Oberli, F., and Meier, M. (1989) U-Th-Pb systematics of morphologically characterised zircon and allanite: A high-resolution isotopic study of the Alpine Rensen pluton (northern Italy). *Earth Planet. Sci. Lett.*, **95**, 235-254.
- Bossart, P.J., Meier, M., Oberli, F., Steiger, R.H. (1986) Morphology versus U-Pb systematics in zircon: a high resolution isotopic study of a zircon population from a Variscan dike in the Central Alps. *Earth Planet. Sci. Lett.*, **78**, 339-354.
- British Geological Survey, (1989) World mineral statistics (1983-87), production, exports, imports. *Keyworth British Geological Survey*, 375.
- Burnett, D.S., and Woodlum, D.S. (1983) *In situ* trace element microanalysis. *Ann. Rev. Earth Planet.*

- Sci.*, **11**, 329-358.
- Byerly, G.R., Markovich, J.V., Malcuit, R.J. (1975) Use of Fourier Shape Analysis in zircon petrogenetic studies. *Geol. Soc. Am. Bull.*, **86**, 956-958.
- Caroll, D. (1953) Weatherability of zircons. *J. Sed. Pet.*, **23**, 106-116.
- Carpéna, J., Gagnol, I., Mailhé, D., and Pupin, J.P. (1987) L'Uranium marqueur de la croissance cristalline: mis en évidence par les trasses de fission dans les zircons gemmes d'Esplay (Haute-Loire, France). *Bull. Mineral*, **110**, 459-463.
- Caruba, R., and Turco, G. (1971) Mise au point sur la notation des faces du zircon. Elaboration d'une méthode d'indexation rapide des faces des zircons accessoires des roches par utilisation d'abaques. *Bull. Soc. Fr. Mineral. Cristallogr.*, **94**, 427-436.
- Caruba, R., Baumer, A., Ganteaume, M., and Iacconi, P. (1985) An experimental study of hydroxyl groups and water in synthetic and natural zircons: a model of the metamict state. *Am. Mineral.*, **70**, 1224-1231.
- Chakoumakos, B.C., Takashi Murakami, Lumpkin, G.R., and Ewing, R.C. (1987) Alpha-decay-induced fracturing in zircon: The transition from crystalline to the metamict state. *Science*, **236**, 1556-1559.
- Chepil, W.S. (1945) Dynamics of wind erosion: I. Nature of movement of soil by wind. *Soil Sci.*, **60**, 305-320.
- Chernov, A.A. (1984) *Modern crystallography III, Crystal growth*. Springer, Berlin, Heidelberg, New York.
- Chernyshev, I.V., Kononova, V.A., Kramm, U., Grauert, B. (1987) Isotope dating of Ural alkali rocks in light of U-Pb data for zircons. *Geochemistry Int.*, **24**, 1-15.
- Clark, G.J., Gulson, B.L., Cookson, J.A. (1979) Pb, U, Tl, Hf and Zr distributions in zircons determined by proton microprobe and fission track techniques. *Geochim. Cosmochim. Acta*, **43**, 905-918.
- Claoué-Long, J.C., King, R.W., Kerrich, R. (1990) Archaean hydrothermal zircon in the Abitibi greenstone belt: constraints on timing of gold mineralisation. *Earth Planet. Sci. Lett.*, **98**, 109-128.
- Claoué-Long, J.C., King, R.W., Kerrich, R. (1992) Reply to comment by F. Corfu and D.W. Davis on "Archaean hydrothermal zircon in the Abitibi greenstone belt: constraints on timing of gold mineralisation." *Earth Planet. Sci. Lett.*, **109**, 601-609.
- Cocherie, A., Guerrot, C., and Rossi, Ph. (1992) Single-zircon dating by step-wise Pb evaporation: Comparison with other geochronological techniques applied to the hercynian granites of Corsica, France. *Chem. Geol.*, **101**, 131-141.
- Corfu, F., and Ayres, L.D. (1984) U-Pb and genetic significance of heterogeneous zircon populations in rocks from Favourable Lake area, Northwestern Ontario. *Contrib. Mineral. Petrol.*, **88**, 86-101.

- Cornell, D.H., and Pietersen, K.J. (1992) *Report on prime zircon calcium and phosphorus investigation*. Confidential report to Richards Bay Minerals.
- Dana, J.D., and Harlbut, C.S. (1959) *Manual of mineralogy*. New York, Wiley.
- Davies, G.R., and Macdonald, R. (1987) Crustal influences in the petrogenesis of the Naivasha basalt-rhyolite complex: combined trace element and Sr-Nd-Pb isotope constraints. *J. Petrol.*, **28**, 1009-1031.
- Deer, W.A., Howie, R.A., and Zussman, J. (1966) *An Introduction to the Rock-Forming Minerals*. Wiley, 528pp.
- Deer, W.A., Howie, R.A., and Zussman, J. (1980) *Orthosilicates*. Wiley, 418-442.
- Dennen, W.H., and Shields, R. (1956) Yttria in zircon. *Am. Min.*, **14**, 655-657.
- Dowty, E. (1976) Crystal structure and crystal growth: 1. The influence of internal structure on morphology. *Am. Min.*, **61**, 448-459.
- Erlank, A.J. (ed) (1984) Petrogenesis of the volcanic rocks of the Karoo Province. *Geol. Soc. S. Africa Spec. Publ.*, **13**. Microfiche.
- Evensen, N.M., Hamilton, P.J., O'nions, R.K. (1978) Rare-earth abundances in chondritic meteorites. *Geochim. Cosmochim. Acta*, **42**, 1199-1212.
- Exley, R.A. (1980) Microprobe studies of REE-rich accessory minerals: Implications for the Skye Granite petrogenesis and REE mobility in hydrothermal systems. *Earth Planet. Sci. Lett.*, **48**, 97-110.
- Farges, F., and Calas, G. (1991) Structural analysis of radiation damage in zircon and thorite: An X-ray absorption spectroscopic study. *Am. Min.*, **76**, 60-73.
- Fielding, P.E. (1970) The distribution of uranium, rare earths, and color centers in crystal of natural zircon. *Am Min.*, **55**, 428-440.
- Fleischer, R.L., Price, P.B., and Walker, R.M. (1965) The ion explosion spike mechanism for formation of charged particle tracks in solids. *J. Appl. Phys.*, **36**, 3645-3652.
- Fockema, P.D. (1986) The heavy mineral deposits of Richards Bay. In *Mineral deposits of Southern Africa*, Anhaeuser, C.R., and Maske, S. (Eds), Vol. II, Geol. Soc. S. Africa, Johannesburg, 2301-2307.
- Frost, C.D., Meier, M., and Oberli, F. (1990) Single-crystal U-Pb zircon age determination of the Red Mountain pluton, Laramie Anorthosite Complex, Wyoming. *Am Min.*, **75**, 21-26.
- Fujimaki, H. (1986) Partition coefficients of Hf, Zr, and REE between zircon, apatite, and liquid. *Contrib. Mineral. Petrol.*, **94**, 42-45.
- Garnar, T.E. (1989) Zirconium and Hafnium resources. In: Carr D.D. and Herz N. (Eds.), *Concise encyclopedia of mineral resources*. Pergamon Press, Oxford. 399-401.
- Gaudette, H.E., Vitrac-Michard, A., Allègre, C.J. (1981) North American Precambrian history recorded in a single sample: high resolution U-Pb systematics of the Potsdam sandstone detrital zircons, New York State. *Earth Planet. Sci. Lett.*, **54**, 248-260.

- Govindaraju, K. (1989) Special issue of geostandards newsletter. *Geostandards Newsletter*, **13**.
- Grauert, B., Seitz, M.G., and Soptrajanova, G. (1974) Uranium and lead gain of detrital zircon studied by isotopic analyses and fission-track mapping. *Earth Planet. Sci. Lett.*, **21**, 389-399.
- Gromet, L.P., and Silver, L.T. (1983) Rare earth element distributions among minerals in a granodiorite and their petrogenic implications. *Geochim. Cosmochim. Acta*, **46**, 925-939.
- Hanchar, J.M. (1992) Interpretation of crustal histories using zircon zonation patterns. *1992 V.M. Goldschmidt conference abstract*.
- Hansen, B.T., and Friderichsen, J.D. (1989) The influence of recent lead loss on the interpretation of disturbed U-Pb systems in zircons from igneous rocks East Greenland. *Lithos*, **23**, 209-223.
- Hansmann, W., and Oberli, F. (1991) Zircon inheritance in an igneous rock suite from the southern Adamello batholith (Italian Alps). *Contr. Mineral. Petrol.*, **107**, 501-518.
- Harris, C., and Erlank, A.J. (1992) The production of large-volumes, low  $\delta^{18}\text{O}$  rhyolites during the rifting of Africa and Antarctica: The Lebombo Monocline, Southern Africa. *Geochim. Cosmochim. Acta*, **56**, 3561-3570.
- Hartman, P., and Perdok, W.G. (1955) On the relations between structure and morphology of crystals. *Acta Crystallogr.*, **8**, 49-52.
- Heaman, L.M., Bowins, R., and Crocket, J. (1990) The chemical composition of igneous zircon suites: Implications for geochemical tracer studies. *Geochim. Cosmochim. Acta*, **54**, 1597-1607.
- Henjes-Kunst, F., Altherr, R., Kreuzer, H., and Hansen, B.T. (1988) Disturbed U-th-Pb systematics of young zircons and uranophorites: The case study of the Miocene Aegean granitoids (Greece). *Chem. Geol.*, **73**, 125-145.
- Hess, H.D. (1962) Hafnium content of domestic and foreign zirconium minerals. *U.S. Bur. Mines. Rep. Invest.*, **5856**.
- Hill, W.B. (1976) Rare earths Western Australia. In: C.L. Knight (Ed), *Economic geology of Australia and Papua, New Guinea*, **4 Industrial Minerals and Rocks**, Parkville, Australia, 331pp.
- Hinton, R.W., and Upton, B.G.J. (1991) The chemistry of zircons: Variations within and between large crystals from syenite and alkali basalt xenoliths. *Geochim. Cosmochim. Acta.*, **55**, 3287-3302.
- Hoffmann, C. (1981) Chi-square testing of zircon populations from an Archean granite-greenstone terrain, Minas Gerais, Brazil. *Neues Jb. Miner. Abh.*, **140**, 202-220.
- Hoffman, J.F., and Long, J.V.P. (1984) Unusual sector zoning in Lewisian zircons. *Min. Mag.*, **48**, 513-517.
- Holland, H.D., and Gottfried, D. (1955) The effect of nuclear radiation on the structure of zircon. *Acta Crystallogr.*, **8**, 291-300.
- Hughes, J.M., and Birnie, R.W. (1980) Density determination of microcrystals in magnetic fluids. *Am. Min.*, **65**, 396-400.
- Hugo, V.E. (1988) *A mineralogical and chemical study of titanium losses at Richards Bay Minerals*. Unpubl. Msc thesis, University of Natal, Durban.

- Hugo, V.E. (1993) *The mineralogy of Ti-bearing minerals in unconsolidated sands from the southern African coastline*. Ph.D. in prep, University of Natal, Durban.
- Ireland, T.R., and Wlotzka, F. (1992) The oldest zircons in the solar system. *Earth Planet. Sci. Lett.*, **109**, 1-10.
- Irving, A.J., and Frey, F.A. (1978) Distribution of trace elements between garnet megacrysts and host volcanic liquids of kimberlitic to rhyolitic composition. *Geochim. Cosmochim. Acta*, **42**, 771-787.
- Jackman, J.A., Hunt, P.A., van Breemen, O., and Hervig, R.L. (1987) Preliminary investigation on spatial distributions of elements in zircon grains by secondary ion mass spectrometry. In: *Radiogenic Age and Isotopic Studies*, Report 1, Geol. Surv. Canada, **Paper 87-2**, 9-12.
- Kapustin Y.L. (1985) Trace element distribution in generations of accessory zircon in pegmatites. *Geochem. Int.*, **22**, 153-166.
- Kermack, K.A., and Haldane, J.B.S. (1950) Organic correlation and allometry. *Biometrika*, **37**, 30-41.
- King, R.W., and Kerrich, R. (1987) Fluorapatite fenitization and gold enrichment in sheeted trondhjemites within the Destor-Porcupine fault zone, Taylor township, Quebec. *Can. J. Earth Sci.*, **24**, 479-502.
- Klemic, H., Gottfried, D., Cooper, M., Marsh, S.P. (1973) Zirconium and Hafnium. In: *U.S. mineral resources*, U.S. Geol. Surv. Prof. Paper, **820**, USGS, Arlington, Virginia, 718-722.
- Köppel, V., and Sommerauer, J. (1974) Trace elements and the behaviour of the U-Pb system in inherited and newly formed zircons. *Contrib. Mineral. Petrol.*, **43**, 71-82.
- Krogh, T.E. (1982a) Improved accuracy of U-Pb zircon ages by the creation of more concordant systems using air abrasion technique. *Geochim. Cosmochim. Acta*, **46**, 637-649.
- Krogh, T.E. (1982b) Improved accuracy of U-Pb zircon dating by selection of more concordant fractions using a high gradient magnetic separation technique. *Geochim. Cosmochim. Acta*, **46**, 631-635.
- Kuenen, P.H. (1960) Experimental abrasion, 4, Eolian action. *J. Geol.*, **68**, 648-658.
- Langmuir, D. (1971) Particle-size effect on the reaction goethite = hematite + water. *Am. J. Sci.*, **271**, 147-156.
- Larsen, L.H., and Poldervaart, A. (1957) Measurement and distribution of zircons in granitic rocks of magmatic origin. *Min. Mag.*, **31**, 544-564.
- Leverenz, H.W. (1968) *An introduction to luminescence of solids*. New York, Dover.
- Lloyd, G.E. (1987) Atomic number and crystallographic contrast images with the SEM: a review of backscattered electron techniques. *Min. Mag.*, **51**, 3-19.
- Lyakhovich, T.T., and Lyakhovich, V.V. (1983) New data on accessory-mineral composition. *Geochemistry Int.*, **20**, 91-108.
- Marfunin, A.S. (1979) *Spectroscopy, luminescence, and radiation centers in minerals*. Translated from Russian publication by Schiffer, V.V., Berlin, Springer Verlag.



- Margolis, S., and Krinsley, D.H. (1971) Submicroscopic frosting on eolian and subaqueous quartz sand grains. *Bull. Geol. Soc. Am.*, **82**, 3395-3406.
- Mariano, A.N. (1978) The application of cathodoluminescence for carbonatite exploration and characterization. In: C.J.Braga (Ed.), *Proceedings of International Symposium on Carbonatites, 1st, Pocos de Caldas, Minas Gerais, Brasil, June 1976*, 39-57. Brasilia, Brasil Departamento Nacional da Produção Mineral.
- Mariano, A.N. (1989) Economic geology of rare earth elements. In: Lipin, B.R. and McKay, G.A. (Eds.), *Geochemistry and Mineralogy of rare earth elements, Reviews in Mineralogy*, **21**, 309-337.
- Marshall, D.J. (1988) *Cathodoluminescence of geological materials*. Boston, Unwin Hyman, 54-56.
- Maslenikov, A.V. and Kotov, N.V. (1991) Recrystallization on natural matamict zircon under different thermodynamic conditions. *Int. Congr. Appl. Min.*, **1**, Paper 33.
- Maurice, O.D. (1949) Transport and deposition of the non-sulphide vein minerals. V. Zirconium minerals. *Econ. Geol.*, **44**, 721-731.
- Medenbach, O. (1976) *Geochimie der elemente in zirkon und ihre räumliche verteilung - Eine untersuchung mit der electronenstrahlmikrosonde*. MSc Thesis, Ruprecht Karl Universität, Heidelberg.
- Michael, P.J. (1988) Partition coefficients for rare earth elements in mafic minerals of high silica rhyolites: The importance of accessory mineral inclusions. *Geochim. Cosmochim. Acta.*, **52**, 275-282.
- Murali, A.V., Parthasarathy, R., Mahadevan, T.M., and Sankar Das, M. (1983) Trace element characteristics, REE patterns and partition coefficients of zircons from different geological environments - A case study on Indian zircons. *Geochim. Cosmochim. Acta*, **47**, 2047-2052.
- Nagasawa, H. (1970) Rare earth concentrations in zircons and apatites and the their host dacites and granites. *Earth Planet. Sci. Lett.*, **9**, 359-364.
- Nicholls, J. and Carmichael, I.S.E. (1969) Peralkaline acid liquids: A petrological study. *Contrib. Mineral. Petrol.*, **20**, 268-294.
- Nickel, E. (1978) The present status of cathodoluminescence as a tool in sedimentology. *Minerals Sci. Eng.*, **10**, 73-100.
- Ohnenstetter, M., Ohnenstetter, D., Vidal, Ph., Cornichet, J., Hermitte, D., Mace, J. (1981) Crystallization and age of zircon from Corsican ophiolitic albitites: consequence for oceanic expansion in Jurassic times. *Earth. Planet. Sci.*, **54**, 397-408.
- Ono, A. (1976) Chemistry and zoning of zircon from some Japanese granitic rocks. *J. Jap. Assoc. Min. Pet. Econ. Geol.*, **71**, 6-17.
- Ortoleva, P.J. (1990) Role of attachment kinetic feedback in oscillatory zoning of crystals grown from melts. *Earth-Sci. Rev.*, **29**, 3-8.
- Owen, M.R. (1987) Hafnium content of detrital zircons, a new tool for provenance studies. *J. Sed. Petrol.*, **57**, 824-830.

- Paranto, J.N., and Patton, C.E. (1981) Methods for the grinding and polishing of sphere samples. *Rev. Sci. Instrum.*, **52**, 262-264.
- Petersen, J.S. (1980) Rare-element fractionation and petrogenetic modelling in charnockite rocks, Southwest Norway. *Contrib. Mineral. Petrol.*, **73**, 161-172.
- Pidgeon, R.T. (1992) Recrystallisation of oscillatory zoned zircon: some geochronological and petrological implications. *Contrib. Mineral. Petrol.*, **110**, 463-472.
- Pidgeon, R.T. and Aftalion, M. (1978) Cogenetic and inherited zircon U-Pb systems in granite: Palaeozoic granites of Scotland and England. *Geol. J. Spec. Issue*, **10**, 183-248.
- Pidgeon, R.T., O'Neil, J.R., Silver, L.T. (1966) Uranium and lead isotopic stability in a metamict zircon under experimental hydrothermal conditions. *Science*, **154**, 1538-1540.
- Price, P.B., and Walker, R.M. (1963) A simple method of measuring low uranium concentrations in natural crystals. *Appl. Phys. Lett.*, **2**, 23-25.
- Pupin, J.P. (1980) Zircon and granite petrology. *Contrib Mineral Petrol*, **73**, 207-220.
- Pupin, J.P., Bonin, B., Tessier, M, and Turco, G. (1978) Rôle de l'eau sur les caracteres morphologiques et la cristallisation du zircon dans les granites. *Bull. Soc. Géol. Fr.*, **20**, 721-725.
- Pupin, J.P., and Turco, G. (1975) Typologie de zircon accessorie dans les roches plutoniques dioritiques, granitiques et syénitiques. Facteurs essentiels déterminant les variations typologiques. *Pétrologie*, **1**, 139-156.
- Rapp, R.P., and Watson E.B. (1986) Monazite solubility and dissolution kinetics: implications for thorium and light rare earth chemistry of felsic magmas. *Contrib. Mineral. Petrol.*, **94**, 304-316.
- Rhône-Poulenc (1987) *Rare earths reminder*. Rhône-Poulenc Chimie, Div. Minerale Fine, Dept. Terres Rares, Les Miroirs-La Défenses 92400 Courbevoie, France.
- Rimsaite, J. (1981) Isotope, scanning electron microscope, and energy dispersive spectrometer studies of heterogenous zircons from radioactive granites in the Grenville structural province, Quebec and Ontario. *Geol. Surv. Canada*, **Paper 81-1B**, 25-45.
- Ring, E.J., Hansen R.G., Steele, T.W. (1981) The preparation of a reference material of South African zirconium concentrate from Richards Bay. *National Institute for Metallurgy*, **Report 2127**, Randburg, South Africa, 1-16 + Erratum.
- Robinson, G.W. (1978) *The occurrence of rare earth elements in zircon*. Ph.d., Queen's University, Kingston, Ontario, Canada.
- Romans, P.A., Brown, L.L., White, J.C. (1975) An electron microprobe study of Yttrium, Rare Earth, and Phosphorus distribution in zoned and ordinary zircon. *Am. Min.*, **60**, 475-480.
- Rosenblum, S., and Mosier, E.L. (1983) Mineralogy and occurrence of europium-rich dark monazite. *U.S. Geol. Surv. Prof. Paper*, **1181**.
- Rubin, J.N., Henry, C.D., Price, J.G. (1989) Hydrothermal zircons and zircon overgrowth, Sierra Blanca Peaks, Texas. *Am. Min.*, **74**, 865-869.

- Sawka, W.N., and Chappel, B.W. (1988) Fractionation of uranium, thorium and rare earth elements in a vertically zoned granodiorite: Implications for heat production distribution in the Sierra Nevada batholith, California, U.S.A. *Geochim. Cosmochim. Acta*, **52**, 1131-1143.
- Saxena, S.K. (1966) Evolution of Zircons in sedimentary and metamorphic rocks. *Sedimentology*, **6**, 1-33.
- Schärer, U., and Allègre, C.J. (1983) The Palung granite (Himalaya); high-resolution U-Pb systematics in zircon and monazite. *Earth Planet. Sci. Lett.*, **63**, 423-432.
- Schreiber, H.D., Lauer, H.V., and Thanyasir, T. (1980) The redox state of cerium in basaltic magmas: An experimental study of iron-cerium interactions in silicate melts. *Geochim. Cosmochim. Acta*, **44**, 1599-1612.
- Schutte, C.E.G. (1966) Die chemiese samestelling en hafnium/zirconium verhouding van Suid-Afrikaanse Sirkone. *Bull. South African Geol. Surv.*, **46**, 1-71.
- Scogings, A.J. (1989) Peralkaline granitoid and associated alkaline mafic gneisses northwest of Eshowe, Natal. *S. Afr. J. Geol.*, **92**, 339-351.
- Scogings, A.J., and Forster, I.F. (1989) Gneissose carbonatites in the Bull's Run Complex, Natal. *S. Afr. J. Geol.*, **92**, 1-10.
- Shannon, R.D. (1976) Revised effective ionic radii and systematic studies of interatomic distances in halides and chalcogenides. *Acta Crystallogr.*, **32**, 751-767.
- Shannon, R.D., and Prewitt, C.T. (1970) Revised values of effective ionic radii. *Acta Crystallogr.*, **26**, 1046-1048.
- Silver, L.T., and Deutsch, S. (1963) Uranium-lead isotopic variations in zircon: A case study. *J. of Geology*, **71**, 721-758.
- Sinha, A.K., Wayne, D.M., and Hewitt, D.A. (1992) The hydrothermal stability of zircon: Preliminary experimental and isotopic studies. *Geochim. Cosmochim. Acta*, **56**, 3551-3560.
- Sommerauer, J. (1974) Trace element distribution patterns and the mineralogical stability of zircon. An application for combined electron microprobe techniques. *Proc. Elect. Microsc. Soc. S. Afr.*, **4**, 71-72.
- Speer J.A. (1980) Zircon. In: *Orthosilicates, Reviews of mineralogy*, **5**, 67-112.
- Steiger, R.H., and Wasserburg, J. (1966) Systematics in the  $Pb^{208}$ - $Th^{232}$ ,  $Pb^{207}$ - $U^{235}$ ,  $Pb^{206}$ - $U^{238}$  systems. *J. Geophys. Res.*, **71**, 6065-6090.
- Stevens, R.E., and Corron, M.K. (1948) Simple field test for distinguishing minerals by abrasion pH. *Am. Min.*, **33**, 31-49.
- Taylor, S.R., and McLennan, S.M. (1981) The composition and evolution of the continental crust: rare earth element evidence from sedimentary rocks. *Phil. Trans. R. Soc. Lond.*, **301**, 381-399.
- Thiel, K., Saager, R., Muff, R. (1979) Distribution of uranium in early precambrian gold-bearing conglomerates of the Kaapvaal craton, South Africa: A review of a case study for the application of fission track micromapping of uranium. *Minerals Sci.Eng.*, **11**, 225-245.

- Tilton, G.R. (1960) Volume diffusion as a mechanism for discordant lead ages. *J. Geophys. Res.*, **65**, 2933-2945.
- Tole, M.P. (1985) The kinetics of dissolution of zircon ( $ZrSiO_4$ ). *Geochim. Cosmochim. Acta*, **49**, 453-458.
- Törnroos, R. (1982) Composition of metamict zircon from Mozambique. *Bull. Geol. Soc. Finland*, **54**, 77-83.
- Towner, R.R. (1992) International Strategic Minerals Inventory Summary Report-Zirconium, *USGS circular*, **930-L**.
- US Bureau of Mines (1988) *Mineral Commodity Summaries 1988*. USBM, Washington, DC.
- van Breemen, O., Henderson, J.B., Loveridge, W.D., Thompson, P.H., (1987) U-Pb zircon and monazite geochronology and zircon morphology of granulites and granite from the Thelon Tectonic Zone, Healey Lake and Artillery Lake map areas, N.W.T. In: *Current Research*, Part A, Geol. Surv. Canada, **Paper 87-1A**, 783-801.
- Vavra, G. (1990) On the kinematics of zircon growth and its petrogenetic significance: a cathodoluminescence study. *Contrib. Mineral. Petrol.*, **106**, 90-99.
- Walker, T.R. (1979) Red colour in dune sand. In: McKee, E.D. (Ed.), A study of global sand seas. *USGS Prof. Paper*, **1052**, 61-81.
- Ward, C.D., McArthur, J.M., and Walsh, J.N. (1992) Rare earth element behaviour during evolution and alteration of the Dartmoor granite, SW England. *J. Petrol.*, **33**, 785-815.
- Watson, E.B. (1980) Some experimentally determined zircon/liquid partition coefficients for the rare earth elements. *Geochim. Cosmochim. Acta*, **44**, 895-897.
- Watson, E.B., and Harrison, T.M. (1983) Zircon saturation revisited: temperature and composition effects in a variety of crustal magma types. *Earth Planet. Sci. Lett.*, **64**, 295-304.
- Wayne, D.M., and Sinha, A.K. (1992) Stability of zircon U-Pb systematics in a greenschist-grade mylonite: An example from the Rockfish Valley Fault Zone, Central Virginia, USA. *J. Geology*, **100**, 593-603.
- Weaver, B.L., and Tarney, J. (1981) Lewisian geochemistry and Archean crustal geochemistry. *Earth Planet. Sci. Lett.*, **55**, 171-180.
- White, B.R. (1982) Two-phase measurements of saltating turbulent boundary-layer flow. *Int. J. Multiphase Flow*, **8**, 459-473.
- Woodhead, J.A., Rossman, G.R., and Silver, L.T. (1991) The metamictization of zircon: Radiation dose-dependent structural characteristics. *Am. Min.*, **76**, 74-82.
- Yada, K., Tanji, T., and Sunagawa, I. (1987) Radiation induced lattice defects in natural zircon ( $ZrSiO_4$ ) observed at atomic resolution. *Phys. Chem. Minerals*, **14**, 197-204.
- Yurimoto, H., Duke, E.F., Papike, J.J. and Shearer, C.K. (1990) Are discontinuous chondrite-normalised REE patterns in pegmatitic granite systems the results of monazite fractionation? *Geochim. Cosmochim. Acta*, **54**, 2141-2145.